



**HAL**  
open science

# Relationship between the structure and the physical properties of polymers based on furandicarboxylic acid obtained from biomass

Aurélie Bourdet

► **To cite this version:**

Aurélie Bourdet. Relationship between the structure and the physical properties of polymers based on furandicarboxylic acid obtained from biomass. Materials Science [cond-mat.mtrl-sci]. Normandie Université; Esposito, 2020. English. NNT : 2020NORMR113 . tel-03376525

**HAL Id: tel-03376525**

**<https://theses.hal.science/tel-03376525>**

Submitted on 13 Oct 2021

**HAL** is a multi-disciplinary open access archive for the deposit and dissemination of scientific research documents, whether they are published or not. The documents may come from teaching and research institutions in France or abroad, or from public or private research centers.

L'archive ouverte pluridisciplinaire **HAL**, est destinée au dépôt et à la diffusion de documents scientifiques de niveau recherche, publiés ou non, émanant des établissements d'enseignement et de recherche français ou étrangers, des laboratoires publics ou privés.



Normandie Université

## THESE

Pour obtenir le diplôme de doctorat

Spécialité : Physique

Préparée au sein de l'Université de Rouen Normandie

### Relations structure/propriétés physiques de polymères à base d'acide furandicarboxylique obtenu de la biomasse

Présentée et soutenue par  
**Aurélie BOURDET**

Thèse soutenue publiquement le 27 Mars 2020  
devant le jury composé de

Mme. Nadia LOTTI	Pr / DICAM Université de Bologne (Italie)	Rapportrice
Mme. Alice MIJA	Pr / UNS Université de Nice	Rapportrice
M. Shanmugam THIYAGARAJAN	Dr / FBR Université de Wageningen (Pays-Bas)	Examineur
M. Loïc LE PLUART	Pr / LMCT Université de Caen Normandie	Examineur
Mme. Antonella ESPOSITO	MCF / GPM Université de Rouen Normandie	Co-encadrante de thèse
M. Eric DARGENT	Pr / GPM Université de Rouen Normandie	Directeur de thèse

Thèse dirigée par Pr. Eric DARGENT et Dr. Antonella ESPOSITO  
Groupe de Physique des Matériaux, GPM UMR 6634





Normandie Université

## PhD THESIS

In partial fulfillment of the requirements for the degree of  
Doctor of Philosophy in Science

Specialty: Physics

Submitted to the University of Rouen Normandie

**Relationship between the structure and the physical properties of polymers based on furandicarboxylic acid obtained from biomass**

Presented and defended by  
**Aurélie BOURDET**

Defended on March 27, 2020  
in the presence of the dissertation committee composed of

Mrs. Nadia LOTTI	Pr / DICAM Bologna University (Italy)	Reviewer
Mrs. Alice MIJA	Pr / UNS University of Nice	Reviewer
Mr. Shanmugam THIYAGARAJAN	Dr / FBR Wageningen University (The Netherlands)	Examiner
Mr. Loïc LE PLUART	Pr / LMCT University of Caen Normandy	Examiner
Mrs. Antonella ESPOSITO	Assistant Pr / GPM University of Rouen Normandy	PhD co-supervisor
Mr. Eric DARGENT	Pr / GPM University of Rouen Normandy	PhD supervisor

Supervised by Pr. Eric DARGENT and Dr. Antonella ESPOSITO  
Groupe de Physique des Matériaux, GPM UMR 6634



# Table of Contents

<b>General Introduction</b> .....	<b>1</b>
<b>CHAPTER I: State of Art</b>	
Introduction .....	8
I.1. Context.....	10
I.1.1. Some historical dates concerning PET and PEF.....	10
I.1.2. Characteristics and some properties of PET and 2,5-PEF .....	11
I.2. Synthesis of PET .....	14
I.2.1. Esterification .....	14
I.2.2. Transesterification .....	15
I.2.3. Pre-polycondensation .....	15
I.2.4. Polycondensation.....	16
I.3. Synthesis of PEF .....	17
I.3.1. The road to 2,5-FuranDiCarboxylic Acid (2,5-FDCA) .....	18
I.3.2. The road to 2,4-furandicarboxylic acid (2,4-FDCA) .....	21
I.3.3. From ethanol to bio-ethylene glycol.....	22
I.3.4. Mixtures of 2,5- and 2,4-FDCA isomers .....	22
References .....	24
<b>CHAPTER II: Materials and Methods</b>	
II.1. Materials .....	30
II.2. Characterization methods.....	31
II.2.1. Structural characterization .....	31
II.2.1.1. Nuclear Magnetic Resonance (NMR) .....	31
II.2.1.2. Fourier-Transform InfraRed Spectroscopy (FTIR) .....	31
II.2.1.3. Polarized Optical Microscopy (POM) .....	32
II.2.1.4. Wide Angle X-ray Diffraction (WAXD).....	33

II.2.2. Thermal analyses .....	35
II.2.2.1. ThermoGravimetric Analysis (TGA).....	35
II.2.2.2. Modulated ThermoGravimetric Analysis (MTGA).....	36
II.2.2.3. Differential Scanning Calorimetry (DSC) .....	37
II.2.2.4. Modulated Temperature-DSC (MT-DSC).....	40
II.2.2.5. Dielectric Relaxation Spectroscopy (DRS) .....	43
II.2.2.6. Thermo-Stimulated Depolarization Currents (TSDC) .....	49
References .....	55

### **CHAPTER III: The Glass Transition**

Introduction .....	61
III.1. Generalities on the glassy state and the glass transition.....	61
III.1.1. Amorphous state.....	61
III.1.2. Glass formation.....	63
III.2. Nature of the glass transition and essential experimental aspects .....	65
III.3. Main structural transitions .....	69
III.3.1. Elementary acts of movement in polymers .....	69
III.3.2. Main and secondary transitions in polymers .....	70
III.3.3. Experimental manifestation of transitions .....	71
III.4. Structural relaxation .....	71
III.4.1. Introduction .....	71
III.4.2. Phenomenological description of the relaxation by enthalpy loss .....	72
III.4.3. Experimental features of the structural relaxation.....	73
III.4.4. Non-exponential behavior and memory effect.....	74
III.4.5. Non-linearity .....	76
III.5. Models for structural relaxation .....	77
III.5.1. Kohlrausch-Williams-Watts (KWW) .....	77
III.5.2. Vogel-Fulcher-Tammann (VFT) .....	78
III.5.3. Classification of glass-forming liquids (strong vs. fragile) .....	79

III.5.4.	Tool-Narayanaswamy-Moynihan (TNM).....	80
III.5.5.	Donth's approach.....	83
III.5.5.1.	Introduction .....	83
III.5.5.2.	Theoretical approach .....	85
III.5.5.3.	Extension of the Donth's model.....	90
References	.....	95

## **CHAPTER IV: Physical Characterization and Investigation of the Molecular Mobility in Amorphous PEFs**

Introduction	.....	103
IV.1.	Preliminary analyses .....	103
IV.1.1.	FTIR spectroscopy .....	103
IV.1.2.	Thermal stability .....	104
IV.1.2.1.	Conventional TGA .....	104
IV.1.2.2.	Determination of the activation energy by MTGA.....	106
IV.1.3.	Thermal properties .....	108
IV.1.3.1.	Conventional DSC.....	108
IV.1.3.2.	Mixing laws .....	111
IV.2.	Molecular dynamics in amorphous PEFs .....	113
IV.2.1.	Investigation of the amorphous phases by MT-DSC .....	113
IV.2.2.	Segmental relaxation investigated by DRS.....	115
IV.2.2.1.	Shape parameters $\alpha$ and $\beta$ of the $\alpha$ relaxation.....	120
IV.2.2.2.	Dielectric relaxation strength $\Delta\varepsilon_{HN}$ .....	122
IV.2.2.3.	Relaxation map .....	125
IV.2.2.4.	Characterization of the $\beta$ relaxation .....	126
IV.2.2.5.	Characterization of the $\alpha$ relaxation .....	126
IV.2.2.6.	Fragility index $m$ .....	127
IV.2.2.7.	Cooperativity length $\xi_\alpha$ and cooperativity degree $N_\alpha$ .....	129
IV.2.3.	Thermally Stimulated Depolarization Current (TSDC).....	130
IV.2.3.1.	Impact of the incorporation of 2,4-FDCA DME on glass transition signature	130
IV.2.3.2.	Relaxation map combining the three techniques .....	132
IV.2.3.3.	Activation energies .....	133
IV.2.3.4.	Fragility indexes .....	134



Conclusion.....	135
References .....	137

## **CHAPTER V: The Crystalline State**

Introduction .....	146
V.1. Semi-crystalline morphologies.....	147
V.1.1. Morphologies of static crystallization: lamellae and spherulites.....	147
V.1.2. Other conditions of crystallization .....	150
V.2. Theory of germination and crystal growth .....	151
V.2.1. Germination .....	152
V.2.2. Growth .....	154
V.2.3. The growth rate $G$ .....	155
V.3. The melting .....	158
V.4. Global theories about crystallization kinetics .....	160
V.4.1. Introduction .....	160
V.4.2. Geometric approach .....	161
V.4.3. Isothermal conditions: the Avrami's theory.....	162
V.4.4. Cooling at a constant rate: the Ozawa's theory.....	162
References .....	163

## **CHAPTER VI: Crystallization Behavior of PEFs**

Introduction .....	168
VI.1. Structural comparison between PET and 2,5-PEF.....	168
VI.1.1. $\alpha$ form of 2,5-PEF .....	170
VI.1.2. $\alpha'$ form of 2,5-PEF .....	171
VI.1.3. $\beta$ form of 2,5-PEF .....	171
VI.2. Comparison of PET and 2,5-PEF in terms of conformation.....	173
VI.3. Comparison of PET and 2,5-PEF in terms of thermal properties .....	174

VI.4. Study of the crystallization kinetics .....	175
VI.4.1. DSC analyses .....	175
VI.4.2. Crystallization kinetics.....	180
VI.4.3. Morphology and growth of spherulites .....	182
VI.5. Characterization of the amorphous phase during crystallization .....	187
VI.6. Influence of the position of the carbonyl group with respect to the furan ring on the crystal structure .....	189
Conclusion.....	192
References .....	193
<b>Conclusions and Prospects .....</b>	<b>199</b>
<b>Abbreviations List .....</b>	<b>203</b>
<b>Annexes .....</b>	<b>209</b>
Annex A: <sup>1</sup> H RMN Spectra .....	209
Annex B: MDS Calculation.....	212
Annex C: Scientific Communications.....	213

# General Introduction

Thermoplastics polymers are materials currently used in packaging, automotive, electronics, and medical applications. Due to the peculiar environmental context required by sustainable innovations, the amount of polymers that are currently under development to be partially or entirely based on renewable resources occupy an increasingly important place in the eco-design of materials to replace plastics from petrochemicals <sup>1-5</sup>.

One of the most interesting bio-based polymers is Poly (Lactic Acid) (PLA), a material generally made from corn starch <sup>6</sup>. Already widely used in the medical field, PLA is particularly interesting for the manufacture of scaffolds for tissue regeneration or systems for drug delivery, mainly because it is biocompatible and bioresorbable. At the beginning of its development, PLA was considered as a potential substitute for Poly (Ethylene Terephthalate) (PET); however its thermal, mechanical and barrier properties have subsequently been found insufficient, and should still be improved to meet food packaging requirements, for instance. Poly (Ethylene 2,5-Furandicarboxylate) (2,5-PEF) (obtained from the reaction of 2,5-furandicarboxylic acid and ethylene glycol) is nowadays considered as the most promising sustainable alternative to PET, as it exhibits similar (and sometimes significantly better) mechanical and barrier properties compared to both PLA and PET <sup>4,7,8</sup>. Knoop et al. <sup>9</sup> showed that 2,5-PEF has a value of the Young's modulus that is similar to PET, the only drawback being its brittle behavior at breaking. One possibility to reduce brittleness could be provided by a new generation of copolyesters obtained from the mixture of the two main isomers of furandicarboxylic acid (FDCA): 2,5-FDCA and 2,4-FDCA.

This work aims at exploring, for the first time, some physical properties of such a series of copolyesters, but also at gaining a deeper understanding about the corresponding homopolymers, in particular about the less-known 2,4-PEF.

This manuscript is organized as follows:

Chapter I introduces the context of the study and provides the different routes to synthesize PET and PEF.

Chapter II presents the materials and the experimental techniques used in this work. The first section is devoted to the materials, the second illustrates the tools and measurement procedures

Chapter III reminds the fundamentals about glass transition and a summary of the main physical models generally used to describe structural relaxation.

Chapter IV reports the results of the physical characterization and the main findings about the molecular mobility of quenched (fully amorphous) PEFs. A discussion is proposed about the thermal stability evaluated by TGA and MTGA, as well as the thermal behavior observed by DSC. The second part of the chapter is focused on the investigation of the molecular dynamics through a correlation between three techniques: MT-DSC, DRS and TSDC. The influence of the position of the carbonyl group with respect to the furan ring on the relaxation phenomena is discussed.

Chapter V is an overview on polymer crystallization and the crystalline state. A description of the steps involved in the crystallization process (germination, crystal growth, secondary crystallization) is provided, along with a summary of the theories used to evaluate the crystallization kinetics.

Chapter VI reports the results obtained about the crystallization kinetics of PEFs, followed by a detailed characterization of the behavior of the amorphous phase as a consequence of crystallization. A tentative discussion about the influence of the position of the carbonyl group with respect to the furan ring on the crystalline structure is also provided.

Finally, some general conclusions and prospects are proposed.

These Appendixes provide:

- $^1\text{H}$  RMN spectra of the PEF samples;
- MDS Calculation method;
- The scientific production related to this work.

This work was financially supported by the Normandy Region and the European Regional Development Fund (Fond Européen de Développement Régional, FEDER) within the frame of the project “Solution pour la Conception et l’Analyses de Matériaux à Propriétés Innovantes” (SCAMPI). It was carried out in the EIRCAP (Equipe Internationale de Recherche et de Caractérisation des Amorphes et des Polymères) research group, SDP (Systèmes Désordonnés et Polymères), “Groupe de Physique des Matériaux” (GPM-UMR CNRS 6634), University of Rouen Normandy.

## References

- (1) Belgacem, M. N.; Gandini, A. *Monomers, Polymers and Composites from Renewable Resources*; Elsevier, 2011.
- (2) Wilsens, C. H. R. M.; Noordover, B. A. J.; Rastogi, S. Aromatic Thermotropic Polyesters Based on 2,5-Furandicarboxylic Acid and Vanillic Acid. *Polymer* **2014**, *55* (10), 2432–2439.  
<https://doi.org/10.1016/j.polymer.2014.03.033>.
- (3) Gubbels, E.; Jasinska-Walc, L.; Koning, C. E. Synthesis and Characterization of Novel Renewable Polyesters Based on 2,5-Furandicarboxylic Acid and 2,3-Butanediol. *J. Polym. Sci. A Polym. Chem.* **2013**, *51* (4), 890–898.  
<https://doi.org/10.1002/pola.26446>.
- (4) Wu, J.; Eduard, P.; Thiyagarajan, S.; Jasinska-Walc, L.; Rozanski, A.; Guerra, C. F.; Noordover, B. A. J.; van Haveren, J.; van Es, D. S.; Koning, C. E. Semicrystalline Polyesters Based on a Novel Renewable Building Block. *Macromolecules* **2012**, *45* (12), 5069–5080.  
<https://doi.org/10.1021/ma300782h>.
- (5) Matos, M.; Sousa, A. F.; Fonseca, A. C.; Freire, C. S. R.; Coelho, J. F. J.; Silvestre, A. J. D. A New Generation of Furanic Copolyesters with Enhanced Degradability: Poly(Ethylene 2,5-Furandicarboxylate)-Co-Poly(Lactic Acid) Copolyesters. *Macromol. Chem. Phys.* **2014**, *215* (22), 2175–2184.  
<https://doi.org/10.1002/macp.201400175>.
- (6) Madhavan Nampoothiri, K.; Nair, N. R.; John, R. P. An Overview of the Recent Developments in Polylactide (PLA) Research. *Bioresource Technology* **2010**, *101* (22), 8493–8501.  
<https://doi.org/10.1016/j.biortech.2010.05.092>.
- (7) Gandini, A.; Silvestre, A. J. D.; Neto, C. P.; Sousa, A. F.; Gomes, M. The Furan Counterpart of Poly(Ethylene Terephthalate): An Alternative Material Based on Renewable Resources. *J. Polym. Sci. A Polym. Chem.* **2009**, *47* (1), 295–298.  
<https://doi.org/10.1002/pola.23130>.
- (8) Pellis, A.; Haernvall, K.; Pichler, C. M.; Ghazaryan, G.; Breinbauer, R.; Guebitz, G. M. Enzymatic Hydrolysis of Poly(Ethylene Furanoate). *Journal of Biotechnology* **2016**, *235*, 47–53.  
<https://doi.org/10.1016/j.jbiotec.2016.02.006>.
- (9) Knoop, R. J. I.; Vogelzang, W.; van Haveren, J.; van Es, D. S. High Molecular Weight Poly(Ethylene-2,5-Furanoate); Critical Aspects in Synthesis and Mechanical Property Determination. *J. Polym. Sci. Part A: Polym. Chem.* **2013**, *51* (19), 4191–4199.  
<https://doi.org/10.1002/pola.26833>.

### Content

Introduction .....	8
I.1. Context.....	10
I.1.1. Some historical dates concerning PET and PEF.....	10
I.1.2. Characteristics and some properties of PET and 2,5-PEF .....	11
I.2. Synthesis of PET .....	14
I.2.1. Esterification .....	14
I.2.2. Transesterification .....	15
I.2.3. Pre-polycondensation .....	15
I.2.4. Polycondensation.....	16
I.3. Synthesis of PEF .....	17
I.3.1. The road to 2,5-FuranDiCarboxylic Acid (2,5-FDCA) .....	18
I.3.2. The road to 2,4-furandicarboxylic acid (2,4-FDCA) .....	21
I.3.3. From ethanol to bio-ethylene glycol.....	22
I.3.4. Mixtures of 2,5- and 2,4-FDCA isomers .....	22
References .....	24

## Introduction

Biobased polymers got the attention from many scientists and industrials during the last two decades. The environmental concerns are the main driving-forces for this trend. The depletion of fossil resources associated to climate changes raised awareness on the international level. To take actions against global warming, a common agreement has been endorsed by some countries through the Kyoto Protocol in 1997 (entered into force in 2005) in order to reduce greenhouse gas emissions. Ten years later, a directive called REACH (Registration, Evaluation, and Authorization of Chemicals) was ratified in the frame of the European Union, increasing the legislation on safety and chemical management with the objective to promote the principles and procedures of Green Chemistry. However, a paradox still exists between the worldwide awareness and the constant global increase of oil consumption driven by a consumption-addicted society. In the run to produce new materials with improved properties in a well-known context of planned obsolescence, the oil consumption increases and the role played by the industry prevails. The entire world economy relies on a locative business in which petroleum industry is dominant. In 2006, J. Goldemberg <sup>1</sup> (a leading expert on energy and environment issues) reported that “the world’s energy system is a 1.5 trillion dollars market dominated by fossil fuels”. Since leaving behind the comfortable system established so far is not going to happen soon, the only pathway to follow consists in developing performant materials from renewable biological sources.

Crude oil, coal, natural gas and biomass are the only sources of carbon we have. For chemical and fuel productions only, the biomass can be used either as a raw material or after selective conversion of its main constituents (essentially lignocellulosic materials) into a series of platform chemicals. The vegetal biomass is naturally structured throughout complex biological processes which exploit the carbon from atmospheric CO<sub>2</sub> and produce energy from water and sunlight. Among the natural polymers present in plants, cellulose is probably the most explored and exploited, and still very promising for new material applications, since the physical-chemical properties of cellulose offer a wide potential for innovation.

It has been estimated that almost half of the carbon in the biosphere is in the form of cellulose <sup>2</sup>. Indeed, petrochemical feedstocks can be considered as “natural”, because they are formed from biomass over geological time frames.



The problem is that the rate at which biomass is converted to fossil resources ( $>10^5$  years) is in total imbalance with the rate at which they are consumed (1-10 years). The use of annually renewable biomass to produce polymers, chemicals, and fuels as an adjunct to fossil resources would help balancing the rate of  $\text{CO}_2$  fixation with the rate at which  $\text{CO}_2$  is released. Furthermore, if we manage the biomass resources effectively by making sure that we plant (trees, crops) more than we use, we can eventually reverse the  $\text{CO}_2$  rate equation and move towards a net balance between  $\text{CO}_2$  fixation/sequestration and release due to consumption. [Figure I.1](#) illustrates these concepts for the global cycling of carbon, and demonstrates that the use of annually renewable biomass resources for the production of polymers, chemicals, and fuels represents a positive contribute to sustainability and global carbon recycling.

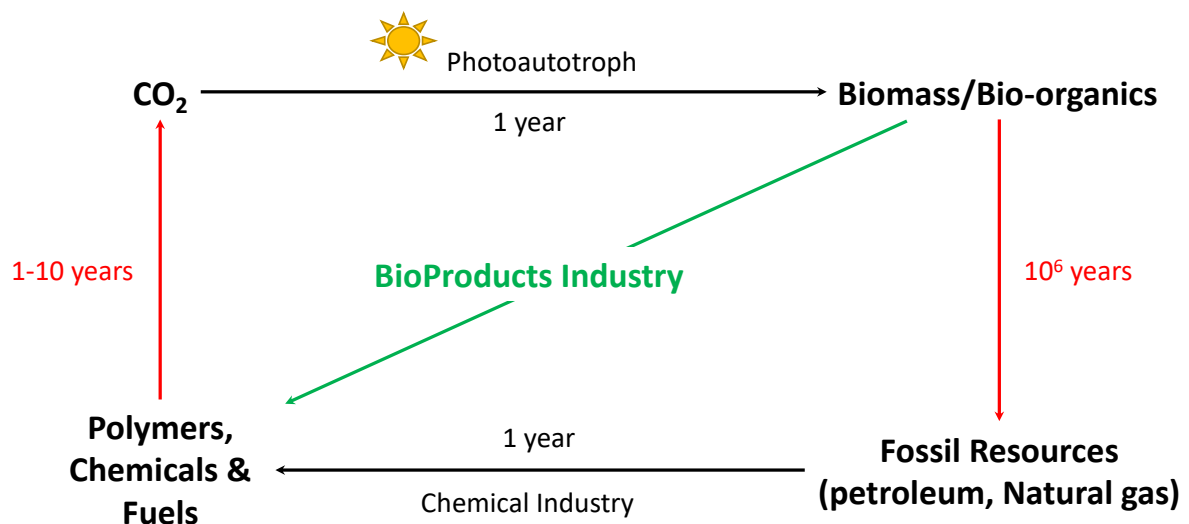


Figure I.1: Global carbon cycling.<sup>3</sup>

## I.1. Context

Poly (Ethylene Terephthalate) (PET) is a thermoplastic polyester generally produced from petroleum. Its strength and good barrier properties have made it a material of choice for packaging. Thanks to its properties and good recyclability, this polymer has quickly become a sort of plastic industry's giant. Unsurprisingly, PET is commonly taken as a term of comparison for new polyesters. In the last years, it has been suggested that petroleum-based PET no longer meets the industrial environmental requirements. As a result, research activities have been oriented towards the quest for alternatives to replace it. It is already possible to produce a greener, more sustainable version of PET, either partially or entirely biosourced (bio-PET) <sup>4</sup>. In the meantime, another 100% biobased polyester with similar (if not better) properties made the news, the Poly (Ethylene-2,5-Furandicarboxylate) (2,5-PEF), or better known by the abbreviation of only PEF.

### I.1.1. Some historical dates concerning PET and PEF

The main historical dates for PET and PEF in the food-packaging sector of plastic bottles are the following:

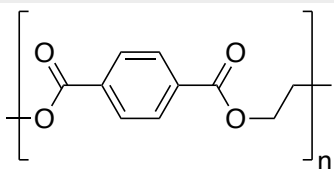
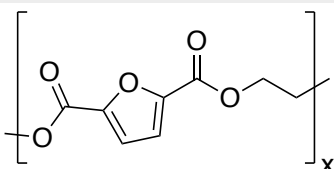
- 1941: PET is patented by two British chemists, John Rex Whinfield and James Tenant Dickson. The invention remained secret for strategic reasons related to the Second World War.
- 1945: The PET patent is purchased by the American group Dupont de Nemours.
- 1950: Dupont de Nemours patents a new brand (Dacron).
- 1984: PET replaces PVC (Poly (Vinyl Chloride)) for the production of bottles. PET is massively produced for the first-time.
- 2009: The "Coca Cola Plant Bottle" made of partially biobased PET is released on the market.
- June 2011: A partnership between Toray and Gevo to produce renewable biobased PET on a laboratory scale is initiated. Bottles and plastic films are successfully produced. Toray produces PET by using terephthalic acid from para-xylene (p-xylene) and Methyl Ethyl Glycol (MEG).
- December 8, 2011: Avantium opens a PEF Pilot Plant in Geleen, The Netherlands.

- December 15, 2011: Coca-Cola, Ford, Heinz, NIKE, and P&G announce the creation of a PTC (PET Technology Collaborative) plant to produce a 100% bio-based PET following the success of the “Plant Bottle”.
- 2014: The Avantium consortium for PEF production is officially started.
- 2016: Avantium plans the production of FDCA and PEF.

### 1.1.2. Characteristics and some properties of PET and 2,5-PEF

PET and 2,5-PEF are both thermoplastic polyesters. Both have been patented more than 60 years ago, but being petroleum-based PET has been widely used since the 1990s, while bio-sourced PEF is still under development. [Table I.1](#) summarizes the main characteristics of PET and 2,5-PEF.

**Table I.1: Characteristics of PET and 2,5-PEF.**

Characteristics	PET	2,5-PEF
<b>Name</b>	Poly (ethylene terephthalate)	Poly (ethylene furanoate) Poly (ethylene-2,5-furandicarboxylate)
<b>Definition</b>	Synthetic polyester produced by polycondensation of Ethylene Glycol (EG) with TerePhthalic Acid (TPA), or EG and DiMethyl Terephthalate (DMT)	Synthetic polyester produced by polycondensation of Ethylene Glycol (EG) and 2,5-FuranDiCarboxylic Acid (2,5-FDCA)
<b>Family</b>	Semi-crystalline thermoplastic	Semi-crystalline thermoplastic
<b>Chemical formula</b>	 $[C_{10}H_8O_4]_n$	 $[C_8H_6O_5]_x$
<b>Invention</b>	Patented in 1941	Patented in 1946
<b>Raw materials</b>	EG: derived from vegetal oil, sugar beet or sugarcane TPA: derived from petroleum	EG: derived from sugarcane 2,5-FDCA: derived from plants and agricultural residues

Since the 1990s, PET has become the main plastic for transparent bottles, especially used for mineral water, fruit juice, or sodas. The environmental concerns and the attempt to reduce the consumption of fossil resources gradually pushed to develop 2,5-PEF with the aim of replacing PET in bottle production. Interestingly, the properties of 2,5-PEF are similar (sometimes even better) than PET, as summarized in [Table I.2](#).

**Table I.2: Main properties of PET and 2,5-PEF.**

Properties	PET	2,5-PEF	Comparison
<b>Composition</b>	Petroleum-based or partially biobased	100% biobased	The production of PEF only uses renewable resources
<b>Density</b>	1.38 g/cm <sup>3</sup>	1.43 g/cm <sup>3</sup>	PEF is denser than PET
<b>Ease of use</b>	Flexible	PEF gets stiffer under stress	PEF is less flexible than PET but it is more resistant
<b>Optical</b>	Colorless	Colorless	Identical
<b>Young's modulus</b>	2.1-3.1 GPa	3.0-3.5 GPa	PEF is 1.1 to 1.4 times stiffer than PET
<b>Thermal</b>	$T_g = 73-76\text{ }^\circ\text{C}$ $T_m = 243-247\text{ }^\circ\text{C}$ $T_d = 413-445\text{ }^\circ\text{C}$	$T_g = 79-85\text{ }^\circ\text{C}$ $T_m = 209-211\text{ }^\circ\text{C}$ $T_d = 389-411\text{ }^\circ\text{C}$	PEF has more interesting thermal properties for industrial applications
<b>Toxicity</b>	Non-toxic and food-safe, UV sensitive	Non-toxic and food-safe	Similar
<b>Permeability</b>	Good barrier to humidity but poor barrier to gases	Barrier to O <sub>2</sub> : 11 times better than PET Barrier to CO <sub>2</sub> : 19 times better than PET Barrier to H <sub>2</sub> O: 2 times better than PET	PEF has better barrier properties

Properties	PET	2,5-PEF	Comparison
<b>End-of-life</b>	Mechanical or chemical recycling	Mechanical recycling (identical to PET) or chemical recycling by depolymerization	Chemical recycling is easier for PEF than PET due to the different composition
<b>Emission of greenhouse gases</b>	During the extraction of raw materials, processing and transport	During the extraction of raw materials, processing and transport, but compensation during the growth of raw materials	The vegetable origin of PEF reduces carbon emissions by 50 to 70%
<b>Price</b>	\$1.350/ton (2018)	\$2.700/ton (2015)	A \$1.200/ton difference between PEF production cost and PET market price

2,5-PEF and PET are comparable in many different ways. However, PEF is definitely better than PET in terms of thermal, mechanical and barrier properties, which are critical aspects for the production of food-safe containers. Moreover, PEF represents a more sustainable material compared to PET.

## I.2. Synthesis of PET

During the Second World War, the production of nylon became complicated and the industrials had to find a substitute. The development of PET made it possible to take on this challenge by offering a material that can be used in many different ways. Since the 1970's, PET has known a huge success and has quickly become unavoidable. PET is a polyester obtained by polycondensation. Condensation is a chemical reaction consisting in the union of two molecules, or two parts of molecules, leading to the formation of a condensate, here a polymer, by elimination of a small molecule (water for example). Polycondensation is a sequence of condensation steps performed to carry out a polymerization. At each step, two monomers with two active centers on either side of their structures react together according to a condensation reaction, in order to form dimers, then oligomers that grow longer and longer, to finally obtain a polymer. On an industrial scale, PET is obtained according to the following stages:

- Esterification (or transesterification)
- Pre-polycondensation
- Polycondensation

The raw material used to synthesize PET is oil. It takes about 1.9 kg of crude oil to obtain 1 kg of PET.

### I.2.1. Esterification

PET synthesis consists in the reaction between a bifunctional acid (terephthalic acid (TPA)) and a bifunctional alcohol (ethylene glycol (EG)) to form dimers according to the following scheme:

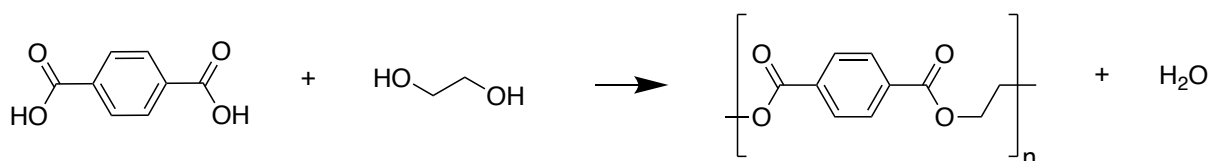


**Figure I.2: Polycondensation of PET by esterification.**

The first step consists in the esterification of TPA carboxyl end-groups with the hydroxyl end-groups of EG. The mechanism of this esterification can be explained as follows: the oxygen atom of the alcohol function of EG carries a partial negative charge.

The carbon atom of the acid function of TPA carries a partial positive charge. As a consequence, the oxygen atom attacks the carbon atom to form a covalent bond.

Since the carbon atom cannot exceed four bonds, the hydroxyl group of TPA separates from the rest of the molecule and combines with the hydrogen previously linked to the attacking oxygen to get stabilized. The result is the formation of a water molecule and an ester linkage between EG and TPA. Esterification is in equilibrium with hydrolysis (the inverse reaction), therefore it is important to continuously remove the water produced during the esterification under vacuum.

### 1.2.2. Transesterification

The second possible pathway is transesterification (Figure I.3). In this case, the synthesis consists in the reaction between a diester (dimethyl terephthalate (DMT)) and a bifunctional alcohol (ethylene glycol (EG)) to form dimers. Indeed, DMT is an ester which is transformed into another ester.

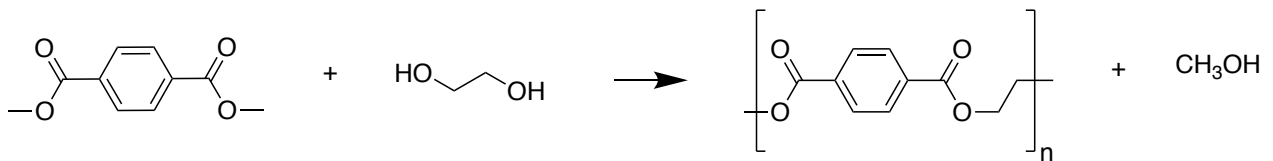


**Figure I.3: Polycondensation of PET by transesterification.**

The only difference between esterification and transesterification is the product eliminated during the reaction (water vs. methanol).

### 1.2.3. Pre-polycondensation

The dimers obtained by esterification or transesterification are then used for the pre-polymerization (or pre-polycondensation) step. This step is carried out under vacuum and allows the dimers to condense to form longer chains (oligomers).

### 1.2.4. Polycondensation

This step is intended to merge the chains formed in the previous steps to form long polymer chains, and occurs in the melt state. A catalyst is typically used to increase the polycondensation rate. However, the use of catalysts strongly influences the crystallization rate, which is intimately linked to the mass transport of volatiles compounds contained in the melt phase; besides, the viscosity progressively increases with the increase in the chain length, and the diffusion also slows down. A higher temperature would solve this issue, but could also cause thermal degradation.

For more details, Rieckmann and Völker <sup>5</sup> wrote a book chapter on the PET polymerization, with information about the catalysts employed and the corresponding reaction kinetics. The degradation occurring at high temperature is a problem shared by all thermoplastic polymers. The activation energies of the primary degradation reactions are higher than the ones associated to the polycondensation reactions. The increasing temperature leads to an increase in the extent of a possible primary degradation. Moreover, the reverse reaction of condensation (glycolysis) should be carefully avoided, as well as any other side reactions. For these reasons, an additional step (a solid-state polymerization) is generally used to achieve the polycondensation in the solid state and then increase the molecular weight.



### I.3. Synthesis of PEF

On the industrial scale, research activities about PEF have started in the 1950s<sup>6</sup>. Indeed, only 5 years after the first patent about the application on PET by Calico Printers Association in 1941<sup>7</sup>, a similar patent about the application of FDCA-based polyesters was published by Celanese Corporation of America in 1946<sup>8</sup>. The process was detailed, but no properties were communicated except the melting point reported at 205-210 °C. In 1958, a Japanese laboratory published the protocol to synthesize PEF with glycols of different lengths<sup>9</sup>. The melting temperature associated to 2,5-PEF crystals was reported to be around 220-225 °C. Twenty years later, in 1978, Moore et al.<sup>10</sup> used another protocol for PEF synthesis. The (trans)esterification was performed with 1,6-hexane diol and dimethyl-2,5-furandicarboxylate (DMF). Later on, two Japanese patents were submitted in 2005<sup>11</sup> and 2007<sup>12</sup> describing the synthesis of three different polyesters (PEF, Poly (Propylene Furandicarboxylate) (PPF) and Poly (Butylene Furandicarboxylate) (PBF)). The different recipes used to synthesize PEF cannot be compared due to insufficient data communicated. In 2006, Avantium (Dutch Biotech) did an important breakthrough in 5-(Hydroxymethyl)-2-Furaldehyde (HMF) production and conversion into building blocks, such as FDCA. Being aware of the great potential of 2,5-PEF, in 2009, Gandini et al.<sup>13</sup> published the first comparison between the properties of PET and 2,5-PEF.

Similarly to PET, the synthesis of PEF requires two reaction steps, i.e. a (trans)esterification followed by a polycondensation. As for PET, two pathways have been explored: the direct esterification of FDCA, and the transesterification of DMF (Figure I.4). Due to the advantages of DMF synthesis (good selectivity and high yield), this route has been widely studied<sup>13-15</sup>.

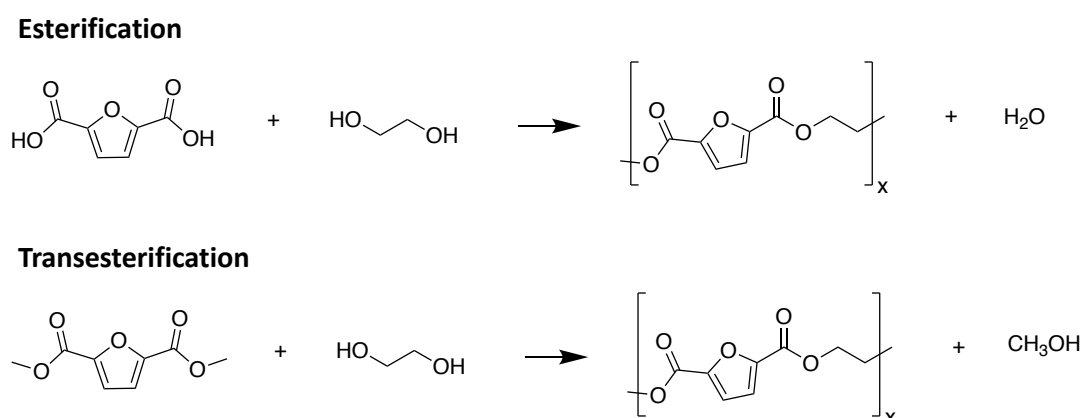


Figure I.4: Polycondensation of 2,5-PEF.

### 1.3.1. The road to 2,5-FuranDiCarboxylic Acid (2,5-FDCA)

Currently, the majority of academic and industrial efforts in the development of 2,5-FDCA are concentrated on synthesis routes that start from food-grade carbohydrates, in particular fructose, via 5-(hydroxymethyl)-2-furaldehyde (HMF) <sup>16</sup>. Since a competition with food production is undesirable for ethical as well as economic reasons, we are rather focusing on the use of non-edible feed stocks, such as lignocellulose, agro residues, and aqueous biomass (e.g. algae) for the production of chemicals and polymer building blocks.

The synthesis of 2,5-FDCA firstly reported goes back to almost 150 years ago, to a paper published by Fittig and Heinzelman <sup>17</sup> in 1876; in that work, 2,5-FDCA was obtained through the reaction of mucic (galactaric) acid with hydrobromic acid (Figure I.5, route 2). However, this route provided relatively low isolated yields, and galactaric acid is (not yet) readily available, therefore little attention has been paid to this route. The situation may change if availability of aldaric acid increased, which is likely to happen because aldaric acid can be obtained from pectin or alginate streams produced by bio-refineries <sup>18,19</sup>. Currently, the most widely explored synthetic route to 2,5-FDCA is based on the catalytic oxidation of HMF <sup>20</sup>, which can be obtained from the acid-catalyzed cyclodehydration of C6 sugars like glucose and fructose (Figure I.5, route 1) <sup>16,21,22</sup>. Fructose is generally preferred to glucose, because it provides substantially higher yields of HMF. The only reported process that efficiently converts glucose into HMF requires Cr-based catalysts in combination with ionic liquids, which is undesirable from a sustainability point of view <sup>23-25</sup>. On the other hand, fructose can be economically obtained by acid-catalyzed hydrolysis of sucrose or inulin, or by the hydrolysis of starch (and potentially cellulose) followed by a selective partial isomerization of glucose to fructose (Figure I.5, route 1) <sup>26,27</sup>. However, the use of sucrose or starch is highly undesirable given their primary use as food component.

In the last decades, much attention has been paid to the development of new technologies to produce HMF with high yields according to efficient and cost-effective methods <sup>16,22</sup>; indeed, HMF is not only a potentially low-cost precursor to 2,5-FDCA, but can also serve as a renewable platform chemical. Furthermore, HMF is a precursor for the next generation of biofuels, e.g. 2,5-DiMethylFuran (DMF), 5-EthoxyMethylFurfural (EMF), Ethyl Levulinate (EL), and  $\gamma$ -ValeroLactone (gVL) <sup>28</sup>.

Till now, no large-scale process for the industrial production and commercialization of HMF is operational, although various companies have announced plans for pilot-scale facilities. The relatively poor stability of HMF under acidic conditions often leads to the formation of undesired by-products, e.g. Levulinic Acid (LA), Formic Acid (FA), and insolubles such as furan resins and humins. These by-products complicate the downstream processing of HMF, and therefore reduce the yield <sup>16,29</sup>. To address these issues, companies like Avantium started developing alternative technologies to dehydrate fructose and glucose in organic solvents (e.g. methanol), yielding more stable HMF-ethers and HMF-esters as products <sup>6,30,31</sup>.

In addition to routes 1 and 2, a third route based on the use of hemicellulose and its components (C5 sugars) is also possible (Figure I.5, route 3). Given that hemicellulose is a non-edible, not easily fermentable residue from both lignocellulosic biorefineries and the agro-food industry, it is an attractive feedstock for the production of chemicals. Analogously to the cyclodehydration of C6 sugars to HMF, the cyclodehydration of C5 sugars (e.g. xylose and arabinose) yields 2-furaldehyde or furfural. Whereas HMF is still in a developmental stage, furfural is already produced for commercial purposes on a 400-500 000 tons scale using agro-residues like bagasse as feedstock <sup>32</sup>. The oxidation of furfural gives 2-Furoic Acid (FA) (or the corresponding ester, depending on the reaction conditions) in high yields; however, the subsequent introduction of a carbon substituent in the C5 structure is non-trivial (Figure I.5, route 3b).

Older reports on the hydroxymethylation using *p*-formaldehyde in sulphuric acid, or the chloromethylation via the Blanc reaction, gave only low to moderate yields of 5-hydroxymethyl- or 5-chloromethyl-2-furoic acid, respectively <sup>9,33</sup>. Subsequently, a further oxidation step is required to transform this intermediate into 2,5-FDCA <sup>34</sup>.

A more attractive synthetic approach for the conversion of FA into 2,5-FDCA is based on the well-known Henkel reaction (Figure I.5, route 3a). This process is based on the thermal disproportionation of alkaline salts of aromatic carboxylates to give the symmetrical aromatic dicarboxylate.

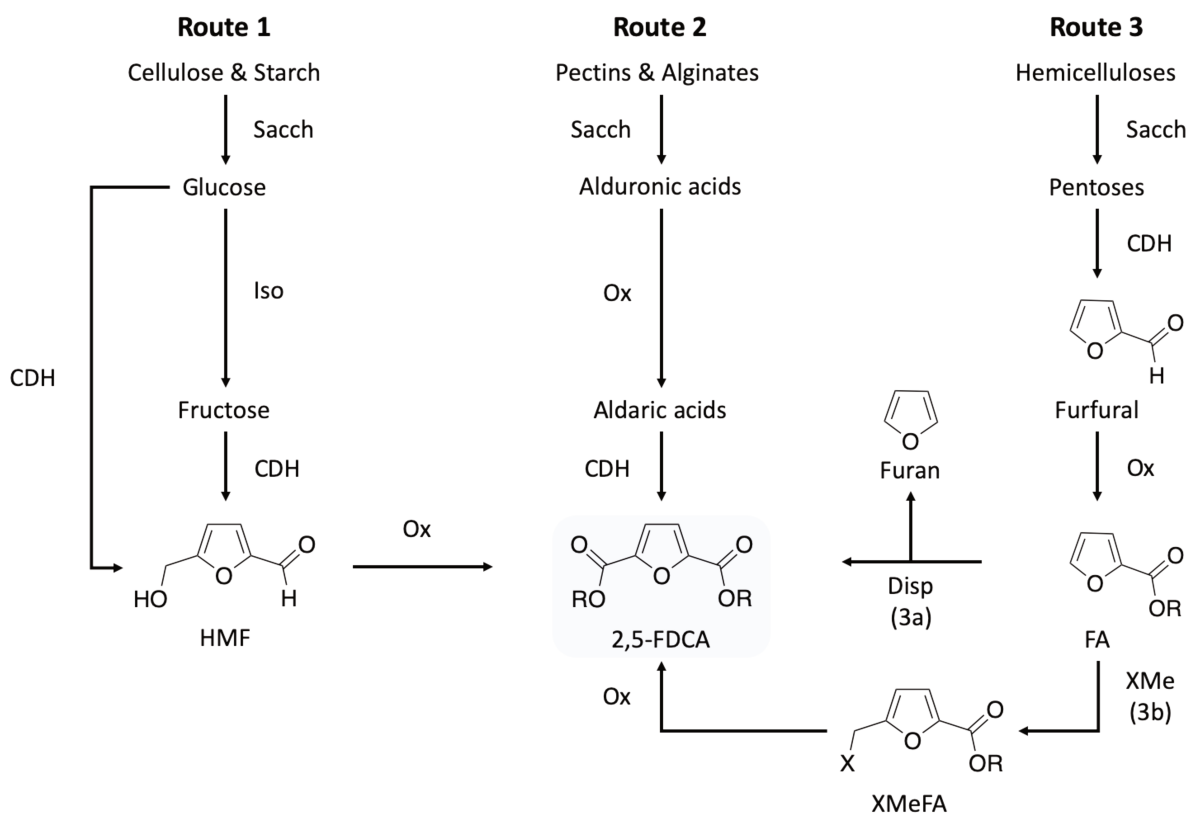


**Figure I.5: Reported routes to 2,5-FDCA starting from different carbohydrate sources.** <sup>35</sup>

Sacch = saccharification; CDH = cyclodehydration; Iso = isomerization; Ox = oxidation; XMe = chloromethylation (X = Cl) or hydroxymethylation (X = OH)

### 1.3.2. The road to 2,4-furandicarboxylic acid (2,4-FDCA)

Thiyagarajan et al.<sup>35</sup> reported that, during the Henkel reaction, depending on the reaction conditions, different FDCA isomers are obtained: the 2,5-isomer (70%), the 2,4-isomer (30%), and to a lesser extent the 3,4-isomer (< 5%) (Figure I.6). The separation of the 2,5- and 2,4-isomers is feasible. Whereas there is an increasing amount of literature on the synthesis and properties of 2,5-FDCA-based polyesters, only a very few reports can be found on either 2,4- or 3,4-FDCA-based polyesters. In 1958, Hachihama et al.<sup>9</sup> reported an example of 2,4-FDCA-based polyester obtained with EG (2,4-PEF); however, the main properties of this polymer, such as the glass transition temperature ( $T_g$ ) and the molecular weight, were not provided. A few decades later, Chaabouni et al.<sup>36</sup> synthesized poly (butylene-furan-3,4-dicarboxylate) from 3,4-FDCA and 1,4-butanediol, but unfortunately only a value of glass transition temperature was reported, without any further investigation.

By controlling the reaction conditions (time and temperature), 2,4-FDCA can be obtained separately by a treatment of methyl-3-bromocoulate with a base, by following the previously reported procedure<sup>37</sup>.

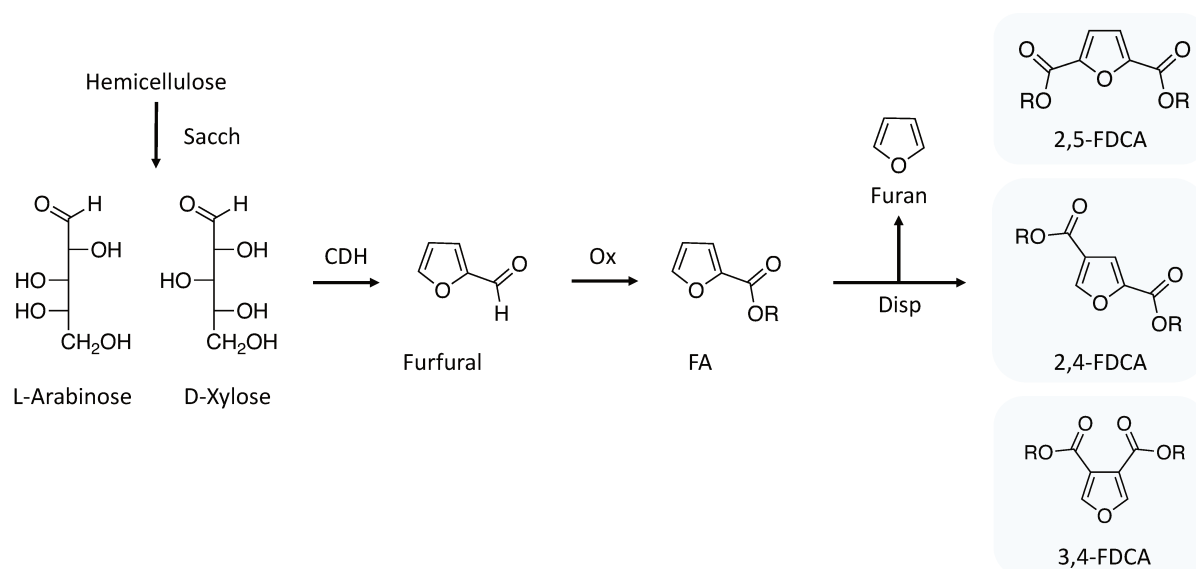


**Figure I.6: Synthesis of FDCAs via disproportionation reaction.**<sup>35</sup>

Sacch = saccharification; CDH = cyclodehydration; Ox = oxidation; Disp = disproportionation

### 1.3.3. From ethanol to bio-ethylene glycol

EG can be obtained from biobased feedstock through several pathways. The main pathway starts from ethanol, which is the most abundant non-food chemical issued from the biomass. The fermentation of sugars also leads to ethanol. Ethylene is then obtained from ethanol by any acid-catalyzed dehydration <sup>16</sup>. This reaction can produce diethyl ether as the main by-product, which can still be converted in ethylene. Afterwards, bio-EG is obtained through the oxidation of ethylene. Another possible pathway consists in using the glycerol which is either naturally present in fatty acid esters, or can be obtained via hydrolysis or methanolysis of triglycerides. Then, EG is obtained from glycerol by hydrogenolysis in the presence of a catalyst <sup>38</sup>. In this case, high hydrogen pressure, high temperature and noble metal catalysts are needed, which limits the industrial application. Another route consists in using glycerol and Raney nickel as a catalyst <sup>39</sup>. This pathway gives a yield of about 50-70 % even if performed under ambient pressure, with diluted aqueous glycerol and no hydrogen; moreover, the catalysts are not expensive and they can be recovered by a suitable treatment. Recently, Liquid Light announced a new collaboration with The Coca-Cola Company to produce EG from carbon dioxide, which is a route that considerably reduces the costs of EG production and is prone to collaborations with companies that produce waste CO<sub>2</sub> (e.g. ethanol producers) <sup>40</sup>.

### 1.3.4. Mixtures of 2,5- and 2,4-FDCA isomers

In 2014, Thiagarajan et al. <sup>41</sup> showed that the position of the carboxylic group on the furan ring has no influence on the reactivity of the FDCA isomers, as proved by the fact that all of them can equally lead to high molecular weight homopolyesters. Moreover, preliminary results obtained by thermal analysis revealed that the homopolyester derived from 2,4-FDCA (2,4-PEF), even if amorphous, has a glass transition temperature that is very similar to 2,5-PEF and PET, which are both semi-crystalline. These results encouraged to further investigate the potential properties of different copolyesters derived from a mixture of 2,5- and 2,4-FDCA isomers. Two approaches can be used to obtain different mixtures of 2,5- and 2,4-FDCA isomers:

- Henkel mixtures: directly obtained from the Henkel reaction, they can be used without further processing <sup>35</sup>.
- Physical mixtures: the isomers are isolated and then physically mixed on purpose, i.e. with specific ratios of the 2,4- and 2,5- FDCA isomers.

Whatever the approach, the copolyesters can be synthesized similarly to the homopolyesters, i.e. by polycondensation after transesterification.

This research thesis will focus on properties of different homo- and co-polyesters derived from several physical mixtures of 2,5- and 2,4-FDCA isomers.

## References

- (1) Goldemberg, J. The Promise of Clean Energy. *Energy Policy* **2006**, *34* (15), 2185–2190. <https://doi.org/10.1016/j.enpol.2005.03.009>.
- (2) Dutta, S.; Pal, S. Promises in Direct Conversion of Cellulose and Lignocellulosic Biomass to Chemicals and Fuels: Combined Solvent–Nanocatalysis Approach for Biorefinary. *Biomass and Bioenergy* **2014**, *62*, 182–197. <https://doi.org/10.1016/j.biombioe.2013.12.019>.
- (3) Narayan, R. Drivers for Biodegradable/Compostable Plastics & Role of Composting in Waste Management & Sustainable Agriculture <https://msu.edu/user/narayan/germanycompostingpaper.htm> (accessed Jan 8, 2020).
- (4) Pang, J.; Zheng, M.; Sun, R.; Wang, A.; Wang, X.; Zhang, T. Synthesis of Ethylene Glycol and Terephthalic Acid from Biomass for Producing PET. *Green Chem.* **2016**, *18* (2), 342–359. <https://doi.org/10.1039/C5GC01771H>.
- (5) Rieckmann, T.; Völker, S. PET Polymerization-Catalysis, Reaction Mechanisms, Kinetics, Mass Transport and Reactor Design. *Modern Polyesters: Chemistry and Technology of Polyesters and Copolymers* **2003**.
- (6) Gruter, G. J. M.; Dautzenberg, F. Method for the Synthesis of 5-Alkoxyethyl Furfural Ethers and Their Use. US8133289B2, March 13, 2012.
- (7) Whinfield, J.; Dickson, J. Improvements Relating to the Manufacture of Highly Polymeric Substances. *British Patent* **1941**, 578, 079.
- (8) Drewitt, J.; Lincoln, J. Improvements in Polymers. *UK Patent GB621971-A* **1946**, 12.
- (9) Hachihama, Y.; Shono, T.; Hyono, K. Synthesis of Polyesters Containing Furan Ring. *Technol. Repts. Osaka Univ* **1958**, *8*, 475–480.
- (10) Moore, J. A.; Kelly, J. E. Polyesters Derived from Furan and Tetrahydrofuran Nuclei. *Macromolecules* **1978**, *11* (3), 568–573. <https://doi.org/10.1021/ma60063a028>.
- (11) Matsuda, K.; Matsuhisa, H.; Horie, H.; Komuro, T. Polymer Compound and Method of Synthesizing the Same. US8143355B2, March 27, 2012.
- (12) Kato, S.; Kasai, A. Method for Producing Polyester Resin Including Furan Structure. *Japanese patent application JP2008/291244* **2007**, 24.
- (13) Gandini, A.; Silvestre, A. J. D.; Neto, C. P.; Sousa, A. F.; Gomes, M. The Furan Counterpart of Poly(Ethylene Terephthalate): An Alternative Material Based on Renewable Resources. *J. Polym. Sci. A Polym. Chem.* **2009**, *47* (1), 295–298. <https://doi.org/10.1002/pola.23130>.
- (14) Papageorgiou, G. Z.; Tsanaktsis, V.; Bikiaris, D. N. Synthesis of Poly(Ethylene Furandicarboxylate) Polyester Using Monomers Derived from Renewable Resources: Thermal Behavior Comparison with PET and PEN. *Phys. Chem. Chem. Phys.* **2014**, *16* (17), 7946–7958. <https://doi.org/10.1039/C4CP00518J>.
- (15) Knoop, R. J. I.; Vogelzang, W.; van Haveren, J.; van Es, D. S. High Molecular Weight Poly(Ethylene-2,5-Furanoate); Critical Aspects in Synthesis and Mechanical Property Determination. *J. Polym. Sci. Part A: Polym. Chem.* **2013**, *51* (19), 4191–4199. <https://doi.org/10.1002/pola.26833>.



- (16) van Putten, R.-J.; van der Waal, J. C.; de Jong, E.; Rasrendra, C. B.; Heeres, H. J.; de Vries, J. G. Hydroxymethylfurfural, A Versatile Platform Chemical Made from Renewable Resources. *Chem. Rev.* **2013**, *113* (3), 1499–1597.  
<https://doi.org/10.1021/cr300182k>.
- (17) Fittig, R.; Heinzelmann, H. Production of 2, 5-Furandicarboxylic Acid by the Reaction of Fuming Hydrobromic Acid with Mucic Acid under Pressure. *Chem Ber* **1876**, *9*, 1198.
- (18) van Es, D. S. Rigid Biobased Building Blocks. *J. renew mater* **2013**, *1* (1), 61–72.  
<https://doi.org/10.7569/JRM.2012.634108>.
- (19) van der Klis, F.; Frissen, A. E.; van Haveren, J.; van Es, D. S. Waste Not, Want Not: Mild and Selective Catalytic Oxidation of Uronic Acids. *ChemSusChem* **2013**, *6* (9), 1640–1645.  
<https://doi.org/10.1002/cssc.201300367>.
- (20) Chheda, J. N.; Román-Leshkov, Y.; Dumesic, J. A. Production of 5-Hydroxymethylfurfural and Furfural by Dehydration of Biomass-Derived Mono- and Poly-Saccharides. *Green Chem.* **2007**, *9* (4), 342–350.  
<https://doi.org/10.1039/B611568C>.
- (21) Antal, M. J.; Leesomboon, T.; Mok, W. S.; Richards, G. N. Mechanism of Formation of 2-Furaldehyde from d-Xylose. *Carbohydrate Research* **1991**, *217*, 71–85.  
[https://doi.org/10.1016/0008-6215\(91\)84118-X](https://doi.org/10.1016/0008-6215(91)84118-X).
- (22) Kuster, B. F. M. 5-Hydroxymethylfurfural (HMF). A Review Focussing on Its Manufacture. *Starch - Stärke* **1990**, *42* (8), 314–321.  
<https://doi.org/10.1002/star.19900420808>.
- (23) Degirmenci, V.; Pidko, E. A.; Magusin, P. C. M. M.; Hensen, E. J. M. Towards a Selective Heterogeneous Catalyst for Glucose Dehydration to 5-Hydroxymethylfurfural in Water: CrCl<sub>2</sub> Catalysis in a Thin Immobilized Ionic Liquid Layer. *ChemCatChem* **2011**, *3* (6), 969–972.  
<https://doi.org/10.1002/cctc.201000426>.
- (24) Corma, A.; Iborra, S.; Velty, A. Chemical Routes for the Transformation of Biomass into Chemicals. *Chem. Rev.* **2007**, *107* (6), 2411–2502.  
<https://doi.org/10.1021/cr050989d>.
- (25) Pidko, E. A.; Degirmenci, V.; van Santen, R. A.; Hensen, E. J. M. Glucose Activation by Transient Cr<sup>2+</sup> Dimers. *Angewandte Chemie International Edition* **2010**, *49* (14), 2530–2534.  
<https://doi.org/10.1002/anie.201000250>.
- (26) Rosatella, A. A.; Simeonov, S. P.; Frade, R. F. M.; Afonso, C. A. M. 5-Hydroxymethylfurfural (HMF) as a Building Block Platform: Biological Properties, Synthesis and Synthetic Applications. *Green Chem.* **2011**, *13* (4), 754–793.  
<https://doi.org/10.1039/C0GC00401D>.
- (27) Zakrzewska, M. E.; Bogel-Łukasik, E.; Bogel-Łukasik, R. Ionic Liquid-Mediated Formation of 5-Hydroxymethylfurfural—A Promising Biomass-Derived Building Block. *Chem. Rev.* **2011**, *111* (2), 397–417.  
<https://doi.org/10.1021/cr100171a>.
- (28) Dutta, S.; De, S.; Saha, B. A Brief Summary of the Synthesis of Polyester Building-Block Chemicals and Biofuels from 5-Hydroxymethylfurfural. *ChemPlusChem* **2012**, *77* (4), 259–272.  
<https://doi.org/10.1002/cplu.201100035>.

- (29) Sidhpuria, K. B.; Daniel-da-Silva, A. L.; Trindade, T.; Coutinho, J. A. P. Supported Ionic Liquid Silica Nanoparticles (SILnPs) as an Efficient and Recyclable Heterogeneous Catalyst for the Dehydration of Fructose to 5-Hydroxymethylfurfural. *Green Chem.* **2011**, *13* (2), 340–349.  
<https://doi.org/10.1039/C0GC00690D>.
- (30) Gruter, G. J. M.; Manzer, L. E.; Dias, A. S. V. D. S.; Dautzenberg, F.; Purmova, J. Hydroxymethylfurfural Ethers and Esters Prepared in Ionic Liquids. US8314260B2, November 20, 2012.
- (31) Sanborn, A. J.; Howard, S. J. Conversion of Carbohydrates to Hydroxymethylfurfural (Hmf) and Derivatives. US20090156841A1, June 18, 2009.
- (32) Zeitsch, K. J. *The Chemistry and Technology of Furfural and Its Many By-Products*; Elsevier, 2000.
- (33) Sanderson, R. D.; Schneider, D. F.; Schreuder, I. Synthesis and Evaluation of Dialkyl Furan-2,5-Dicarboxylates as Plasticizers for PVC. *Journal of Applied Polymer Science* **1994**, *53* (13), 1785–1793.  
<https://doi.org/10.1002/app.1994.070531308>.
- (34) Moldenhauer, O.; Trautmann, G.; Irion, W.; Pfluger, R.; Döser, H.; Mastaglio, D.; Marwitz, H. Beiträge Zur Furanchemie I. *Justus Liebigs Annalen der Chemie* **1953**, *580* (3), 169–190.  
<https://doi.org/10.1002/jlac.19535800302>.
- (35) Thiyagarajan, S.; Pukin, A.; Haveren, J. van; Lutz, M.; Es, D. S. van. Concurrent Formation of Furan-2,5- and Furan-2,4-Dicarboxylic Acid: Unexpected Aspects of the Henkel Reaction. *RSC Advances* **2013**, *3* (36), 15678–15686.  
<https://doi.org/10.1039/C3RA42457J>.
- (36) Chaabouni, A.; Gharbi, S.; Abid, M.; Boufi, S.; El Gharbi, R.; Gandini, A. Polyesters Furaniques: Transitions et Stabilité Thermiques. *J Soc Chim Tunisie* **1999**, *4*, 547–558.
- (37) Feist, F. Ueberführung Der Cumalinsäure in Ein Isomeres Der Dehydroschleimsäure. *Berichte der deutschen chemischen Gesellschaft* **1901**, *34* (2), 1992–1996.  
<https://doi.org/10.1002/cber.190103402110>.
- (38) Zhou, C.-H. (Clayton); Beltramini, J. N.; Fan, Y.-X.; Lu, G. Q. (Max). Chemoselective Catalytic Conversion of Glycerol as a Biorenewable Source to Valuable Commodity Chemicals. *Chem. Soc. Rev.* **2008**, *37* (3), 527–549.  
<https://doi.org/10.1039/B707343G>.
- (39) Yin, A.-Y.; Guo, X.-Y.; Dai, W.; Fan, K.-N. The Synthesis of Propylene Glycol and Ethylene Glycol from Glycerol Using Raney Ni as a Versatile Catalyst. *Green Chemistry - GREEN CHEM* **2009**, *11*.  
<https://doi.org/10.1039/b913395j>.
- (40) Liquid Light partners with Coca-Cola to accelerate development of bio-MEG - bioplastics MAGAZINE  
<https://www.bioplasticsmagazine.com/en/news/meldungen/20150722-LiquidLight-partners-with-Coca-Cola.php> (accessed Jan 13, 2020).
- (41) Thiyagarajan, S.; Vogelzang, W.; Knoop, R. J. I.; E. Frissen, A.; Haveren, J. van; Es, D. S. van. Biobased Furandicarboxylic Acids (FDCAs): Effects of Isomeric Substitution on Polyester Synthesis and Properties. *Green Chemistry* **2014**, *16* (4), 1957–1966.  
<https://doi.org/10.1039/C3GC42184H>.

### Content

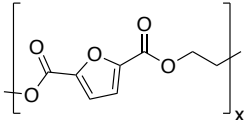
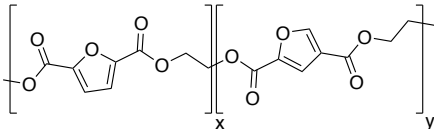
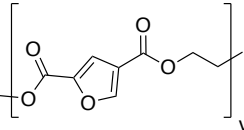
II.1. Materials .....	30
II.2. Characterization methods.....	31
II.2.1. Structural characterization .....	31
II.2.1.1. Nuclear Magnetic Resonance (NMR) .....	31
II.2.1.2. Fourier-Transform InfraRed Spectroscopy (FTIR) .....	31
II.2.1.3. Polarized Optical Microscopy (POM) .....	32
II.2.1.4. Wide Angle X-ray Diffraction (WAXD) .....	33
II.2.2. Thermal analyses .....	35
II.2.2.1. ThermoGravimetric Analysis (TGA).....	35
II.2.2.2. Modulated ThermoGravimetric Analysis (MTGA).....	36
II.2.2.3. Differential Scanning Calorimetry (DSC) .....	37
II.2.2.4. Modulated Temperature-DSC (MT-DSC).....	40
II.2.2.5. Dielectric Relaxation Spectroscopy (DRS) .....	43
II.2.2.6. Thermo-Stimulated Depolarization Currents (TSDC) .....	49
References .....	55

This chapter present all the samples analyzed in this work. The experimental techniques and protocols used are described in details.

## II.1. Materials

This work consists in investigating the properties of different homo- and co-polyesters derived from several mixtures of 2,5- and 2,4-FDCA isomers. Five polyesters were studied more in details: two homopolymers (2,5-PEF and 2,4-PEF) and three copolymers (obtained with mixtures of 2,5- and 2,4-FDCA, as reported in [Table II.1](#)). All the samples were synthesized at the Food and Biobased Research (FBR), Wageningen University and Research (WUR)(The Netherlands). The copolymers were obtained by physical mixtures, i.e. the isomers were isolated and then physically mixed on purpose, with specific ratios of the 2,4- and 2,5-FDCA isomers. Both the homopolyesters and copolyesters were synthesized with the same protocol, i.e. by polycondensation (transesterification). The chemical structures, weight-average molecular weights ( $\overline{M}_w$ ) and number-average molecular weights ( $\overline{M}_n$ ), determined by NMR (Nuclear Magnetic Resonance) and Gel Permeation Chromatography (GPC) respectively, are reported in [Table II.1](#). The ratio of 2,5-FDCA DME (dimethyl-2,5-furandicarboxylate) for each sample was verified by  $^1\text{H}$  NMR (the corresponding spectra are reported in [Annex A](#)).

**Table II.1: Ratio of 2,5-FDCA DME, weight-average molecular weights ( $\overline{M}_w$ ) and number-average molecular weights ( $\overline{M}_n$ ) of 2,5-PEF, 2,4-PEF and 2,5-2,4-copolymers.**

Sample	Repeating unit	2,5-FDCA	$\overline{M}_w$	$\overline{M}_n$
		DME ratio (%)	(kg/mol)	(kg/mol)
2,5-PEF		100	18.2	15.3
PE-2,5[90]-2,4[10]F		90	14.7	9.1
PE-2,5[85]-2,4[15]F		85	15.2	9.2
PE-2,5[50]-2,4[50]F		50	23.3	13.2
2,4-PEF		0	11.4	8.5

Prior to characterization, all the freshly prepared samples were dried for 3 days at  $T_g + 15\text{ }^\circ\text{C}$  (i.e.  $95\text{ }^\circ\text{C}$ ) to remove any residual solvents used during the synthesis, and stored in a desiccator over phosphorus pentoxide ( $\text{P}_2\text{O}_5$ ) until measurement.

## II.2. Characterization methods

### II.2.1. Structural characterization

#### II.2.1.1. Nuclear Magnetic Resonance (NMR)

Nuclear Magnetic Resonance (NMR) spectroscopy uses the magnetic properties of selected atomic nuclei to provide information about the structure, dynamics, reaction state and chemical environment of molecules. The intramolecular magnetic field surrounding any given atom in a molecule has a different resonance frequency, which in turns can be related to the electronic structure of the molecule.

In this work, NMR spectroscopy was used to verify the position of the carbonyls on the furan ring and to determine the ratio of each isomer introduced in the copolymer. NMR spectra were recorded on a Bruker Advance III spectrometer operating at 400.17 MHz ( $^1\text{H}$ ) and 100.62 MHz ( $^{13}\text{C}$ ) (the analyses were performed at FBR, WUR). Solutions were prepared using deuterated dimethylsulfoxide (DMSO, Sigma Aldrich) and chloroform ( $\text{CHCl}_3$ , Sigma Aldrich) as solvents.

#### II.2.1.2. Fourier-Transform InfraRed Spectroscopy (FTIR)

Fourier-Transform InfraRed spectroscopy (FTIR) provides information on the chemical structure of organic molecules, as well. The vibrational frequencies of different chemical bonds are typically evidenced through characteristic absorption peaks. Before FTIR analyses, the samples (in the form of powders) were compacted into pellets of 5 mm diameter using an Atlas Series Evacuatable Pellet Press Die under a pressure of 1 ton. FTIR spectra were then collected at room temperature in Attenuated Total Reflectance (ATR) mode on a Thermo Scientific Nicolet iS10 spectrometer equipped with a diamond crystal. Absorbance spectra were obtained by collecting 16 scans with a resolution of  $4\text{ cm}^{-1}$ . A blank scan was recorded prior to sample scan to correct for atmospheric  $\text{CO}_2$  and  $\text{H}_2\text{O}$ .

### II.2.1.3. Polarized Optical Microscopy (POM)

Polarized Optical Microscopy (POM) is a simple technique to observe anisotropic structures at the micro-scale. In addition to the conventional optical microscope, which uses visible light passing through a system of lenses, POM involves polarized light and requires the use of two additional polarizing filters: the first one placed between the light source and the sample (polarizer), and the second one placed between the sample and the eyepiece or camera (analyzer). These filters are used to restrict the electro-magnetic field vectors constituting visible light to a single plane, as shown in [Figure II.1](#). As a result, all the electro-magnetic field vectors hitting the sample are vibrating in the same plane (polarized light). In a cross-polarization setup, the analyzer and the polarizer are oriented perpendicularly. This position aims at blocking the unwanted electro-magnetic field vectors. Consequently, when no sample is placed in the light field, the polarized light is blocked by the analyzer, resulting in no visible light in the eyepiece (black image). The same result is obtained if the sample placed in the light field is isotropic (as in the case of amorphous polymers). However, when birefringent samples, such as anisotropic materials (as in the case of semi-crystalline polymers) is placed in the light field, the restricted electro-magnetic field vectors passing through the sample are transmitted according to many different perpendicular planes. Therefore, the electro-magnetic field vectors that are parallel to the polarization direction of the analyzer can go through and be visualized in the eyepiece.

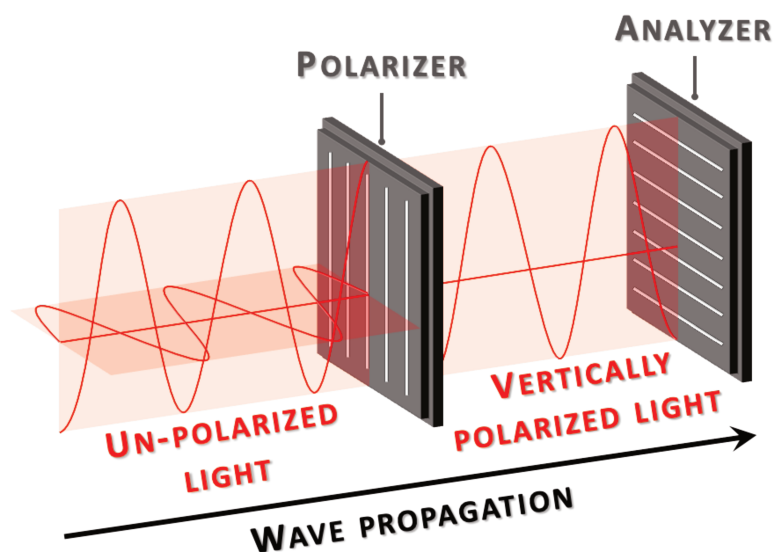


Figure II.1: Schematic representation of a light wave passing through crossed polarizers. <sup>1</sup>

In this work, POM observations were performed by using a universal Nikon EPI-illuminator with Nikon M plan lenses ( $\times 2.5$ ;  $\times 5$ ;  $\times 10$ ) connected with a Sony CCD-IRIS camera, either in transmission or reflection mode. The samples were placed between two glass slides, then heated onto a Mettler FP82HT hot stage to 250 °C at 10 °C/min and annealed for 3 min. Finally, the samples were quickly placed on a second hot stage (Mettler FP90 central processor) previously set as the defined crystallization temperature ( $T_c$ ). Pictures were analyzed by the software ImageJ.

#### II.2.1.4. Wide Angle X-ray Diffraction (WAXD)

The diffraction of X-rays is a non-destructive analytical technique that allows determining the spatial arrangement of atoms or larger molecules in ordered structures. With regards to polymer science, the diffraction of X-rays is used to detect and quantify the crystalline fractions that can be found within amorphous matrixes, as in the case of semi-crystalline polymers. In [Figure II.2](#) shows the principle of WAXD: the sample is hit by an X-ray beam forming an angle  $\theta$  with its surface, and intensity of the diffracted X-rays is measured as a function of the scattered angle  $2\theta$ . Any arrangement of atoms or molecules, either regular or irregular, diffracts and scatters the X-rays to different directions as a consequence of elastic interactions; the extent of these two phenomena (diffraction and scattering) depends on the degree of order/disorder of the crystalline stacking and the its connections avec the surrounding amorphous environment.

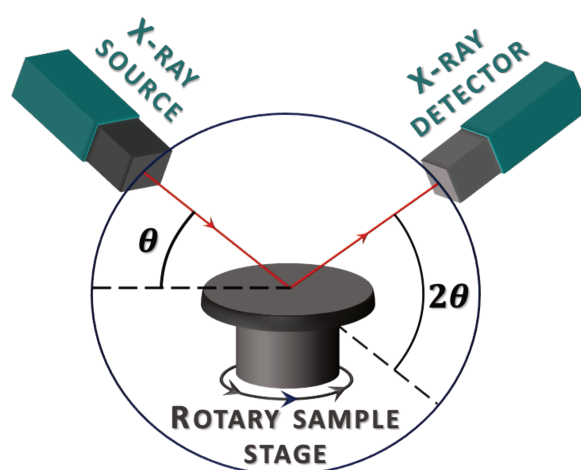


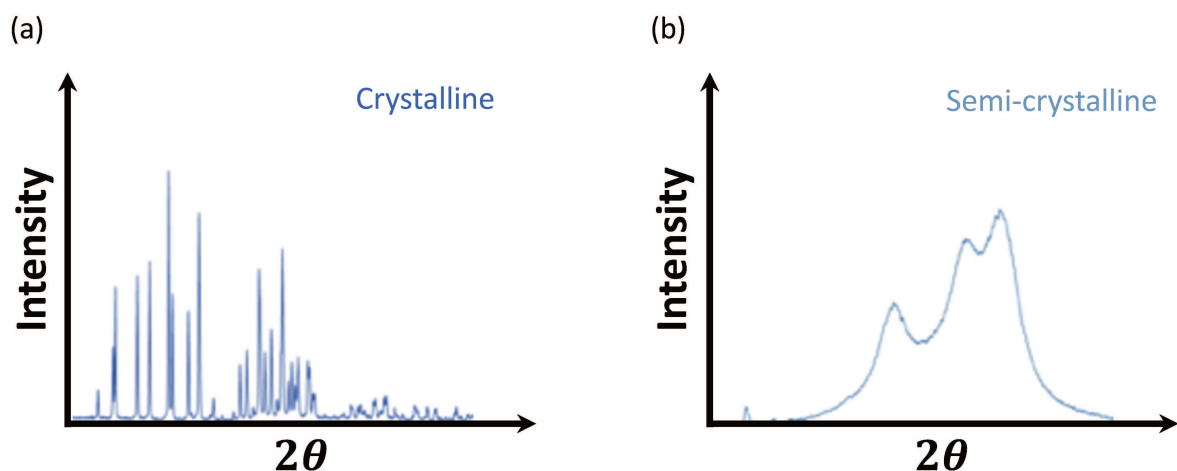
Figure II.2: Schematic representation of a WAXD setup with a Bragg-Brentano  $\theta - 2\theta$  geometry. <sup>1</sup>

As a consequence, in semi-crystalline polymers, high intensity diffraction peaks associated to low intensity halos are recorded, as illustrated in Figure II.3. For each diffraction peak, a relation between the angle of diffraction and the distance between crystalline layers can be established through the Bragg's law <sup>2</sup>:

$$n\lambda = 2d\sin(\theta) \quad (II.1)$$

Where  $n$  is the order of diffraction,  $\lambda$  is the wavelength of the incident X-ray beam,  $d$  is the spacing between successive diffracting planes and  $\theta$  is the angle between the incident X-ray beam and the sample.

In the case of crystalline materials, such as metals, the diffractogram only contains narrow peaks related to the diffraction generated by a sequence of crystalline planes, and therefore positioned at characteristic angular values (Figure II.3 (a)). Polymers cannot be perfectly crystalline; in the case of semi-crystalline materials, in addition to the diffraction peaks, a second contribution is observed due to the presence of an amorphous phase (amorphous halo). The amorphous halo is due to the fact that the amorphous phase, which is disordered, diffuses the incident X-rays in all directions, and therefore the recorded intensity varies continuously and statistically with the diffraction angle (Figure II.3 (b)). Obviously, the diffractogram of a completely amorphous material only contains an amorphous halo (Figure II.3 (c)).





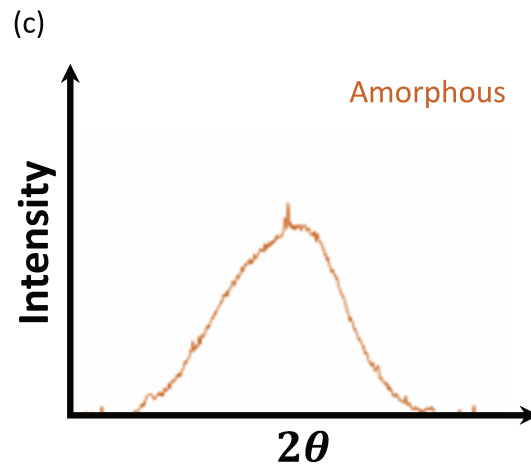


**Figure II.3: Typical XRD diffractograms of (a) crystalline; (b) semi-crystalline; (c) amorphous samples.**

In this work, WAXD measurements were performed on a D8 Advance Bruker AXS diffractometer in a Bragg-Brentano configuration. The generator was set at 35 kV and 40 mA and the copper  $Co_{K\alpha}$  radiation ( $\lambda = 0.179 \text{ \AA}$ ) was selected. The measurements were run at room temperature within the range  $2\theta = 5^\circ\text{-}50^\circ$ . The scan speed was fixed at 1 s/step with increments of 0.01  $^\circ$ /step.

## II.2.2. Thermal analyses

### II.2.2.1. ThermoGravimetric Analysis (TGA)

ThermoGravimetric Analysis (TGA) is a technique in which the variations of sample mass (mass loss or gain) is measured as function of time and/or temperature under controlled conditions. The information about mass variation allows to highlight the different physical and chemical transitions that the sample may experience, such as degradation, dehydration, volatilization, etc. TGA is extensively used to characterize polymeric materials, in particular to determine their relative thermal stability, their moisture or additive contents, their stability with respect to oxidation, the composition of polymer blends and many other parameters required for specific applications.

In this work, TGA measurements were performed with a TGA Discovery (TA instruments). The samples were heated from room temperature to 600  $^\circ\text{C}$  at 10  $^\circ\text{C}/\text{min}$  under a flow of 25 mL/min of different atmospheres: gaseous nitrogen (inert) or synthetic air (oxidative).

### II.2.2.2. Modulated ThermoGravimetric Analysis (MTGA)

Modulated TGA (MTGA) was also carried out to obtain the kinetic parameters associated to mass loss, i.e., the activation energy as a function of reaction extent, mass loss or temperature. The kinetics of a reaction can be expressed by the rate equation, which gives the relationship between the rate of reaction, time, and the amount of material that progressively undergoes the reaction. The temperature dependence of the rate of reaction can be described by the Arrhenius equation. Indeed, the rate equation and the Arrhenius equation are frequently combined into a single equation of the following form <sup>3</sup>:

$$\frac{d\alpha}{dt} = Z[f(\alpha)]e^{-E_a/RT} \quad (\text{II.2})$$

Where  $\alpha$  is the fraction of sample that has already reacted,  $d\alpha/dt$  is the rate of reaction,  $Z$  is a pre-exponential factor,  $f(\alpha)$  is the kinetic expression,  $E_a$  is the activation energy,  $R$  is the universal gas constant, and  $T$  is the temperature.

MTGA is based on a method initially proposed by Flynn in 1968 <sup>4</sup>, and recently implemented and patented by TA Instruments <sup>5</sup>. In MTGA experiments, a sinusoidal temperature modulation is superimposed on the underlying linear heating-rate profile used in conventional TGA. This results in an oscillatory response in the rate of weight loss, whose deconvolution via real-time discrete Fourier transform gives the kinetic parameters. The activation energy of thermal degradation can then be determined at any step of decomposition reaction from [Equation II.2](#):

$$E_a = \frac{R(T^2 - A^2)L}{2A} \quad (\text{II.3})$$

Where  $T$  is the average temperature,  $A$  is the amplitude temperature and  $L$  is the natural logarithmic ratio between the maximum and minimum rates of degradation, as determined from the amplitude of the weight loss signal by discrete Fourier transform <sup>5</sup>.

The calculation of  $E_a$  can be done without assuming any kinetic model, i.e., it is “model free”. However, a kinetic model must be assumed to calculate  $\log Z$ . Assuming a first-order kinetics,  $\log Z$  can be obtained from the value of  $E_a$  via the following equation <sup>5</sup>:

$$\log Z = \log \left[ \frac{d\alpha}{1 - \alpha} \right] + \frac{E_a}{2.303RT} \quad (\text{II.4})$$

In this work, MTGA was performed with the following sinusoidal temperature program: the samples were heated from room temperature to 600 °C at 2 °C/min with a continuous amplitude modulation of  $\pm 5$  °C and a period of 200s under a continuous flow of gaseous nitrogen (25 mL/min).

### II.2.2.3. Differential Scanning Calorimetry (DSC)

Differential Scanning Calorimetry (DSC) is a technique used to study thermal events, such as crystallizations, melting or oxidations, as well as any other evolution of a material as a function of temperature or over time, such as physical aging. During physical transitions, heat is either absorbed (endothermic) or released (exothermic). The principle of DSC relies on the quantification of the difference in amount of heat required to increase the temperature of a sample with respect to a reference. Thus, the apparatus provides a signal that corresponds to the heat flow absorbed or released by the sample as a function of time and temperature, determined as a differential measurement of temperatures. Two types of DSCs exist, namely heat-flux DSC and power-compensation DSC.

In this work, DSC experiments were performed by using two heat-flux DSC equipment, the DSC Q2000 and the DSC 2920 (TA instruments). The DSC 2920 was mostly used for the crystallization studies.

In conventional DSC, the temperature ramp applied to the sample and the reference is linear:

$$T(t) = T_i + \beta t \quad (II.5)$$

In which  $T(t)$  is the temperature at the time  $t$ ,  $T_i$  is the initial temperature and  $\beta$  is the scanning rate.

The heat flow  $\phi$  resulting in the heat transfer  $Q$  is expressed as follow:

$$\phi = \frac{dQ}{dt} = C \frac{dT}{dt} \quad (II.6)$$

Where  $C$  is the heat capacity.

In a heat-flux calorimeter, the sample and the reference are placed in the same furnace, as presented in [Figure II.4](#). A variation of temperature is applied to the entire furnace and the heat  $Q_S$  and  $Q_R$  are transferred to the sample and the reference, respectively.

Thus, exothermic or endothermic events occurring to the sample as a consequence of temperature variations will lead to a temperature difference  $\Delta T = T_S - T_R$  between the sample and the reference. The resulting heat flow can be simplified by a thermal equivalent of the Ohm's law:

$$\phi = Q_S - Q_R = \frac{\Delta T}{R} \quad (II.7)$$

In which R is the thermal resistance.

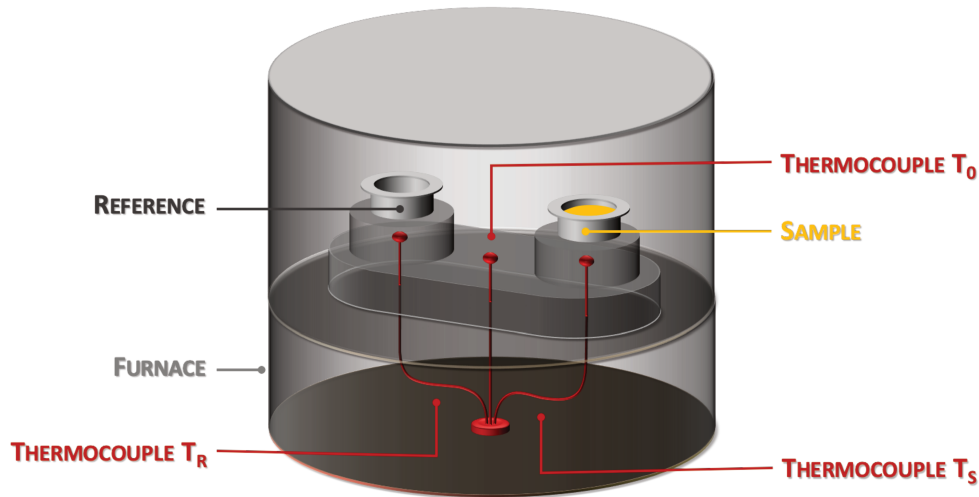


Figure II.4: Schematic representation of heat-flux DSC cells. [Reworked from <sup>1</sup>]

The measurement principle of the heat-flux calorimeter DSC Q2000 is based on the  $T_{zero}^{TM}$  technology, which uses a more complex equation to calculate the heat flow. Two thermal resistances ( $R_{SCP}$  and  $R_{RCP}$ ) and two heat capacities ( $C_{SCP}$  and  $C_{RCP}$ ), related to the sample and the reference respectively, are taken into account in the heat flow expression. Thus, by measuring the temperatures  $T_S$  and  $T_R$  at the sample and reference's platforms respectively, as a function of a fixed temperature  $T_0$ , the measured heat flow is expressed as follow <sup>6</sup>:

$$\phi = -\frac{T_S - T_R}{R} + (T_0 - T_S) \left( \frac{1}{R_{SCP}} - \frac{1}{R_{RCP}} \right) + (C_{RCP} - C_{SCP}) \frac{dT_S}{dt} - C \frac{d\Delta T}{dt} \quad (II.8)$$

Specific calibration procedures were used with the  $T_{zero}^{TM}$  technology. First, a constant heating rate experiment was performed without sample and pan (empty furnace). Second, a constant heating rate experiment was performed with standard sapphire disks directly placed on the sample's and reference's platforms, providing the values of  $R_{SCP}$ ,  $R_{RCP}$ ,  $C_{SCP}$  and  $C_{RCP}$ .

Then, a temperature and energy calibration was carried out by matching the melting temperature ( $T_m = 156.6\text{ °C}$ ) and enthalpy ( $\Delta H_m = 28.6\text{ J/g}$ ) obtained for a standard sample of indium, plus the melting temperature of a standard sample of benzophenone ( $T_m = 48.5\text{ °C}$ ). The entire procedure ensured a calibration over the temperature range from  $-90\text{ °C}$  to  $600\text{ °C}$ . All calibrations and experiments were carried out under a nitrogen atmosphere ( $50\text{ mL/min}$ ).

The characterization of the crystallization behavior was performed with a heat-flux calorimeter DSC2920, calibrated with indium and benzophenone standards.

To characterize the crystallization from the melt, the samples were heated to the melt and held at  $250\text{ °C}$  for  $3\text{ min}$  to erase any previous thermo-mechanical history, quenched to the crystallization temperature  $T_c = 140\text{ °C}$  and maintained in isothermal conditions during the crystallization time  $t_c$ .

To characterize the crystallization behavior from the solid state, the samples were heated to the melt and held at  $250\text{ °C}$  for  $3\text{ min}$  to erase any previous thermo-mechanical history, quenched to  $0\text{ °C}$  into a solid amorphous state, heated at  $10\text{ °C/min}$  to the crystallization temperature  $T_c = 140\text{ °C}$  and maintained in isothermal conditions during the crystallization time  $t_c$ .

In both cases, the crystallized samples were quenched to  $0\text{ °C}$  before being analyzed at a heating rate of  $10\text{ °C/min}$  from  $0\text{ °C}$  to  $250\text{ °C}$ . The thermal programs used are depicted in [Figure II.5](#).

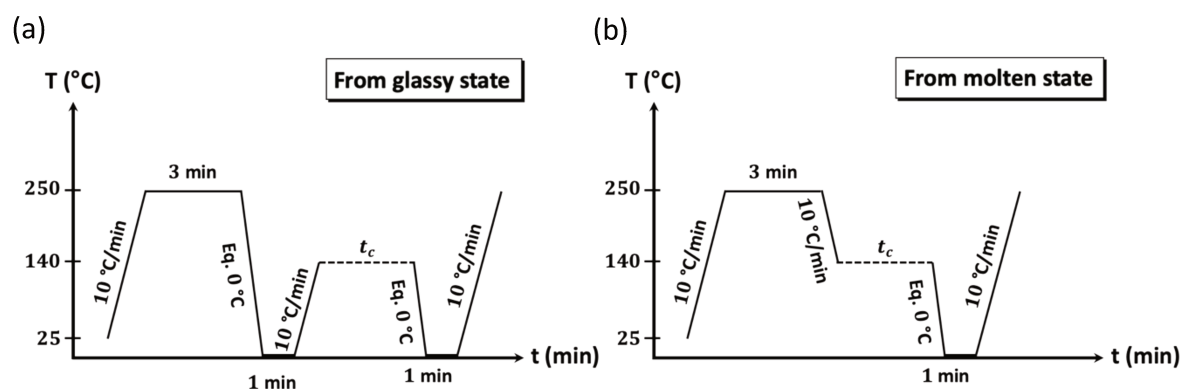


**Figure II.5:** Schematic representation of DSC protocols used for the analysis of the crystallization kinetics from (a) the glassy state and (b) the molten state.

#### II.2.2.4. Modulated Temperature-DSC (MT-DSC)

During the heating and cooling ramps of conventional DSC experiments, the samples experience thermal reactions that change their physical and/or chemical properties. These reactions include glass transition, crystallization, melting, oxidation, curing, evaporation, etc. Some of these reactions may occur at the same time or in the same range of temperature, and the respective heat flows may therefore be overlapped and impossible to distinguish. According to Reading et al. <sup>7</sup>, the heat flow  $\phi$  measured from conventional DSC experiments can be expressed as follow:

$$\phi = \frac{dQ}{dt} = C^*\beta + f(t, T) \quad (\text{II.9})$$

Where  $f(t, T)$  represents the part of the heat flow related to the kinetics (or non-reversing events), also called non-reversing heat flow  $\phi_{NR}$ .

The part of the heat flow related to the thermodynamics, also called reversing heat flow  $\phi_R$ , is expressed as the product of the complex heat capacity  $C$  and the scanning rate  $\beta$ . Conventional DSC applies linear temperature ramps; in MT-DSC, Lacey et al. <sup>8</sup> proposed to super-impose a sinusoidal temperature oscillation to the linear temperature ramp, in order to dissociate reversing and non-reversing events:

$$T = T_i + \beta t + A \sin(\omega t) \quad (\text{II.10})$$

In which  $A$  is the amplitude and  $\omega$  is the angular frequency of the temperature modulation, with a period of oscillation  $p = 2\pi/\omega$ .

Equation II.10 can be written as:

$$\phi = \frac{dQ}{dt} = C^*(\beta + A\omega \cos(\omega t)) \quad (\text{II.11})$$

Where  $C^*$  is the complex heat capacity defined as:

$$C^* = \frac{A_{HF}}{A_\beta} \quad (\text{II.12})$$

Where  $A_{HF}$  and  $A_\beta$  are the amplitudes of the heat flow modulation and the heating rate modulation, respectively.

The thermodynamic events are related to the vibrational and translational motions of the molecules; these motions are very fast and can easily follow any sample temperature modulation. On the other hand, the kinetic events cannot react to the temperature modulation and do not contribute to the modulated part of the heat flow.

$$\phi_R = C^* \beta = \frac{A_{HF}}{A_\beta} \beta \quad (\text{II.13})$$

$$\phi_{NR} = \frac{dQ}{dt} - C^* \beta \quad (\text{II.14})$$

In addition, a phase lag  $\phi$  exists between the calorimeter's response function (the total heat flow) and the temperature modulation.

As a consequence, two components of the apparent heat capacity can be calculated according to the following equations:

$$C' = |C^*| \cos(\phi) \quad (\text{II.15})$$

$$C'' = |C^*| \sin(\phi) \quad (\text{II.16})$$

$C'$  is the in-phase component of the heat capacity (related to  $\phi_R$ ) and  $C''$  is the out-of-phase component of the heat capacity (related to  $\phi_{NR}$ ).

The calibration of MT-DSC is similar to the calibration of conventional DSC; an additional step should be performed to calibrate the heat capacity in temperature-modulation mode. This last step uses a standard sample of sapphire because sapphire does not undergo any transition in the temperature range typically explored for polymers. The heat capacity of sapphire as a function of temperature is highly repeatable and precisely known. Similarly to the calibration step performed with indium, that should be repeated whenever the heating rate is changed, the calibration step with sapphire in temperature-modulation mode should be repeated whenever the amplitude, the scanning rate or the period of oscillation are changed. A calibration factor  $K_{C_p}$  is then calculated from the comparison of the experimental and theoretical heat capacity values. The  $K_{C_p}$  factor is averaged on the selected temperature range and then used to correct the apparent heat capacity of the samples.

$$K_{C_p}(T) = \frac{C_{pSapphire\ theoretical}(T)}{C_{pSapphire\ experimental}(T)} \quad (\text{II.17})$$

Temperature modulation can be performed with three different modes<sup>7</sup> as reported in Figure II.6: heat-only, heat-iso and heat-cool. The heat-only mode is generally used to investigate the coupling of different thermal events, such as glass transition and cold-crystallization, or crystallization and melting. The heat-iso mode is used to investigate melting. The heat-cool mode is used to investigate the glass transition and the molecular mobility associated with the glass transition.

In this work, the MT-DSC experiments were performed with a heat-flux calorimeter DSC Q2000 (TA Instruments) in temperature-modulation mode. The calibration in temperature and energy was carried out using standard samples of indium and benzophenone. The calibration in specific heat capacity was carried out using sapphire standard samples. A heat-cool temperature modulation mode was selected (oscillation amplitude  $A = 3\text{ }^{\circ}\text{C}$ , oscillation period  $p = 120\text{ s}$  and heating rate  $\beta = 1\text{ }^{\circ}\text{C}/\text{min}$ ).

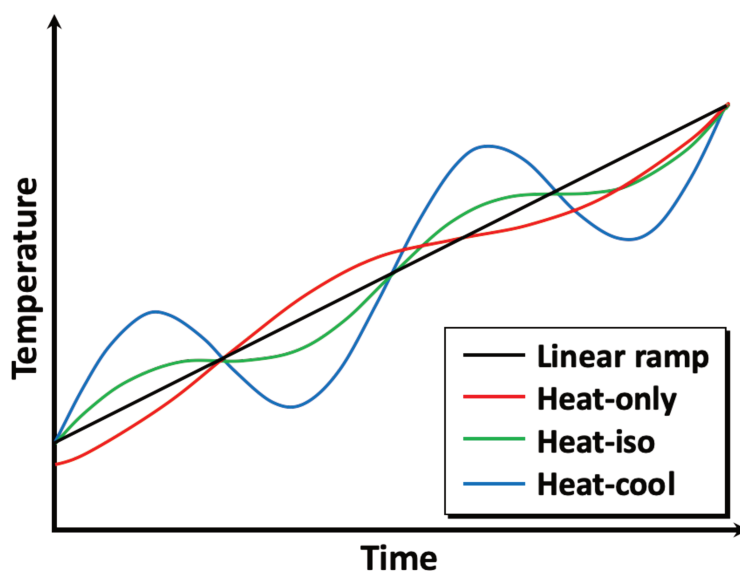


**Figure II.6: Illustration of the possible heating ramps selected for MT-DSC experiments.** Heat-only (red), heat-iso (green), heat-cool (blue) and the underlying linear ramp (black).



### II.2.2.5. Dielectric Relaxation Spectroscopy (DRS)

Dielectric Relaxation Spectroscopy (DRS) is a powerful technique to study the relaxation dynamics in dielectric materials. The advantage of this technique is that it routinely covers a range between 9 and 12 decades of frequency (or time)<sup>9</sup>. DRS consists in studying the motion of permanent dipoles present in dielectric materials as an effect of an applied alternating electric field  $E(\omega)$ . In the case of polymer dielectrics, the net dipole moment per unit volume (i.e. the polarization) corresponds to the vector summation of the dipoles present in the repeating unit itself, plus the dipoles resulting from the sequence of repeating units within the polymer chain and the assembly of polymer chains in the overall system. The electric stimulus deforms the electronic clouds with respect to the atomic nuclei (electronic polarization) and creates an induced dipole moment in the atoms (atomic polarization).

The polarization phenomena observed in polymers arise from the rotational mobility of permanent dipole moments ( $\mu$ ). The reorientation of the permanent dipoles of the molecules can be used to determine sample properties such as permittivity, energy storage, resistivity and dissipation. Such properties give information on molecular motions occurring within the materials as a function of frequency and temperature. For all these reasons, DRS is nowadays widely employed to investigate the molecular mobility in a wide range of materials<sup>10-14</sup>.

In the frequency range  $10^{-6}$ - $10^7$  Hz, the sample can be regarded as a circuit composed of an ideal capacitor and an ohmic resistor assembled in parallel or in series. The complex impedance  $Z^*(\omega)$  of the circuit is measured by the spectrometer and expressed in terms of energy dissipation or resistance  $R(\omega)$ , and energy storage or capacitance  $C(\omega)$ , where  $\omega$  is the angular frequency calculated from the frequency  $f$  through the following equation:

$$\omega = 2\pi f \quad (\text{II.18})$$

Other properties, such as the electrical modulus  $M^*(\omega)$ , the electrical conductivity  $\sigma^*(\omega)$ , the resistivity  $R^*(\omega)$  and the complex dielectric permittivity  $\varepsilon^*(\omega)$  are directly derived from the complex electrical impedance  $Z^*(\omega)$ .

To measure  $Z^*(\omega)$ , a sinusoidal voltage  $U^*(\omega)$  at a fixed frequency is applied to the sample:

$$U^*(\omega) = U_0 \exp(j(\omega t)) \quad (\text{II.19})$$

The current  $I_S^*(\omega)$  is then measured across the sample:

$$I_S^*(\omega) = I_0 \exp(j(\omega t + \varphi)) \quad (II.20)$$

Where  $\varphi$  is the phase shift between the applied voltage and the measured current.

The value of  $Z^*(\omega)$  is then obtained as <sup>15</sup>:

$$Z^*(\omega) = \frac{U^*(\omega)}{I_S^*(\omega)} \quad (II.21)$$

The experimental equipment used in this work calculates the impedance from the measurements of two voltages  $V_1$  and  $V_2$  corresponding to the voltage generated and applied to the sample cell and the voltage converted from the sample current  $I_S(\omega)$ , respectively. A schematic representation of the equivalent circuit is shown in [Figure II.7](#). These voltages are then analyzed with the Fourier transform technique to extract information on their amplitudes and phases.

The complex dielectric permittivity ( $\varepsilon^*$ ) can be derived from the measurement of  $Z^*(\omega)$ :

$$\varepsilon^*(\omega) = \frac{1}{i\omega Z^*(\omega)C_0} \quad (II.22)$$

$$\varepsilon^*(\omega) = \varepsilon'(\omega) - i\varepsilon''(\omega) \quad (II.23)$$

Where  $\varepsilon'(\omega)$  is the real part of  $\varepsilon^*$  (related to the energy stored within the medium) and  $\varepsilon''(\omega)$  is the imaginary part of  $\varepsilon^*$  (related to the energy dissipated throughout the medium).

The dielectric permittivity characterizes the ability of the charges within a material to displace or reorient in the presence of an external electric field. Its experimental determination is highly valuable to obtain information on the mobility of the dipoles within a material. Assuming that the electric field penetrates only in the sample and its substrate, the measured capacity  $C_m^*$  is given by <sup>16</sup>:

$$C_m^* = C_0(\varepsilon_s^* + \varepsilon_{su}^*) \quad (II.24)$$

Where  $\varepsilon_s^*$  and  $\varepsilon_{su}^*$  are the complex permittivity of the sample and the substrate, respectively.

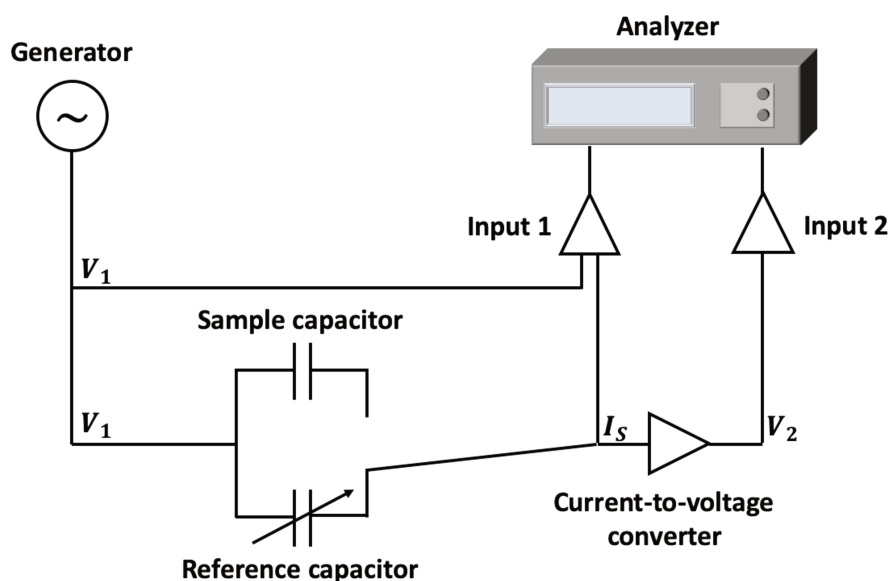


**Figure II.7:** Schematic representation of the equivalent circuit representing the spectrometer analyzer. [Reworked from <sup>15</sup>]

In this work, DRS experiments were performed using interdigit electrodes (IE) (DRS1410-20-150, Novocontrol Technologies, with a sensor diameter of 20 mm, gold-plated copper combs, and an accuracy in loss factor equal to  $\tan \delta = 0.001$ ). The spacing between the comb fingers is 150  $\mu\text{m}$  and their thickness is 35  $\mu\text{m}$ . Prior to sample deposition, each electrode was calibrated by measuring its respective geometric (i.e. empty cell) capacity  $C_0$  and substrate capacity  $C_{su}$  through the measurement of a standard material with known permittivity (mineral B-oil, Vacuubrand). The measurements were carried out over a  $10^{-1}$  Hz to  $2 \times 10^6$  Hz frequency range with an Alpha-A frequency analyzer (Novocontrol Technologies) allowing a measurement of the complex impedance as a function of frequency. Non-isothermal dielectric spectra were collected over a wide range of temperature (from  $-150$  to  $150$   $^\circ\text{C}$ ) with appropriate successive steps. Accurate temperature control was implemented using a Quatro system (Novocontrol Technologies) allowing a temperature stability of  $\pm 0.2$   $^\circ\text{C}$ . The samples were kept in a nitrogen atmosphere over the entire time of measurement.

### Analysis of the experimental data

One of the most important applications of DRS is the investigation of the relaxation processes, which is generally done with different model functions. One of the theoretical models allowing to calculate the time-dependence of the dielectric behavior is the Debye function <sup>17</sup>.

The Debye function expresses the frequency-dependence of the complex dielectric permittivity as:

$$\varepsilon^*(\omega) = \varepsilon_{\infty} + \frac{\Delta\varepsilon}{[1 + (i\omega\tau_D)]} \quad (\text{II.25})$$

Where  $\Delta\varepsilon$  is the dielectric relaxation strength and  $\tau_D$  is the Debye relaxation time related to the position of the maximum of the loss peak.

In this case, the shape of the loss peak is supposed to be symmetric. In practice, the Debye function is not sufficient to fit the experimental results obtained for complex systems like amorphous polymers. In most cases, the loss peak is not symmetric; a broadening of the loss peak and an increasing asymmetry is often observed, with the appearance of a high-frequency tail (non-Debye relaxation behavior). The broadening of the dielectric function can be taken into account thanks to the Cole-Cole (CC) function <sup>18</sup>:

$$\varepsilon^*(\omega) = \varepsilon_{\infty} + \frac{\Delta\varepsilon}{[1 + (i\omega\tau_{CC})]^{1-\alpha}} \quad (\text{II.26})$$

Where,  $0 < \alpha \leq 1$  expresses the asymmetric broadening of the relaxation function.

Equation II.26 can be used to fit the dielectric spectra of glass-forming liquids or polymers having asymmetrical loss peaks and wider dispersion areas in comparison with the Debye formula. For higher frequency ranges, Cole and Davidson (CD) suggested the following formula, particularly suitable for liquids and low molecular glass-forming substances having an asymmetric broadening of the loss peak <sup>19</sup>:

$$\varepsilon^*(\omega) = \varepsilon_{\infty} + \frac{\Delta\varepsilon}{[1 + (i\omega\tau_{CD})]^\beta} \quad (\text{II.27})$$

Where  $0 < \beta \leq 1$  and  $\alpha = 1$  are the parameters that take into account the asymmetric broadening of the relaxation function for the Cole/Davidson-relaxation time.

A more general model function was introduced by Havriliak and Negami (HN) <sup>20</sup>, which is a combination of the Cole/Cole and Cole/Davidson functions. The HN function can be expressed as:

$$\varepsilon^*(\omega) = \varepsilon_\infty + \frac{\Delta\varepsilon}{[1 + (i\omega\tau_{HN})^{\alpha_{HN}}]^{\beta_{HN}}} \quad (II.28)$$

For  $\alpha = 1$  and  $\beta = 1$ , the HN equation is reduced to the Debye function.

The CC and DC dispersions in a given range of frequency are broader than for Debye relaxation, as shown in [Figure II.8](#).

[Figure II.8](#) shows that the dielectric loss ( $\varepsilon''$ ) is broader and its intensity decreases when the shape parameters  $\alpha$  and  $\beta$  change <sup>11</sup>. In practice, the dielectric spectra of a complex system do not exhibit isolated loss peaks. Instead, various relaxation processes and conduction effects might altogether contribute to the dielectric spectra. The conduction effects are usually analyzed by including an additional contribution to the function fitting the dielectric loss:

$$\varepsilon'' = \frac{\sigma_0}{(\omega^s \varepsilon_0)} \quad (II.29)$$

Where  $\sigma_0$  accounts for the Ohmic conduction related to the mobile charge carriers,  $s$  is a fitting parameter and  $\varepsilon_0$  is the dielectric permittivity of vacuum.

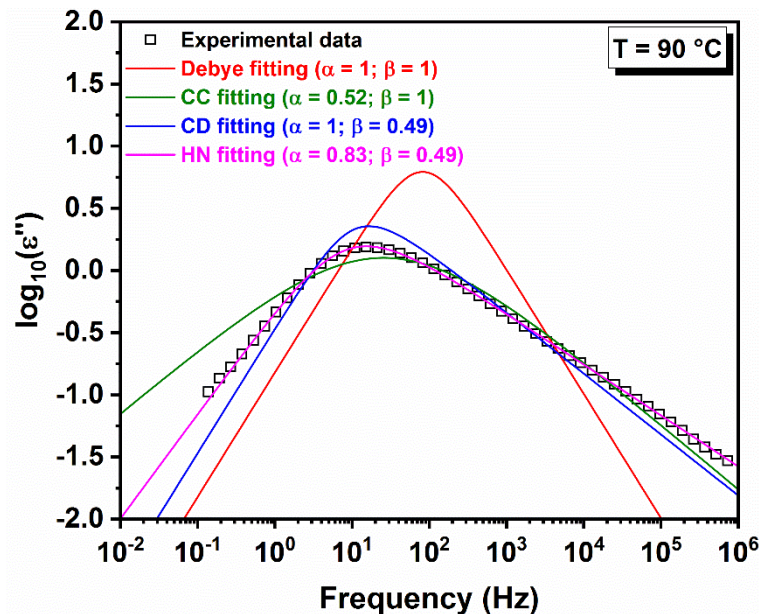


**Figure II.8:** Imaginary part of the complex dielectric spectra as a function of frequency for a 2,5-PEF sample at 90 °C. Several fitting functions (Debye, Cole-Cole (CC), Cole-Davidson (CD) and Havriliak-Negami (HN)) have been represented to illustrate how they take into account the eventual asymmetry and broadening of the dielectric loss peak.

Throughout this work, the analysis of DRS data has been performed using the software Grafity v.0.5.5. If two relaxation processes were observed in the experimental frequency window, a sum of two HN functions was used to fit the experimental data. The HN function for the real part of the complex dielectric permittivity is expressed as:

$$\varepsilon' = \varepsilon_{\infty} + \Delta\varepsilon_{HN} \times \frac{\cos(\beta_{HN}\varphi)}{\left[1 + 2(\omega\tau_{HN})^{\alpha_{HN}} \sin\left(\frac{\pi(1-\alpha_{HN})}{2}\right) + (\omega\tau_{HN})^{2\alpha_{HN}}\right]^{\frac{\beta_{HN}}{2}}} \quad (II.30)$$

The HN function for the imaginary part of the complex dielectric function is expressed as:

$$\varepsilon'' = \Delta\varepsilon_{HN} \times \frac{\sin(\beta_{HN}\varphi)}{\left[1 + 2(\omega\tau_{HN})^{\alpha_{HN}} \sin\left(\frac{\pi(1-\alpha_{HN})}{2}\right) + (\omega\tau_{HN})^{2\alpha_{HN}}\right]^{\frac{\beta_{HN}}{2}}} \quad (II.31)$$

With

$$\varphi = \arctan \left[ \frac{\sin\left(\frac{\beta_{HN}\pi}{2}\right)}{(\omega\tau_{HN})^{-\beta} + \cos\left(\frac{\beta_{HN}\pi}{2}\right)} \right] \quad (II.32)$$

Where  $\varepsilon_{\infty}$  is the unrelaxed dielectric permittivity,  $\Delta\varepsilon_{HN}$  is the relaxation strength,  $\tau_{HN}$  is a characteristic relaxation time and  $\alpha_{HN}$  and  $\beta_{HN}$  are shape parameters describing the symmetric and asymmetric broadening factors of the dielectric spectra.

From the estimated values of  $\tau_{HN}$ ,  $\alpha_{HN}$  and  $\beta_{HN}$ , a relaxation time associated to the maximum of the relaxation peak  $\tau_{max} = 1/(2\pi f_{max})$  was calculated according to <sup>15</sup>:

$$\tau_{max} = \tau_{HN} \times \left[ \frac{\sin\left(\frac{\alpha_{HN}\beta_{HN}\pi}{2 + 2\beta_{HN}}\right)}{\sin\left(\frac{\alpha_{HN}\pi}{2 + 2\beta_{HN}}\right)} \right]^{\frac{1}{\alpha_{HN}}} \quad (II.33)$$

More consistent fitting results have been obtained by performing, for all the considered samples, the same fitting procedure on both the real and imaginary parts of the dielectric signals.

### II.2.2.6. Thermo-Stimulated Depolarization Currents (TSDC)

The analysis of Thermo-Stimulated Depolarization Currents (TSDC) is part of the dielectric spectroscopy techniques for it makes it possible to characterize the relaxation phenomena (i.e. the molecular motions of dipoles) at low temperature (below  $T_g$ ) by applying a constant electric polarization at high temperature, cooling down to quench the system, and then heating it up again to measure the currents associated with depolarization. Similarly to DRS, TSDC signals may contain several relaxation peaks that have to be fitted by suitable functions.

Figure II.9 shows a typical TSDC spectrum for an amorphous polymer. The peak with the highest intensity is observed at high temperature and is the dielectric manifestation of the glass transition ( $\alpha$  relaxation). The peaks with lower amplitudes, obtained at lower temperatures, correspond to secondary relaxations ( $\beta$  and  $\gamma$  relaxations). The so-called  $\rho$  peak appearing at a temperature higher than the  $\alpha$  relaxation is generally attributed to the space charges that accumulate at the electrode/sample interfaces <sup>21</sup>.

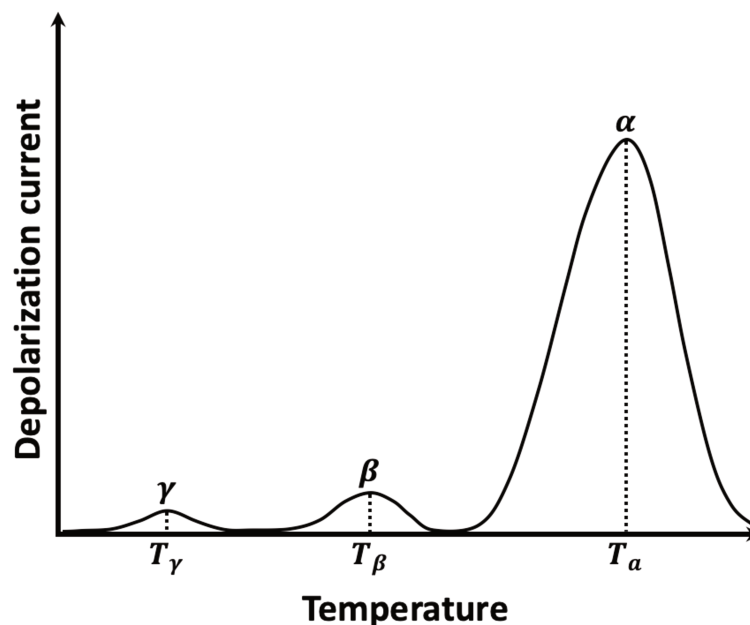


Figure II.9: Manifestation of the principal ( $\alpha$ ) and secondary transitions ( $\beta$  and  $\gamma$ ) as revealed by Thermo-Stimulated Depolarization Currents (CDTS) for an amorphous material.

### Polarization and dielectric relaxations

When a dielectric material is subjected to an external electric field, the electric charges are displaced, the existing dipoles align with respect to the electric field and new dipoles are created on the surface and in the volume of the solid. Once the material is polarized over a given temperature range, depolarization can be triggered by increasing the temperature, and currents are measured as the material goes back to equilibrium, which allows to characterize the corresponding dielectric relaxation phenomena.

A dielectric material, placed between the electrodes of a capacitor, is polarized when subjected to an electric field  $\vec{E}$ . The polarization  $\vec{P}$ , which is proportional to the electric field  $\vec{E}$  in the case of an isotropic dielectric material, results from the superposition of several phenomena, including:

- Electronic polarization: when the electric field is applied, the electron cloud of each atom is deformed with respect to the nucleus, which creates an induced dipole. Electronic polarization has a very short settling time (about  $10^{-15}$ s).



**Figure II.10: Electronic polarization.**

- Atomic polarization: some molecules have no permanent dipole moment, however the electrons participating in their bonds are preferentially displaced towards the most electronegative atom. In this case, the application of an electric field creates an induced dipole moment. The time required to establish atomic polarization is in the order of  $10^{-13}$  to  $10^{-12}$ s.

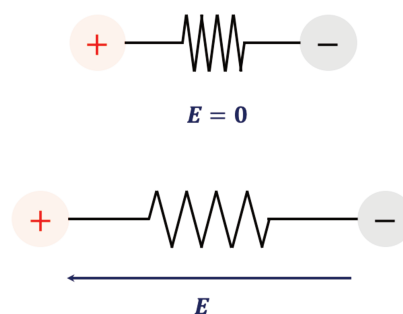


**Figure II.11: Atomic polarization.**



- Debye orientation polarization: if the resultant of the dipole moments is different from zero, the molecule has a permanent dipole moment. If the molecule has sufficient mobility, it may align according to the electric field. The time required to align a permanent dipole moment, which is only possible for molecules having a structural charge dissymmetry, is in the order of  $10^{-6}$ s.

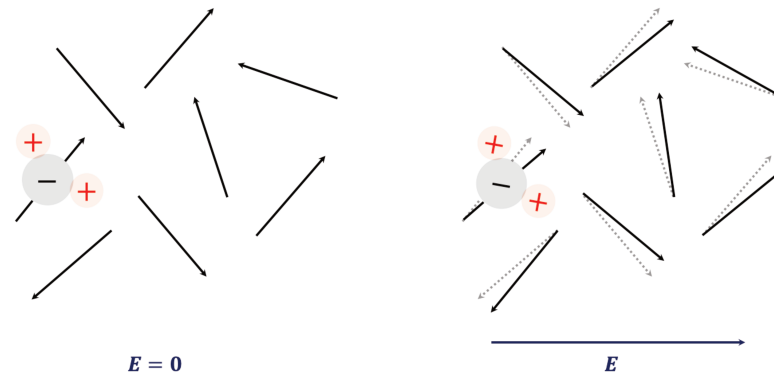


Figure II.12: Orientation polarization.

- Polarization by space charge: this polarization is due to the presence of an excess of charge carriers (electronic and ionic). In this case, the polarization is associated with a macroscopic transfer of charges from one electrode to the other. Their origin of this polarization is either produced by injection mechanisms from the electrodes or by imperfect contacts.

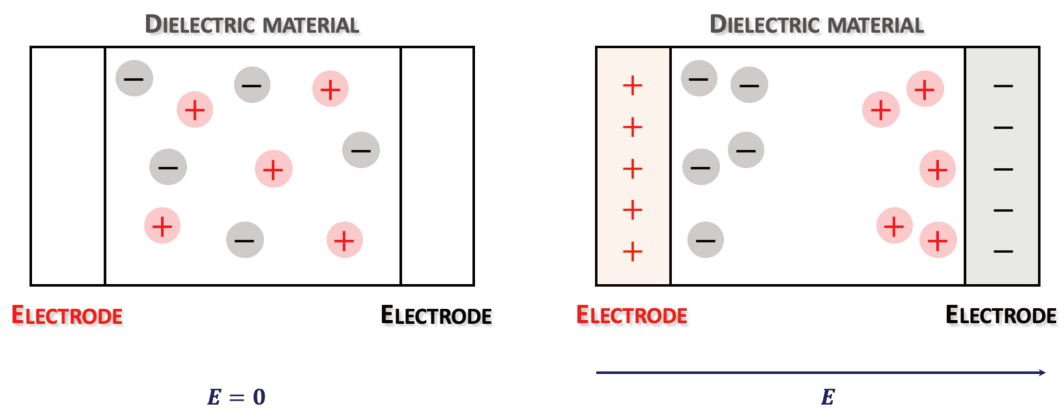


Figure II.13: Space charge polarization.

- Maxwell-Wagner-Sillars polarization: this type of polarization appears in heterogeneous materials and comes from the accumulation of charges at the interfaces between different phases, when the phases have different values of permittivity and conductivity.

Consider a set of identical dipoles in thermodynamic equilibrium at a temperature  $T$ , and assume that they can orientate in space. Because of thermal agitation, the dipoles make translational and rotational movements. In the absence of an applied field, the collisions due to thermal agitation maintain the dipoles in a statistically isotropic orientation. In the presence of an electric field, however, the dipoles are subjected to pairs which tend to orient them parallel to the electric field. The thermal agitation is opposite to any alignment and the system reaches the equilibrium polarization within a certain delay of time (Figure II.14).

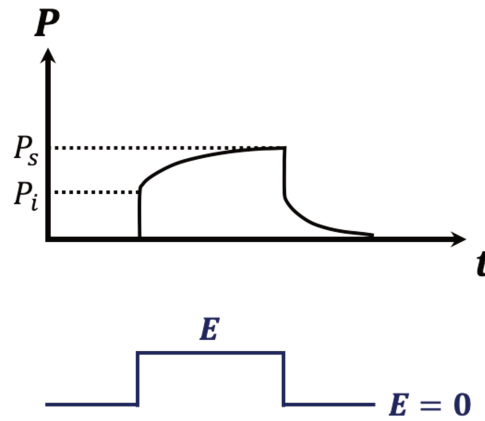


Figure II.14: Polarization evolution.

When an electric field is applied, the polarization reaches a value  $P_i$  corresponding to the instantaneous polarization (electronic and atomic) of the system, then gradually increases as the orientation of the dipoles is achieved, until reaching a limit value  $P_s$  given by:

$$\vec{P}_s = \vec{P}_i + \vec{P}_o \quad (\text{II.34})$$

The orientation polarization at saturation of modulus  $P_o$ , calculated by Langevin, is equal to:

$$P_o = \frac{N_o \mu^2}{3k_B T} E \quad (\text{II.35})$$

In which  $N_o$  is the number of polarized entities at temperature  $T$ ,  $\mu$  is the dipole moment of the polarizable entities and  $k_B$  is the Boltzmann's constant.

The polarization of a set of dipoles subjected to a constant field is expressed by an equation of the following form <sup>22</sup>:

$$P = P_o \left[ 1 - \exp\left(-\frac{t}{\tau}\right) \right] \quad (\text{II.36})$$

Where  $\tau$  is the dielectric relaxation time characteristic of the sample.

Likewise, at the switch-over of the field, the polarization decreases according to a law of the following form:

$$P = P_o \exp\left(-\frac{(t - t_p)}{\tau}\right) \quad (II.37)$$

With  $t_p$  is the polarization time.

In this work, TSDC experiments were performed using interdigit electrodes (IE) placed in the TSDC sample cell, in a 6517B electrometer/high resistance meter (Keithley) provided by Novocontrol Technologies. IE calibration was performed as previously described in the case of DRS measurements. The temperature was controlled with a nitrogen gas flow heated and cooled with the help of a Novocontrol Quarto system. The samples were first heated up to 5 °C above the calorimetric glass transition temperature  $T_{g_{MT-DSC}}$  in order to erase their previous thermos-mechanical history. Then, a protocol was performed to select the optimal polarization temperature, during which the samples were polarized with a direct field of  $1 \times 10^5$  V/m from  $T_{g_{MT-DSC}} - 2$  °C to  $T_{g_{MT-DSC}} + 10$  °C every 2 °C and then rapidly cooled down to 0 °C while keeping the applied electric field. The depolarization current was recorded while applying a linear ramp from 0 °C to 110 °C at 5 °C/min. This procedure was found to provide the best compromise to obtain well-defined non-partial polarization peaks while avoiding parasite phenomena such as conductivity. The different protocols to select a polarization temperature is presented in the [Figure II.15](#). Finally, we choose to keep  $T_{g_{MT-DSC}} + 6$  °C like polarization temperature.

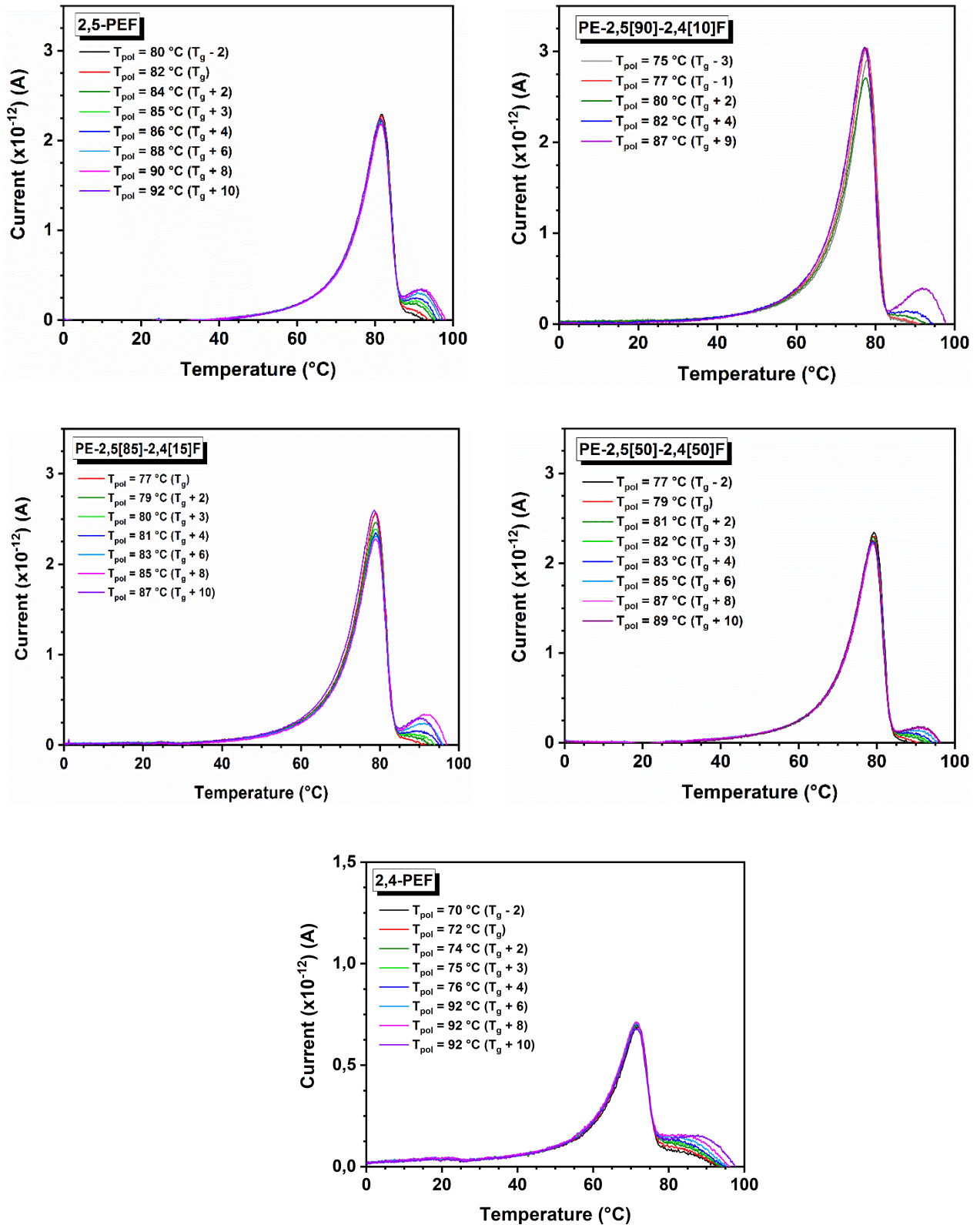


Figure II.15: TSDC results obtained with different polarization temperatures.

## References

- (1) Monnier, X. Molecular Dynamics in Complex Polymer Systems: From Anisotropy to Confinement Effects. phdthesis, Normandie Université, 2017.
- (2) Bragg, W. H.; Bragg, W. L. The Reflection of X-Rays by Crystals. *Proceedings of the Royal Society A: Mathematical, Physical and Engineering Sciences* **1913**, *88* (605), 428–438.  
<https://doi.org/10.1098/rspa.1913.0040>.
- (3) Blaine, R. A Faster Approach to Obtaining Kinetic Parameters. *American Laboratory* **1998**, *30*, 21–23.
- (4) Flynn, J. H. THE HISTORICAL DEVELOPMENT OF APPLIED NONISOTHERMAL KINETICS. In *Thermal Analysis*; Schwenker, R. F., Garn, P. D., Eds.; Academic Press, 1969; pp 1111–1126.  
<https://doi.org/10.1016/B978-0-12-395734-4.50035-7>.
- (5) Blaine, R. L.; Hahn, B. K. Obtaining Kinetic Parameters by Modulated Thermogravimetry. *Journal of Thermal Analysis and Calorimetry* **1998**, *54* (2), 695–704.  
<https://doi.org/10.1023/A:1010171315715>.
- (6) Danley, R. L. New Heat Flux DSC Measurement Technique. *Thermochimica Acta* **2002**, *395* (1), 201–208.  
[https://doi.org/10.1016/S0040-6031\(02\)00212-5](https://doi.org/10.1016/S0040-6031(02)00212-5).
- (7) Reading, M.; Luget, A.; Wilson, R. Modulated Differential Scanning Calorimetry. *Thermochimica Acta* **1994**, *238*, 295–307.  
[https://doi.org/10.1016/S0040-6031\(94\)85215-4](https://doi.org/10.1016/S0040-6031(94)85215-4).
- (8) Lacey, A. A.; Price, D. M.; Reading, M. Theory and Practice of Modulated Temperature Differential Scanning Calorimetry. In *Modulated Temperature Differential Scanning Calorimetry: Theoretical and Practical Applications in Polymer Characterisation*; Reading, M., Hourston, D. J., Eds.; Hot Topics in Thermal Analysis and Calorimetry; Springer Netherlands: Dordrecht, 2006; pp 1–81.  
[https://doi.org/10.1007/1-4020-3750-3\\_1](https://doi.org/10.1007/1-4020-3750-3_1).
- (9) Lunkenheimer, P.; Loidl, A. Dielectric Spectroscopy of Glass-Forming Materials:  $\alpha$ -Relaxation and Excess Wing. *Chemical Physics* **2002**, *284* (1), 205–219.  
[https://doi.org/10.1016/S0301-0104\(02\)00549-9](https://doi.org/10.1016/S0301-0104(02)00549-9).
- (10) Yin, H.; Napolitano, S.; Schönhals, A. Molecular Mobility and Glass Transition of Thin Films of Poly(Bisphenol A Carbonate). *Macromolecules* **2012**, *45* (3), 1652–1662.  
<https://doi.org/10.1021/ma202127p>.
- (11) Lukichev, A. A. Graphical Method for the Debye-like Relaxation Spectra Analysis. *Journal of Non-Crystalline Solids* **2012**, *358* (3), 447–453.  
<https://doi.org/10.1016/j.jnoncrysol.2011.10.022>.
- (12) Nobukawa, S.; Urakawa, O.; Shikata, T.; Inoue, T. Dynamics of a Probe Molecule Dissolved in Several Polymer Matrices with Different Side-Chain Structures: Determination of Correlation Length Relevant to Glass Transition. *Macromolecules* **2013**, *46* (6), 2206–2215.  
<https://doi.org/10.1021/ma302567j>.
- (13) Brás, A. R.; Viciosa, M. T.; Wang, Y.; Dionísio, M.; Mano, J. F. Crystallization of Poly(L-Lactic Acid) Probed with Dielectric Relaxation Spectroscopy. *Macromolecules* **2006**, *39* (19), 6513–6520.  
<https://doi.org/10.1021/ma061148r>.

- (14) Pieruccini, M.; Alessandrini, A.; Sturniolo, S.; Corti, M.; Rigamonti, A. Small and Large Scale Segmental Motion in Polymers: Estimating Cooperativity Length by Ordinary Relaxation Experiments. *Polymer International* **2015**, *64* (11), 1506–1512.  
<https://doi.org/10.1002/pi.4894>.
- (15) Schönhals, A.; Kremer, F. Analysis of Dielectric Spectra. In *Broadband Dielectric Spectroscopy*; Kremer, P. D. F., Schönhals, P.-D. D. A., Eds.; Springer Berlin Heidelberg, 2003; pp 59–98.  
[https://doi.org/10.1007/978-3-642-56120-7\\_3](https://doi.org/10.1007/978-3-642-56120-7_3).
- (16) G. Schaumburg. Novocontrol Introduces High Quality Low Cost Interdigitated Comb Electrodes. *Dielectrics Newsletter* **2006**, No. 22, 5–7.
- (17) Debye, P. Polar Molecules, The Chemical Catalog Company. *Inc.*, New York **1929**, 77–108.
- (18) Cole, K. S.; Cole, R. H. Dispersion and Absorption in Dielectrics I. Alternating Current Characteristics. *J. Chem. Phys.* **1941**, *9* (4), 341–351.  
<https://doi.org/10.1063/1.1750906>.
- (19) Davidson, D. W.; Cole, R. H. Dielectric Relaxation in Glycerol, Propylene Glycol, and N-Propanol. *The Journal of Chemical Physics* **1951**, *19* (12), 1484–1490.  
<https://doi.org/10.1063/1.1748105>.
- (20) Havriliak, S.; Negami, S. A Complex Plane Representation of Dielectric and Mechanical Relaxation Processes in Some Polymers. *Polymer* **1967**, *8*, 161–210.  
[https://doi.org/10.1016/0032-3861\(67\)90021-3](https://doi.org/10.1016/0032-3861(67)90021-3).
- (21) Van Turnhout, J. The Use of Polymers for Electrets. *Journal of Electrostatics* **1975**, *1* (2), 147–163.  
[https://doi.org/10.1016/0304-3886\(75\)90045-5](https://doi.org/10.1016/0304-3886(75)90045-5).
- (22) Bucci, C.; Fieschi, R. Ionic Thermoconductivity. Method for the Investigation of Polarization in Insulators. *Phys. Rev. Lett.* **1964**, *12* (1), 16–19.  
<https://doi.org/10.1103/PhysRevLett.12.16>.

# CHAPTER III

---

## The Glass Transition

### Content

Introduction .....	61
III.1. Generalities on the glassy state and the glass transition.....	61
III.1.1. Amorphous state.....	61
III.1.2. Glass formation.....	63
III.2. Nature of the glass transition and essential experimental aspects .....	65
III.3. Main structural transitions .....	69
III.3.1. Elementary acts of movement in polymers .....	69
III.3.2. Main and secondary transitions in polymers.....	70
III.3.3. Experimental manifestation of transitions .....	71
III.4. Structural relaxation .....	71
III.4.1. Introduction .....	71
III.4.2. Phenomenological description of the relaxation by enthalpy loss .....	72
III.4.3. Experimental features of the structural relaxation.....	73
III.4.4. Non-exponential behavior and memory effect.....	74
III.4.5. Non-linearity .....	76
III.5. Models for structural relaxation .....	77
III.5.1. Kohlrausch-Williams-Watts (KWW) .....	77
III.5.2. Vogel-Fulcher-Tammann (VFT) .....	78
III.5.3. Classification of glass-forming liquids (strong vs. fragile) .....	79
III.5.4. Tool-Narayanaswamy-Moynihan (TNM).....	80
III.5.5. Donth's approach.....	83
III.5.5.1. Introduction .....	83
III.5.5.2. Theoretical approach .....	85
III.5.5.3. Extension of the Donth's model.....	90

References ..... 95



## Introduction

The glass transition is a phenomenon which determines the physical behavior of non-crystalline systems, such as mineral glasses and polymers, as a function of temperature. It corresponds to a transition of a glassy system from the solid behavior to a liquid-like behavior. Many physical properties (specific volume, viscosity, dynamic elastic modulus, conductivity, specific heat, etc.) undergo a modification in the region of the glass transition. The study of the glass transition is interesting from a theoretical point of view, because it deals with the physics of condensed matter, but it is also relevant from a technological point of view, because the glass transition is often taken as a key-parameter to select the most suitable material for a given application.

### III.1. Generalities on the glassy state and the glass transition

#### III.1.1. Amorphous state

Non-crystalline (also called amorphous) state is defined as a disordered configuration of atoms or molecules characterized, from a microscopic point of view, by a lack of long-range order. The atomic or molecular stacks can be represented by the radial distribution function  $g(r)$ , defined such that  $g(r)dr$  represents the number of atoms whose distance from a given atom is between  $r$  and  $r + dr$ .

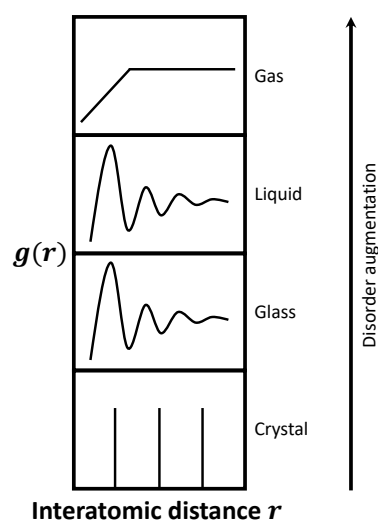


Figure III.1: Evolution the radial distribution function for different degrees of disorder.

Figure III.1 shows that short-distance order (nearest neighbor distance) is sensibly the same for crystals, glasses and liquids. It also shows that the distribution functions for glasses and liquids are similar. When the degree of disorder increases, the distance between atoms decreases and becomes less defined. In perfect crystals,  $g(r)$  comes in the form of a sequence of Dirac's peaks, which are responsible for the Bragg diffraction peaks observed in X-Ray Diffraction (XRD). When the degree of disorder increases (as it happens when glasses are compared to perfect crystals), the average distance between nearest neighbors is substantially preserved but its value becomes distributed, while distances between distant neighbors are no longer defined. For this reason, the X-ray diffractograms of amorphous materials have no Bragg diffraction peaks but only a so-called amorphous halo. Figure III.2 gives an example of X-ray diffractograms obtained for a drug in its amorphous and crystalline states. When the degree of disorder is maximum (as it happens in gases), the distribution function  $g(r)$  has no maximum, all the interatomic distances are equally probable beyond a threshold that depends on the repulsive term of the interaction potential.

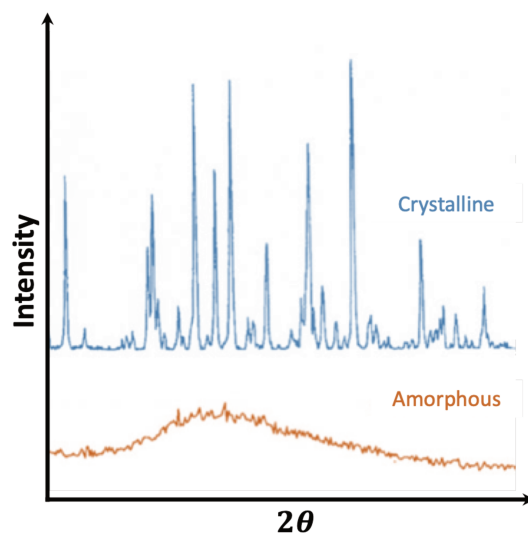
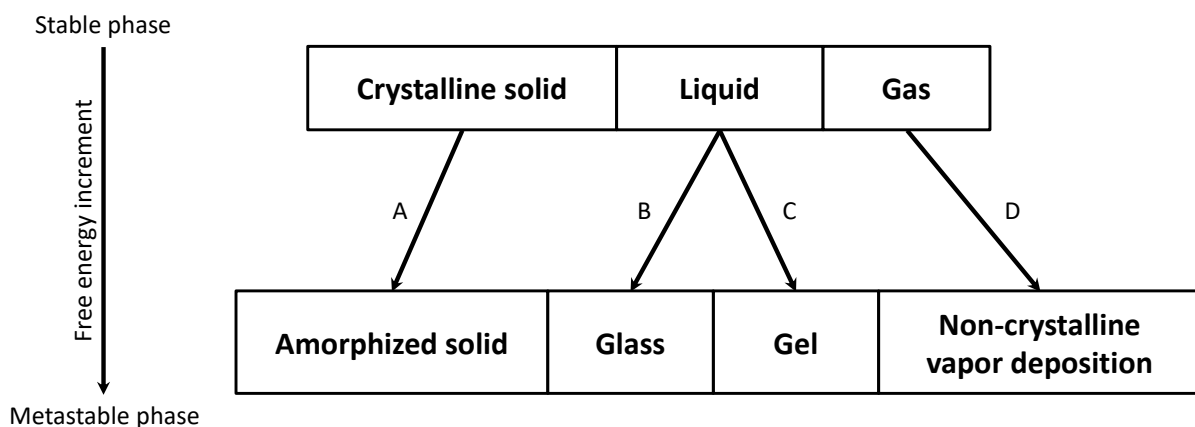


Figure III.2: Typical X-ray powder diffraction patterns of crystalline and amorphous drug. <sup>1</sup>

### III.1.2. Glass formation

At temperatures below the crystallization temperature  $T_c$ , the crystalline phase is the most stable phase. Theoretically, there are many ways to obtain non-crystalline materials at  $T < T_c$ , as shown by [Figure III.3](#):

- Deposition by condensation (evaporation under vacuum, sputtering, etc.)
- Rapid solvent evaporation
- Precipitation or coprecipitation
- Crystal destruction (by mechanical grinding or irradiation)
- Rapid cooling of the liquid



**Figure III.3: Different ways to form a material in the amorphous state at  $T < T_c$ .**

In the case of polymers, the D path is not possible. Indeed, the transition to the vapor state would require to overcome a large number of secondary bonds (Van der Waals, hydrogen, etc.) and involve so much energy that the macromolecule would be exposed to degradation temperatures. B path is the most conventional route to obtain a polymer in the glassy amorphous state. Any liquid can form a glass if the cooling rate is sufficiently high to avoid the crystallization at  $T_c$ .

The thermodynamic path associated to the formation of a glass by cooling a liquid at sufficiently high cooling rates is shown in [Figure III.4](#). This figure represents the evolution of the specific volume  $V$  as a function of the temperature  $T$  (enthalpy and entropy follow similar evolutions). Firstly, the coefficient of thermal expansion for a liquid is higher than for a solid (being it glassy or crystalline).

In the solid state, only atomic vibrations are allowed, whereas in the liquid state both atomic vibrations and changes in atomic configuration are present. During the cooling of a supercooled liquid, the excess of specific volume in the liquid with respect to the solid decreases; the number of weak bonds overcome by thermal activation decreases, and subsequently the cohesion increases. As a consequence, the modes for configurational changes become slower and slower. Below a certain temperature, such a metastable state of equilibrium can no longer be maintained and the system gets stuck in a given spatial configuration, as if it were frozen, while the temperature keeps on decreasing: this step corresponds to the formation of a glass. The temperature at which freezing is observed is called the glass transition temperature  $T_g$ .

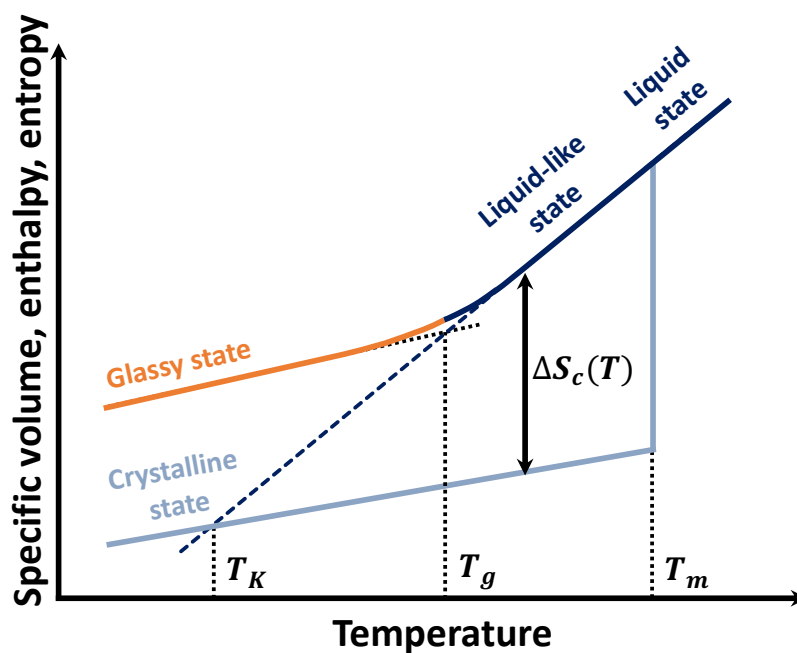


**Figure III.4: Schematic illustration of the temperature dependence of the thermodynamic properties (specific volume, enthalpy or entropy) of a glass-forming liquid.**

$T_K$ : Kauzmann's temperature;  $T_g$ : glass transition temperature;  $T_m$ : melting temperature;  $\Delta S_c$ : configurational entropy  $\Delta S_c = S_{liquid} - S_{crystal}$ ; Dotted line: thermodynamic equilibrium.

## III.2. Nature of the glass transition and essential experimental aspects

The glass transition is not a thermodynamic transition *stricto sensu*. The first and second derivatives of the temperature evolution of the thermodynamic variable free energy  $G$  (Figure III.5), are represented by the specific volume  $V$ , the specific enthalpy  $H$  and the specific entropy  $S$  on one hand, and the coefficient of expansion  $\alpha$ , the specific heat  $C_p$  and the isothermal compressibility  $\kappa_T$  on the other hand):

$$V = \left( \frac{\partial G}{\partial p} \right)_T \quad (\text{III.1})$$

$$H = G - T \left( \frac{\partial G}{\partial T} \right)_p \quad (\text{III.2})$$

$$H = G - T \left( \frac{\partial G}{\partial T} \right)_p \quad (\text{III.3})$$

$$S = - \left( \frac{\partial G}{\partial T} \right)_p \quad (\text{III.4})$$

And:

$$\alpha = \frac{1}{V} \left( \frac{\partial V}{\partial T} \right)_p = \frac{1}{V} \left( \frac{\partial^2 G}{\partial p \partial T} \right) \quad (\text{III.5})$$

$$C_p = \left( \frac{\partial H}{\partial T} \right)_p = -T \left( \frac{\partial^2 G}{\partial T^2} \right)_p \quad (\text{III.6})$$

$$\kappa_T = - \frac{1}{V} \left( \frac{\partial V}{\partial p} \right)_T = - \frac{1}{V} \left( \frac{\partial^2 G}{\partial p^2} \right)_T \quad (\text{III.7})$$

A first-order transition is a transition for which  $G$  is a continuous function of the state variables ( $P$ ,  $V$  and  $T$ ), but its first-order partial derivatives ( $V$ ,  $H$  and  $S$ ) are discontinuous<sup>3,4</sup>. In the case of second-order transitions, the  $G$  function is continuous as well as its first-order partial derivatives  $V$ ,  $H$  and  $S$ , but the second-order partial derivatives are discontinuous ( $\alpha$ ,  $C_p$ ,  $\kappa_T$ ). Even if some of its behaviors are similar to those of a second-order transition, the glass transition does not show any discontinuity in the second-order partial derivatives of  $G$ . Therefore, the glass transition cannot be considered as a second-order transition.

This attempt at thermodynamic interpretation of the glass transition highlighted a phenomenon called Kauzmann's paradox<sup>5</sup>.

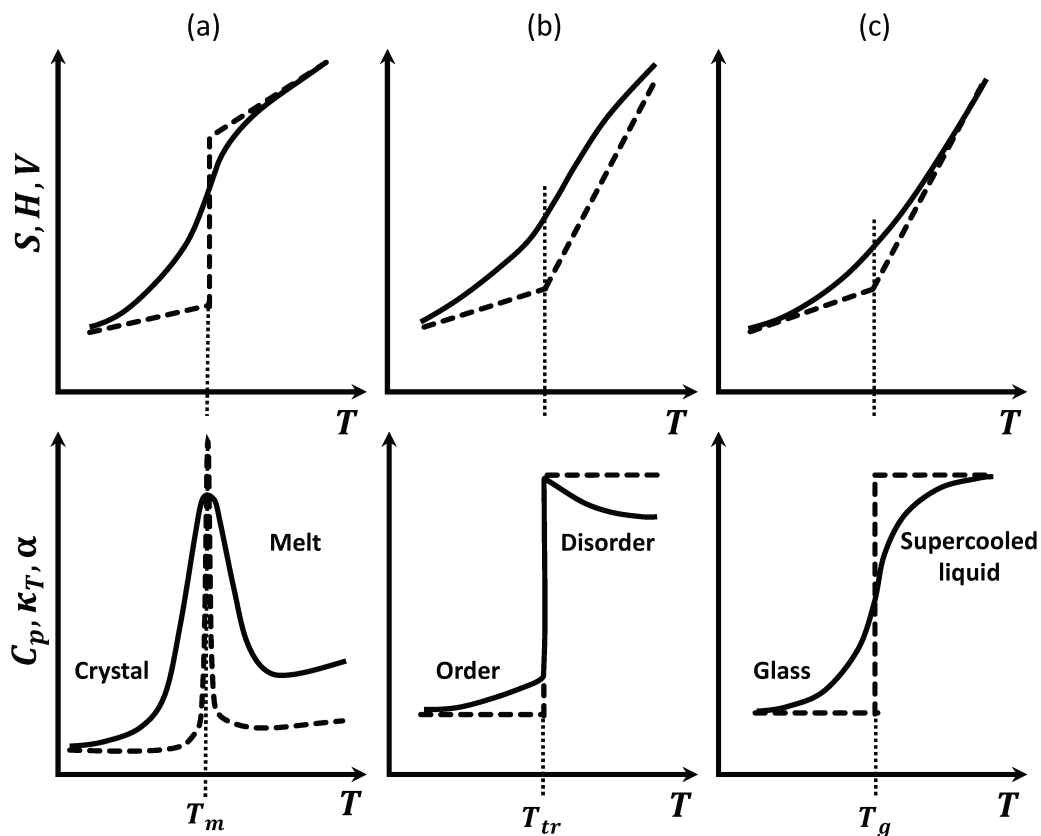


**Figure III.5: Schematic representation of the quantities derived from the temperature dependence of the thermodynamic variable free energy.**

(a) First-order phase transition, e.g. melting of a crystal with defects (—) vs. melting of a perfect infinite crystal (---). (b) Second-order transition, e.g. dominated by intermolecular cooperative phenomena (—) vs. involving only intermolecular non-cooperative phenomena (---). (c) Glass transition: experimental response (—) vs. ideal response in an infinitely slow experiment (---).<sup>2</sup>

As pointed out by Kauzmann<sup>5</sup>, the heat capacity at constant pressure for a liquid is higher than for a solid. Thus, a decrease in temperature forces the liquid to decrease its entropy faster than the enthalpy of the crystal. In a material that is sensitive to crystallization, the entropy of the equilibrium liquid  $S_{liquid}$  is supposed to be equal to the entropy of the crystals  $S_{crystal}$  at a temperature  $T_K$ , the Kauzmann's temperature. Besides, a further decrease in temperature would lead to  $\Delta S_c < 0$ . Such inequality is a violation of the third law of thermodynamics<sup>6</sup>.

As previously mentioned, vitrification results from the impossibility for the liquid to equilibrate in the limited time imposed by the selected cooling rate.

The cooling rate  $\beta^-$  is defined as the first derivative of the temperature  $T$  with respect to time  $t$ :

$$\beta^- = \frac{dT}{dt} \quad (\text{III.8})$$

By assimilating the cooling process to a series of temperature steps, it is possible to obtain information about the time  $t$  spent at each temperature  $T$  plateau:

$$t = \frac{T}{\beta^-} \quad (\text{III.9})$$

Obviously, the higher the cooling rate, the shorter the time spent at each temperature (and vice-versa). This interpretation allows to introduce the notion of relaxation time  $\tau$ , i.e. the time required by a system to recover equilibrium after an external perturbation (thermic, mechanical, electrical...) <sup>7</sup>. During cooling, the liquid goes out of equilibrium whenever the time spent at each temperature is smaller than the relaxation time. Unsurprisingly, most investigations about the glass transition aim at evaluating the temperature dependence of the relaxation time. The glass transition is also interesting because it is a phenomenon that is shared by various glass-forming liquids having different chemical natures, involving ionic interactions, van der Waals forces, hydrogen bonds, covalent bonds or metallic bonds; every material that shows a glass transition may have a liquid-like structure, but a solid-like mechanical behavior at different temperatures and time scales.

Due to its temperature dependence, the vitrification process can be more or less delayed by using lower cooling rates. If the cooling rate is too high, the rearrangement of the atoms or molecules within the material will be limited, and the system will quickly “freeze”.

On the other hand, if the cooling rate is low enough, the rearrangement of the atoms or molecules will be facilitated and the system will “freeze” less rapidly.

Figure III.6 shows that the glass transition temperature is a phenomenon depending on the cooling rate: fast cooling rates lead to high glass transition temperature values, and vice-versa. This dependence has been widely observed through experiments <sup>8,9</sup> and points out the kinetic nature of the glass transition, namely its frequency dependence.

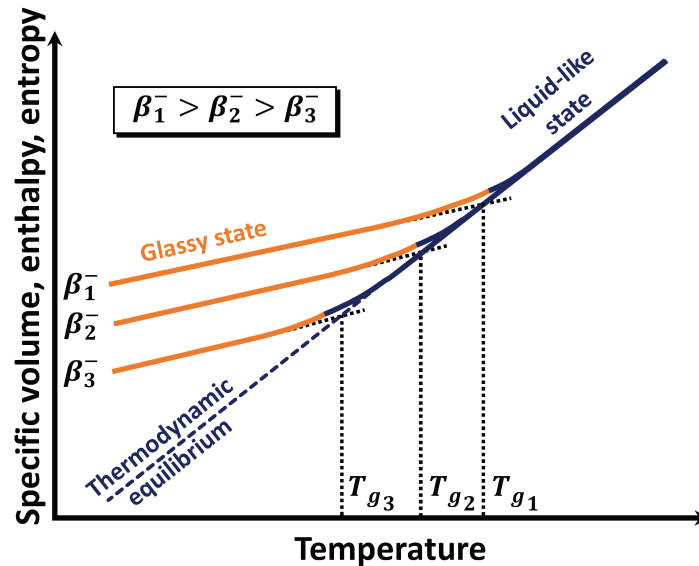


Figure III.6: Schematic illustration of the temperature dependence of the specific volume, the enthalpy or the entropy for a glass-forming liquid upon three different cooling rates:  $\beta_1^- > \beta_2^- > \beta_3^-$ .  $T_{g1}$ ,  $T_{g2}$  and  $T_{g3}$  are the respective glass transition temperatures.

The fundamental understanding of the glass transition is still under debate. The glass transition is a complex process that involves equilibrium, thermodynamic and kinetic factors, which themselves are somehow related to the structure of the material. Many physical properties of polymers dramatically change at  $T_g$ , and obviously this is particularly true for amorphous polymers. It is therefore likely that any structural features, or externally imposed conditions, that could potentially influence chain mobility, will also affect the glass transition. The glass transition is not a transition in strict thermodynamic sense, but has a kinetic character. The kinetic character implies that  $T_g$  is not unequivocally defined for each polymer, but depends on the nature of the observation and the experimental time allocated to observe it. One should rather speak of a glass-to-liquid transition domain, instead of a glass transition temperature. The fact that a glass is intrinsically out-of-equilibrium also implies that its structural state is prone to evolve over time: this phenomenon is known as physical aging. The glass transition depends on both kinetic and entropic aspects which are related to the material structure.



The most important structural factors that influence the glass transition are:

- The flexibility of the chain
- The steric factors that occur when the additional groups are found as substituents of the main chain
- The configuration effects (i.e. the configuration of the chains in the material)
- The polarity of the groups of the macromolecule (or inter-chain attractive forces)
- The nodes of crosslinking
- The molecular mass
- The crystallization

In general, any modification of the structure which is supposed to limit the amplitude of the macromolecular movements, also leads to an increase in the glass transition temperature.

### III.3. Main structural transitions

#### III.3.1. Elementary acts of movement in polymers

The elementary acts of molecular movement in polymers are related to a rotation around single covalent bonds. During the rotation, the bond angle does not change. Rotations are favored by an elevation in temperature but disadvantaged by other parameters, such as the rigidity of the backbone, the sterical hindrance of the lateral groups, the existence of secondary bonds between atoms or functions beard by lateral groups and neighboring molecules. At low temperature, only the movements of short segments are possible, involving a few repeating units. As temperature increases, the mobility extends to bigger portions of the macromolecular chains, and the rotation of several tens of repeating units becomes possible. Finally, when the temperature becomes sufficiently high, all the polymer chains are able to move with respect to each other.

### III.3.2. Main and secondary transitions in polymers

The structural transitions that can be observed in polymers depend on the scale of the molecular segments involved in each considered type of movement. It is possible to distinguish two major types of transitions <sup>3,10–13</sup>, those concerning the interactions between neighboring chains (intra-chain) involving long chain segments, and those concerning the interactions within each chain (inter-chain) involving movements that are localized on small group of atoms or short chain segments.

The first major type of transition is related to the movements of long segments of the main polymer chain, implying a generalized mobility of the macromolecular structure. This corresponds to the main transition (the glass transition), also called the  $\alpha$  relaxation and characterized by a temperature  $T_\alpha$ , which is the transition of the amorphous portions of the polymer from the vitreous to the rubbery state. At  $T < T_\alpha$ , the molecular mobility is almost entirely blocked; only short-range localized movements can occur on specific sites of the molecular chains, corresponding to the so-called secondary relaxations noted  $\beta$  and  $\gamma$ . The movements that generally occur during secondary relaxations are schematically shown in Figure III.7 and can be classified into three categories <sup>12</sup>:

- Type A movements, involving a short sequence of the main polymer chain.
- Type B movements, relate to the movements of side-chains with respect to the main polymer chain.
- Type C movements, which are limited to the movements of a group of atoms on side-chains.

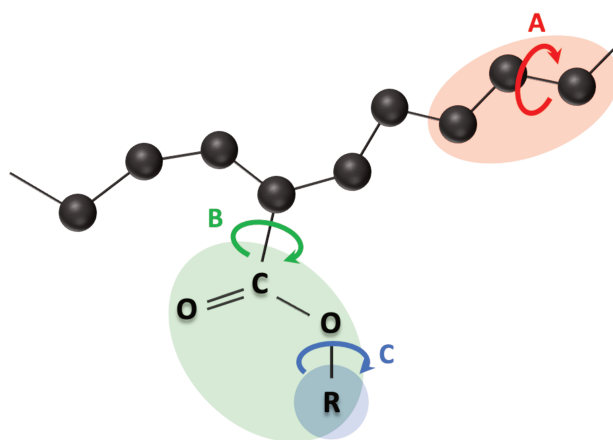


Figure III.7: Location of the three types of movements associated to the secondary transitions (or relaxations).  $\beta$  relaxation: A or B type of movements.  $\gamma$  relaxation: C type of movements.

### III.3.3. Experimental manifestation of transitions

Both the main and secondary transitions can be observed experimentally. Differential Scanning Calorimetry (DSC) is not able to detect  $\beta$  and  $\gamma$  transitions, as the energies involved are too low. The DSC signature characteristic of the glass transition is clearly observable given that the heat capacity step ( $\Delta C_p = C_p(\text{liq}) - C_p(\text{glass})$ ) recorded upon heating is sufficiently large ( $\Delta C_p > 0.1 \text{ J}/(\text{g}\cdot\text{K})$ ).

$\beta$  and  $\gamma$  secondary transitions can be observed by other spectroscopy techniques, such as Dynamic Mechanical Analysis (DMA), Thermally Stimulated Depolarization Current (TSDC) or Dielectric Relaxation Spectroscopy (DRS).

## III.4. Structural relaxation

### III.4.1. Introduction

The transition from the liquid to the vitreous state takes place in a temperature range called the glass transition domain. A glass is thermodynamically out of equilibrium and is therefore characterized by an excess of internal energy. Structural relaxation is a phenomenon that appears when a liquid, in its equilibrium state at a temperature  $T_1$ , is quenched to a temperature  $T_2 < T_1$ . During the cooling process, the structure undergoes at first a steep contraction, then follows a series of gradual rearrangements that aim at reaching the equilibrium. An instantaneous (elastic) contraction of the system would be purely due to vibrational relaxations; the rearrangements observed after vitrification are gradual and are known as the structural relaxation. A variation of several physical (thermal, mechanical, electrical, optical, etc.) properties can be observed over time for polymers maintained at temperatures right below and close to their glass transition temperature. These effects are the manifestation of a process called physical aging<sup>14</sup>. Physical aging can be totally reversed by thermal treatment; in this case the glass is generally referred to as rejuvenated. As such, physical aging is opposed to chemical aging (by oxidation, UV radiation, etc.), which is associated to an irreversible change of the system.

### III.4.2. Phenomenological description of the relaxation by enthalpy loss

Figure III.8 shows the changes in enthalpy and heat capacity observed during isothermal aging and the subsequent heating of an amorphous material.

Consider a glass undergoing an isothermal aging of duration  $t_a$  at the aging temperature  $T_a < T_g$ . Over time, its enthalpy will tend to reach the curve extrapolated from the supercooled liquid. This phenomenon is accompanied by a decrease in the excess of enthalpy (and free volume, because the structure becomes denser, the interactions grow stronger, the configuration enthalpy and the associated entropy decreases). Such a relaxation phenomenon is therefore described by an enthalpy loss.

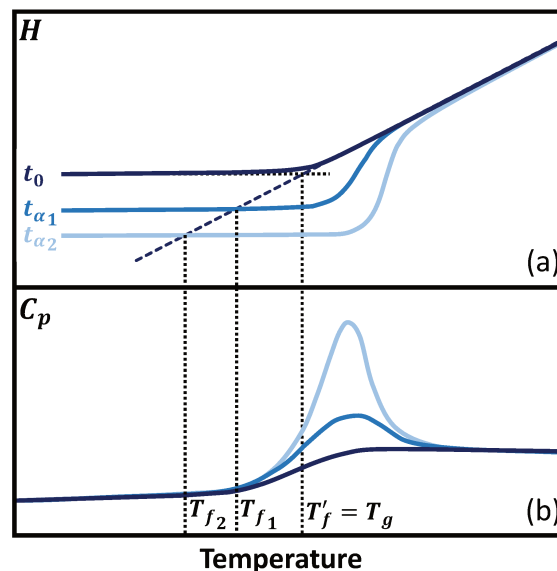


**Figure III.8:** Diagram of changes in enthalpy  $H$  (a) and specific heat capacity  $C_p$  (b) of an amorphous material as a function of temperature during physical aging.

Heating the glass, already partially relaxed, to a temperature  $T > T_g$ , leads to a so-called inverse relaxation phenomenon (Figure III.8 (a)). During the transition from the vitreous to the supercooled liquid state, the compactness decreases, the specific volume increases, the interactions weaken and the enthalpy increases. This phenomenon corresponds to an enthalpy recovery.

Experimentally, this is observed by measuring the changes in the specific heat capacity as a function of temperature (Figure III.8 (b)). Physical aging shows up at the glass transition as a superposed endothermic peak whose intensity and position increase with the aging time.

In addition to the aging time, the aging temperature is also an important experimental parameter. Indeed, if the aging temperature is too far from the glass transition, no evolution of the structure can be observed in an experimentally reasonable time; on the other hand, if the aging temperature is too close to the glass transition temperature, the evolution will be almost instantaneous.

Structural relaxation has two aspects: one is kinetical and the other is thermodynamical.

The kinetical aspect of the structural relaxation is given by the influence of the cooling rate on the glass transition: the lower the cooling rate, the lower the glass transition temperature.

The mechanisms of the structural relaxation being slower than those appearing at the glass transition, it is reasonable to think that more information on the vitreous state can be obtained by investigating the kinetics of the structural relaxation.

### III.4.3. Experimental features of the structural relaxation

The structural relaxation can be studied using calorimetric, dilatometric or more generally thermal, mechanical or electrical measurements<sup>15–20</sup>. The characteristics of the structural relaxation that emerge from the works in the literature are that:

- The structural relaxation is a phenomenon observed for all vitreous materials or any material containing a significant amount of amorphous phase.
- The return to a metastable equilibrium is faster when the isothermal aging is carried out at a temperature close to the glass transition temperature.
- The return to equilibrium is an "intrinsically slowing down" process: the longer the aging time  $t_a$ , and the bigger the difference between the aging temperature  $T_a$  and the glass transition temperature, the lower the molecular mobility<sup>14</sup>.
- The evolution towards equilibrium in isothermal conditions is non-linear<sup>16</sup>.
- The evolution of the material depends on its thermal history<sup>16,21,22</sup>.
- The structural relaxation cannot be described by a single time constant or a single relaxation time<sup>14,19,20,23,24</sup>, but requires the use of a distribution of relaxation times reflecting the non-exponential nature of its kinetics.

### III.4.4. Non-exponential behavior and memory effect

The non-exponential nature of the structural relaxation has been demonstrated by Rekhson<sup>21</sup> and Goldstein<sup>25</sup>, who carried out the "cross-over" or "memory effect" experiments<sup>24,26,27</sup> described in [Figure III.9](#). In these experiments, it is proposed to follow the variations of a property  $\phi(T, t)$  of the material with time at a temperature  $T$ . It is also possible to follow the variations of the quantity  $\delta\phi(T, t)$  defined by:

$$\delta\phi(T, t) = \phi(T, t) - \phi_{eq}(T) \quad (\text{III.10})$$

Where  $\phi_{eq}(T)$  is the equilibrium value of the  $\phi$  property at the temperature  $T$ .

Consider a sample in its equilibrium state at a temperature  $T > T_g$ . The sample is cooled down to a temperature  $T_2 < T_g$  and kept in isothermal conditions during a time sufficiently long for the property  $\phi$  to reach a  $\phi^*$  value. The variation  $\delta\phi^*(T_2, t_2) = \phi(T_2, t) - \phi^*(T_2, t_2)$  corresponds to  $\delta\phi^*(T_1, t_1) = \phi(T_1, t) - \phi_{eq}(T_1)$ , which is the variation necessary to reach the equilibrium at a temperature  $T_1$  ( $T_2 < T_1 < T_g$ ) within a time  $t_1 < t_2$  (pathway 1 in [Figure III.9](#)). Pathways 1 (AD) and 2 (ABC) can be considered as equivalent from the point of view of structural relaxation. Pathway 2 is then terminated by heating the material to the temperature  $T_1$  (CD), where the property  $\phi$  is measured as a function of time. As the variation  $\delta\phi^*$  allows to reach the equilibrium for the property  $\phi$  at temperature  $T_1$ , and since the pathway (ABC) is supposed to bring the material in the same state of equilibrium as the AD path, it can be expected that this property stays constant as a function of time. [Figure III.10](#) presents the trends for isothermal recovery of property  $\phi$  at temperature  $T_1$  as a function of time (from point A to point D for pathway 1, and from point D to point D for pathway 2). This figure shows that, even in the case of pathway 2, the property  $\phi$  changes with time and has a "memory effect" due to the thermal history of the material. The two systems are therefore not in the same state.

The hypothesis of a model with a first-order parameter that implies a unique delay mechanism, where the characteristic time only depends on the instantaneous structure of the material, cannot account for such a "memory effect".

“Memory” can be attributed to various phenomena:

- The existence of at least two relaxation processes or two delay mechanisms, one fast and the other slower, which follow exponential laws <sup>28</sup>.
- A recovery or relaxation function that could decrease slower than the exponential function  $\exp(-t/\tau)$ .

These two phenomena are complementary. The first case may be related to the existence of "sub- $T_g$ " relaxation peaks <sup>28,29</sup> whereas the second case makes it possible to introduce the non-exponential character of the recovery function into the expression of the relaxation time.

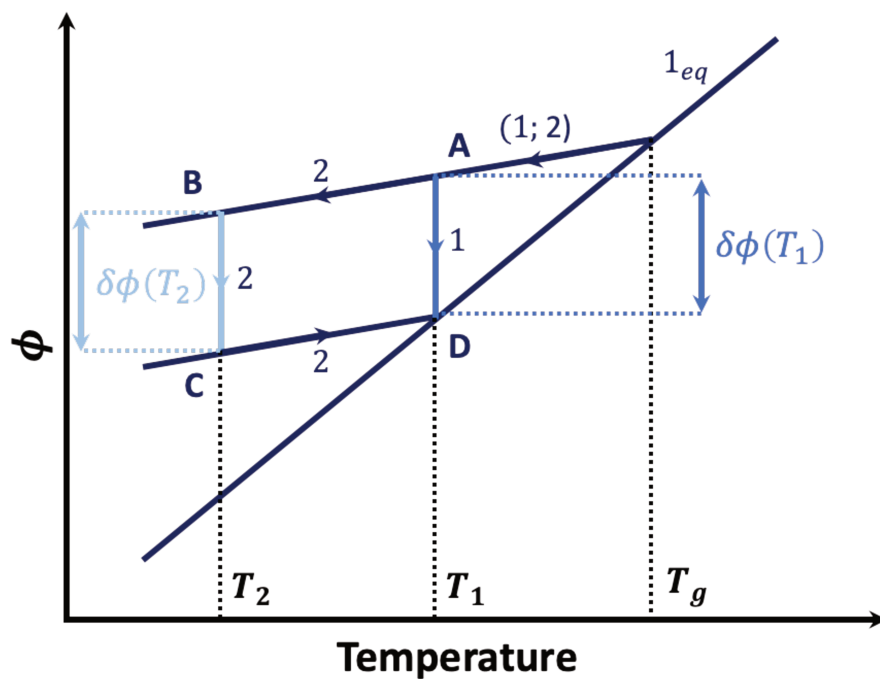


Figure III.9: Schematic description of the “cross-over” experiments drawn onto a diagram showing the variations of a physical property  $\phi$  property as a function of temperature.

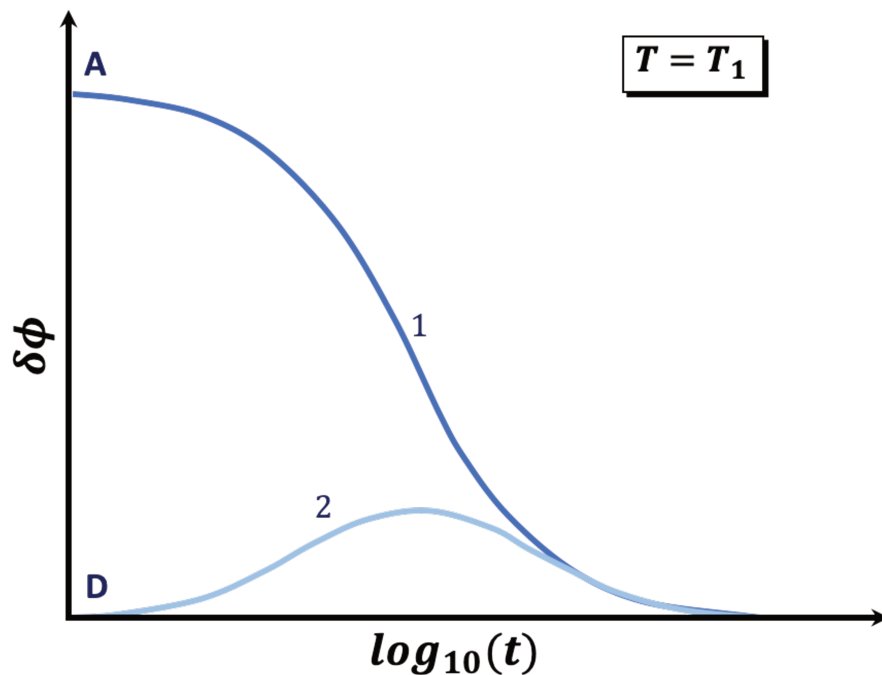


Figure III.10: Isothermal recovery for a physical property  $\phi$  as a function of time at temperature  $T_1$ , at the point D after the pathway 2, and from point A to point D during the pathway 1, as illustrated in Figure V.2.

### III.4.5. Non-linearity

Figure III.11 shows the evolution of volume excess for isotactic polystyrene (PS) obtained both in contraction ( $\delta > 0$ ) and dilatation ( $\delta < 0$ ) during dilatometry experiments performed by Kovacs et al. <sup>24,26,27</sup>. Dilatometry experiments consist in recording the contraction or expansion of a sample in isothermal conditions at a temperature  $T_r$  after cooling or heating the sample from temperatures noted by their deviations  $\Delta T$  with respect to the reference temperature  $T_r$ . The results show that the curves obtained in contraction and in dilatation are not symmetrical. Figure III.11 also shows, according to the interpretation proposed by Kovacs et al. <sup>24</sup>, the time required for the material to lose 15% of its deformation by returning to the equilibrium state after compression or dilation (black dots). If relaxation was a linear phenomenon, an identical value of time should be obtained for each curve. In other words, the points should be aligned vertically, which is not the case. This proves that the relaxation phenomenon bringing the material back to the equilibrium does not follow a linear law. The isothermal recovery or the function for structural relaxation presents has a non-linear dependence with time.



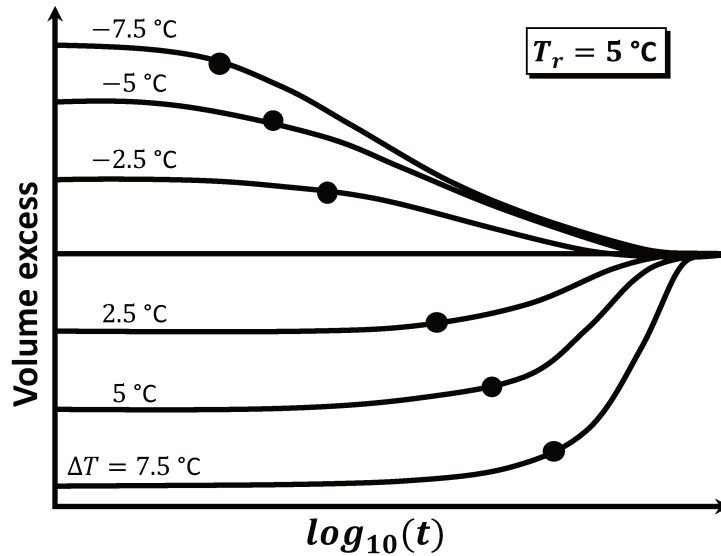


Figure III.11: Contraction and expansion isotherms at  $T_r = 5\text{ °C}$  after quenching or annealing for a sample of isotactic polystyrene from the temperatures  $T_r \pm \Delta T$ .

## III.5. Models for structural relaxation

### III.5.1. Kohlrausch-Williams-Watts (KWW)

Kohlrausch<sup>30</sup> considered a property  $H(T, t)$  that, submitted to a stress, changes its values from  $H_i$  (initial value, under zero stress) to  $H_s$  (final value, under stress). He then showed that, by releasing the stress at the beginning of a new time-scale  $t = 0$  while keeping the temperature constant,  $H(T, t)$  recovers its initial value in a non-exponential way. He therefore proposed a relaxation function  $\phi(T, t)$  that could be used to describe the return to equilibrium of a property, and introduced the term  $\beta_{KWW}$  to take into account the non-exponential character of such a function:

$$\phi(T, t) = \exp\left(-\left(\frac{t}{\tau_{KWW}}\right)^{\beta_{KWW}}\right) \quad (\text{III.11})$$

Where,  $\beta_{KWW}$  is the stretch exponent (whose value is generally in the range between 0 and 1) and  $\tau_{KWW}$  is the relaxation time.

$\beta_{KWW} \sim 0$  corresponds to a distribution of the relaxation times that is very broad, whereas  $\beta_{KWW} \sim 1$  corresponds to a distribution of the relaxation times which is very close to a single exponential phenomenon (Debye relaxation i.e. the time behavior of liquids above the melting point).

Williams and Watts<sup>31</sup> were the first authors to suggest that the peaks obtained by DRS on the curves of the loss factor have an asymmetric shape that is not related to the distribution of the relaxation times, but should be taken into account by a non-exponential correlation function (e.g. Kohlrausch's formula) which would rather be due to the cooperativity of the molecular movements during relaxation. Cooperativity expresses the "degree of connection" of all the acts of movement of the relaxing moieties. Non-cooperative systems relax through movements that are independent from each other, whereas in cooperative systems the movement of each relaxing unit is possible only if the surrounding molecular moieties are relaxing too. The exponent  $\beta$  is therefore a parameter that could be used to evaluate the degree of cooperativity of a system (infinite if  $\beta = 0$ , zero if  $\beta = 1$ ).

### III.5.2. Vogel-Fulcher-Tammann (VFT)

An equation describing the variations of the viscosity  $\eta$  (or the relaxation time  $\tau$ ) in the temperature range from  $T_g$  to  $T_g + 100$  K has been proposed by Vogel<sup>32</sup>, Fulcher<sup>33</sup> and Tammann<sup>34</sup> and (VFT equation):

$$\eta(T) = \eta_0 \exp\left(\frac{B}{T - T_0}\right) \quad (\text{III.12})$$

Where  $\eta_0$  (or  $\tau_0$ ) is a pre-exponential factor,  $B$  is a fitting parameter that is dimensionally homogeneous to a temperature, and  $T_0$  (sometimes found as  $T_V$ ) is the Vogel's temperature, i.e. the temperature at which an asymptote is observed for the relaxation time as a function of  $1/T$  ( $\tau \rightarrow \infty$ ).  $B$  corresponds to  $DT_0$ , where  $D$  is a quantity also known as the "timescale steepness" characteristic of the glass formation. Besides, in the literature,  $T_0$  is sometimes considered as the timescale equivalent of the Kauzmann's temperature  $T_K$ .

The viscosity  $\eta$  and the relaxation time  $\tau$  are linked to each other by the following relation<sup>35</sup>:

$$\eta = G_\infty \tau \quad (\text{III.13})$$

Where  $G_\infty$  is the modulus of elasticity after infinite time, corresponding to a state of complete relaxation.

### III.5.3. Classification of glass-forming liquids (strong vs. fragile)

Angell<sup>36</sup> found out that the variations of  $\log_{10}(\eta)$  (or  $\log_{10}(\tau)$ ) as a function of  $T_g/T$ , regardless of the nature of the material, could be divided into two large families (Figure III.12). When  $\ln(\eta)$  (or  $\ln(\tau)$ ) as a function of  $1/T$  can be fitted by an Arrhenius law, the behavior is defined as “strong”:

$$\ln(\eta) = A + B \frac{T_g}{T} \quad (\text{III.14})$$

Strong glass-forming liquids typically show small variations of the specific heat capacity at the glass transition  $\Delta C_p(T_g)$ , which can be interpreted as a good stability of short and medium range molecular arrangements.

Angell<sup>37</sup> proposed an approach based on a so-called diagram of potential energy landscape, which takes into account all the possible configurational states of the material. Based on this concept, two physical parameters (the height of the potential barriers to cross  $\Delta\mu$  and the number of accessible minima  $N_E$ ) should be considered. From this point of view, strong glass-forming liquids are characterized by large heights of potential barriers and a relatively low numbers of accessible minima (Figure III.13).

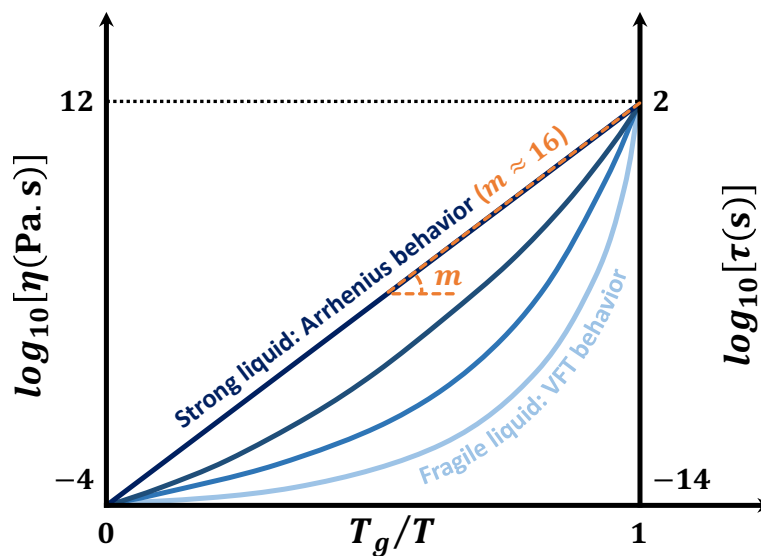
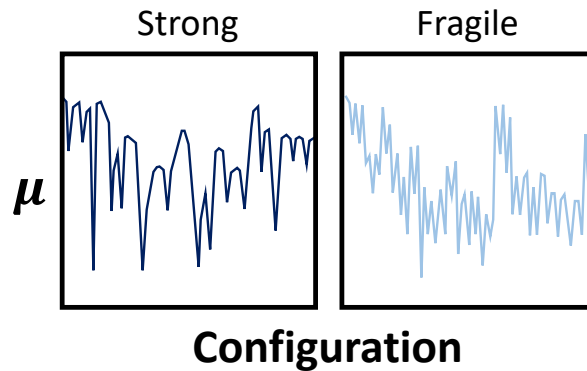


Figure III.12: Angell’s plot: variations of the viscosity (or the relaxation time) as a function of the temperature normalized to the glass transition temperature  $T_g/T$ . This plot defines two main classes of glass-forming liquids: “fragile” (non-linear temperature dependence) and “strong” (linear temperature dependence). The slope at  $T = T_g$  defines the so-called fragility.

The behavior of “fragile” glass-forming liquids, for which the variations of  $\ln(\eta)$  (or  $\ln(\tau)$ ) as a function of  $1/T$  is non-linear, can be described by a VFT law (Equation III.12). Fragility is associated with large variations in the specific heat capacity at the glass transition, a greater number of possible energy minima, and smaller heights of the barriers of potential energy that should be overcome for relaxation to occur (Figure III.13).



**Figure III.13:** Example of energy landscapes in the configuration space for "strong" and "fragile" glass-forming liquids.

A quantification of the "strong" or "fragile" characters has been proposed by Plazek and Ngai<sup>38</sup>, who defined the fragility index  $m$  as:

$$m = \left. \frac{d \log_{10}(\tau)}{d(T_g/T)} \right|_{T=T_g} \quad (\text{III.15})$$

The calculation of  $m$  is directly related to the derivative value of  $\log(\eta)$  (or  $\log(\tau)$ ) as a function of  $T_g/T$  at  $T = T_g$ . Fragile to strong transitions are associated with a switch from Arrhenius to non-Arrhenius viscosity behavior.

#### III.5.4. Tool-Narayanaswamy-Moynihan (TNM)

The model based on Tool, Narayanaswamy and Moynihan's work (TNM)<sup>39–41</sup> describes the enthalpic relaxation using the notion of fictive temperature, which defines the instantaneous structural state of a vitreous material. The concept of fictive temperature, introduced by Tool<sup>39,42</sup> on the basis of dilatometry measurements, can be generalized to other properties such as volume, enthalpy, refractive index, polarization, etc. When a sample is cooled from a temperature  $T_0 > T_g$  to a temperature  $T_a < T_g$ , the property  $\phi$  reaches the value  $\phi(T_a)$  following the evolution shown in Figure III.14. The fictive temperature  $T_f$  of the sample at  $T_a$  is defined as the temperature for which the out-of-equilibrium value  $\phi(T_a)$  would actually correspond to an equilibrium value.

The fictive temperature  $T_f(T_a)$  is determined graphically by considering the abscissa of the point where the line parallel to the linear variation of the vitreous state and passing through the point  $\phi(T_a)$  crosses the line extrapolated from the supercooled liquid (i.e. from the equilibrium state).

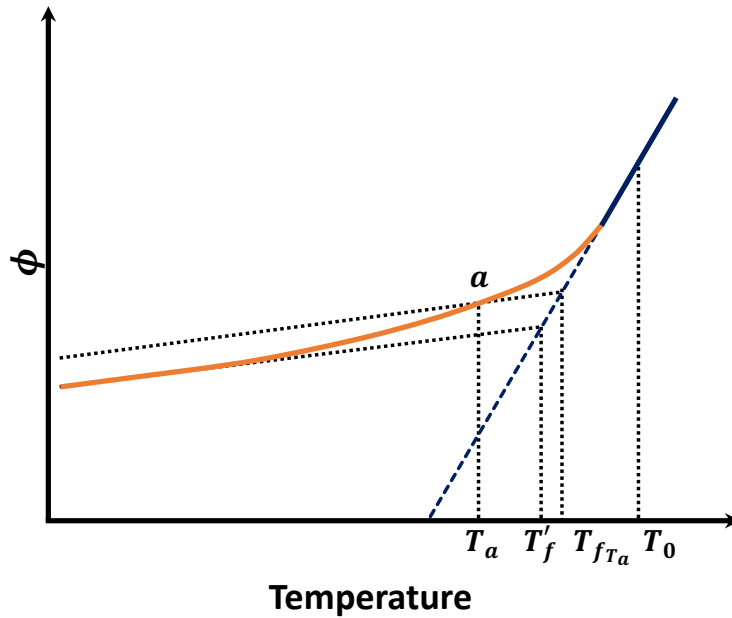


**Figure III.14: Graphical definition of the fictive temperature  $T_f(T_a)$ .**

It should be noted that the fictive temperature reaches a constant limit value, noted  $T_f'$ , when the temperature of the sample is much lower than  $T_g$ . In the liquid state, which is an equilibrium state, the fictive temperature  $T_f$  is equal to the temperature  $T$ . In the case of an isothermal plateau carried out at the temperature  $T_a$ , the return to the equilibrium of the structure of the glass is translated by a decrease of the fictive temperature. In the TNM model, after a temperature jump of amplitude  $\Delta T$  from an equilibrium state at  $T_0$ , the recovery of the fictive temperature is described by a relaxation function such as:

$$T_f(t) = T_0 + \Delta T(1 - \phi(t - t_1, t)) \quad (\text{III.16})$$

Where  $t_1$  is the moment when the abrupt change of temperature occurs.

Thus, during an abrupt temperature change at time  $t_1$ , the relaxation function at time  $t$  is defined by:

$$\phi(t - t_1, t) = \exp \left[ - \left( \int_{t_1}^t \frac{dt'}{\tau} \right)^\beta \right] \quad \text{for } t \geq t_1 \quad (\text{III.17})$$

Narayanaswamy<sup>40</sup> proposed the following expression for the relaxation time:

$$\tau = A \exp\left(\frac{H_g}{RT} + \frac{H_s}{RT_f}\right) \quad (\text{III.18})$$

Where  $A$ ,  $H_g$ , and  $H_s$  are material-dependent constants, and  $R$  is the gas constant.

The thermal and the structural contributions to the global relaxation phenomenon are described below, depending respectively on the temperature  $T$  and the fictive temperature  $T_f$ . When the system is at a thermodynamic equilibrium ( $T_f = T$ ), Equation III.18 is reduced to an Arrhenius equation with activation energy  $H_g + H_s$ .

Later on, a parameter of partition  $x$  was introduced to distinguish the thermal and structural contributions<sup>41</sup>:

$$\tau = A \exp\left(\frac{x\Delta h^*}{RT} + \frac{(1-x)\Delta h^*}{RT_f}\right) \quad (\text{III.19})$$

Where  $\Delta h^*$  is the energy associated with the relaxation process,  $A$  is a pre-exponential factor and  $x$  is a non-linearity parameter with  $0 \leq x \leq 1$ .

It must be emphasized that the apparent activation energy  $\Delta h^*$  is a constant in the expression of  $\tau$ , which indicates that the shape of the relaxation spectrum cannot be modified; such a thermo-rheological simplification is also a fundamental hypothesis of the TNM model.

The introduction of Equation III.17 (stretched exponential function) in the expression of the fictive temperature (Equation III.16) constitutes the basis of the TNM model. Equation III.16 (evolution of the fictive temperature after a temperature jump) can therefore be written as:

$$T_f(t) = T_0 + \Delta T \left(1 - \exp\left[-\left(\int_{t_1}^t \frac{dt'}{\tau}\right)^\beta\right]\right) \quad \text{for } t \geq t_1 \quad (\text{III.20})$$

A generalization of this expression in the case of several temperature jumps is obtained by writing that the evolution of  $T_f$  with time after the last temperature change (i.e.  $t \geq t_m$ ) is given by the superposition of the responses to each temperature changes of amplitude  $\Delta T_j$  made at the respective times  $t_j$ :

$$T_f(t) = T_0 + \sum_{j=1}^m \Delta T_j \left(1 - \phi(t - t_j, t)\right) \quad (\text{III.21})$$

The evaluation of the  $j^{\text{th}}$  integral of the  $\phi$  function (Equation III.17) should take into account that the fictive equilibrium temperature changes at each temperature jump, and is therefore different with respect to the temperature used for the  $j - 1^{\text{th}}$  jump.

Moynihan<sup>41</sup> verified that Equation III.21 correctly describes the memory effect, experimentally observed by considering the evolution of the fictive equilibrium temperature determined from refractive index measurements after two temperature jumps of opposite signs on a sample of boric anhydride ( $\text{B}_2\text{O}_3$ ).

Although correct, the description of the glass transition and the structural relaxation by this model presents several disadvantages. For example, the choice for  $\tau$  (Equation III.19) giving the temperature-dependence of an Arrhenius behavior when an equilibrium state is reached ( $T_f = T$ ) is not in agreement with all the WLF behaviors observed experimentally.

### III.5.5. Donth's approach

#### III.5.5.1. Introduction

The  $\alpha$  and  $\beta$  relaxation processes in a material can be studied by stressing it in dynamical conditions over a wide range of frequencies. Donth<sup>43</sup> defines the  $\alpha$  relaxation process revealed by dynamical measurements as a dynamic vitreous transition. This notion is based on the variations in molecular mobility ( $\log_{10}(\omega)$ , where  $\omega$  is the angular pulsation) recorded as a function of temperature  $T$ . The molecular mobility corresponds to the ease of movement of the structural units within a polymer chain, and is therefore inversely proportional to the relaxation time. Figure III.15 shows the evolution of molecular mobility expected when temperature changes.

At very high temperatures, the temperature dependence of molecular mobility follows an Arrhenius law (Region "A" in Figure III.15). This general behavior appears modified as the temperature decreases and reach a critical value, called the "crossover" temperature  $T_C$  (point "C" in Figure III.15). The idea of a "crossover" region was evoked for the first time in the 70's by Johari<sup>44</sup>, who predicted an increase in cooperativity at  $T < T_C$ .

The "crossover" region separates the linear Arrhenius behavior occurring in the so-called hot liquid ( $T > T_C$ ) from the non-linear  $\alpha$  relaxation process occurring in the so-called cold liquid ( $T < T_C$ ).

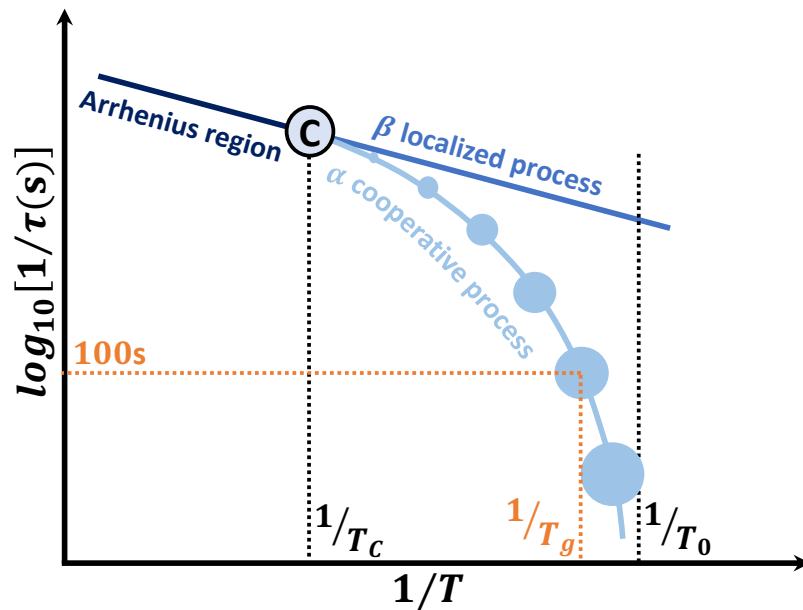


Figure III.15: A schematic plot of  $\log(1/\tau)$  versus  $1/T$  depicting the main relaxation process ( $\alpha$  process), the  $\beta$  relaxation process (localized or secondary), the cross-over region (C) where the temperature dependences of the  $\alpha$  and  $\beta$  processes merge, and high temperature process called relaxation A (Arrhenius).

$T_c$  is the cross-over temperature;  $T_g$  is the glass transition temperature and  $T_0$  is the Vogel temperature.

The existence a critical value of temperature  $T_c$  suggests a change in the relaxational dynamics: at  $T > T_c$  the molecular movements are characterized by a spatial homogeneity that is not ensured at  $T < T_c$ , when dynamical heterogeneities appear and the main relaxation process becomes cooperative. The notions of cooperativity and Cooperative Rearrangement Regions (CRR) were introduced as early as 1965 by Adam and Gibbs<sup>45</sup>. The basic assumption is that local molecular motions are not sufficient to maintain molecular mobility at low values of free volume. As they get closer (because the glass-forming liquid contracts during cooling) and their interactions increases, the molecular segments become unable to relax independently from each other, and the movement of each relaxing unit depends on the movement of its neighbors. As a consequence, relaxation is only possible if a minimum number  $N_\alpha$  of neighboring structural units is concomitantly relaxing. The  $N_\alpha$  structural units required for global relaxation constitute a sort of “region of cooperative rearrangements”. The structural units in a CRR can consist of one atom, a group of atoms, a molecule or the repeating unit of a polymer, according to the model used and the material investigated (Donth<sup>43</sup>, Solunov<sup>46</sup>, or Ngai<sup>47</sup>).



A CRR is defined as the smallest subsystem which, provided enough thermal agitation, rearranges into a different configuration with movements that do not depend on its environment. The average size of CRR depends on temperature, and is expected to increase as temperature decreases. The  $\alpha$  relaxation process starting at  $T = T_C$  is a cooperative process including the so-called thermal glass transition according to Donth, which occurs at the temperature  $T_g$  or  $T_\alpha$ . At  $T = T_C$ , the  $\beta$  relaxation process is distinguished from the  $\alpha$  relaxation process, because their temperature dependence keeps on following an Arrhenius law, is thermally activated and non-cooperative.

### III.5.5.2. Theoretical approach

The work carried out in the laboratory on the study of the dynamics of the molecular motions associated with structural relaxation requires a good understanding of Donth's theoretical approach. The PhD thesis of Hugues Couderc <sup>48</sup> and Nicolas Delpouve <sup>49</sup> provided a good background of Donth's approach and its possible applications to polymer systems.

In the Adam and Gibbs' concept, each glass-forming liquid is virtually composed of independent subsystems (CRR) that schematically correspond to the volume occupied by all the relaxing units that are able to relax independently of the surrounding relaxing units. At the glass transition, each CRR will therefore be characterized by a specific value of the relaxation time  $\tau$  and a specific temperature of dynamic vitreous transition  $T_\alpha$ . The average size of a CRR is generally expressed as a cooperativity length  $\xi_\alpha$ . Macroscopically, a glass-forming liquid at the glass transition has its own distribution of relaxation times, with an average value  $\langle\tau\rangle$ , and its own distribution of temperature of dynamic glass transition, with an average value  $\langle T_\alpha\rangle$ .

On the basis of this theoretical assumptions, Donth <sup>50</sup> considers that the molecular mobility  $\log(\omega)$  (and also the relaxation time  $\tau$ , because  $\omega = 1/\tau$ ) is not constant throughout a CRR. Each CRR can therefore be divided into  $i$  systems (or structural entities) of frequency  $\omega_i(t)$  and local free volume  $v_i(t)$  which fluctuate over time, under the assumption that  $\omega_i$  is a function of  $v_i$ . As a result, each CRR has a distribution of frequencies, with an average value  $\langle\omega\rangle$ , and a distribution of free volumes, with an average value  $\langle v\rangle$ . Generalized to the entire sample, the material is characterized by a distribution of frequencies with an average value  $\langle\Omega\rangle$ , and a distribution of free volumes, with an average value  $\langle V\rangle$ . A schematic representation is provided in [Figure III.16](#).

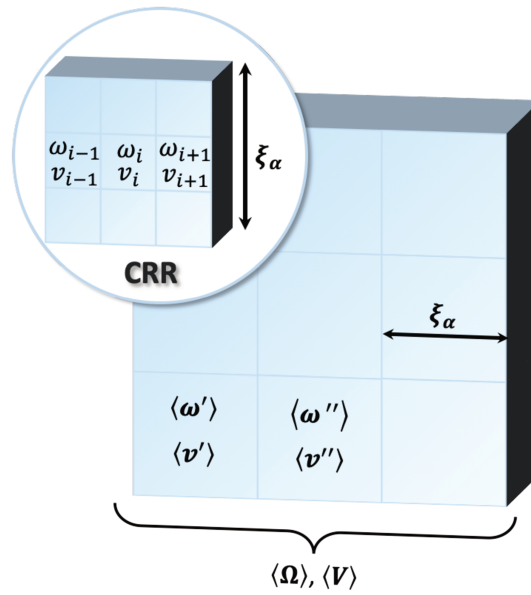


**Figure III.16:** Schematic representation of the cooperative rearranging regions proposed by Donth. Each CRR has its own free volume  $v$  and frequency  $\omega$ .

The average fluctuation of mobility around the average value for each CRR is noted  $\delta \log(\omega)$ . The different populations  $\{\omega_i\}$  are associated with different temperatures, and a mean temperature fluctuation noted  $\delta T$  is defined between the populations  $\{\omega_i\}$  in the CRR. The other hypotheses of Donth's theory are that:

- The functions  $\omega_i(t)$  of the partial systems are statistically independent stochastic functions.
- The cooperative movements come from the diffusion of free volume between the partial systems, which is associated with a redistribution of the free volume in an equilibrium area considered as the smallest representative subsystem (CRR). This means that, if the mobility in a partial system is modified, its variation will be randomly counterbalanced by a variation in some other partial systems within the CRR.

The local free volume  $V_i$  on a partial system varies over time. The average product of the  $V_i(t)$  values at two instants which differ from  $t_0$  defines the autocovariance function  $R_{V_i}(t_0)$ :

$$R_{V_i}(t_0) = \overline{V_i(t)V_i(t+t_0)} \quad (\text{III.22})$$

The function describing the distribution of free volume with respect to frequency, also called the spectral density of free volume and denoted  $\Delta V^2(\omega)$ , is defined as the Fourier transform of the autocovariance function  $R_{V_i}(t_0)$ :

$$\Delta V^2(\omega) = \frac{1}{\sqrt{2\pi}} \int_{-\infty}^{+\infty} R_{V_i}(t_0) e^{-i\omega t_0} dt_0 = \frac{1}{\sqrt{2\pi}} \int_{-\infty}^{+\infty} \overline{V_i(t)V_i(t+t_0)} e^{-i\omega t_0} dt_0 \quad (\text{III.23})$$

Donth<sup>43</sup> deduced that the spectral density  $\Delta V^2(\omega)$  is a distribution having a shape as shown in Figure III.17. This distribution has a preponderant component  $j$  with a high local mobility  $\log_{10}(\omega_j)$  and a high concentration of free volume  $V_j$ .

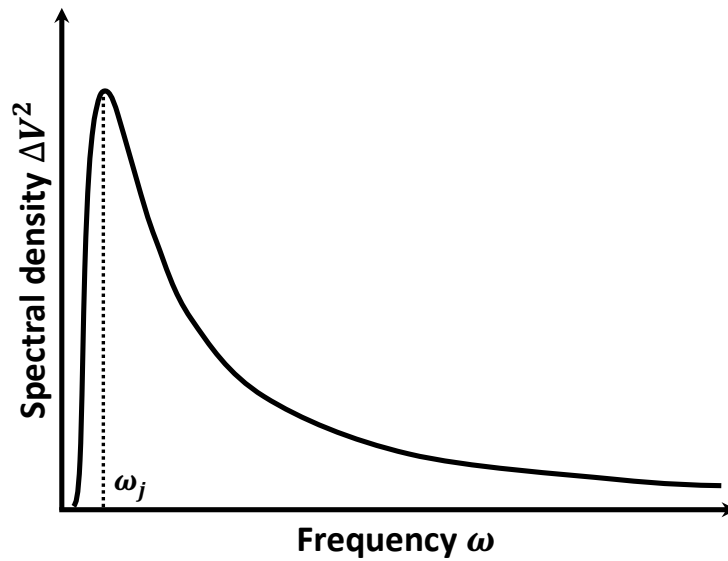


**Figure III.17:** Graphical representation of the spectral density of free volume according to Donth's approach.

The stochastic variation of the functions  $\omega_i(t)$  is associated with the random appearance and disappearance of mobility clusters in the spatial scale of a CRR and in the time scale of the  $\alpha$  process. This spatio-temporal distribution of molecular mobility corresponds to the dynamic heterogeneities appearing at  $T < T_C$  and the average distance between any two of these dynamic heterogeneities is the correlation length  $\xi_\alpha$ .

Donth's approach suggests that mobility at a given temperature is not constant in all points of the material, which means that mobility should be represented as a dispersion area rather than as a simple curve, as shown schematically in Figure III.18.

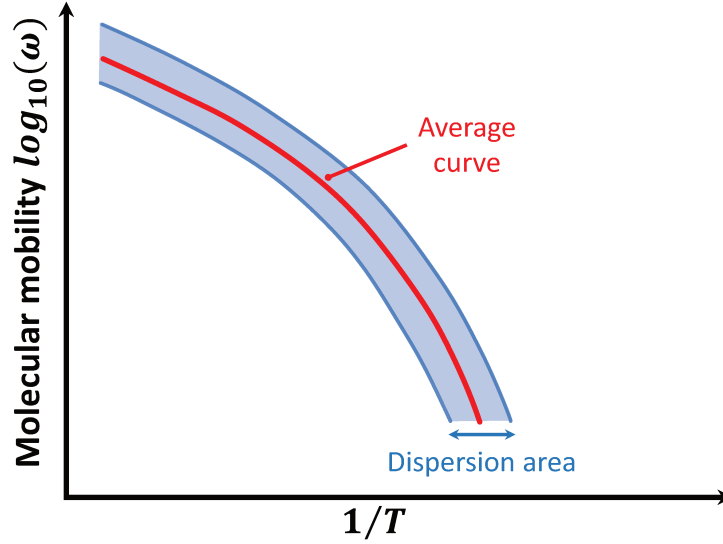


**Figure III.18:** Schematics of the notion of a dispersion area applied to a diagram showing the molecular mobility as a function of the inverse of the temperature.

Consider a generic response measured on a sample at the glass transition. If the sample is divided into two equal parts and the same measurement is repeated under the same conditions on one half of the sample, the result should be the same. Imagine to repeat the same procedures as long as the result remains unchanged. The result would eventually change when the size of the sample becomes smaller than the representative independent subsystem, i.e. smaller than a CRR. This would mean that the macroscopic linear response provides exactly the same response as a medium-sized CRR. Under this assumption, the response of the entire sample to the dynamic glass transition is indeed representative of the fluctuations of an average CRR. A CRR containing  $N_\alpha$  partial systems has an internal energy equals to:

$$\bar{E} = \frac{1}{Q} \sum_{i=1}^{i=N_\alpha} E_i P_i \quad (\text{III.24})$$

Where  $E_i$  denotes the possible energy states,  $P_i$  is the probability that the partial system  $i$  is in the energy state  $E_i$ , and  $Q = \sum_i P_i$  is the partition function. Using Boltzmann's statistical function, the probability  $P_i$  can be written as:

$$P_i = e^{-\frac{E_i}{k_B T}} \quad (\text{III.25})$$

Where  $T$  is the mean temperature and  $k_B$  is the Boltzmann's constant.

The energy  $E$  can be separated into two contributions <sup>51</sup>:

$$E = E^{(vib)} + E^{(\alpha)} \quad (III.26)$$

Where  $E^{(vib)}$  corresponds to the vibrational energy and is associated to the vitreous state, and  $E^{(\alpha)}$  is associated to the  $\alpha$  relaxation.

Equation III.26 implies the following approximate relationship, which uses the definition of the heat capacity:

$$\frac{\partial E^{(\alpha)}}{\partial T} = \frac{\partial E}{\partial T} - \frac{\partial E^{(vib)}}{\partial T} \approx C_{Vliquid} - C_{Vglass} = \Delta C_V \quad (III.27)$$

The energy fluctuations within a CRR are characterized by the standard deviation  $\delta E$  defined as:

$$\delta E^2 = \overline{E^2} - \bar{E}^2 \quad (III.28)$$

By deriving the average energy with respect to temperature, in the case of the  $\alpha$  relaxation it is possible to write the following equation:

$$\delta E^2 = k_B T^2 \frac{\partial E^{(\alpha)}}{\partial T} \quad (III.29)$$

Where  $\frac{\partial E^{(\alpha)}}{\partial T}$  is the derivative of the energy associated with the  $\alpha$  relaxation occurring within a CRR.

So, at the glass transition temperature:

$$\delta E^2 = k_B T^2 \Delta C_V \quad (III.30)$$

Starting from the definition of the heat capacity, one can also write that:

$$\delta E = C_V \delta T \quad (III.31)$$

At the glass transition temperature, Equation III.31 becomes:

$$\delta E = C_V \delta T_g \quad (III.32)$$

By comparing Equation III.30 and Equation III.32, the following expression is obtained:

$$k_B T_g^2 \frac{\Delta C_V}{C_V^2} = (\delta T_g)^2 \quad (III.33)$$

Or

$$\frac{\Delta C_V}{C_V^2} \approx \Delta \left( \frac{1}{C_V} \right) = \frac{1}{C_{Vglass}} - \frac{1}{C_{Vliquid}} \quad (III.34)$$

Assuming that the variations of  $1/C_p$  are identical to those of  $1/C_v$ , Equation III.33 can be rewritten as:

$$k_B T_g^2 \Delta \left( \frac{1}{C_p} \right) = (\delta T_g)^2 \quad (\text{III.35})$$

With:

$$\Delta \left( \frac{1}{C_p} \right) = \frac{1}{C_{p_{glass}}} - \frac{1}{C_{p_{liquid}}} \quad (\text{III.36})$$

The heat capacity  $C_p$  can be expressed as a function of the specific heat capacity  $c_p$  ( $C_p = \rho V_\alpha c_p$ ), therefore the volume of a CRR is given by:

$$V_\alpha = \frac{\Delta \left( \frac{1}{c_p} \right)}{\rho (\delta T_g)^2} k_B T_g^2 \quad (\text{III.37})$$

Assuming that the CRR is a cube, the cooperativity length is obtained from  $V_\alpha = \xi_\alpha^3$ .

Equation III.37 can also be rewritten as:

$$N_\alpha = \frac{\rho V_\alpha}{M_0 N_A} = \frac{\Delta \left( \frac{1}{c_p} \right)}{M_0 (\delta T_g)^2} R T_g^2 \quad (\text{III.38})$$

Where  $N_\alpha$  is the number of partial systems or structural entities in a CRR,  $M_0$  is the molar mass of each partial system, and  $N_A$  is the Avogadro number.

Equation III.37 and Equation III.38 are called the fluctuation formulas. They allow to calculate the average size of a CRR from the average temperature fluctuation  $\delta T$ .

### III.5.5.3. Extension of the Donth's model

The initial model proposed by Donth<sup>52</sup> to estimate the CRR size applies only to a narrow range of temperature and frequency close to the calorimetric glass transition temperature  $T_g$ . An extended form of the Donth's model, which allows to estimate the cooperativity size in a wider range of temperature and frequency by combining two experimental techniques (MT-DSC and DRS), has been recently proposed by Saiter et al.<sup>53,54</sup>.

These two techniques are perfectly complementary for the investigation of the glass transition for several reasons. Both methods probe the dynamic glass transition by applying a periodic perturbation to the sample (a modulated temperature ramp in MT-DSC, an oscillating electrical field in DRS), which allows to obtain complex quantities: the complex heat capacity  $C_p^*$  for MT-DSC, and the complex dielectric permittivity  $\varepsilon^*$  for DRS.

Both these quantities have a real and an imaginary component ( $C_p'$  and  $C_p''$ ,  $\varepsilon'$  and  $\varepsilon''$ , respectively) <sup>55,56</sup>. From the point of view of the linear response theory, both the complex permittivity and the complex heat capacity are generalized compliances. Therefore, both quantities can be directly compared.

In MT-DSC results, the dynamic glass transition is detected as a heat capacity step  $\Delta C_p$  in the real component of the signal, and a dissipative peak in the imaginary component of the signal. In DRS results, the dynamic glass transition is detected as a step commonly known as the dielectric strength  $\Delta\varepsilon$  in the real component of the signal, and a peak in the imaginary component of the signal.  $\Delta C_p$  and  $\Delta\varepsilon$  are both due to the response of the amorphous phase contributing to the glass transition <sup>32,34</sup>.

The function describing the distribution of relaxation times for a glass-forming liquid is temperature-dependent. In an Arrhenius diagram, this distribution is represented by a dispersion zone <sup>57</sup> that broadens as temperature increases.

This dependence corresponds to the broadening and shift of the loss peak towards higher temperatures as the frequency of the applied perturbation increases, which is observable by DRS <sup>34,57,58</sup>. Different quantities are measured by MT-DSC and DRS: it is worth reminding that the temperature  $T$  and the electric field  $E$  are intensive variables, whereas the entropy  $S$  and the orientation polarization  $P$  are extensive variables. The Callen-Welton theorem applied to MT-DSC gives the following relations <sup>57</sup>:

$$G_T''(\omega) = \frac{\pi\omega\Delta T^2(\omega)}{k_B T} \quad (\text{III.39})$$

$$J_S''(\omega) = \frac{\pi\omega\Delta S^2(\omega)}{k_B T} \quad (\text{III.40})$$

Where  $G_T''(\omega)$  is the imaginary component of the complex temperature modulus ( $G_T^* = \partial T/\partial S = T/C_V^*$ ) and  $J_S''(\omega)$  is the imaginary component of the complex entropy compliance ( $J_T^* = \partial S/\partial T = C_V^*/T$ ),  $\Delta T^2(\omega)$  and  $\Delta S^2(\omega)$  are the spectral densities of temperature and entropy fluctuations respectively, and  $C_V^*$  is the complex specific heat capacity at constant volume.

In the case of DRS, the equivalent relations are <sup>34</sup>:

$$M''(\omega) = \frac{\pi\omega\Delta E^2(\omega)}{k_B T} \quad (\text{III.41})$$

$$\chi''(\omega) = \frac{\pi\omega\Delta P^2(\omega)}{k_B T} \quad (\text{III.42})$$

Where  $M''(\omega)$  is the imaginary component of the complex electric modulus ( $M^* = \partial E / \partial P$ ) and  $\chi''(\omega)$  is the imaginary component of the dielectric susceptibility ( $\chi^* = \varepsilon^* - 1 = \partial P / \partial E$ ),  $\Delta E^2(\omega)$  and  $\Delta P^2(\omega)$  are the spectral densities of the local electric field and the polarization respectively, and  $\varepsilon^*$  is the complex dielectric permittivity.

The combination of Equation III.41 and Equation III.42 gives:

$$\frac{\Delta T^2(\omega)}{\Delta P^2(\omega)} = \frac{G_T''(\omega)}{\chi''(\omega)} \quad (\text{III.43})$$

Assuming that  $G_T''(\omega)$  and  $\chi''(\omega)$  can be factorized in an intensity factor and a spectral shape function of  $(\omega)$ :

$$G_T''(\omega) = G_0(T)f_T(\omega) \quad (\text{III.44})$$

$$\chi''(\omega) = \chi_0(T)f_\chi(\omega) \quad (\text{III.45})$$

It is possible to write that:

$$\frac{\Delta T^2(\omega)}{\Delta P^2(\omega)} = \frac{G_0(T)f_T(\omega)}{\chi_0(T)f_\chi(\omega)} \quad (\text{III.46})$$

If the temperature and polarization fluctuations have approximately the same spectral shape function  $f_T(\omega) \approx f_\chi(\omega)$ , which seems to be a reasonable assumption, the width of the temperature fluctuations can be estimated from the width of the polarization fluctuations.

So, the evolution of the CRR size as a function of time and temperature can be determine by the extended Donth's approach.

To determine the cooperativity length  $\xi_\alpha$  (Equation III.37) and the number of units that cooperatively rearrange at the glass transition  $N_\alpha$  (Equation III.38), the average temperature fluctuation  $\delta T$  needs to be determined.

This value can be obtained from MT-DSC measurements performed in a heat-cool mode, but also from DRS investigations, as already detailed in the literature<sup>53</sup>. In particular,  $\delta T$  is extracted from the imaginary component of the complex heat capacity  $C_p''(T)$ , or from the imaginary component of the complex dielectric permittivity  $\varepsilon''(T)$ .



Figure III.19 shows the calculation process that allows to estimate  $\delta T$  from the Full-Width Half-Maximum (FWHM) of the Gaussian peak function ( $\delta T = FWHM/2.355$ ), which was used to fit the imaginary components of both MT-DSC and DRS spectra, where the maximum of the peak corresponds to the dynamic glass transition  $T_\alpha$ :

$$C''(T) \text{ or } \varepsilon''(T) = \frac{A}{\sigma_T \sqrt{2\pi}} \exp\left(-\frac{(T-T_\alpha)^2}{2\sigma_T^2}\right) \quad (\text{III.47})$$

Where  $A$  is the peak area,  $\sigma_T$  is the standard deviation and  $T_\alpha$  the dynamic glass transition temperature.

The quantity  $\Delta C_p^{-1}$  (i.e. the difference in the inverse values of the isobaric heat capacity between the liquid and glassy states extrapolated at the dynamic glass transition temperature  $T_\alpha$ ) is calculated from MT-DSC measurements performed with a heat-cool protocol, as illustrated by Figure III.19.

To resume, combining the experimental data obtained by MT-DSC and DRS allows to extend the Donth's model (generally applied to MT-DSC results) to a wider range of frequencies, which in turn allows the calculation of the temperature-dependence of  $N_\alpha$  in a wide temperature range, starting from the onset of cooperativity in the crossover region down to the calorimetric glass transition temperature  $T_g$ .

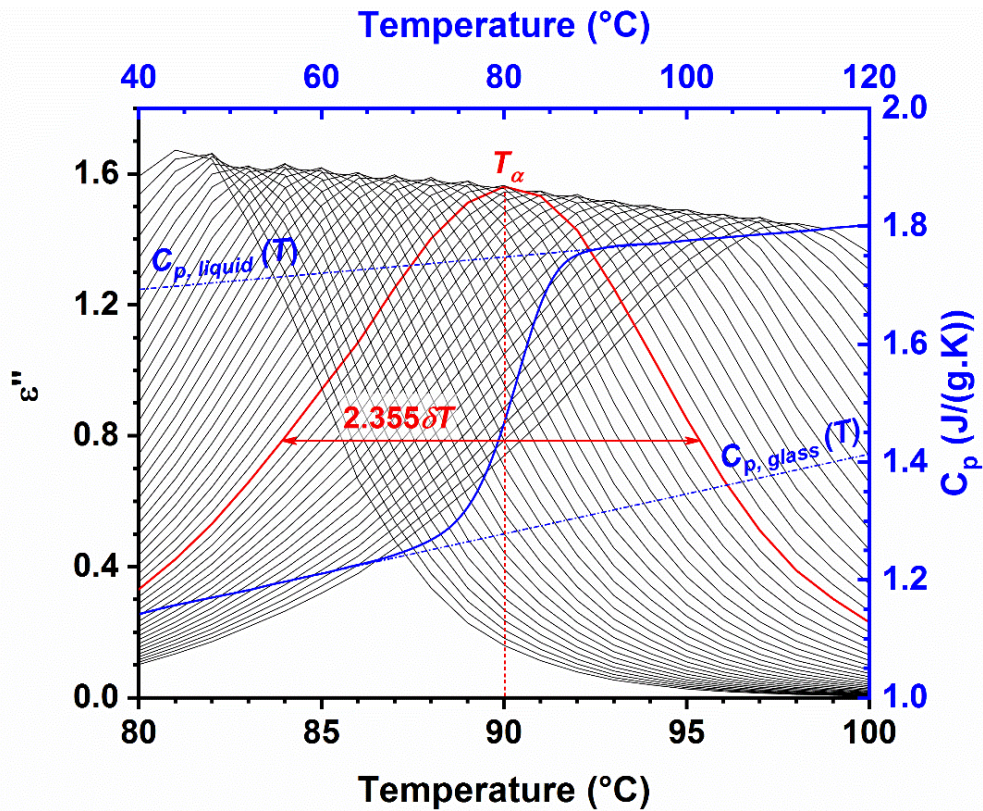


Figure III.19: Heat capacity  $C_p$  as a function of temperature obtained from MT-DSC measurements with a heat-cool mode vs. dielectric loss  $\epsilon''$  (after subtraction of conductivity) as a function of temperature from DRS measurements.

The blue dashed dot lines represent the heat capacity in the glassy and liquid states extrapolated to the entire temperature range of the glass transition. The red solid line corresponds to the Gaussian fit of a dielectric loss spectrum. The dynamic glass transition temperature  $T_\alpha$  is read at the maximum of the PearsonVII peak for each dielectric or calorimetric relaxation peak. The average temperature fluctuation  $\delta T$  is estimated from the FWHM.

## References

- (1) Typical-x-ray-powder-diffraction-pattern-of-crystalline-and-amorphous-drug.jpg [http://www.ivtnetwork.com/sites/default/files/imagecache/gallery\\_full/Typical-x-ray-powder-diffraction-pattern-of-crystalline-and-amorphous-drug.jpg](http://www.ivtnetwork.com/sites/default/files/imagecache/gallery_full/Typical-x-ray-powder-diffraction-pattern-of-crystalline-and-amorphous-drug.jpg) (accessed Jan 19, 2020).
- (2) Kalogeras, I. M. Glass-Transition Phenomena in Polymer Blends. In *Encyclopedia of Polymer Blends*; Isayev, A. I., Ed.; Wiley-VCH Verlag GmbH & Co. KGaA: Weinheim, Germany, 2016; pp 1–134.  
<https://doi.org/10.1002/9783527653966.ch1>.
- (3) Haward, R. The Nature of Polymer Glasses, Their Packing Density, and Mechanical Behavior. *The Physics of Glassy Polymers* **1973**, 1–51.
- (4) Ehrenfest, P. Phasenumwandlungen Im Ueblichen Und Erweiterten Sinn, Classifiziert Nach Den Entsprechenden Singularitaeten Des Thermodynamischen Potentiales. *NV Noord-Hollandsche Uitgevers Maatschappij* **1933**.
- (5) Kauzmann, Walter. The Nature of the Glassy State and the Behavior of Liquids at Low Temperatures. *Chem. Rev.* **1948**, *43* (2), 219–256.  
<https://doi.org/10.1021/cr60135a002>.
- (6) Callen, H. Thermodynamics and an Introduction to Thermostatistics. *Wiley, Singapore* **1985**.
- (7) Debenedetti, P. G.; Stillinger, F. H. Supercooled Liquids and the Glass Transition. *Nature* **2001**, *410* (6825), 259–267.  
<https://doi.org/10.1038/35065704>.
- (8) Weyer, S.; Huth, H.; Schick, C. Application of an Extended Tool–Narayanaswamy–Moynihan Model. Part 2. Frequency and Cooling Rate Dependence of Glass Transition from Temperature Modulated DSC. *Polymer* **2005**, *46* (26), 12240–12246.  
<https://doi.org/10.1016/j.polymer.2005.10.097>.
- (9) Dhotel, A.; Rijal, B.; Delbreilh, L.; Dargent, E.; Saiter, A. Combining Flash DSC, DSC and Broadband Dielectric Spectroscopy to Determine Fragility. *J Therm Anal Calorim* **2015**, *121* (1), 453–461.  
<https://doi.org/10.1007/s10973-015-4650-9>.
- (10) McCrum, N. G.; Read, B. E.; Williams, G. Anelastic and Dielectric Effects in Polymeric Solids. **1967**.
- (11) Boyer, R. F. Glassy Transitions in Semicrystalline Polymers. *Journal of Polymer Science: Polymer Symposia* **1975**, *50* (1), 189–242.  
<https://doi.org/10.1002/polc.5070500114>.
- (12) Monnerie, L. Dynamique Locale Des Polymères et Influence Sur Les Propriétés Mécaniques. *Initiation à la chimie et à la physico-chimie macromoléculaires* **1990**, *8*, 183–232.
- (13) Perez, J. Physique et mécanique des polymères amorphes. **2017**.
- (14) Struik, L. Physical Aging in Polymers and Other Amorphous Materials. *Elsevier, Amsterdam* **1978**.
- (15) Kovacs, A. J. La contraction isotherme du volume des polymères amorphes. *Journal of Polymer Science* **1958**, *30* (121), 131–147.  
<https://doi.org/10.1002/pol.1958.1203012111>.
- (16) Kovacs, A.; Hutchinson, J.; Aklonis, J. The Structure of Non-Crystalline Materials. *Taylor and Francis, London* **1977**, 153.

- (17) Bauwens-Crowet, C.; Bauwens, J.-C. Annealing of Polycarbonate below the Glass Transition: Quantitative Interpretation of the Effect on Yield Stress and Differential Scanning Calorimetry Measurements. *Polymer* **1982**, *23* (11), 1599–1604.  
[https://doi.org/10.1016/0032-3861\(82\)90178-1](https://doi.org/10.1016/0032-3861(82)90178-1).
- (18) Bauwens-Crowet, C.; Bauwens, J.-C. Annealing of Polycarbonate below the Glass Transition Temperature up to Equilibrium: A Quantitative Interpretation of Enthalpy Relaxation. *Polymer* **1986**, *27* (5), 709–713.  
[https://doi.org/10.1016/0032-3861\(86\)90128-X](https://doi.org/10.1016/0032-3861(86)90128-X).
- (19) Ritland, H. N. Limitations of the Fictive Temperature Concept. *Journal of the American Ceramic Society* **1956**, *39* (12), 403–406.  
<https://doi.org/10.1111/j.1151-2916.1956.tb15613.x>.
- (20) Struik, L. C. E. The Mechanical and Physical Ageing of Semicrystalline Polymers: 1. *Polymer* **1987**, *28* (9), 1521–1533.  
[https://doi.org/10.1016/0032-3861\(87\)90353-3](https://doi.org/10.1016/0032-3861(87)90353-3).
- (21) Rekhson, S. M. Memory Effects in Glass Transition. *Journal of Non-Crystalline Solids* **1986**, *84* (1), 68–85.  
[https://doi.org/10.1016/0022-3093\(86\)90763-5](https://doi.org/10.1016/0022-3093(86)90763-5).
- (22) Berens, A. R.; Hodge, I. M. Effects of Annealing and Prior History on Enthalpy Relaxation in Glassy Polymers. 1. Experimental Study on Poly(Vinyl Chloride). *Macromolecules* **1982**, *15* (3), 756–761.  
<https://doi.org/10.1021/ma00231a015>.
- (23) Kovacs, A. J.; Hutchinson, J. M. Isobaric Thermal Behavior of Glasses during Uniform Cooling and Heating: Dependence of the Characteristic Temperatures on the Relative Contributions of Temperature and Structure to the Rate of Recovery. II. A One-Parameter Model Approach. *Journal of Polymer Science: Polymer Physics Edition* **1979**, *17* (12), 2031–2058.  
<https://doi.org/10.1002/pol.1979.180171201>.
- (24) Kovacs, A. J.; Aklonis, J. J.; Hutchinson, J. M.; Ramos, A. R. Isobaric Volume and Enthalpy Recovery of Glasses. II. A Transparent Multiparameter Theory. *Journal of Polymer Science: Polymer Physics Edition* **1979**, *17* (7), 1097–1162.  
<https://doi.org/10.1002/pol.1979.180170701>.
- (25) Goldstein, M. Modern Aspects of the Vitreous State. *JD Mackenzie, Ed* **1964**, *3*, 90.
- (26) Kovacs, A. Glass Transition in Amorphous Polymers: A Phenomenological Study. *Adv. Polym. Sci* **1963**, *3* (3), 394–507.
- (27) Aklonis, J.; Kovacs, A. Contemporary Topics in Polymer Science. *M. Shen, ed* **1979**, *3*, 267.
- (28) Macedo, P. B.; Napolitano, A. Effects of a Distribution of Volume Relaxation Times in the Annealing of Bsc Glass. *J. RES. NATL. BUR. STAN. SECT. A.* **1967**, *71A* (3), 231.  
<https://doi.org/10.6028/jres.071A.031>.
- (29) Hodge, I. M.; Berens, A. R. Effects of Annealing and Prior History on Enthalpy Relaxation in Glassy Polymers. 2. Mathematical Modeling. *Macromolecules* **1982**, *15* (3), 762–770.  
<https://doi.org/10.1021/ma00231a016>.
- (30) Kohlrausch, R. Theorie Des Elektrischen Rückstandes in Der Leidener Flasche. *Annalen der Physik* **1854**, *167* (2), 179–214.  
<https://doi.org/10.1002/andp.18541670203>.

- (31) Williams, G.; C. Watts, D. Non-Symmetrical Dielectric Relaxation Behaviour Arising from a Simple Empirical Decay Function. *Transactions of the Faraday Society* **1970**, *66* (0), 80–85.  
<https://doi.org/10.1039/TF9706600080>.
- (32) Vogel, H. Z. Phys 1921, *22*, 645.[CAS]. *The law of the relation between the viscosity of liquids and the temperature Vogel*, *Hans Physikalische Zeitschrift* **1921**, *22*, 645–646.
- (33) Fulcher, G. S. Analysis of Recent Measurements of the Viscosity of Glasses. *Journal of the American Ceramic Society* **1925**, *8* (6), 339–355.  
<https://doi.org/10.1111/j.1151-2916.1925.tb16731.x>.
- (34) Tammann, G.; Hesse, W. Die Abhängigkeit Der Viscosität von Der Temperatur Bie Unterkühlten Flüssigkeiten. *Z. Anorg. Allg. Chem.* **1926**, *156* (1), 245–257.  
<https://doi.org/10.1002/zaac.19261560121>.
- (35) Zarzycki, J. Les Verres et l'état Vitreux. *Edition Masson, Paris* **1982**.
- (36) Angell, C. A.; Kadiyala, R. K.; MacFarlane, D. R. Glass-Forming Microemulsions. *J. Phys. Chem.* **1984**, *88* (20), 4593–4596.  
<https://doi.org/10.1021/j150664a031>.
- (37) Angell, C. A. Perspective on the Glass Transition. *Journal of Physics and Chemistry of Solids* **1988**, *49* (8), 863–871.  
[https://doi.org/10.1016/0022-3697\(88\)90002-9](https://doi.org/10.1016/0022-3697(88)90002-9).
- (38) Plazek, D. J.; Ngai, K. L. Correlation of Polymer Segmental Chain Dynamics with Temperature-Dependent Time-Scale Shifts. *Macromolecules* **1991**, *24* (5), 1222–1224.  
<https://doi.org/10.1021/ma00005a044>.
- (39) Tool, A. Q.; Eicitlin, C. G. Variations Caused in the Heating Curves of Glass by Heat Treatment1. *Journal of the American Ceramic Society* **1931**, *14* (4), 276–308.  
<https://doi.org/10.1111/j.1151-2916.1931.tb16602.x>.
- (40) Narayanaswamy, O. S. A Model of Structural Relaxation in Glass. *Journal of the American Ceramic Society* **1971**, *54* (10), 491–498.  
<https://doi.org/10.1111/j.1151-2916.1971.tb12186.x>.
- (41) Moynihan, C. T.; Eastal, A. J.; Bolt, M. A. D.; Tucker, J. Dependence of the Fictive Temperature of Glass on Cooling Rate. *Journal of the American Ceramic Society* **1976**, *59* (1–2), 12–16.  
<https://doi.org/10.1111/j.1151-2916.1976.tb09376.x>.
- (42) Tool, A. Q. Viscosity and the Extraordinary Heat Effects in Glass. *J. Am. Ceram. Soc* **1946**, *29* (9).
- (43) Donth, E.; Hempel, E. Structural Relaxation above the Glass Temperature: Pulse Response Simulation with the Narayanaswamy Moynihan Model for Glass Transition. *Journal of Non-Crystalline Solids* **2002**, *306* (1), 76–89.  
[https://doi.org/10.1016/S0022-3093\(02\)01052-9](https://doi.org/10.1016/S0022-3093(02)01052-9).
- (44) Johari, G. P. Glass Transition and Secondary Relaxations in Molecular Liquids and Crystals. *Annals of the New York Academy of Sciences* **1976**, *279* (1), 117–140.  
<https://doi.org/10.1111/j.1749-6632.1976.tb39701.x>.
- (45) Adam, G.; Gibbs, J. H. On the Temperature Dependence of Cooperative Relaxation Properties in Glass-Forming Liquids. *The Journal of Chemical Physics* **1965**, *43* (1), 139–146.  
<https://doi.org/10.1063/1.1696442>.

- (46) Solunov, C. A. Cooperative Molecular Dynamics and Strong/Fragile Behavior of Polymers. *European Polymer Journal* **1999**, *35* (8), 1543–1556.  
[https://doi.org/10.1016/S0014-3057\(98\)00226-2](https://doi.org/10.1016/S0014-3057(98)00226-2).
- (47) Ngai, K. L. An Extended Coupling Model Description of the Evolution of Dynamics with Time in Supercooled Liquids and Ionic Conductors. *J. Phys.: Condens. Matter* **2003**, *15* (11), S1107–S1125.  
<https://doi.org/10.1088/0953-8984/15/11/332>.
- (48) Couderc, H. Composites Polyester Amorphe - Montmorillonite : Influence Des Nanoparticules Sur Les Dynamiques Des Relaxations Moléculaires. thesis, Rouen, 2008.
- (49) Delpouve, N. Étude de La Microstructure et Des Phénomènes de Relaxation Dans Un Polyester Biodégradable : Le Poly (Acide Lactique) (PLA). thesis, Rouen, 2009.
- (50) Donth, E. Phenomenological Treatment of Dynamic Glass Transition Heterogeneity. *Acta Polym.* **1999**, *50* (7), 240–251.  
[https://doi.org/10.1002/\(SICI\)1521-4044\(19990701\)50:7<240::AID-APOL240>3.0.CO;2-H](https://doi.org/10.1002/(SICI)1521-4044(19990701)50:7<240::AID-APOL240>3.0.CO;2-H).
- (51) Sillescu, H. Heterogeneity at the Glass Transition: A Review. *Journal of Non-Crystalline Solids* **1999**, *243* (2), 81–108.  
[https://doi.org/10.1016/S0022-3093\(98\)00831-X](https://doi.org/10.1016/S0022-3093(98)00831-X).
- (52) Donth, E. The Size of Cooperatively Rearranging Regions at the Glass Transition. *Journal of Non-Crystalline Solids* **1982**, *53* (3), 325–330.  
[https://doi.org/10.1016/0022-3093\(82\)90089-8](https://doi.org/10.1016/0022-3093(82)90089-8).
- (53) Saiter, A.; Delbreilh, L.; Couderc, H.; Arabeche, K.; Schönhals, A.; Saiter, J.-M. Temperature Dependence of the Characteristic Length Scale for Glassy Dynamics: Combination of Dielectric and Specific Heat Spectroscopy. *Phys. Rev. E* **2010**, *81* (4), 041805.  
<https://doi.org/10.1103/PhysRevE.81.041805>.
- (54) Saiter, A.; Prevosto, D.; Passaglia, E.; Couderc, H.; Delbreilh, L.; Saiter, J. M. Cooperativity Length Scale in Nanocomposites: Interfacial and Confinement Effects. *Phys. Rev. E* **2013**, *88* (4), 042605.  
<https://doi.org/10.1103/PhysRevE.88.042605>.
- (55) Schönhals, A.; Kremer, F. Analysis of Dielectric Spectra. In *Broadband Dielectric Spectroscopy*; Kremer, P. D. F., Schönhals, P.-D. D. A., Eds.; Springer Berlin Heidelberg, 2003; pp 59–98.  
[https://doi.org/10.1007/978-3-642-56120-7\\_3](https://doi.org/10.1007/978-3-642-56120-7_3).
- (56) Dalle-Ferrier, C.; Thibierge, C.; Alba-Simionesco, C.; Berthier, L.; Biroli, G.; Bouchaud, J.-P.; Ladieu, F.; L'Hôte, D.; Tarjus, G. Spatial Correlations in the Dynamics of Glassforming Liquids: Experimental Determination of Their Temperature Dependence. *Phys. Rev. E* **2007**, *76* (4), 041510.  
<https://doi.org/10.1103/PhysRevE.76.041510>.
- (57) Donth, E. *The Glass Transition: Relaxation Dynamics in Liquids and Disordered Materials*; Springer Science & Business Media, 2013.
- (58) Reading, M.; Luget, A.; Wilson, R. Modulated Differential Scanning Calorimetry. *Thermochimica Acta* **1994**, *238*, 295–307.  
[https://doi.org/10.1016/S0040-6031\(94\)85215-4](https://doi.org/10.1016/S0040-6031(94)85215-4).

# CHAPTER IV

## Physical Characterization and Investigation of the Molecular Mobility in Amorphous PEFs

### Content

Introduction .....	103
IV.1. Preliminary analyses .....	103
IV.1.1. FTIR spectroscopy .....	103
IV.1.2. Thermal stability .....	104
IV.1.2.1. Conventional TGA .....	104
IV.1.2.2. Determination of the activation energy by MTGA.....	106
IV.1.3. Thermal properties .....	108
IV.1.3.1. Conventional DSC.....	108
IV.1.3.2. Mixing laws .....	111
IV.2. Molecular dynamics in amorphous PEFs .....	113
IV.2.1. Investigation of the amorphous phases by MT-DSC .....	113
IV.2.2. Segmental relaxation investigated by DRS.....	115
IV.2.2.1. Shape parameters $\alpha$ and $\beta$ of the $\alpha$ relaxation.....	120
IV.2.2.2. Dielectric relaxation strength $\Delta\epsilon_{HN}$ .....	122
IV.2.2.3. Relaxation map .....	125
IV.2.2.4. Characterization of the $\beta$ relaxation .....	126
IV.2.2.5. Characterization of the $\alpha$ relaxation .....	126
IV.2.2.6. Fragility index $m$ .....	127
IV.2.2.7. Cooperativity length $\xi_\alpha$ and cooperativity degree $N_\alpha$ .....	129
IV.2.3. Thermally Stimulated Depolarization Current (TSDC).....	130
IV.2.3.1. Impact of the incorporation of 2,4-FDCA DME on glass transition signature	130
IV.2.3.2. Relaxation map combining the three techniques .....	132
IV.2.3.3. Activation energies .....	133
IV.2.3.4. Fragility indexes .....	134

Conclusion.....	135
References .....	137



## Introduction

This chapter starts with the analyses typically performed after synthesis. Then, the influence of the position of the carbonyl group on the furan ring onto the molecular mobility of amorphous PEFs will be presented. Molecular mobility was investigated by Modulated-Temperature Differential Scanning Calorimetry (MT-DSC), Dielectric Relaxation Spectroscopy (DRS) and Thermally-Stimulated Depolarization Current (TSDC). The combination of these techniques provided information about both the primary and secondary relaxations. In addition, the parameters characteristic of the  $\alpha$  relaxation, such as the dielectric strength, the relaxation times and the fragility index, are presented and discussed.

### IV.1. Preliminary analyses

#### IV.1.1. FTIR spectroscopy

Infrared spectroscopic analyses were performed to evaluate the possible effect of a change in the position of the carbonyl group onto the absorption bands. FTIR spectra are showed in [Figure IV.1](#).

FTIR confirmed the expected chemical structure, because the spectra obtained for 2,5-PEF are comparable with those reported in the literature <sup>1,2</sup>. The absorption bands and peaks characteristic of the furan ring in furan-aromatic polyesters are regularly detected, such as the C–H bond at 3119  $\text{cm}^{-1}$ , the C=C bond at 1576  $\text{cm}^{-1}$ , the furan ring breathing peak around 1044 and 1020  $\text{cm}^{-1}$ , and the furan bending motions around 963, 830 and 758  $\text{cm}^{-1}$ . In addition, the peaks corresponding to the C=O bond of the ester carbonyl group (1715  $\text{cm}^{-1}$ ), to the C–O bond of the ester carbonyl group (1273-1266  $\text{cm}^{-1}$ ) and to the C–H and –CH<sub>2</sub> (2965  $\text{cm}^{-1}$ ) are also recorded. Few differences can be observed, which have been highlighted in grey in [Figure IV.1](#). There may be an influence on C–H bending, because the second peak at 1519  $\text{cm}^{-1}$  increases whereas the intensity of the absorption at 1379  $\text{cm}^{-1}$  decreases as the amount of 2,4-FDCA DME increases. The introduction of 2,4-FDCA DME repeating units in the polymer backbone would also have an impact on the C–O and C–C stretching, because the peak at 1219  $\text{cm}^{-1}$  decreases, the shoulder at 1291  $\text{cm}^{-1}$  disappears, two additional peaks appear at 1196  $\text{cm}^{-1}$  and 1079  $\text{cm}^{-1}$  and the peak at 936  $\text{cm}^{-1}$  decreases.

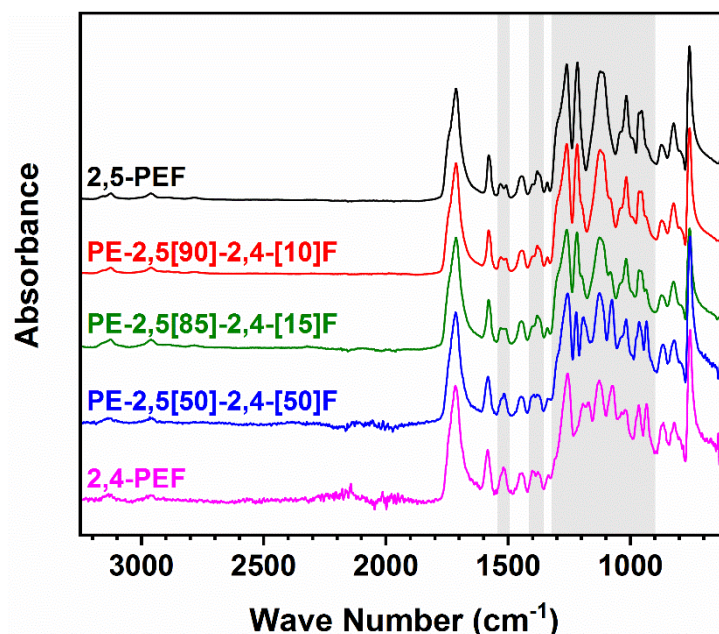


Figure IV.1: FTIR spectra of 2,5-PEF, 2,4-PEF and PE-[2,5-co-2,4]F copolymers. All the spectra were normalized with respect to the carbonyl peak ( $1715\text{ cm}^{-1}$ ).

## IV.1.2. Thermal stability

### IV.1.2.1. Conventional TGA

A preliminary TGA scan is necessary to make sure that the synthesized polymers are stable in the temperature range targeted for the subsequent DSC scans. Figure IV.2 shows the thermograms obtained by TGA along with the derivatives curves as a function of temperature under nitrogen (inert) or air (oxidative) atmosphere recorded with a heating rate of  $10\text{ °C/min}$ . All the samples have similar degradation behaviors when the temperature is increased, whatever the ratio of the FDCA isomers. In particular, they are stable up to  $250\text{ °C}$  (mass loss  $< 1\text{ wt\%}$ ), which authorizes quite broad processing windows.

Under nitrogen, their thermal decomposition occurs in a single stage decomposition mechanism and is observed between  $300$  and  $450\text{ °C}$ , with residual masses between  $9$  and  $12\%$ . Under air, a second stage appears in the decomposition mechanism after  $500\text{ °C}$  and  $600\text{ °C}$ , which allows the complete degradation of the material. Whatever the atmosphere, the incorporation of 2,4-FDCA into 2,5-FDCA-based polyesters tends to increase the thermal stability (Table IV.1). For instance, under nitrogen,  $T_{d\text{ max}}$  is recorded at its minimum ( $428\text{ °C}$ ) for 2,5-PEF and at its maximum ( $444\text{ °C}$ ) for 2,4-PEF, and the values found for the copolyesters are intermediate. Compared to the literature, PEFs have a thermal stability which is intermediate between PLA ( $325\text{ °C}$ <sup>3</sup>), PET ( $451\text{ °C}$ <sup>2</sup>) and PEN ( $465\text{ °C}$ <sup>4</sup>).

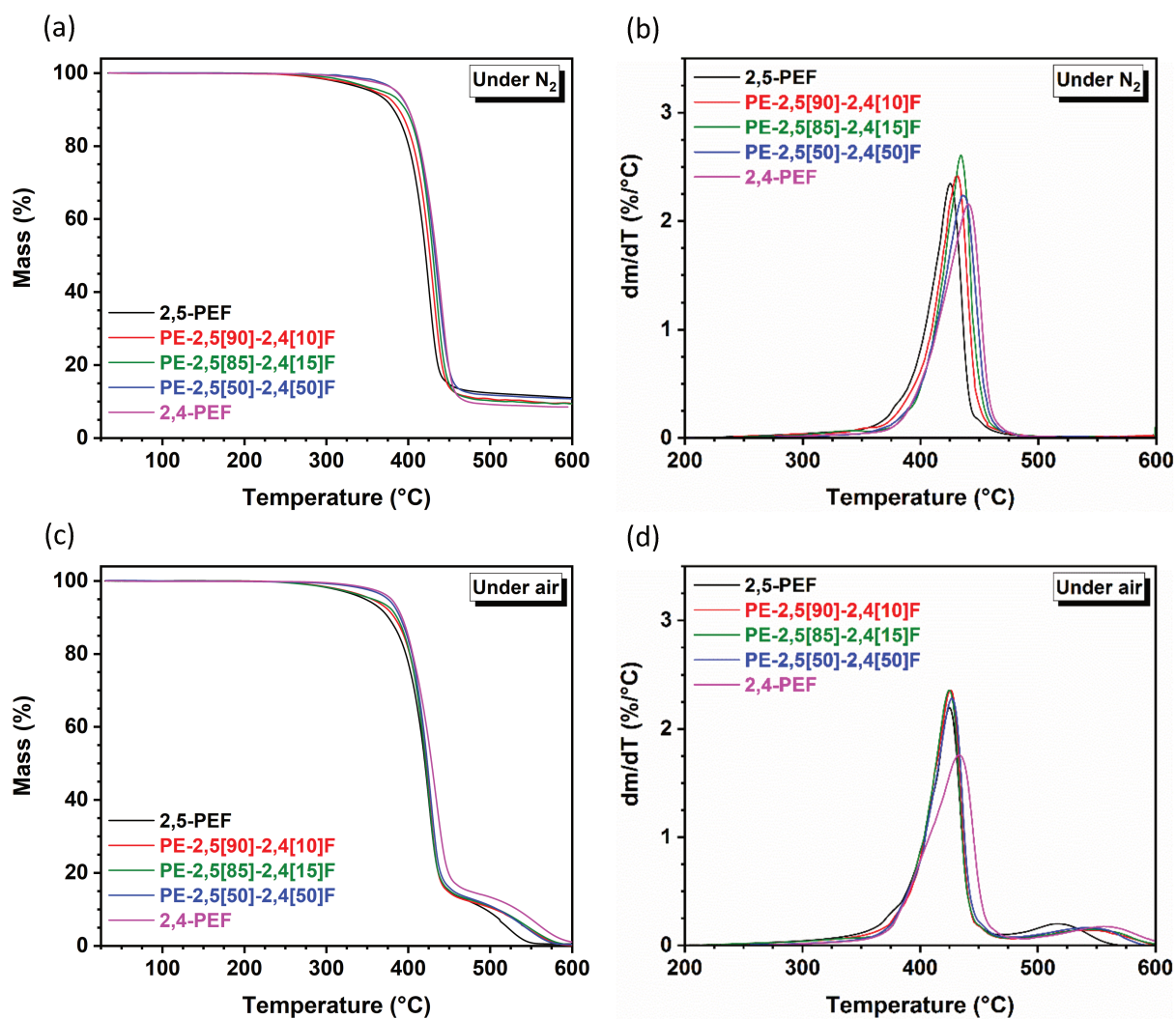


Figure IV.2: TGA curves (on the left) and their derivative curves (on the right) as a function of temperature recorded for PEFs under nitrogen and air at 10 °C/min.

Table IV.1: Thermal stability of PEFs under nitrogen and air at 10 °C/min.

Sample	Under nitrogen		Under air		
	$T_{d\ 5\%}^a$ (°C)	$T_{d\ max}^b$ (°C)	$T_{d\ 5\%}^a$ (°C)	$T_{d\ max\ peak\ I}^c$ (°C)	$T_{d\ max\ peak\ II}^d$ (°C)
2,5-PEF	362 ± 3	428 ± 1	347	425	517
PE-2,5[90]-2,4[10]F	372 ± 4	431 ± 3	355	426	538
PE-2,5[85]-2,4[15]F	372 ± 8	433 ± 3	357	425	546
PE-2,5[50]-2,4[50]F	384 ± 2	434 ± 4	375	427	542
2,4-PEF	388 ± 2	444 ± 1	379	433	557

<sup>a</sup> Temperature at which a mass loss of 5% is observed. <sup>b</sup> Temperature corresponding to the maximum rate of mass loss. <sup>c</sup> Temperature corresponding to the maximum rate of mass loss associated to the peak I. <sup>d</sup> Temperature corresponding to the maximum rate of mass loss associated to the peak II.

This behavior is due to the presence or absence of a ring in the chemical repeating unit: Poly (Lactid Acid) (PLA) contains no ring, PEFs contain the furan ring, PET contains the benzene ring and Poly (Ethylene Naphthalate) (PEN) contains the naphthalene ring.

The decomposition mechanisms leading to the thermal degradation of furanoate polyester have been already extensively discussed by Papageorgiou et al.<sup>5</sup> and Terzopoulou et al.<sup>6</sup>, who characterized several furanic polyesters and their terephthalate equivalents by performing TGA measurements under N<sub>2</sub> atmosphere. In particular, Terzopoulou et al.<sup>6</sup> investigated the decomposition mechanism of polyesters based on 2,5-FDCA and aliphatic diols with medium and long chain methylene groups, and confirmed that all polyesters decompose in a similar way. They evidenced that the thermal decomposition takes place mainly via  $\beta$ -hydrogen bond scission and less extensively by homolytic scission. By combining the results reported in the literature for the polyesters obtained with 2,5-FDCA and different aliphatic diols, with the results obtained in this work, one may deduce that neither the number of methylene groups in the parent diol monomer, nor the positional isomerism of the carbonyl group on the furan ring, seem to affect the decomposition mechanism of the final polyesters.

#### IV.1.2.2. Determination of the activation energy by MTGA

Papageorgiou et al.<sup>5</sup> reported relevant information about the thermal degradation of furanoate polyesters along with their decomposition mechanisms. However, they did not provide any information about the activation energy for thermal degradation. So, in this work, the synthesized polymers were purified, dried and further characterized by MTGA under N<sub>2</sub> to obtain not only the mass loss as a function of the temperature (Figure IV.3), but also the kinetic parameters associated to the mass loss<sup>7-9</sup>, i.e. the activation energy ( $E_a$ ) and  $\log_{10}(Z)$  as a function of the mass loss (Figure IV.4).

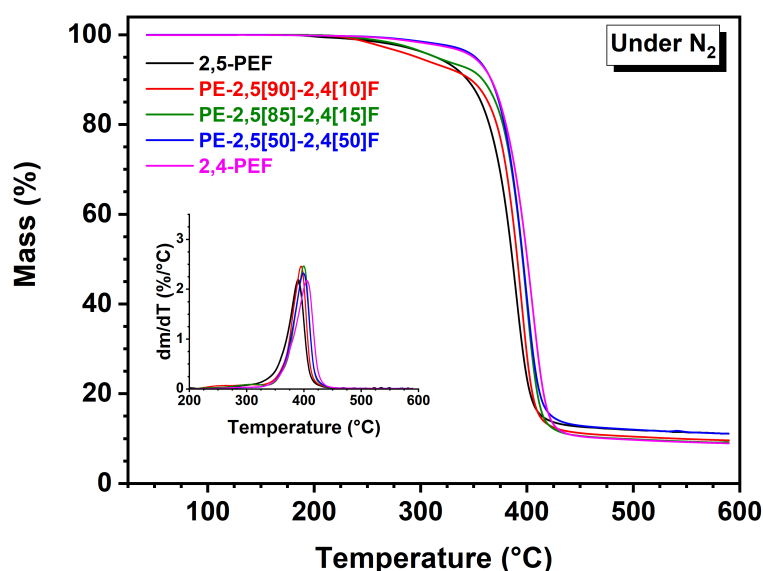


Figure IV.3: MTGA curves for PEFs under nitrogen and air at 2 °C/min ( $\alpha = \pm 5$  °C;  $T = 200$ s).

MTGA curves have a similar shape with respect to the TGA curves (Figure IV.3 (a)) and confirm that most of the samples degrade in one main degradation step. However, due to the slower rate used for the heating ramp in modulation mode, or maybe due to an intrinsically better sensitivity of MTGA with respect to TGA, in some cases the mechanism for thermal degradation seem to proceed in two steps. Further investigations are required and already planned to confirm this eventuality and elucidate the mechanisms of thermal degradation. The degradation temperatures (both  $T_{d\ 5\%}$  and  $T_{d\ max}$ ) obtained by MTGA and TGA are different essentially because of the different heating rate (10 °C/min for TGA and 2 °C/min for MTGA).

Table IV.2: Thermal stability and kinetic parameters associated to the mass loss of homopolyesters and copolyesters obtained from FDCA isomers (2,5- and 2,4-FDCA) and ethylene glycol performed by MTGA under  $N_2$  at 2 °C/min ( $\alpha = \pm 5$  °C;  $T = 200$ s).

Sample	$T_{d\ 5\%}$ <sup>a</sup> (°C)	$T_{d\ max}$ <sup>b</sup> (°C)	$E_a$ <sup>c</sup> (kJ/mol)	$\log_{10}(Z)$ <sup>d</sup> (1/min)
2,5-PEF	315	390	$195 \pm 17$	$14 \pm 1$
PE-2,5[90]-2,4[10]F	297	395	$201 \pm 14$	$15 \pm 1$
PE-2,5[85]-2,4[15]F	315	399	$210 \pm 47$	$15 \pm 4$
PE-2,5[50]-2,4[50]F	352	399	$202 \pm 30$	$15 \pm 2$
2,4-PEF	350	405	$200 \pm 15$	$14 \pm 1$

<sup>a</sup> Temperature at which a mass loss of 5% is observed. <sup>b</sup> Temperature corresponding to the maximum rate of mass loss. <sup>c</sup> Activation energy for thermal degradation. <sup>d</sup> Z is the pre-exponential factor.

The  $E_a = f(\text{mass loss})$  and  $\log_{10}(Z) = f(\text{mass loss})$  curves are mostly flat (which would suggest that the degradation actually occur in a single step) but present some fluctuations that are more or less visible and would require further investigations; for a preliminary analysis, the upper and lower bounds of such fluctuations were used to estimate the uncertainty on the  $E_a$  values reported in Table IV.2. The average value of the activation energy obtained by MTGA for the thermal degradation under nitrogen is consistent with the values determined by the second step/n-th order model described by Tsanaktis et al. <sup>10</sup> and intermediate between the values previously reported for PLA (110 kJ/mol <sup>11</sup>, 120 kJ/mol <sup>12</sup>) and PET (227 kJ/mol <sup>11</sup>).

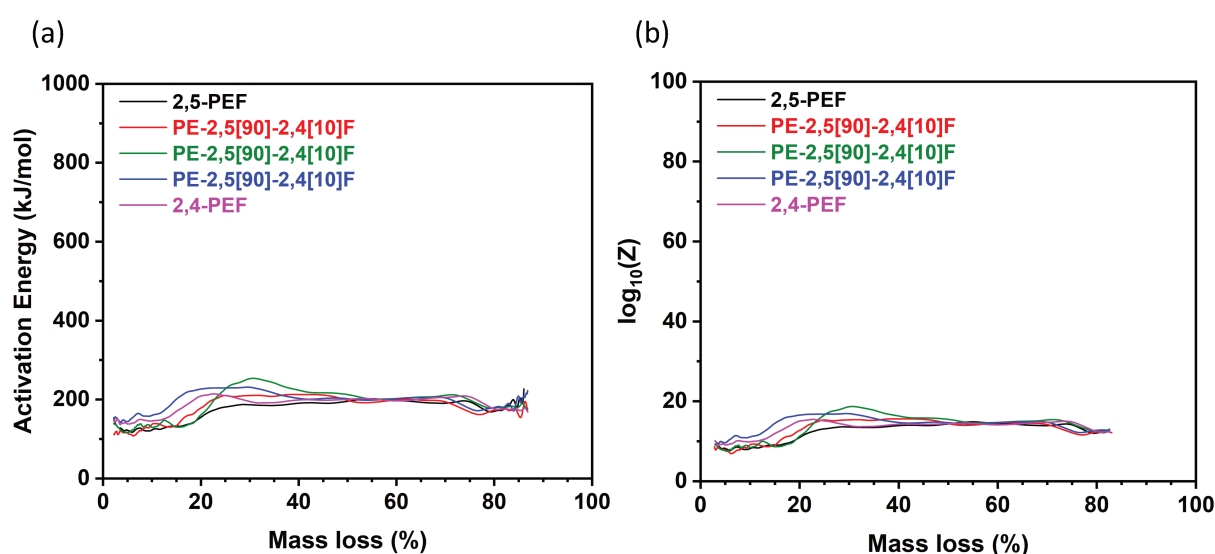


Figure IV.4: (a) Activation energy and (b)  $\log_{10}(Z)$  as a function of the weight loss.

### IV.1.3. Thermal properties

#### IV.1.3.1. Conventional DSC

DSC analyses (Figure IV.5) were performed on the quenched samples to investigate any possible difference in their thermal behavior upon heating (10 °C/min), including their aptitude to crystallize from the solid glassy state. The parameters associated with the main thermal events observed during the heating ramps, i.e. the mid-point glass transition temperature  $T_g$ , the heat capacity step at the glass transition temperature  $\Delta c_p$  and the melting temperature  $T_m$ , are reported in Table IV.3. The dispersion of the experimental data and the uncertainties of measurement were evaluated by characterizing 5 samples per batch.

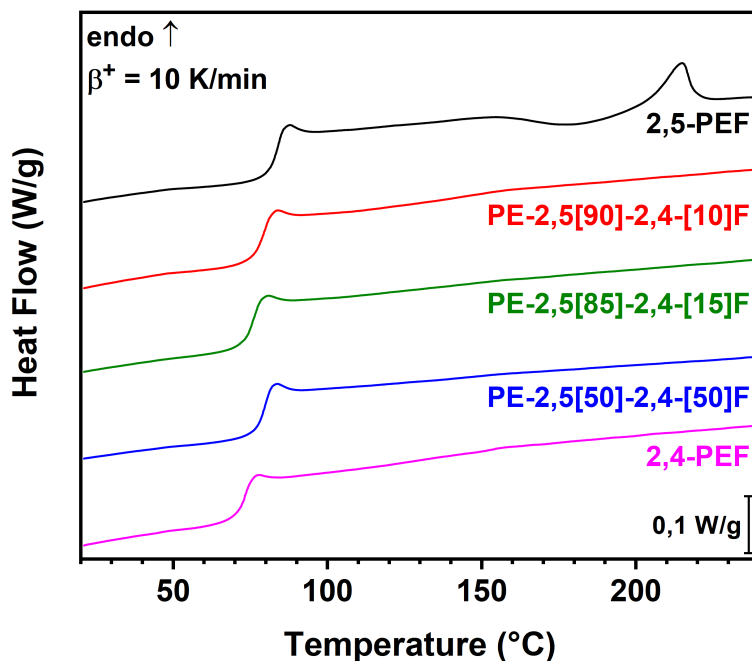


Figure IV.5: DSC thermograms (second scans) obtained by heating at 10 K/min for amorphous PEFs.

The glass transition temperature is higher for 2,5-PEF (82 °C) than for 2,4-PEF (72 °C). This difference is not necessarily due to a difference in the molecular weight, because Thiyagarajan et al. <sup>2</sup> reported similar values of  $T_g$  for 2,5-PEF and 2,4-PEF, in spite of a higher molecular weight recorded for the latter. Both the  $T_g$  values are closer to the values previously reported for PET (73 °C, 76 °C <sup>2</sup>) compared to PLA (62 °C <sup>13</sup>).

Table IV.3: Thermal properties of amorphous copolyesters from FDCA isomers (2,5- and 2,4-FDCA DME).

Sample	$T_g^a$ (°C)	$\Delta c_p^b$ (J/(g·K))	$T_m^c$ (°C)
2,5-PEF	82 ± 1	0.42 ± 0.03	215 ± 1
PE-2,5[90]-2,4[10]F	78 ± 1	0.42 ± 0.03	/
PE-2,5[85]-2,4[15]F	77 ± 2	0.45 ± 0.02	/
PE-2,5[50]-2,4[50]F	79 ± 1	0.43 ± 0.02	/
2,4-PEF	72 ± 1	0.42 ± 0.01	/

<sup>a</sup> Mid-point glass transition temperature measured upon heating after melt-quenching. <sup>b</sup> Heat capacity step at the glass transition estimated on the basis of the Normalized Heat Flow measured upon heating by DSC. <sup>c</sup> Melting temperature measured at the maximum of the melting endotherm.

Similarly to the results obtained by TGA and MTGA, DSC also reveals a sort of synergetic effect of the combination of 2,4- and 2,5-isomers onto the glass transition temperature, i.e. the  $T_g$  values obtained for the copolymers are quasi-identical and intermediate between those of the two homopolymers (2,4-PEF and 2,5-PEF).

No significant effects are observed on the heat capacity step at the glass transition temperature  $\Delta c_p$ , whatever the proportion of the two FDCA isomers. It could be interesting to evaluate the possible influence of intermolecular dipole-driven interactions (mostly related to the positional isomerism of the carbonyl group on the furan ring) on the molecular dynamics, along with the subsequent physical properties, the development of controlled microstructures, the overall performance (mechanical properties, barrier properties, etc.) and the evolutions over time (physical aging).

The endothermic peak superimposed to the heat capacity step typical of the glass transition corresponds to the enthalpy recovery peak associated to physical ageing and/or structural relaxation of the initial glasses or due to the difference between the heating and the cooling rate, and has been already observed in other studies <sup>14–16</sup>.

Figure IV.5 clearly shows that, at a heating rate of 10 °C/min, an amount of units based on 2,4-FDCA DME as little as 10 wt% is enough to make it impossible for the crystals to nucleate and grow upon heating from the glassy state. Indeed, cold crystallization is observed only in 2,5-PEF, starting at approximately 160 °C and being closely followed by a melting peak, whose maximum is observed at 215 °C.

The enthalpies of cold crystallization and melting are equal, meaning that the considered sample of 2,5-PEF can be considered as fully amorphous prior to the DSC heating ramp. However, the melting peak is weak (approximately 5 J/g) confirming that 2,5-PEF has slower crystallization kinetics as compared to other polyesters submitted to similar heating rates, such as PLA with a small amount of D-lactide <sup>17–19</sup>.

So, the incorporation of 2,4-FDCA-based repeating units, which are asymmetrical, is highly efficient for disrupting the crystallization of the 2,5-FDCA-based units.



### IV.1.3.2. Mixing laws

Considering the complex dependence of the glass transition temperature on the chemical composition and arrangement of polymer subunits, the values of  $T_g$  reported in [Table IV.3](#) were plotted as a function of the content of 2,5-FDCA DME and 2,4-FDCA DME repeating units and then fitted by different mixing laws ([Figure IV.6](#)).

The first law used for fitting is the Fox equation <sup>20</sup>, which describes a weighted-average relationship between  $T_g$  and the mass fraction of each component:

$$\frac{1}{T_g} = \frac{x}{T_{g_1}} + \frac{1-x}{T_{g_2}} \quad (\text{IV.1})$$

Where  $T_g$  is the glass transition temperature of the copolymer,  $T_{g_1}$  and  $T_{g_2}$  are the glass transition temperatures for each homopolymer,  $x$  is the weight fraction of one of the isomers and  $1-x$  is the weight fraction of the other isomer.

[Equation IV.1](#) is symmetrical with respect to the weight fraction of each isomer, and could help predicting the properties of the copolymers from the properties of the corresponding homopolymers.

Gordon and Taylor <sup>21</sup> also proposed an equation:

$$T_g = \frac{xT_{g_1} + k_{GT}(1-x)T_{g_2}}{x + k_{GT}(1-x)} \quad (\text{IV.2})$$

In this case,  $k_{GT}$  has to be evaluated from the experimental data and is incorporated into the simple weighted-average relation to better represent the eventual unequal contributions of each isomer to the final value of  $T_g$ .

Finally, Kwei <sup>22</sup> proposed another equation including two additional parameters,  $k_{Kw}$  and  $q$ :

$$T_g = \frac{xT_{g_1} + k_{Kw}(1-x)T_{g_2}}{x + k_{Kw}(1-x)} + qx(1-x) \quad (\text{IV.3})$$

The  $k_{Kw}$  parameter is defined similarly to the  $k_{GT}$  parameter in [Equation IV.2](#), whereas the  $q$  parameter is proportional to the number of specific intermolecular interactions eventually existing in the copolymer. This model is generally used to take into account dipole-driven intermolecular interactions, such as hydrogen bonding <sup>22,23</sup>.

The fitting procedure provided the following values:  $R^2 = 0.69$  for the Fox's equation,  $R^2 = 0.70$  with  $k_{GT} = 0.77 \pm 0.59$  for the Gordon-Taylor's equation, and  $R^2 \approx 1$  with  $k_{KW} = 16.40 \pm 2.04$  and  $q = 25.51 \pm 1.15$  for the Kwei's equation.

So, the best fitting results are obtained with Kwei's equation ( $R^2$  is close to 1), probably thanks to the peculiar dielectric properties observed by dielectric spectroscopy for 2,4-PEF as compared to 2,5-PEF <sup>24</sup>. However, these values need to be taken with caution, indeed, more mixtures are recommended especially for the small amount of 2,4-FDCA DME as realized more recently in the publication of Thiyagarajan et al. <sup>25</sup>.

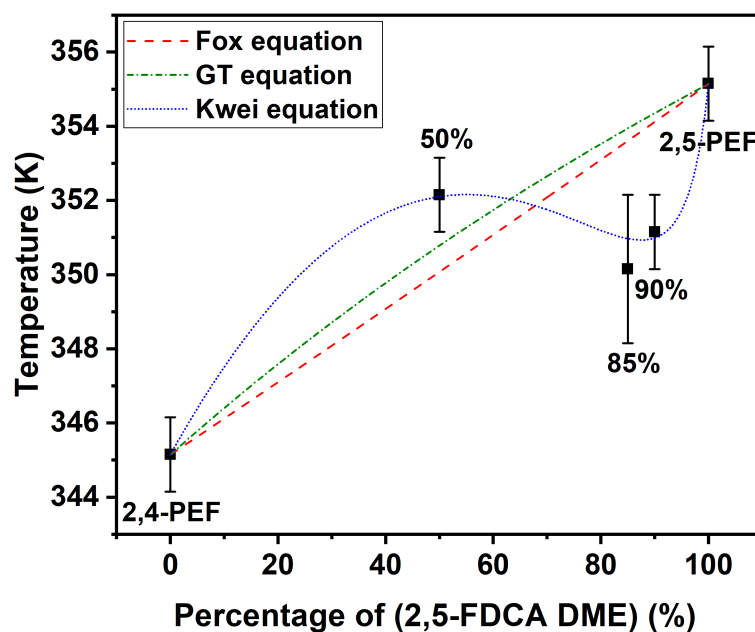


Figure IV.6: Values of the glass transition temperature  $T_g$  plotted against the relative content of 2,5-FDCA DME and fitted by Fox's, Gordon-Taylor's and Kwei's equations.

## IV.2. Molecular dynamics in amorphous PEFs

### IV.2.1. Investigation of the amorphous phases by MT-DSC

MT-DSC analyses were performed to investigate the amorphous phases and determine the calorimetric glass transition temperature of the samples. Since the material's barrier properties are associated with the molecular mobility and the free volume, Donth's approach was used to investigate the free volume and size of the CRR (the theoretical approach is detailed in [Chapter III](#)).

As mentioned in the literature for several amorphous or semi-crystalline polymers, differences are clearly observable about the evolution of the heat capacity as a function of temperature <sup>26–28</sup>. The key to an accurate measurement of the heat capacity is the system linearity, which includes the linearity of the MT-DSC device (including the calibration of the MT-DSC device and the samples size) and the linearity of the thermal response. However, several experimental parameters (such as the underlying heating or cooling rate, the temperature modulation amplitude and oscillation period) can affect the overall system linearity and the accuracy of the measured heat capacity values.

All the heat capacity curves obtained in this work were aligned to the value of  $c_{p, glass}$  (1.18 J/(g·°C)) at  $T = 50$  °C) obtained by Codou et al. <sup>29</sup> for 2,5-PEF, which was considered as a value of reference in the absence of values from the ATHAS databank.

[Figure IV.7](#) shows the  $C'$  signals recorded by MT-DSC as a function of temperature in the region of the glass transition (endothermic steps) along with their derivative (peaks); the temperature corresponding to the maximum of each peak has been taken as the dynamic glass transition temperature  $T_{\alpha}$ .

The curves in [Figure IV.7](#) were used to determine  $T_{\alpha}$  and the heat capacity step at the glass transition  $\Delta c_p(T_{\alpha})$ . The formalism allowing to estimate the degree of cooperativity ( $N_{\alpha}$ ) and the cooperativity length ( $\xi_{\alpha}$ ) from calorimetric investigations also requires the parameter  $\delta T$ , which was obtained according to Donth's method <sup>30</sup>. This method assumes that the mean temperature fluctuation  $\delta T$  in the CRR is somehow associated with the standard deviation of the distribution of relaxation times, obtained by fitting the MT-DSC signal with a Gaussian function ( $\delta T = FWHM/2.355$  with FWHM = Full Width Half Maximum). More details about the calculation of  $N_{\alpha}$  are given in [Chapter III](#) and data are reported in [Table IV.4](#).

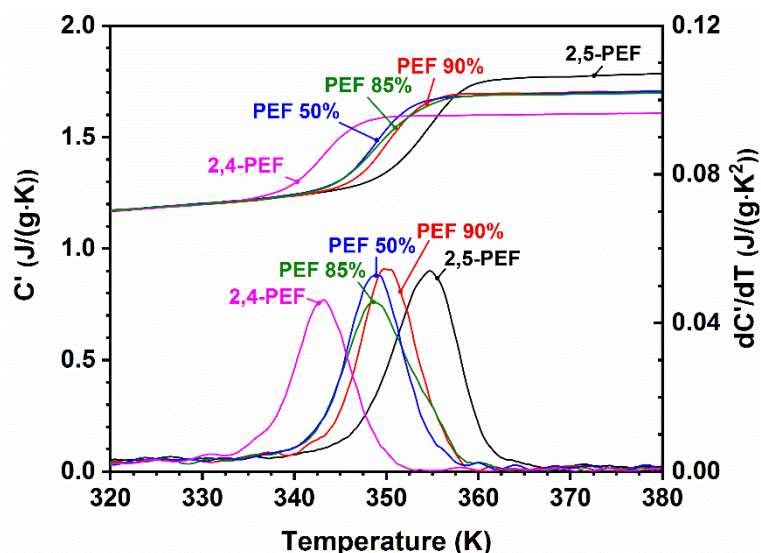


Figure IV.7:  $C'$  signals recorded by MT-DSC as a function of temperature in the region of the glass transition and their derivatives ( $dC'/dT$ ) for PEFs.

As previously observed, the dynamic glass transition temperature  $T_\alpha$  is higher for 2,5-PEF than for 2,4-PEF, as a consequence of the difference in the carbonyl position on the furan ring. As expected, the copolymers undergo just one endothermic event due to the random distribution of the isomeric repeating units, and have a value of  $T_\alpha$  which is intermediate between the value of the homopolymers, as already pointed out on the basis of the DSC measurements.

Table IV.4: Values involved in Donth's model: temperature of the maximum of the derivative peak ( $T_\alpha$ ), heat capacity step at  $T_\alpha$  ( $\Delta c_p(T_\alpha)$ ), cooperativity length ( $\xi_\alpha$ ) and average number of equivalent relaxation units in the CRR ( $N_\alpha$ ).

Sample	$\Delta c_p(T_\alpha)$ (J/(g·K))	$T_\alpha$ (°C)	$\xi_\alpha$ (nm)	$N_\alpha$
2,5-PEF	$0,45 \pm 0,09$	$81 \pm 2$	$2,8 \pm 0,2$	$99 \pm 10$
PE-2,5[90]-2,4[10]F	$0,46 \pm 0,04$	$77 \pm 2$	$2,9 \pm 0,2$	$118 \pm 10$
PE-2,5[85]-2,4[15]F	$0,43 \pm 0,09$	$76 \pm 3$	$2,6 \pm 0,3$	$81 \pm 15$
PE-2,5[50]-2,4[50]F	$0,44 \pm 0,01$	$76 \pm 2$	$3,0 \pm 0,2$	$128 \pm 10$
2,4-PEF	$0,38 \pm 0,04$	$70 \pm 1$	$2,9 \pm 0,2$	$119 \pm 10$

The average volume of the CRR was calculated assuming  $\rho = 1.434 \text{ g/cm}^3$ <sup>31</sup> and  $M_0 = 182.14 \text{ g/mol}$  for all PEFs. The  $\xi_\alpha$  value obtained for 2,5-PEF from MT-DSC measurements is in good agreement with the value reported by Codou et al.<sup>29</sup> (2.9 nm).

All the samples have similar CCR sizes and approximately the same number of equivalent relaxation units in the CRR. It is well known that the CRR size could be modified by any geometric restriction, such as the presence of crystalline lamellae or a specific morphology of the sample (multi-nanolayers films, etc). When the amorphous domains are isotropic and unconfined, a value of CRR size of 3 nm at the glass transition seems to be a sort of universal value. This work shows that both the homopolymers (2,5-PEF and 2,4-PEF) and all the copolymers have similar values of cooperativity at  $T_\alpha$  in perfect agreement with other amorphous polymers<sup>30,32</sup>.

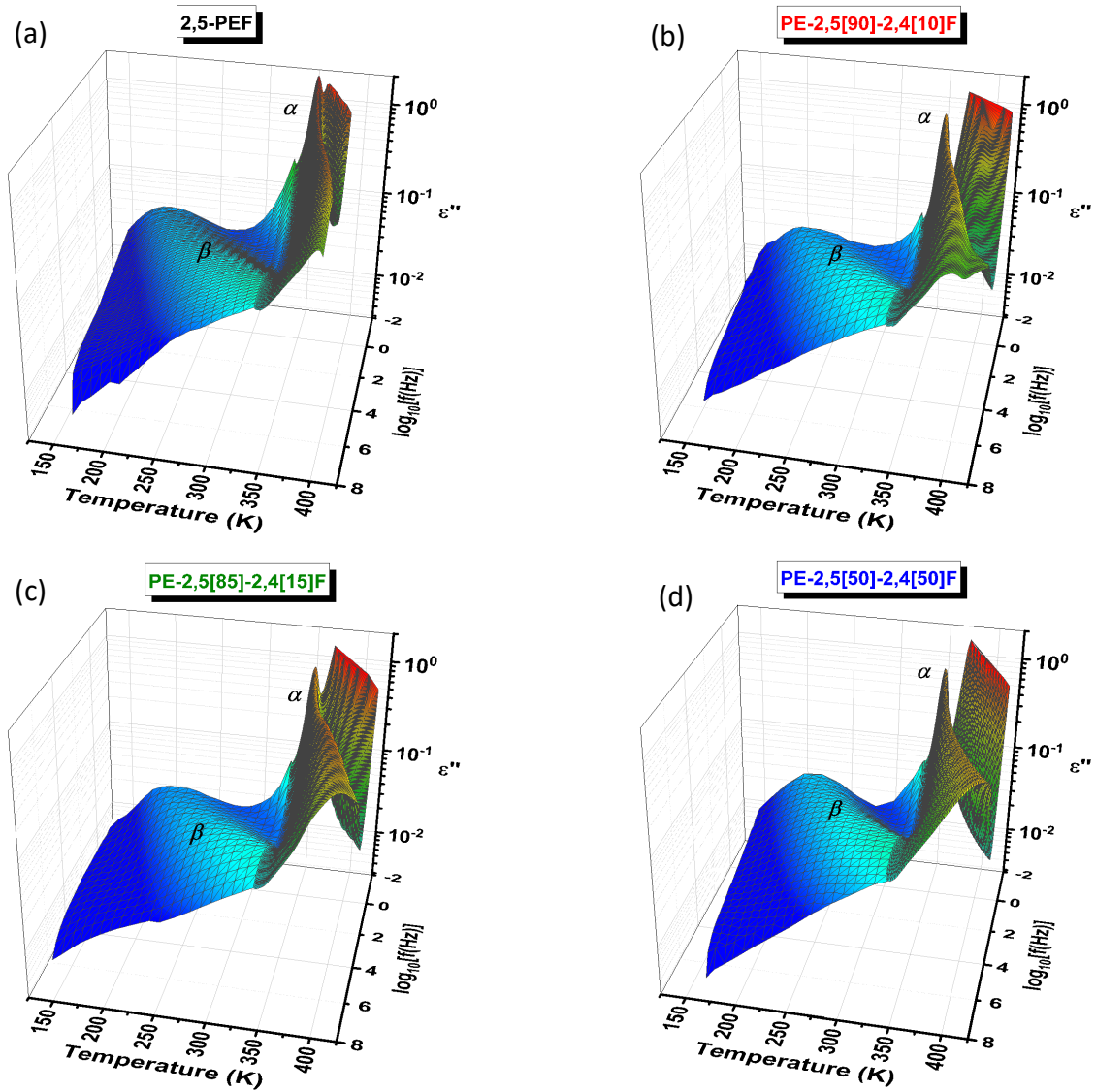
#### IV.2.2. Segmental relaxation investigated by DRS

The molecular dynamics of all the amorphous samples was investigated by means of dielectric relaxation spectroscopy (DRS). The main parameters of the  $\alpha$  relaxation, such as the dielectric strength, the relaxation time and the fragility index, were calculated and evaluated in combination with the results of MT-DSC.

Figure IV.8 presents the experimental raw data obtained by DRS for all the considered samples. All the samples show a single wide  $\beta$  relaxation at low temperature and high frequency, and a single narrow and more intense  $\alpha$  relaxation at higher temperature. The latter corresponds to the segmental relaxation and is the dielectric manifestation of the glass transition. At higher temperature and low frequency, a typical increase in the loss factor ( $\varepsilon''$ ) is observed, which is associated to conductivity phenomena ( $\sigma$ ).

The dielectric relaxation process in the glass transition region can be characterized by a step-like decrease of  $\varepsilon'$  signal and a peak in  $\varepsilon''$  signal when they are plotted against frequency in isothermal conditions. The essential quantities that characterize a dielectric relaxation process can be extracted either from  $\varepsilon'$  or  $\varepsilon''$  as a function of frequency. For example, the relaxation time can be obtained from the frequency  $f_{max}$  at which  $\varepsilon''$  reaches its maximum value at a fixed temperature. The model function introduced by Havriliak-Negami<sup>33</sup> (details are given in Chapter II) can be used to analyze the dielectric spectra quantitatively with the Grafity software (version 0.5.5).

Since all the samples considered in this study undergo two complex relaxation processes ( $\alpha$  and  $\beta$ ) in the explored frequency window, a sum of two HN functions was used to fit the experimental data (the conductivity contribution was also added to properly fit the  $\varepsilon''(f)$  signal).



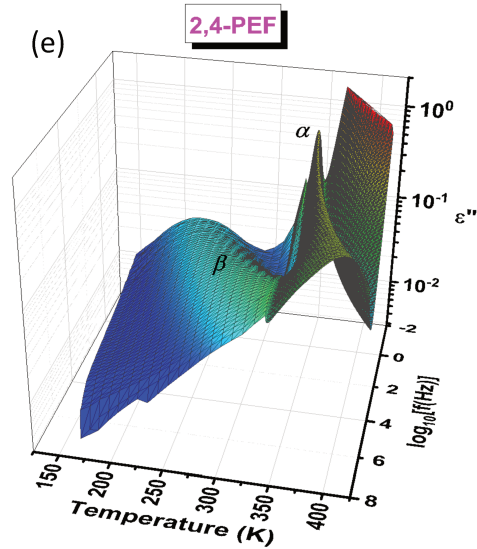


Figure IV.8: Imaginary component of the complex dielectric permittivity vs. frequency and temperature for amorphous PEFs.

Figure IV.9 provides an example of the HN fitting procedure for the imaginary components of the complex permittivity vs. frequency signals recorded for 2,5-PEF, PE-2,5[50]-2,4[50]F and 2,4-PEF at 90 °C. The fitting procedure was applied to both the imaginary and real components of the signal in order to improve the accuracy of the fitting results.

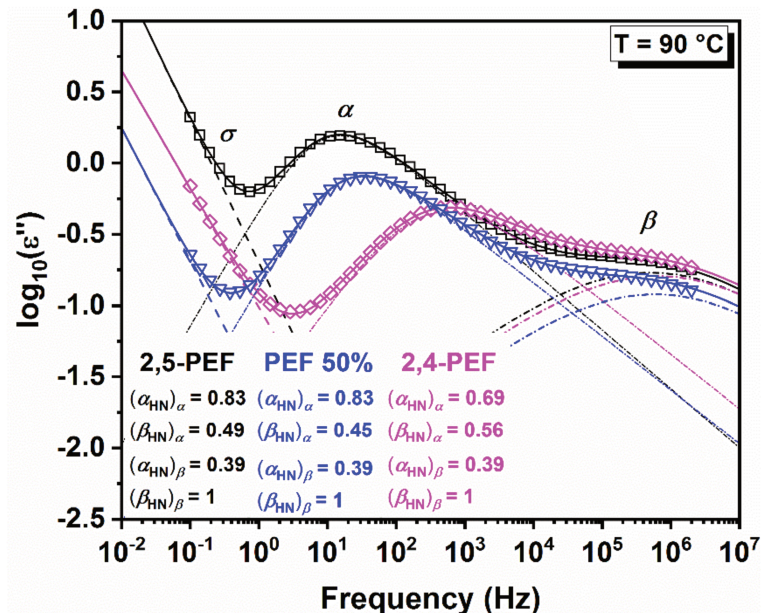


Figure IV.9: Illustration of the analytical procedure used to investigate the relaxation phenomena by fitting with a conductivity contribution  $\sigma$  and two Havriliak-Negami (HN) complex functions ( $\alpha$  and  $\beta$ ) at 90 °C. The HN shape parameters for both the  $\alpha$  and  $\beta$  processes in amorphous 2,5-PEF, PE-2,5[50]-2,4[50]F and 2,4-PEF at 90 °C are also reported.

The fact that a single  $\beta$  relaxation is observed for all the samples is supported by the work of Dimitriadis et al. <sup>34</sup> on semi-crystalline 2,5-PEF. However, most polyesters (PET <sup>35,36</sup>, PEN <sup>37</sup>, PLA <sup>38</sup> and PHAs <sup>18</sup>) are known to exhibit complex secondary relaxations including at least two contributions. A paper recently published by Soccio et al. <sup>39</sup> on biobased poly(butylene 2,5-furanoate) reports a broad  $\beta$  relaxation phenomenon that involves two processes: a faster  $\beta_1$  relaxation associated with the more mobile subunit (the four  $-\text{CH}_2-$  in the aliphatic glycolic subunit connected to the C–O of the ester function) and a slower  $\beta_2$  relaxation due to the stiffer moiety (corresponding to the connection between the aromatic ring and the C=O of the ester function).

In the case of PEFs, the isothermal measurements of the  $\beta$  relaxation (Figure IV.9) could be properly analyzed using just one symmetrical HN function, may be due to a favorable superposition of these two processes. The analytical procedure illustrated in Figure IV.9 for a temperature of 90 °C was extended to the measurements performed at different temperatures. Figure IV.10 shows the plots of the dielectric loss recorded in isothermal conditions for all the PEFs samples, normalized to the maximum ( $\log_{10}(\varepsilon''/\varepsilon''_{max})$ ) vs. frequency and scaled to  $f_{max}$  ( $f/f_{max}$ ). A very good overlapping of all the curves on a single master curve was obtained for all the considered samples. The breadth of the  $\alpha$  relaxation peaks, which can be characterized by the Kohlrausch stretch exponent  $\beta_{KWW}$  or the coupling parameter  $n$  ( $n = 1 - \beta_{KWW}$ ) introduced by Ngai <sup>40</sup>, is correlated with many dynamical properties, such as the fragility, the dynamical crossover region and the degree of cooperativity of glass-forming liquids <sup>41</sup>. The master plots reported in Figure IV.10 were obtained by shifting the spectra recorded at different temperatures (from 85 to 110 °C with a step of 1 °C) in order to superimpose them onto a reference spectrum (at 90 °C). This procedure allows to graphically visualize the stretching parameter  $\beta_{KWW}$  and ascertain whether the temperature plays an active role in the shape of the structural relaxation process (in this case, different distributions of the relaxation times at different temperatures should have been obtained). The HN function is commonly used to represent the dielectric relaxation data, but this function is also used to extract the different relaxation parameters such as the shape parameters  $\alpha_{HN}$  and  $\beta_{HN}$ , the dielectric strength  $\Delta\varepsilon_{HN}$  and the relaxation time  $\tau_{HN}$ .



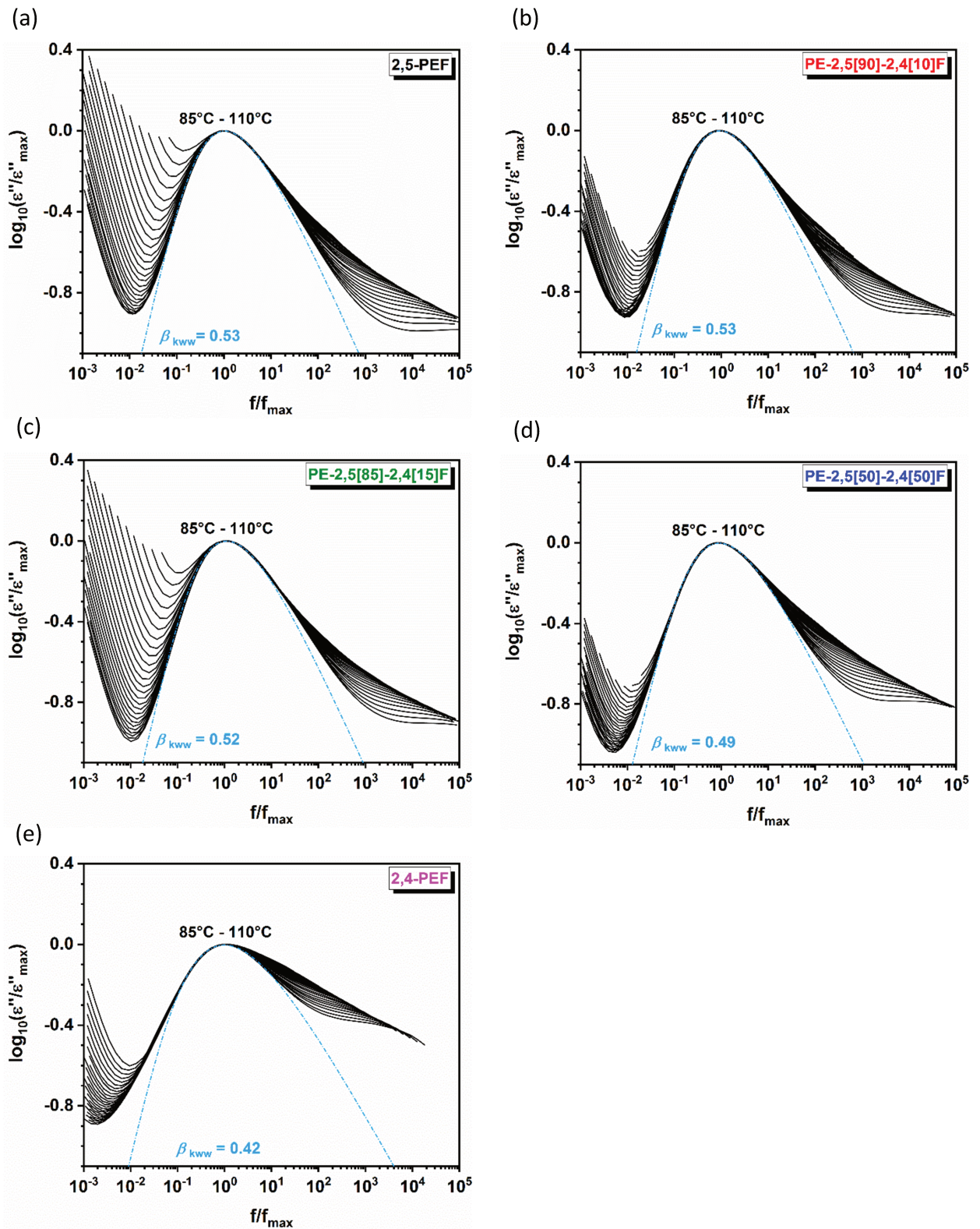


Figure IV.10: Master plots obtained by horizontally shifting at  $f/f_{\max}$  the isothermal spectra recorded from 85 to 110 °C for amorphous PEFs.

### IV.2.2.1. Shape parameters $\alpha$ and $\beta$ of the $\alpha$ relaxation

The shape parameters obtained from the HN fits for the  $\alpha$  relaxation process are plotted in Figure IV.11. They describe the symmetric and asymmetric broadening of the complex dielectric function<sup>42</sup>. Their values are found to be less than 1, i.e.  $\alpha_{HN}$  and  $\beta_{HN} < 1$ , for all the considered samples, as shown in Figure IV.11 and in agreement with the literature<sup>42</sup>.

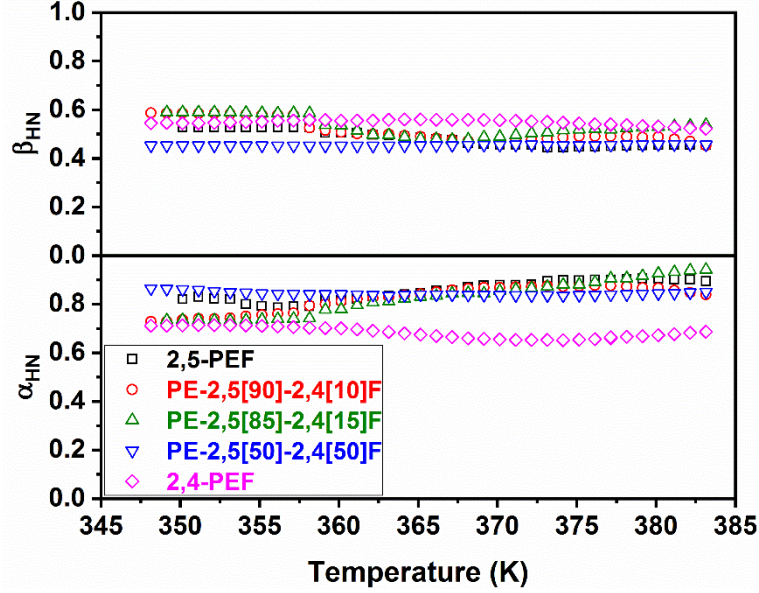


Figure IV.11: Shape parameters obtained from the HN fitting procedure as a function of temperature for the  $\alpha$  relaxation process of amorphous PEFs.

The HN functions in the frequency domain were then converted into the time domain by the inverse Fourier transform. The distribution of relaxation times could therefore be expressed as<sup>43</sup>:

$$f(\tau) = \frac{1}{\pi} \frac{\left(\frac{\tau}{\tau_{HN}}\right)^{\alpha_{HN}\beta_{HN}} \sin(\beta_{HN}\varphi)}{\left[1 + \left(\frac{\tau}{\tau_{HN}}\right)^{2\alpha_{HN}} + 2\left(\frac{\tau}{\tau_{HN}}\right)^{\alpha_{HN}} \cos(\pi\alpha_{HN})\right]^{\frac{\beta_{HN}}{2}}} \quad (IV.4)$$

With:

$$\varphi = \frac{\pi}{2} - \tan^{-1} \left[ \frac{\left(\frac{\tau}{\tau_{HN}}\right)^{\alpha_{HN}} + \cos(\pi\alpha_{HN})}{\sin(\pi\alpha_{HN})} \right] \quad (IV.5)$$

Where  $f(\tau)$  is the distribution function,  $\tau_{HN}$  is the HN relaxation time,  $\alpha_{HN}$  and  $\beta_{HN}$  are the HN shape parameters and  $\tau$  corresponds to time.

In term of distribution of relaxation times, the correlation function  $\phi(t)$  is expressed as <sup>43</sup>:

$$\phi(t) = \int_0^{\infty} f(\tau) e^{-(t/\tau)} dt \quad (IV.6)$$

In the time domain,  $\phi(t)$  is empirically described by the Kohlrausch–Williams–Watts (KWW) function as follows <sup>44</sup>:

$$\phi(t) = e^{-(t/\tau_{KWW})^{\beta_{KWW}}} \quad (IV.7)$$

Where  $\beta_{KWW}$  ( $0 < \beta_{KWW} \leq 1$ ) is a stretching parameter, and  $\tau_{KWW}$  is the relaxation time for  $\beta_{KWW} = 1$ .

The stretching parameter  $\beta_{KWW}$  allows to compare any asymmetrical broadening behavior of the relaxation process at short times (i.e. high frequencies) with the exponential decay corresponding to a Debye relaxation having  $\beta_{KWW} = 1$ . The HN parameters are correlated with  $\beta_{KWW}$  as follows <sup>45</sup>:

$$\log_{10} \left( \frac{\tau_{HN}}{\tau_{KWW}} \right) \approx 2.6(1 - \beta_{KWW})^{0.5} e^{-3\beta_{KWW}} \quad (IV.8)$$

A good approximation of Equation IV.8 is given by the following equation:

$$\beta_{KWW} \approx (\alpha_{HN} \beta_{HN})^{0.813} \quad (IV.9)$$

The values of the  $\beta_{KWW}$  parameter can be plotted as a function of temperature, as reported in Figure IV.12 for all the considered amorphous PEFs samples.

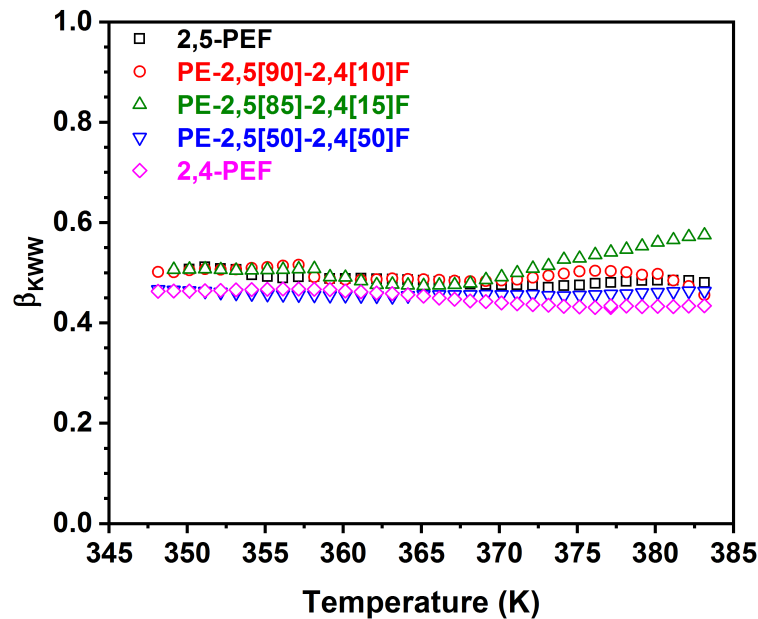


Figure IV.12: Variation of the  $\beta_{KWW}$  parameter obtained by Equation IV.9 (that we will call  $\beta_{KWW th.}$ ) as a function of temperature for all the amorphous PEFs samples.

Figure IV.12 did not show a significant difference between  $\beta_{KWW\ th.}$  values whatever the ratio of 2,5/2,4-FDCA DME.

The values of  $\beta_{KWW}$  experimentally obtained (from the master plots:  $\beta_{KWW\ exp.}$ ) for 2,5-PEF, PE-2,5[90]-2,4[10]F, PE-2,5[85]-2,4[15]F, PE-2,5[50]-2,4[50]F and 2,4-PEF are reported in Table IV.5 and are in agreement with the  $\beta_{th.}$  values obtained by Equation IV.9 as well as with the values previously reported for PETg ( $\beta_{KWW} \approx 0.40$ )<sup>46</sup> and PLA ( $\beta_{KWW} \approx 0.35$ )<sup>47</sup>.

**Table IV.5:  $\beta_{KWW}$  values obtained both experimentally (master curves) and theoretically (Equation II.2).**

Sample	$\beta_{KWW\ exp.}$	$\beta_{KWW\ th.}$
2,5-PEF	0.53	0.49 ± 0.02
PE-2,5[90]-2,4[10]F	0.53	0.49 ± 0.03
PE-2,5[85]-2,4[15]F	0.52	0.51 ± 0.06
PE-2,5[50]-2,4[50]F	0.49	0.46 ± 0.01
2,4-PEF	0.42	0.45 ± 0.02

So, the incorporation of 2,4-FDCA does not seem to impact the shape of the  $\alpha$  relaxation process.

#### IV.2.2.2. Dielectric relaxation strength $\Delta\varepsilon_{HN}$

The dielectric strength  $\Delta\varepsilon_{HN}$  is obtained by fitting the relaxation data with the HN function. The starting point for the analysis of  $\Delta\varepsilon_{HN}$  is the generalized form of the Debye theory by Onsager, Fröhlich and Kirkwood<sup>42</sup>:

$$\Delta\varepsilon_{HN} = \frac{1}{\varepsilon_0} g_K F \frac{\mu^2}{k_B T} \frac{N}{V} \quad (\text{IV.10})$$

Where  $\varepsilon_0$  is the dielectric permittivity of vacuum,  $\mu$  is the mean dipole moment of moving units in vacuum,  $F$  is the Onsager factor ( $F = 1$  for sake of simplicity),  $N/V$  is the volume density of dipoles involved in the relaxation process, and  $g_K$  is the Kirkwood correlation factor that takes into account short-range intermolecular interactions leading to specific static dipole–dipole orientations.

Figure IV.13 presents the temperature dependence of the dielectric strength  $\Delta\varepsilon_{HN}$  of the  $\alpha$  relaxation vs. temperature. As expected,  $\Delta\varepsilon_{HN}$  decreases on increasing temperature for all the considered samples<sup>42,48</sup>. Similar temperature dependencies of  $\Delta\varepsilon_{HN}$  are also found for other kinds of glass-forming liquids, polymers and thin polymer films<sup>42,48–50</sup>.

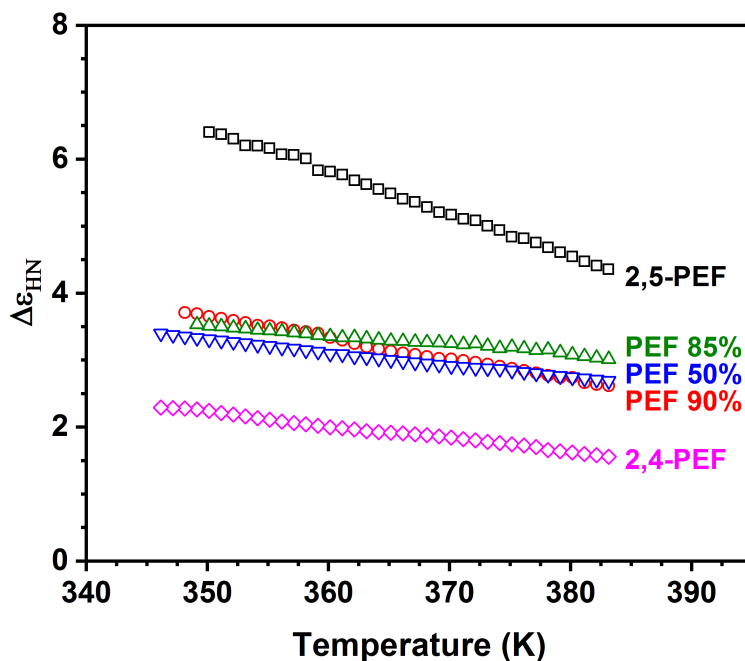


Figure IV.13: Dielectric strength ( $\Delta\varepsilon_{HN}$ ) as a function of temperature for amorphous PEFs.

Analogously to other properties (i.e. the glass transition temperature obtained by calorimetric and dielectric measurements), the value of  $\Delta\varepsilon_{HN}$  obtained for the copolymers is intermediate with respect to the values obtained for the homopolymers. However, compared to other polyesters, the value of  $\Delta\varepsilon_{HN}$  for the homopolymer 2,5-PEF is significantly higher and has a significantly different temperature dependence with respect to the homopolymer 2,4-PEF. This remarkable result deserves to be pointed out and was finally better elucidated thanks to a collaboration with by Prof. Frédéric AFFOUARD (UMET, Université de Lille), who performed Molecular Dynamics Simulations (MDS). More details about the MDS calculations are provided in the [Annex B](#).

The individual dipole moment of a given polymer chain at a time  $t$  can be calculated by MDS according to the following expression:

$$\vec{\mu}(t) = \sum_{\alpha=1}^{N_a} q_{\alpha} \vec{r}_{\alpha}(t) \quad (\text{IV.11})$$

Where  $q_{\alpha}$  and  $\vec{r}_{\alpha}(t)$  are respectively the fixed charge localized on the atom  $\alpha$  and its position at the time  $t$ , and  $N_a$  is the number of atoms in the considered polymer chain.

The dipole moment distributions  $P(\mu)$  obtained by MDS runs on 2,5-PEF and 2,4-PEF polymer chains are shown in [Figure IV.14](#).

2,5-PEF and 2,4-PEF polymer chains contain a broad range of dipole moments because of their intrinsic flexibility; besides, the average dipole moment of 2,4-PEF polymer chains is significantly lower with respect to the average dipole moment of 2,5-PEF polymer chains ( $\mu \approx 6.2$  and  $8.2$  D for 2,4-PEF and 2,5-PEF, respectively), likely because of symmetry reasons. Dipole correlations are well described by the so-called Kirkwood correlation factor  $G_K$  given by the following relation:

$$G_K = 1 + (N - 1) \langle \vec{\mu}_i \cdot \vec{\mu}_j \rangle / \langle \mu^2 \rangle \quad (\text{IV.12})$$

Where  $\vec{\mu}_i$  is the dipole moment of the molecule  $i$  and  $\langle \vec{\mu}_i \cdot \vec{\mu}_j \rangle$  indicates an average value of dipole moment over distinct pairs of molecules ( $i \neq j$ ).

The Kirkwood correlation factor accounts for the orientational correlation of neighboring dipoles. In this study,  $G_K \approx 1$  was computed for both 2,4-PEF and 2,5-PEF systems, suggesting no specific correlation between dipoles. Based on both  $\mu$  and  $G_K$  values and on the expression of the dielectric strength defined in [Equation IV.10](#), it is thus possible to propose that the significant difference in the dielectric strength obtained between 2,4-PEF and 2,5-PEF mostly originates from the different values found for the average dipole moment, which is higher for 2,5-PEF polymer chains with respect to 2,4-PEF polymer chains.

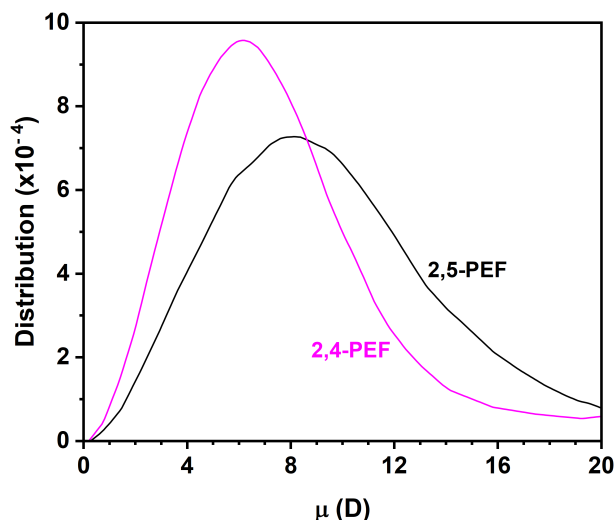


Figure IV.14: Distribution of dipole moments for 2,5-PEF and 2,4-PEF polymer chains obtained from MDS.

#### IV.2.2.3. Relaxation map

Figure IV.15 shows  $\tau_{max}$  as a function of the inverse temperature (Arrhenius diagram) for all the considered samples. The temperature dependence of the relaxation time for the  $\alpha$  relaxation usually presents a super-Arrhenius behavior (i.e. a deviation from the Arrhenius behavior) being described by the empirical Vogel-Fulcher-Tamman (VFT) equation <sup>51–53</sup> (Equation III.12).

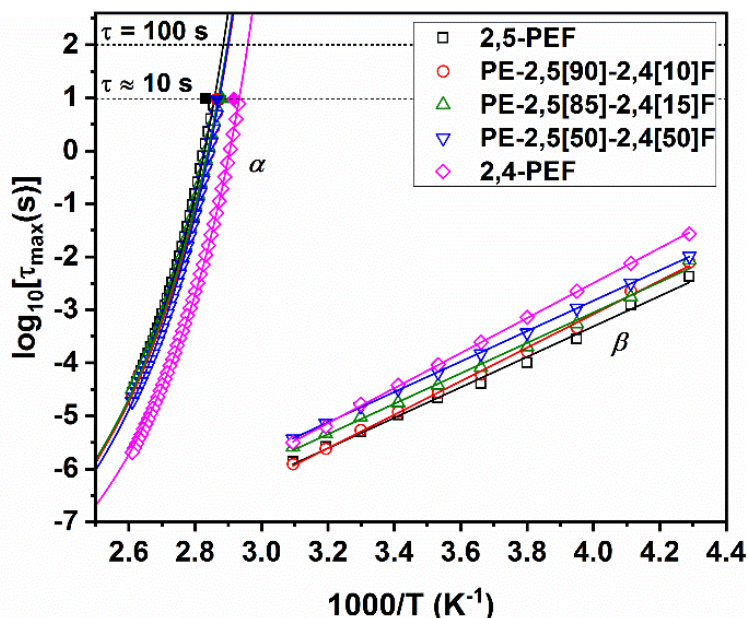


Figure IV.15: Logarithmic plot of the dielectric relaxation time ( $\tau_{max}$ ) for the  $\alpha$  relaxation as a function of the inverse of temperature for PEFs. Hollow symbols are from DRS experiments and filled symbols from MT-DSC experiments (period = 60s,  $\tau \sim 10$ s).

#### IV.2.2.4. Characterization of the $\beta$ relaxation

As previously pointed out, all the considered PEFs samples present a  $\beta$  relaxation that can be resolved with a single HN relaxation function (Figure IV.9). To extend this analysis versus temperature, the values of relaxation time  $\tau_{max}$  associated to each contribution are reported in the relaxation maps (Figure IV.15). The experimental data for the  $\beta$  relaxation is in good agreement with the Arrhenius law and are fitted with the following equation:

$$\tau = \tau_{0,A} \exp\left(\frac{E_a}{RT}\right) \quad (\text{IV.13})$$

Where  $E_a$  is the activation energy,  $R$  is the gas constant and  $\tau_{0,A}$  is a pre-exponential factor.

The amount of 2,4-FDCA-based repeating units has an impact on the  $\beta$  relaxation, because the relaxation time increases by almost one decade when the amount of 2,4-FDCA-based repeating units increases. By comparing the molecular structures of the two isomers and considering that the lowest value of relaxation time was found for 2,5-PEF, this variation could be ascribed to the difference in symmetry between 2,5- and 2,4-FDCA. The values of  $E_a$  obtained by Equation IV.13 for the copolymers are reported in Table IV.6.

They are quite close to the values obtained for the homopolymers 2,5-PEF and 2,4-PEF, and are in agreement with the values given in the literature for other polyesters, for which they have been associated with the local motions on the ester group:  $E_a$  (PLA) = 36 kJ/mol<sup>38</sup>,  $E_a$  (PHBV) = 55 kJ/mol<sup>18</sup>,  $E_a$  (PET) = 79 ± 10 kJ/mol<sup>37</sup>.

To conclude, the incorporation of 2,4-FDCA-based repeating units as a noticeable effect on the localized molecular movements associated with the  $\beta$  relaxation process due to the non-symmetry of the 2,4-isomer with respect to the furan ring.

#### IV.2.2.5. Characterization of the $\alpha$ relaxation

As shown in Figure IV.15, the temperature dependence of the relaxation time is not linear and presents a curvature usually corresponding to the appearance of cooperative molecular motions, which is well fitted by the VFT law. The glass transition temperature can therefore be estimated by extrapolating the VFT fit to the conventional value of relaxation time  $\tau = 100\text{s}$  or  $\log_{10}(\tau) = 2$ . The values of the parameters obtained from the extrapolated VFT fit are reported in Table IV.6.



To correlate the temperature dependence of the relaxation times to the values of dynamic glass transitions, the data obtained by MT-DSC at  $\tau \sim 10$ s were also added for all the considered samples<sup>54</sup>. The glass transition temperature estimated from MT-DSC is in good agreement with the value obtained by dielectric spectroscopy measurements for all the considered samples.

#### IV.2.2.6. Fragility index $m$

The degree of deviation of the relaxation times from an Arrhenius-type temperature dependence near  $T_g$  provides a useful classification of glass-forming liquids<sup>55,56</sup>. The fragility index  $m$  can be calculated by DRS (that we will call  $m_{liquid}$ ), measuring the  $\alpha$  relaxation times over a range of temperatures above the glass transition temperature  $T_g$  of the material. Figure IV.16 reports the temperature dependence of the  $\alpha$  relaxation time on a temperature scale normalized to  $T_g$  (i.e. Angell's plot) for all the considered samples.

The values of  $m_{liquid}$  calculated from the slope of the curves in Figure IV.16 (Equation III.15) are reported in Table IV.6.

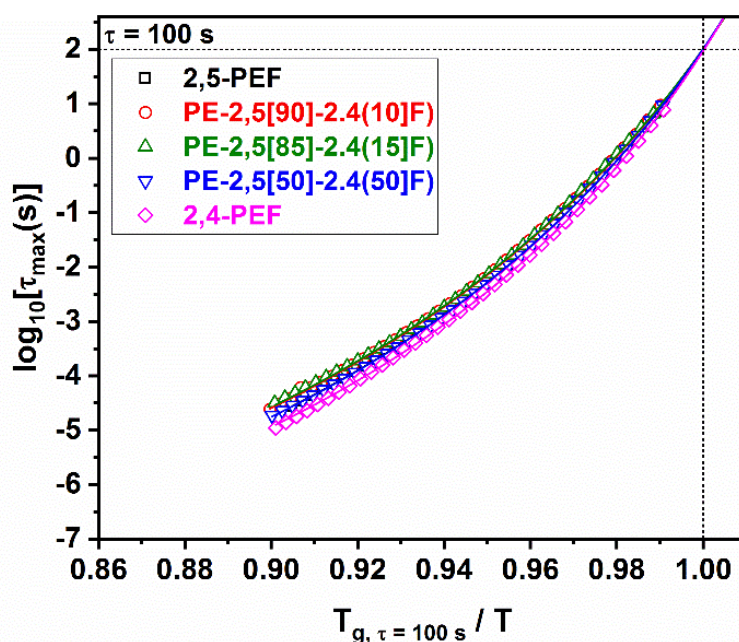


Figure IV.16: Angell's plot for amorphous 2,5/2,4-PEF copolymers compared to the homopolymers 2,5-PEF and 2,4-PEF.

Earlier studies on a large number of glass-forming liquids including polymers<sup>57,58</sup> show that polymers exhibit a qualitative correlation between fragility and the glass transition temperature: high- $T_g$  polymers usually have high fragilities.

However, this trend does not apply to every glass-forming liquid<sup>59</sup>. According to Dudowicz et al.<sup>60</sup> the fragility in polymers is related to the packing efficiency. As such, polymers containing a stiff backbone and bulky side groups experience some difficulties in packing due to their stiff and complex-shaped molecules, and therefore form glasses with a larger excess of free volume.

On the other hand, polymers containing a flexible backbone and smaller side groups show a better packing efficiency and therefore form denser glasses. The chain flexibility seems to be the main parameter influencing the packing efficiency of amorphous polymer chains into the glassy state, and consequently the fragility index<sup>59–61</sup>. In this study, very small variations were observed in the series of PEFs samples. The  $m$  values (given in Table IV.6) are 118 for 2,5-PEF and 125 for 2,4-PEF. The copolymers have  $m$  values which are closer to 2,5-PEF. On a whole, all these values are quite comparable, and just a little lower with respect to other polyesters: 142 for PET<sup>62</sup>, 144 for PETg<sup>63</sup>, 170 for PC<sup>14</sup> 150 for PLA<sup>17</sup>).

According to their  $m_{liquid}$  value, PEFs can be considered as “fragile” glass-forming macromolecular liquids, which indeed is a quite conventional behavior for macromolecules with Van der Waals interactions or hydrogen bonds between chains<sup>55,64</sup>.

**Table IV.6: Glass transition temperatures  $T_g$  obtained by DRS for  $\tau = 100s$  and  $\tau = 10s$ .  $D$  is a dimensionless parameter of the VFT function,  $T_0$  is a reference temperature selected for the VFT fitting,  $m_{liquid}$  is the fragility index and  $E_a(\beta)$  is the activation energy of the  $\beta$  relaxation.**

Sample	$T_{g_{\tau=100s}}$ (°C)	$T_{g_{\tau=10s}}$ (°C)	$D$	$T_0$ (°C)	$\log_{10}(\tau_0)$ (s)	$m_{liquid}$	$\log_{10}(\tau_{0,A})$ (s)	$E_a(\beta)$ (kJ/mol)
2,5-PEF	74	77	4.42	31	-12	117 ± 10	-15	56
PE-2,5[90]- 2,4[10]F	72	75	4.64	29	-12	112 ± 10	-16	61
PE-2,5[85]- 2,4[15]F	72	75	4.67	29	-12	112 ± 10	-15	55
PE-2,5[50]- 2,4[50]F	72	75	4.40	31	-12	118 ± 10	-14	55
2,4-PEF	65	68	4.10	27	-12	125 ± 10	-16	64

#### IV.2.2.7. Cooperativity length $\xi_\alpha$ and cooperativity degree $N_\alpha$

The cooperativity length  $\xi_\alpha$  and the cooperativity degree  $N_\alpha$  were estimated for all the considered PEFs samples in a wide range of temperatures and relaxation times. Figure IV.17 presents the cooperativity length  $\xi_\alpha$  associated with the  $\alpha$  relaxation as a function of temperature estimated from both calorimetric and dielectric measurements.

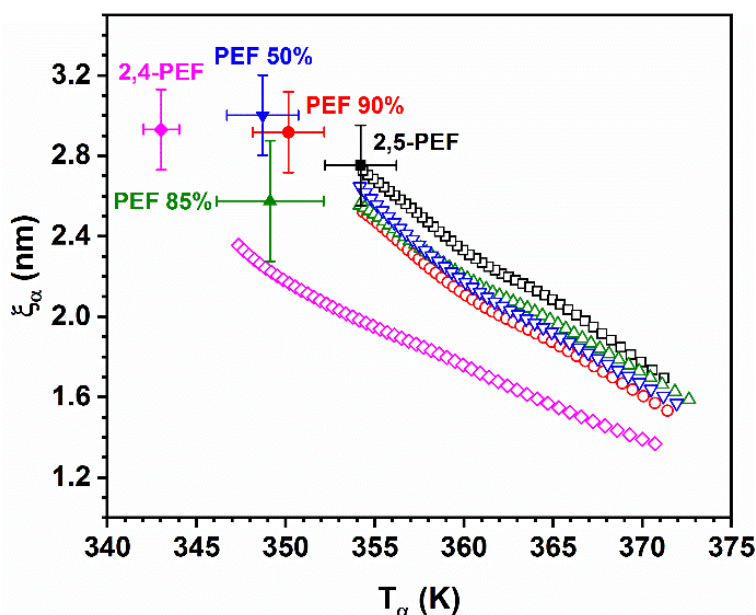


Figure IV.17: Cooperativity length  $\xi_\alpha$  versus temperature  $T_\alpha$  for amorphous PEFs samples as deduced from DRS (hollow symbols) and MT-DSC (filled symbols) measurements.

As expected,  $\xi_\alpha$  decreases with increasing temperature. It can be noted that the extrapolations of  $\xi_\alpha$  estimated from DRS over a wide range of relaxation times fit quite well with the values estimated by MT-DSC investigations. According to Figure IV.17, 2,4-PEF has the lowest cooperativity and the copolyesters have cooperativity values that are intermediate between those of the homopolymers. The cooperativity length shift can be related to the impact of the isomeric modification on the segmental relaxation.

Figure IV.18 shows the cooperativity degree  $N_\alpha$  versus the temperature normalized to  $T_g$  (taken from MT-DSC measurements). As already observed for the cooperativity length, the evolution of  $N_\alpha$  measured from MT-DSC and DRS investigations are consistent for all the considered samples.

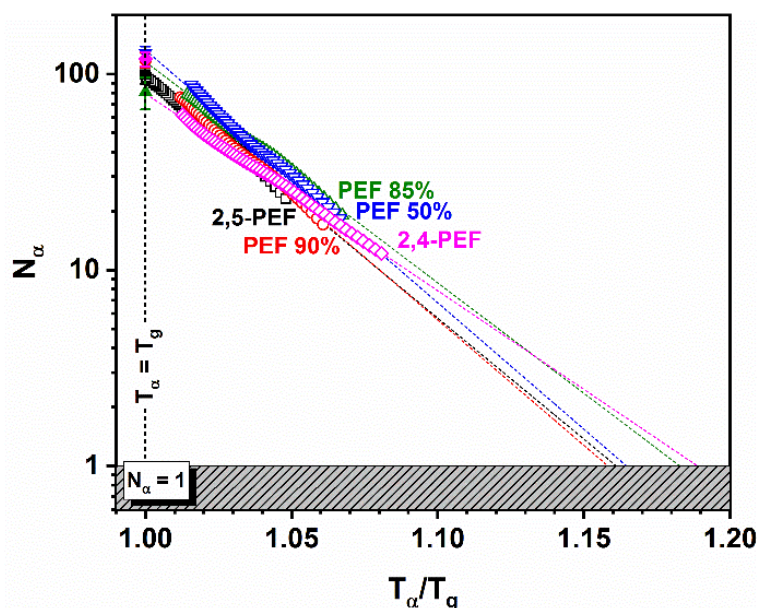


Figure IV.18: Evolution of the cooperativity degree  $N_\alpha$  (number of relaxing units in a CRR) as a function of the temperature normalized to  $T_g$  for amorphous PEFs as deduced from DRS (hollow symbols) and MT-DSC (filled symbols) measurements.

### IV.2.3. Thermally Stimulated Depolarization Current (TSDC)

The experimental method based on the measurement of thermally stimulated depolarization currents (TSDC) was also successfully used to characterize the large-scale segmental motions responsible for the glass transition.

#### IV.2.3.1. Impact of the incorporation of 2,4-FDCA DME on glass transition signature

In Figure IV.19 is given the dielectric manifestation of the glass transition signature obtained by TSDC for the considered PEFs samples from the depolarization currents versus temperature from glassy state to rubbery state.  $T_{\alpha,TSDC}$  (reported in Table IV.7), the temperature corresponding to the maximum of the depolarization peak, shifts towards lower temperatures when the 2,4-isomer content increases in consistent with MT-DSC ( $T_{\alpha,MT-DSC}$ ) and DRS ( $T_{\alpha,DRS}$ ) results (Figure IV.20). On a whole, a good agreement is obtained between these three techniques.

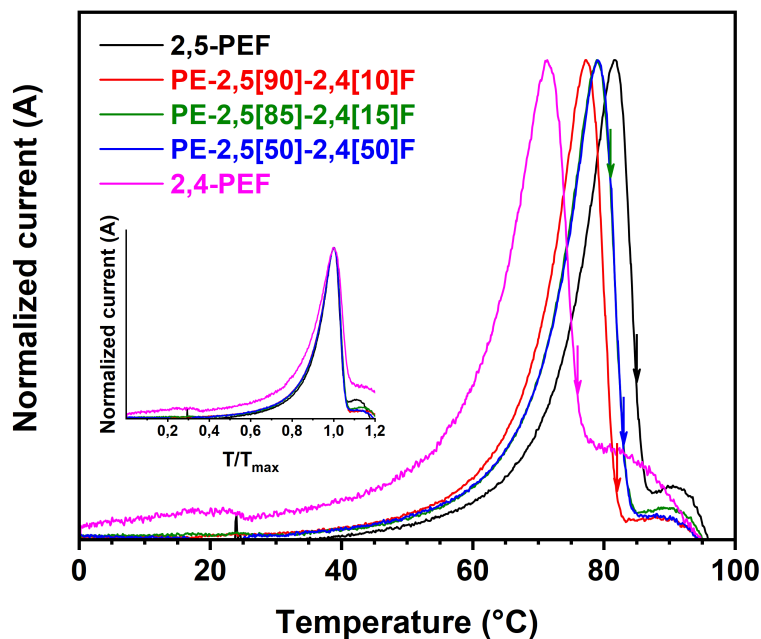


Figure IV.19: Normalized current in function of temperature from TSDC; Inset: glass transition temperature signature normalized to  $T_{max}$ . Arrows correspond to the polarization temperature for each depolarization spectrum.

Table IV.7: Parameters characterizing the segmental relaxation in amorphous PEFs.

2,5-FDCA DME %	100	90	85	50	0
$T_{\alpha,MT-DSC}$ (°C) <sup>a</sup>	81 ± 2	77 ± 2	76 ± 3	76 ± 2	70 ± 1
$T_{\alpha,DRS}$ (°C) <sup>a</sup>	77	75	75	75	68
$T_{\alpha,TSDC}$ (°C) <sup>a</sup>	82	77	79	79	71
$E_{\alpha,DRS}$ (kJ/mol) <sup>b</sup>	662	656	653	684	651
$E_{\alpha,TSDC}$ (kJ/mol) <sup>b</sup>	512	489	438	444	503
$m_{liquid}$ <sup>c</sup>	117	112	112	118	125
$m_{glass}$ <sup>d</sup>	82	78	80	83	85
$\xi_{\alpha,MT-DSC}$ <sup>e</sup>	2.8 ± 0.2	2.9 ± 0.2	2.6 ± 0.3	3.0 ± 0.2	2.9 ± 0.2
$\beta_{KWW}$ <sup>f</sup>	0.53	0.53	0.52	0.49	0.42

<sup>a</sup> Dynamic glass transition temperature. <sup>b</sup> Activation energy. <sup>c</sup> Fragility index obtained from DRS. <sup>d</sup> Fragility index obtained from TSDC. <sup>e</sup> Cooperativity length. <sup>f</sup> Stretching parameter obtained from the master curves.

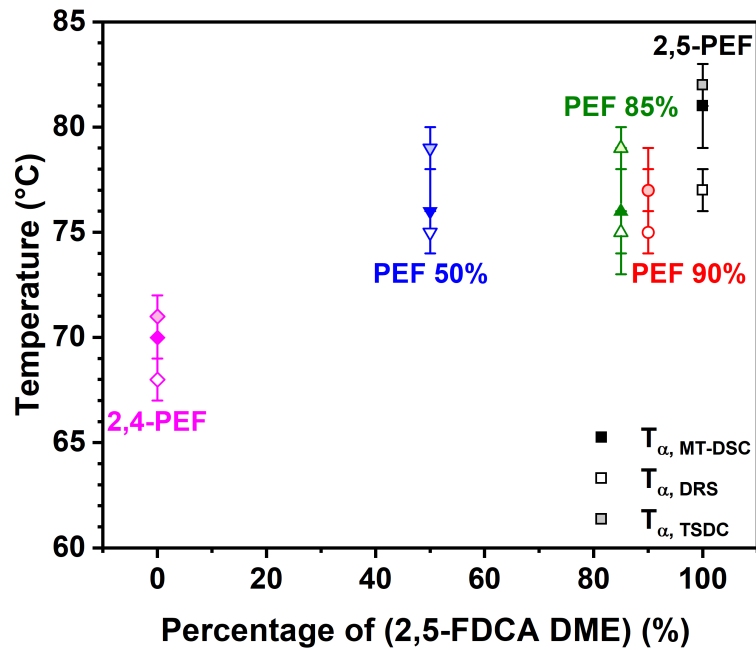


Figure IV.20: Dynamic glass transition temperature vs. the relative content of 2,5-FDCA DME assessed from MT-DSC (filled symbols), DRS (half-filled symbols) and TSDC (empty symbols) measurements.

#### IV.2.3.2. Relaxation map combining the three techniques

As previously said, the segmental relaxation in the liquid-like state observed by DRS exhibits a non-Arrhenius character, which can be described by a Vogel–Fulcher–Tammann (VFT) equation. From TSDC experiments, as proposed by Alegría et al. <sup>65</sup>, the segmental relaxation can be consistently analyzed with the Kohlrausch–Williams–Watts (KWW) equation <sup>44,66</sup>. The relaxation times ( $\tau$ ) associated with the segmental relaxation were therefore calculated according to the following equation <sup>67</sup>:

$$\tau = \beta \frac{Q}{I} \left[ \ln \left( \frac{Q_0}{Q} \right) \right]^{1-1/\beta} \quad (\text{IV.14})$$

Where  $Q(t) = \int_t^\infty I dt$ ,  $Q_0$  is the value of the initial stored charge,  $I$  is the current intensity, and  $\beta$  is a parameter depicting the non-Debye character of the segmental relaxation. The  $\beta$  or  $\beta_{KWW}$  parameter was determined by DRS (Table IV.7).

The segmental relaxation obtained by combination of MT-DSC, DRS and TSDC results are presented in Figure IV.21. The relaxation map highlights the difference in the dynamics for the segmental relaxation of PEFs in both the glassy and liquid-like states. The relaxation times extracted from TSDC experiments exhibit an Arrhenius-like behavior when  $T$  is far from the glass transition, and just a slight curvature when  $T$  gets closes to the glass transition.

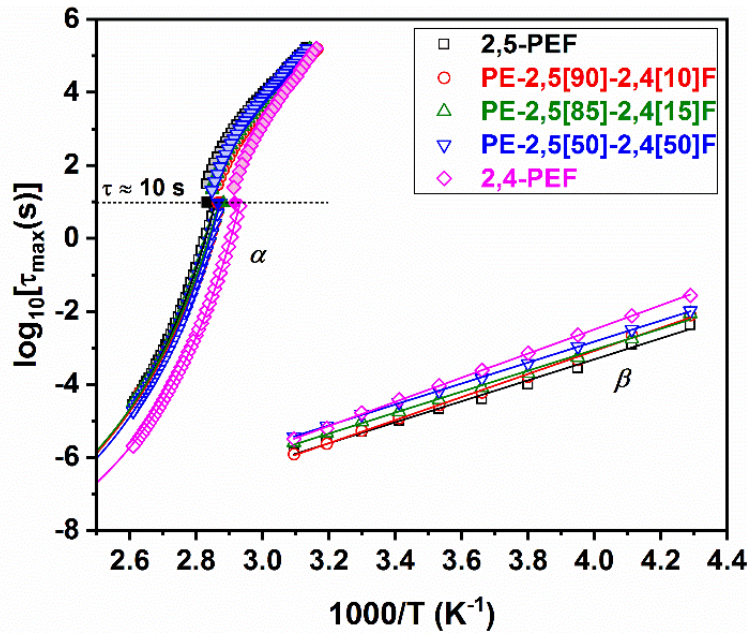


Figure IV.21: Relaxation map picturing the characteristic times for segmental relaxation as a function of the inverse temperature obtained by MT-DSC (filled symbols), TSDC (half-filled symbols) and DRS (empty symbols).

Concerning segmental relaxation times, a good agreement is also obtained between the three techniques.

#### IV.2.3.3. Activation energies

The activation energy associated with the segmental relaxation was calculated as:

$$E_a = \frac{\partial \ln(\tau)}{\partial (1/T_\alpha)} R \quad (\text{IV.15})$$

Where  $\tau$  is the characteristic time of the segmental relaxation at  $T_\alpha$  and  $R$  is the gas constant.

The activation energy is represented in Figure IV.22 as a function of  $T_\alpha/T$ . The values of activation energy obtained at  $T_\alpha/T = 1$  from the liquid-like state  $E_{a,DRS}$  and the glassy state  $E_{a,TSDC}$  are given in Table IV.7. In the supercooled liquid, i.e. for  $T_\alpha/T \leq 1$ , the activation energy is roughly the same independently of the 2,4-FDCA DME content. When the temperature decreases, the activation energy increases exponentially until reaching a maximum value of 670 kJ/mol for  $T_\alpha/T = 1$ . The trends obtained by TSDC are quite different. For low temperatures, the activation energy versus  $T_\alpha/T$  seems to reach an asymptotic value. It is worth analyzing these results in the frame of the cooperative rearranging region (CRR) concept introduced by Adam and Gibbs<sup>68</sup>.

Many studies associate the so-called viscous slowing down of supercooled liquids with the increase in the energy barrier that the structural units must overcome for the relaxation process to occur<sup>69–72</sup>.

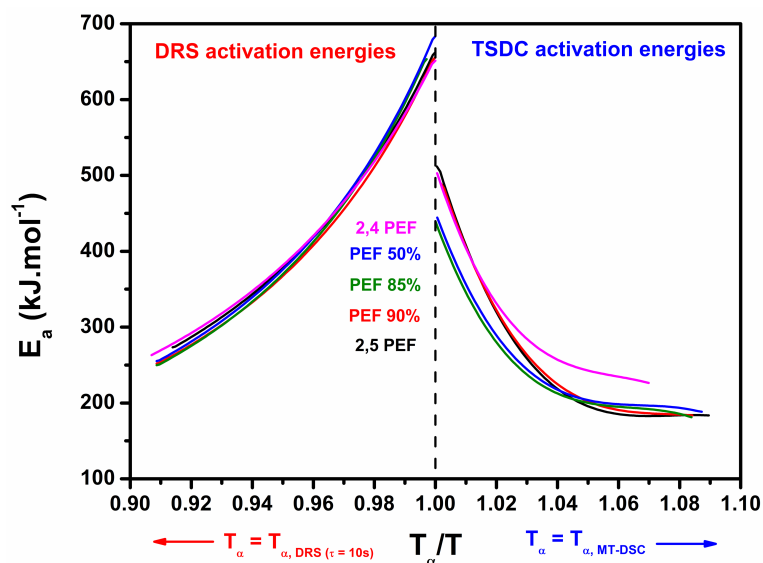


**Figure IV.22:** Activation energy as a function of  $T_\alpha/T$  calculated from TSDC and DRS results.

It is therefore reasonable to accept that  $E_{\alpha,DRS}$  is constant whatever the 2,4-FDCA DME content because of the similar cooperative character of the segmental relaxation dynamics obtained for all the considered PEFs samples.

#### IV.2.3.4. Fragility indexes

Besides, the fragility index may be calculated from both techniques, DRS and TSDC<sup>73</sup>, with Equation III.15. Alegría et al.<sup>67</sup> showed that TSDC experiments can be consistently analyzed to investigate the segmental relaxation of polymers in the same framework often used for conventional DRS experiments, that is to say, by using the Kohlrausch–Williams–Watts (KWW) equation<sup>44,66</sup>. As such, TSDC and DRS are absolutely complementary, because the latter provides the temperature dependence of the relaxation time in the liquid-like state when the former extends the representation of the relaxation map to the glassy state<sup>15</sup>. It is however noteworthy to stress out that the fragility index calculated from these two techniques may differ because the pathway to the glass transition is different. Some systems, such as diglycidyl ether of bisphenol-A<sup>74</sup> or glycerol<sup>75</sup>, have similar values of  $m_{glass}$  (calculated by TSDC as  $T$  approaches  $T_g$  from the glassy state) and  $m_{liquid}$  (calculated by DRS as  $T$  approaches  $T_g$  from the liquid-like state). In other cases, higher values of  $m_{liquid}$  are reported<sup>62,76,77</sup> with respect to  $m_{glass}$ .



Several authors <sup>78-80</sup> reported that the discrepancy between fragility values obtained from various experimental techniques is more pronounced for high-fragility glass-forming liquids. According to Hutchinson <sup>78</sup>, strong glass-forming supercooled liquids are those for which there is very little change in the slope of the fragility plot on passing from the equilibrium melt to the non-equilibrium glass, whereas fragile glass-forming liquids exhibit a large change in the slope of the fragility plot as the glass-transition region is traversed on cooling. A correlation between  $m_{liquid}$  and the molecular structure has been proposed by Kunal et al. <sup>61</sup> and Dudowicz et al. <sup>60</sup>. Polymers with very stiff backbones exhibit high fragility indexes. As an example, values of  $m_{liquid}$  equal to 132, 156, and 214 for polycarbonate (PC), poly(ethylene terephthalate), and poly(etherimide), respectively, were reported <sup>58</sup>. On the other hand, polymers with very flexible backbones, such as polyisobutylene and polyethylene, for which  $m_{liquid}$  is close to 50 <sup>58</sup>, are among the strongest glass-forming macromolecular liquids. However, no clear correlation has yet been established between the polymer structure and the difference between the values of fragility  $m_{glass}$  and  $m_{liquid}$ . As a consequence,  $m_{glass}$  and  $m_{liquid}$  calculated according to Equation III.15, are different, but no influence of the content of 2,4-FDCA DME was observed.

## Conclusion

The influence of the position of the carbonyl group on the molecular dynamics of wholly amorphous PEFs samples was investigated. The segmental relaxation ( $\alpha$  process) was characterized by DRS and TSDC measurements, and the glass transition temperature was measured by different techniques (MT-DSC, DRS and TSDC), always obtaining consistent values. The investigation of the structural relaxation was carried out by DRS analysis for wholly amorphous samples, which allowed to investigate both the  $\alpha$  and  $\beta$  processes in terms of dielectric properties, such as the relaxation time, the dielectric strength, and the fragility. The cooperativity length  $\xi_{\alpha}$  was estimated according to Donth's approach for all the considered samples and was found to be very similar at the glass transition ( $\approx 3$  nm).

To conclude, in this chapter, the incorporation of 2,4-FDCA based repeating units into 2,5-PEF polymer chains did not show a significative effect on the physical and thermal properties. Indeed, the physical properties evaluated for the copolymers in the amorphous state ( $T_d$ ,  $T_g$ , CRR size, fragility, segmental relaxation time, activation energy) are intermediate and almost identical with respect to the homopolymers whatever the ratio of 2,5/2,4-FDCA. However, the incorporation of 2,4-FDCA-based repeating units into 2,5-PEF present an impact on the local motion, in fact, the augmentation of this last induces a slowdown in local movements.

## References

- (1) Gandini, A.; Silvestre, A. J. D.; Neto, C. P.; Sousa, A. F.; Gomes, M. The Furan Counterpart of Poly(Ethylene Terephthalate): An Alternative Material Based on Renewable Resources. *J. Polym. Sci. A Polym. Chem.* **2009**, *47* (1), 295–298.  
<https://doi.org/10.1002/pola.23130>.
- (2) Thiyagarajan, S.; Vogelzang, W.; Knoop, R. J. I.; E. Frissen, A.; Haveren, J. van; Es, D. S. van. Biobased Furandicarboxylic Acids (FDCAs): Effects of Isomeric Substitution on Polyester Synthesis and Properties. *Green Chemistry* **2014**, *16* (4), 1957–1966.  
<https://doi.org/10.1039/C3GC42184H>.
- (3) Silverajah, V. S. G.; Ibrahim, N. A.; Zainuddin, N.; Yunus, W. M. Z. W.; Hassan, H. A. Mechanical, Thermal and Morphological Properties of Poly(Lactic Acid)/Epoxidized Palm Olein Blend. *Molecules* **2012**, *17* (10), 11729–11747.  
<https://doi.org/10.3390/molecules171011729>.
- (4) Papageorgiou, G. Z.; Tsanaktsis, V.; Bikiaris, D. N. Synthesis of Poly(Ethylene Furandicarboxylate) Polyester Using Monomers Derived from Renewable Resources: Thermal Behavior Comparison with PET and PEN. *Phys. Chem. Chem. Phys.* **2014**, *16* (17), 7946–7958.  
<https://doi.org/10.1039/C4CP00518J>.
- (5) Papageorgiou, G. Z.; Papageorgiou, D. G.; Terzopoulou, Z.; Bikiaris, D. N. Production of Bio-Based 2,5-Furan Dicarboxylate Polyesters: Recent Progress and Critical Aspects in Their Synthesis and Thermal Properties. *European Polymer Journal* **2016**, *83*, 202–229.  
<https://doi.org/10.1016/j.eurpolymj.2016.08.004>.
- (6) Terzopoulou, Z.; Tsanaktsis, V.; Nerantzaki, M.; Achilias, D. S.; Vaimakis, T.; Papageorgiou, G. Z.; Bikiaris, D. N. Thermal Degradation of Biobased Polyesters: Kinetics and Decomposition Mechanism of Polyesters from 2,5-Furandicarboxylic Acid and Long-Chain Aliphatic Diols. *Journal of Analytical and Applied Pyrolysis* **2016**, *117*, 162–175.  
<https://doi.org/10.1016/j.jaap.2015.11.016>.
- (7) Blaine, R. A Faster Approach to Obtaining Kinetic Parameters. *American Laboratory* **1998**, *30*, 21–23.
- (8) Blaine, R. L.; Hahn, B. K. Obtaining Kinetic Parameters by Modulated Thermogravimetry. *Journal of Thermal Analysis and Calorimetry* **1998**, *54* (2), 695–704.  
<https://doi.org/10.1023/A:1010171315715>.
- (9) Flynn, J. H. THE HISTORICAL DEVELOPMENT OF APPLIED NONISOTHERMAL KINETICS. In *Thermal Analysis*; Schwenker, R. F., Garn, P. D., Eds.; Academic Press, 1969; pp 1111–1126.  
<https://doi.org/10.1016/B978-0-12-395734-4.50035-7>.
- (10) Tsanaktsis, V.; Vouvoudi, E.; Papageorgiou, G. Z.; Papageorgiou, D. G.; Chrissafis, K.; Bikiaris, D. N. Thermal Degradation Kinetics and Decomposition Mechanism of Polyesters Based on 2,5-Furandicarboxylic Acid and Low Molecular Weight Aliphatic Diols. *Journal of Analytical and Applied Pyrolysis* **2015**, *112*, 369–378.  
<https://doi.org/10.1016/j.jaap.2014.12.016>.
- (11) Girija, B. G.; Sailaja, R. R. N.; Madras, G. Thermal Degradation and Mechanical Properties of PET Blends. *Polymer Degradation and Stability* **2005**, *90* (1), 147–153.  
<https://doi.org/10.1016/j.polymdegradstab.2005.03.003>.

- (12) Wachsen, O.; Platkowski, K.; Reichert, K.-H. Thermal Degradation of Poly-L-Lactide—Studies on Kinetics, Modelling and Melt Stabilisation. *Polymer Degradation and Stability* **1997**, *57* (1), 87–94.  
[https://doi.org/10.1016/S0141-3910\(96\)00226-1](https://doi.org/10.1016/S0141-3910(96)00226-1).
- (13) Cao, X.; Mohamed, A.; Gordon, S. H.; Willett, J. L.; Sessa, D. J. DSC Study of Biodegradable Poly(Lactic Acid) and Poly(Hydroxy Ester Ether) Blends. *Thermochimica Acta* **2003**, *406* (1), 115–127.  
[https://doi.org/10.1016/S0040-6031\(03\)00252-1](https://doi.org/10.1016/S0040-6031(03)00252-1).
- (14) Delbreilh, L.; Dargent, E.; Grenet, J.; Saiter, J.-M.; Bernès, A.; Lacabanne, C. Study of Poly(Bisphenol A Carbonate) Relaxation Kinetics at the Glass Transition Temperature. *European Polymer Journal* **2007**, *43* (1), 249–254.  
<https://doi.org/10.1016/j.eurpolymj.2006.09.019>.
- (15) Delbreilh, L.; Negahban, M.; Benzohra, M.; Lacabanne, C.; Saiter, J. M. Glass Transition Investigated by a Combined Protocol Using Thermostimulated Depolarization Currents and Differential Scanning Calorimetry. *J Therm Anal Calorim* **2009**, *96* (3), 865–871.  
<https://doi.org/10.1007/s10973-009-0060-1>.
- (16) Hutchinson, J. Studying the Glass Transition by DSC and TMDSC. *Journal of Thermal Analysis and Calorimetry* **2004**.
- (17) Arnoult, M.; Dargent, E.; Mano, J. F. Mobile Amorphous Phase Fragility in Semi-Crystalline Polymers: Comparison of PET and PLLA. *Polymer* **2007**, *48* (4), 1012–1019.  
<https://doi.org/10.1016/j.polymer.2006.12.053>.
- (18) Crétois, R.; Delbreilh, L.; Dargent, E.; Follain, N.; Lebrun, L.; Saiter, J. M. Dielectric Relaxations in Polyhydroxyalkanoates/Organoclay Nanocomposites. *European Polymer Journal* **2013**, *49* (11), 3434–3444.  
<https://doi.org/10.1016/j.eurpolymj.2013.07.009>.
- (19) Groeninckx, G.; Reynaers, H.; Berghmans, H.; Smets, G. Morphology and Melting Behavior of Semicrystalline Poly(Ethylene Terephthalate). I. Isothermally Crystallized PET. *J. Polym. Sci. Polym. Phys. Ed.* **1980**, *18* (6), 1311–1324.  
<https://doi.org/10.1002/pol.1980.180180612>.
- (20) Fox, T. G. Influence of Diluent and of Copolymer Composition on the Glass Temperature of a Poly-Mer System. *Bull. Am. Phys. Soc.* **1956**, *1*, 123.
- (21) Gordon, M.; Taylor, J. S. Ideal Copolymers and the Second-Order Transitions of Synthetic Rubbers. i. Non-Crystalline Copolymers. *Journal of Applied Chemistry* **1952**, *2* (9), 493–500.  
<https://doi.org/10.1002/jctb.5010020901>.
- (22) Kwei, T. K. The Effect of Hydrogen Bonding on the Glass Transition Temperatures of Polymer Mixtures. *Journal of Polymer Science: Polymer Letters Edition* **1984**, *22* (6), 307–313.  
<https://doi.org/10.1002/pol.1984.130220603>.
- (23) Kuo, S. W.; Huang, C. F.; Chang, F. C. Study of Hydrogen-Bonding Strength in Poly( $\epsilon$ -Caprolactone) Blends by DSC and FTIR. *Journal of Polymer Science Part B: Polymer Physics* **2001**, *39* (12), 1348–1359.  
<https://doi.org/10.1002/polb.1107>.

- (24) Bourdet, A.; Esposito, A.; Thiyagarajan, S.; Delbreilh, L.; Affouard, F.; Knoop, R. J. I.; Dargent, E. Molecular Mobility in Amorphous Biobased Poly(Ethylene 2,5-Furandicarboxylate) and Poly(Ethylene 2,4-Furandicarboxylate). *Macromolecules* **2018**, *51* (5), 1937–1945.  
<https://doi.org/10.1021/acs.macromol.8b00108>.
- (25) Thiyagarajan, S.; Meijlink, M. A.; Bourdet, A.; Vogelzang, W.; Knoop, R. J. I.; Esposito, A.; Dargent, E.; van Es, D. S.; van Haveren, J. Synthesis and Thermal Properties of Bio-Based Copolyesters from the Mixtures of 2,5- and 2,4-Furandicarboxylic Acid with Different Diols. *ACS Sustainable Chem. Eng.* **2019**, *acssuschemeng.9b04463*.  
<https://doi.org/10.1021/acssuschemeng.9b04463>.
- (26) Pak, J.; Pyda, M.; Wunderlich, B. Rigid Amorphous Fractions and Glass Transitions in Poly(Oxy-2,6-Dimethyl-1,4-Phenylene). *Macromolecules* **2003**, *36* (2), 495–499.  
<https://doi.org/10.1021/ma021487u>.
- (27) Pyda, M.; Wunderlich, B. Reversible and Irreversible Heat Capacity of Poly(Trimethylene Terephthalate) Analyzed by Temperature-Modulated Differential Scanning Calorimetry. *Journal of Polymer Science Part B: Polymer Physics* **2000**, *38* (4), 622–631.  
[https://doi.org/10.1002/\(SICI\)1099-0488\(20000215\)38:4<622::AID-POLB14>3.0.CO;2-U](https://doi.org/10.1002/(SICI)1099-0488(20000215)38:4<622::AID-POLB14>3.0.CO;2-U).
- (28) Pyda, M.; Wunderlich, B. Reversing and Nonreversing Heat Capacity of Poly(Lactic Acid) in the Glass Transition Region by TMDSC. *Macromolecules* **2005**, *38* (25), 10472–10479.  
<https://doi.org/10.1021/ma051611k>.
- (29) Codou, A.; Moncel, M.; Berkel, J. G. van; Guigo, N.; Sbirrazzuoli, N. Glass Transition Dynamics and Cooperativity Length of Poly(Ethylene 2,5-Furandicarboxylate) Compared to Poly(Ethylene Terephthalate). *Phys. Chem. Chem. Phys.* **2016**, *18* (25), 16647–16658.  
<https://doi.org/10.1039/C6CP01227B>.
- (30) Donth, E. The Size of Cooperatively Rearranging Regions at the Glass Transition. *Journal of Non-Crystalline Solids* **1982**, *53* (3), 325–330.  
[https://doi.org/10.1016/0022-3093\(82\)90089-8](https://doi.org/10.1016/0022-3093(82)90089-8).
- (31) van Berkel, J. G.; Guigo, N.; Kolstad, J. J.; Sipos, L.; Wang, B.; Dam, M. A.; Sbirrazzuoli, N. Isothermal Crystallization Kinetics of Poly(Ethylene 2,5-Furandicarboxylate). *Macromol. Mater. Eng.* **2015**, *300* (4), 466–474.  
<https://doi.org/10.1002/mame.201400376>.
- (32) Hempel, E.; Hempel, G.; Hensel, A.; Schick, C.; Donth, E. Characteristic Length of Dynamic Glass Transition near T<sub>g</sub> for a Wide Assortment of Glass-Forming Substances. *J. Phys. Chem. B* **2000**, *104* (11), 2460–2466.  
<https://doi.org/10.1021/jp991153f>.
- (33) Havriliak, S.; Negami, S. A Complex Plane Representation of Dielectric and Mechanical Relaxation Processes in Some Polymers. *Polymer* **1967**, *8*, 161–210.  
[https://doi.org/10.1016/0032-3861\(67\)90021-3](https://doi.org/10.1016/0032-3861(67)90021-3).
- (34) Dimitriadis, T.; Bikiaris, D. N.; Papageorgiou, G. Z.; Floudas, G. Molecular Dynamics of Poly(Ethylene-2,5-Furanoate) (PEF) as a Function of the Degree of Crystallinity by Dielectric Spectroscopy and Calorimetry. *Macromol. Chem. Phys.* **2016**, *217* (18), 2056–2062.  
<https://doi.org/10.1002/macp.201600278>.
- (35) Sperling, L. h. Multicomponent Polymeric Materials. In *Introduction to Physical Polymer Science*; John Wiley & Sons, Inc., 2005; pp 687–756.  
<https://doi.org/10.1002/0471757128.ch13>.

- (36) Okazaki, I.; Wunderlich, B. Reversible Local Melting in Polymer Crystals. *Macromol. Rapid Commun.* **1997**, *18* (4), 313–318.  
<https://doi.org/10.1002/marc.1997.030180407>.
- (37) Mackintosh, A. R.; Liggat, J. J. Dynamic Mechanical Analysis of Poly(Trimethylene Terephthalate)—A Comparison with Poly(Ethylene Terephthalate) and Poly(Ethylene Naphthalate). *J. Appl. Polym. Sci.* **2004**, *92* (5), 2791–2796.  
<https://doi.org/10.1002/app.20290>.
- (38) Starkweather, H. W.; Avakian, P.; Fontanella, J. J.; Wintersgill, M. C. Internal Motions in Polylactide and Related Polymers. *Macromolecules* **1993**, *26* (19), 5084–5087.
- (39) Soccio, M.; Martínez-Tong, D. E.; Alegría, A.; Munari, A.; Lotti, N. Molecular Dynamics of Fully Biobased Poly(Butylene 2,5-Furanoate) as Revealed by Broadband Dielectric Spectroscopy. *Polymer* **2017**.  
<https://doi.org/10.1016/j.polymer.2017.09.007>.
- (40) Ngai, K. L. Correlation between the Secondary  $\beta$ -Relaxation Time at  $T_g$  with the Kohlrausch Exponent of the Primary  $\alpha$  Relaxation or the Fragility of Glass-Forming Materials. *Phys. Rev. E* **1998**, *57* (6), 7346–7349.  
<https://doi.org/10.1103/PhysRevE.57.7346>.
- (41) Roland, C. M. Relaxation Phenomena in Vitriifying Polymers and Molecular Liquids. *Macromolecules* **2010**, *43* (19), 7875–7890.  
<https://doi.org/10.1021/ma101649u>.
- (42) Schönhals, A.; Kremer, F. Analysis of Dielectric Spectra. In *Broadband Dielectric Spectroscopy*; Kremer, P. D. F., Schönhals, P.-D. D. A., Eds.; Springer Berlin Heidelberg, 2003; pp 59–98.  
[https://doi.org/10.1007/978-3-642-56120-7\\_3](https://doi.org/10.1007/978-3-642-56120-7_3).
- (43) Bello, A.; Laredo, E.; Grimau, M.; Nogales, A.; Ezquerro, T. A. Relaxation Time Distribution from Time and Frequency Domain Dielectric Spectroscopy in Poly(Aryl Ether Ether Ketone). *The Journal of Chemical Physics* **2000**, *113* (2), 863–868.  
<https://doi.org/10.1063/1.481862>.
- (44) Williams, G.; C. Watts, D. Non-Symmetrical Dielectric Relaxation Behaviour Arising from a Simple Empirical Decay Function. *Transactions of the Faraday Society* **1970**, *66* (0), 80–85.  
<https://doi.org/10.1039/TF9706600080>.
- (45) Alvarez, F.; Alegria, A.; Colmenero, J. Relationship between the Time-Domain Kohlrausch-Williams-Watts and Frequency-Domain Havriliak-Negami Relaxation Functions. *Phys. Rev. B* **1991**, *44* (14), 7306–7312.  
<https://doi.org/10.1103/PhysRevB.44.7306>.
- (46) Massa, D. J.; O'Reilly, J. M.; Perchak, D. R.; Gillmor, J. R. Physical Aging, Coreset Curl, and Stress Relaxation of PETG Polyester; 2000.
- (47) Mano, J. F.; Gómez Ribelles, J. L.; Alves, N. M.; Salmerón Sanchez, M. Glass Transition Dynamics and Structural Relaxation of PLLA Studied by DSC: Influence of Crystallinity. *Polymer* **2005**, *46* (19), 8258–8265.  
<https://doi.org/10.1016/j.polymer.2005.06.096>.
- (48) Yin, H.; Napolitano, S.; Schönhals, A. Molecular Mobility and Glass Transition of Thin Films of Poly(Bisphenol A Carbonate). *Macromolecules* **2012**, *45* (3), 1652–1662.  
<https://doi.org/10.1021/ma202127p>.

- (49) Rotella, C.; Napolitano, S.; De Cremer, L.; Koeckelberghs, G.; Wübbenhorst, M. Distribution of Segmental Mobility in Ultrathin Polymer Films. *Macromolecules* **2010**, *43* (20), 8686–8691.  
<https://doi.org/10.1021/ma101695y>.
- (50) Pluta, M.; Jeszka, J. K.; Boiteux, G. Polylactide/Montmorillonite Nanocomposites: Structure, Dielectric, Viscoelastic and Thermal Properties. *European Polymer Journal* **2007**, *43* (7), 2819–2835.  
<https://doi.org/10.1016/j.eurpolymj.2007.04.009>.
- (51) Vogel, H. Z. Phys 1921, 22, 645.[CAS]. *The law of the relation between the viscosity of liquids and the temperature Vogel, Hans Physikalische Zeitschrift* **1921**, 22, 645–646.
- (52) Fulcher, G. S. Analysis of Recent Measurements of the Viscosity of Glasses. *Journal of the American Ceramic Society* **1925**, 8 (6), 339–355.  
<https://doi.org/10.1111/j.1151-2916.1925.tb16731.x>.
- (53) Tammann, G.; Hesse, W. Die Abhängigkeit Der Viscosität von Der Temperatur Bie Unterkühlten Flüssigkeiten. *Z. Anorg. Allg. Chem.* **1926**, 156 (1), 245–257.  
<https://doi.org/10.1002/zaac.19261560121>.
- (54) Saiter, J. M.; Grenet, J.; Dargent, E.; Saiter, A.; Delbreilh, L. Glass Transition Temperature and Value of the Relaxation Time at Tg in Vitreous Polymers. *Macromol. Symp.* **2007**, 258 (1), 152–161.  
<https://doi.org/10.1002/masy.200751217>.
- (55) Angell, C. A. Spectroscopy Simulation and Scattering, and the Medium Range Order Problem in Glass. *Journal of Non-Crystalline Solids* **1985**, 73 (1), 1–17.  
[https://doi.org/10.1016/0022-3093\(85\)90334-5](https://doi.org/10.1016/0022-3093(85)90334-5).
- (56) Angell, C. A. Formation of Glasses from Liquids and Biopolymers. *Science* **1995**, 267 (5206), 1924–1935.  
<https://doi.org/10.1126/science.267.5206.1924>.
- (57) Huang, D.; McKenna, G. B. New Insights into the Fragility Dilemma in Liquids. *J. Chem. Phys.* **2001**, 114 (13), 5621–5630.  
<https://doi.org/10.1063/1.1348029>.
- (58) Qin, Q.; McKenna, G. B. Correlation between Dynamic Fragility and Glass Transition Temperature for Different Classes of Glass Forming Liquids. *Journal of Non-Crystalline Solids* **2006**, 352 (28–29), 2977–2985.  
<https://doi.org/10.1016/j.jnoncrysol.2006.04.014>.
- (59) Hong, L.; Novikov, V. N.; Sokolov, A. P. Dynamic Heterogeneities, Boson Peak, and Activation Volume in Glass-Forming Liquids. *Phys. Rev. E* **2011**, 83 (6), 061508.  
<https://doi.org/10.1103/PhysRevE.83.061508>.
- (60) Dudowicz, J.; Freed, K. F.; Douglas, J. F. Fragility of Glass-Forming Polymer Liquids. *J. Phys. Chem. B* **2005**, 109 (45), 21350–21356.  
<https://doi.org/10.1021/jp053693k>.
- (61) Kunal, K.; Robertson, C. G.; Pawlus, S.; Hahn, S. F.; Sokolov, A. P. Role of Chemical Structure in Fragility of Polymers: A Qualitative Picture. *Macromolecules* **2008**, 41 (19), 7232–7238.  
<https://doi.org/10.1021/ma801155c>.
- (62) Dargent, E.; Bureau, E.; Delbreilh, L.; Zumailan, A.; Saiter, J. M. Effect of Macromolecular Orientation on the Structural Relaxation Mechanisms of Poly(Ethylene Terephthalate). *Polymer* **2005**, 46 (9), 3090–3095.  
<https://doi.org/10.1016/j.polymer.2005.01.096>.

- (63) Couderc, H.; Delbreilh, L.; Saiter, A.; Grenet, J.; De Souza, N.; Saiter, J. M. Relaxation in Poly-(Ethylene Terephthalate Glycol)/Montmorillonite Nanocomposites Studied by Dielectric Methods. *Journal of Non-Crystalline Solids* **2007**, *353* (47), 4334–4338. <https://doi.org/10.1016/j.jnoncrysol.2007.03.046>.
- (64) Delpouve, N.; Vuillequez, A.; Saiter, A.; Youssef, B.; Saiter, J. M. Fragility and Cooperativity Concepts in Hydrogen-Bonded Organic Glasses. *Physica B: Condensed Matter* **2012**, *407* (17), 3561–3565. <https://doi.org/10.1016/j.physb.2012.05.024>.
- (65) Alegría, A.; Goitiandía, L.; Tellería, I.; Colmenero, J.  $\alpha$ -Relaxation in the Glass-Transition Range of Amorphous Polymers. 2. Influence of Physical Aging on the Dielectric Relaxation. *Macromolecules* **1997**, *30* (13), 3881–3887. <https://doi.org/10.1021/ma961266m>.
- (66) Kohlrausch, R. Theorie Des Elektrischen Rückstandes in Der Leidener Flasche. *Annalen der Physik* **1854**, *167* (2), 179–214. <https://doi.org/10.1002/andp.18541670203>.
- (67) Alegría, A.; Goitiandia, L.; Colmenero, J. Interpretation of the TSDC Fractional Polarization Experiments on the  $\alpha$ -Relaxation of Polymers. *Journal of Polymer Science Part B: Polymer Physics* **2000**, *38* (16), 2105–2113. [https://doi.org/10.1002/1099-0488\(20000815\)38:16<2105::AID-POLB40>3.0.CO;2-7](https://doi.org/10.1002/1099-0488(20000815)38:16<2105::AID-POLB40>3.0.CO;2-7).
- (68) Adam, G.; Gibbs, J. H. On the Temperature Dependence of Cooperative Relaxation Properties in Glass-Forming Liquids. *The Journal of Chemical Physics* **1965**, *43* (1), 139–146. <https://doi.org/10.1063/1.1696442>.
- (69) Dyre, J. C. Colloquium: The Glass Transition and Elastic Models of Glass-Forming Liquids. *Rev. Mod. Phys.* **2006**, *78* (3), 953–972. <https://doi.org/10.1103/RevModPhys.78.953>.
- (70) Ediger, M. D.; Angell, C. A.; Nagel, S. R. Supercooled Liquids and Glasses. *J. Phys. Chem.* **1996**, *100* (31), 13200–13212. <https://doi.org/10.1021/jp953538d>.
- (71) Hecksher, T.; Nielsen, A. I.; Olsen, N. B.; Dyre, J. C. Little Evidence for Dynamic Divergences in Ultraviscous Molecular Liquids. *Nature Phys* **2008**, *4* (9), 737–741. <https://doi.org/10.1038/nphys1033>.
- (72) Martinez-Garcia, J. C.; Rzoska, S. J.; Drozd-Rzoska, A.; Martinez-Garcia, J. A Universal Description of Ultraslow Glass Dynamics. *Nat Commun* **2013**, *4* (1), 1–9. <https://doi.org/10.1038/ncomms2797>.
- (73) Correia, N. T.; Alvarez, C.; Moura Ramos, J. J.; Descamps, M. Molecular Motions in Molecular Glasses as Studied by Thermally Stimulated Depolarisation Currents (TSDC). *Chemical Physics* **2000**, *252* (1), 151–163. [https://doi.org/10.1016/S0301-0104\(99\)00354-7](https://doi.org/10.1016/S0301-0104(99)00354-7).
- (74) Viciosa, M. T.; Ramos, J. J. M.; Diogo, H. P. Molecular Dynamics of an Epoxy Resin Studied by Thermally Stimulated Depolarization Currents. *Journal of Non-Crystalline Solids* **2010**, *356* (50), 2858–2864. <https://doi.org/10.1016/j.jnoncrysol.2010.09.069>.
- (75) Böhmer, R.; Ngai, K. L.; Angell, C. A.; Plazek, D. J. Nonexponential Relaxations in Strong and Fragile Glass Formers. *J. Chem. Phys.* **1993**, *99* (5), 4201–4209. <https://doi.org/10.1063/1.466117>.



- (76) Saiter, J. M.; Dargent, E.; Kattan, M.; Cabot, C.; Grenet, J. Fragility Index of Drawn or Annealed Poly(Ethylene Terephthalate) Films Studied by Thermally Stimulated Depolarisation Currents. *Polymer* **2003**, *44* (14), 3995–4001.  
[https://doi.org/10.1016/S0032-3861\(03\)00312-4](https://doi.org/10.1016/S0032-3861(03)00312-4).
- (77) Correia, N. T.; Diogo, H. P.; Ramos, J. J. M. Slow Molecular Mobility in the Amorphous Solid State of Fructose: Fragility and Aging. *Journal of Food Science* **2009**, *74* (9), E526–E533.  
<https://doi.org/10.1111/j.1750-3841.2009.01363.x>.
- (78) Hutchinson, J. M. Interpretation of Glass Transition Phenomena in the Light of the Strength–Fragility Concept. *Polymer International* **1998**, *47* (1), 56–64.  
[https://doi.org/10.1002/\(SICI\)1097-0126\(199809\)47:1<56::AID-PI996>3.0.CO;2-Y](https://doi.org/10.1002/(SICI)1097-0126(199809)47:1<56::AID-PI996>3.0.CO;2-Y).
- (79) Wang, L.-M.; Angell, C. A.; Richert, R. Fragility and Thermodynamics in Nonpolymeric Glass-Forming Liquids. *J. Chem. Phys.* **2006**, *125* (7), 074505.  
<https://doi.org/10.1063/1.2244551>.
- (80) Ramos, J. J. M.; Correia, N. T.; Diogo, H. P. TSDC as a Tool to Study Slow Molecular Mobility in Condensed Complex Systems. *Journal of Non-Crystalline Solids* **2006**, *352* (42), 4753–4757.  
<https://doi.org/10.1016/j.jnoncrysol.2006.01.157>.

### Content

Introduction .....	146
V.1. Semi-crystalline morphologies.....	147
V.1.1. Morphologies of static crystallization: lamellae and spherulites.....	147
V.1.2. Other conditions of crystallization .....	150
V.2. Theory of germination and crystal growth .....	151
V.2.1. Germination .....	152
V.2.2. Growth .....	154
V.2.3. The growth rate $G$ .....	155
V.3. The melting .....	158
V.4. Global theories about crystallization kinetics .....	160
V.4.1. Introduction .....	160
V.4.2. Geometric approach .....	161
V.4.3. Isothermal conditions: the Avrami's theory.....	162
V.4.4. Cooling at a constant rate: the Ozawa's theory.....	162
References .....	163

## Introduction

Chapter III introduced the fundamentals about the amorphous state, which is characterized by a long-range disorder. Amorphous polymers can be seen as frozen liquids. The peculiar features of amorphous materials are:

- The absence of a melting temperature  $T_m$
- The existence of a glass transition temperature  $T_g$ : at  $T < T_g$  the polymer is solid and rigid (vitreous state), at  $T > T_g$  it is in the rubbery state
- The glass transition is a second-order thermal transition which involves a change in the specific heat  $\Delta C_p$  and no absorption or release of latent heat

On the other hand, the crystalline state is characterized by the existence of a long-range order, where the polymer chains are arranged in regular arrays generating specific crystalline unit cells (microstructure). The peculiar features of crystalline materials are:

- The existence of a melting temperature  $T_m$
- The specific volume of the crystalline phase is lower with respect to the amorphous phase (molecular arrangements improves packing efficiency)
- The rigidity of a crystalline material is usually higher with the respect to the amorphous counterpart

Due to the intrinsically large scale of polymer chains, and to the presence of eventual irregularities and defects, polymers never crystallize completely: at best, there may be the coexistence of different proportions of amorphous and crystalline phases in a complex arrangement, and the material is therefore referred as semi-crystalline. Semi-crystalline thermoplastic polymers are characterized by two thermal transitions: glass transition and melting. During cooling, crystallization is likely to occur over a temperature range between these transitions. Melting and crystallization are first-order thermal transitions: they involve a change in the specific heat capacity as well as the absorption or release of latent heat. The ability of a polymer to crystallize is favored by:

- the structural simplicity of the repeating unit (e.g. polyethylene)
- the symmetry of bonds that allow strong intermolecular interaction forces (e.g. polyamides)

However, symmetry alone is not enough for a polymer to crystallize. Indeed, polymers with a rigid structure, such as the ones containing aromatic or aliphatic cyclic groups in their backbones (e.g. PET or cellulose) are not prone to crystallization; sometimes mechanical stretching or chemical treatments can help out. Polymer chain can form crystals if they can fold and assemble in a compact and regular fashion. The most favorable situation is that of linear and symmetrical chains, as it the case for polyethylene. Polar inter-chain interactions, such as hydrogen bonding, stabilize the structure and increase the melting temperature. If a polymer chain has side groups, only the regular syndiotactic and isotactic forms will be able to crystallize (the atactic form can crystallize only if the side groups are small). Isotactic polymers generally form helical chains to minimize the steric hindrance between side groups, which is possible only if rotations around the axis of the backbone are possible.

## V.1. Semi-crystalline morphologies

### V.1.1. Morphologies of static crystallization: lamellae and spherulites

Crystalline lamellae, with thicknesses of the order of 10 nm, are the basic units formed during the crystallization of a molten polymer under static conditions <sup>1</sup>. A polymer crystalline lamella is made of aligned macromolecular chain segments brought to the growing structure from the melt thanks to diffusion/reptation processes. Different models exist regarding the formation mechanisms of polymer crystalline lamellae and their structure. A model was proposed by Schlesinger et al.<sup>2</sup>, Keller<sup>3</sup> and Jaccodine<sup>4</sup> between 1957 and 1960 as a result of the study of monocrystals formed from dilute solution by. These studies confirmed the notion of chain folding previously introduced by Storks<sup>5</sup>. Two models describing the mechanisms of macromolecule folding can be mentioned. The first is an "adjacent re-entry" model<sup>6</sup>, in which the chain folds to the surface of the lamella to form a loop while occupying the neighboring site ([Figure V.1 \(a\)](#)); the second is a "random switchboard" model<sup>7</sup>, in which a chain can fold on the surface of the lamella eventually forming a looser loop and returning into a more distant point ([Figure V.1 \(b\)](#)).

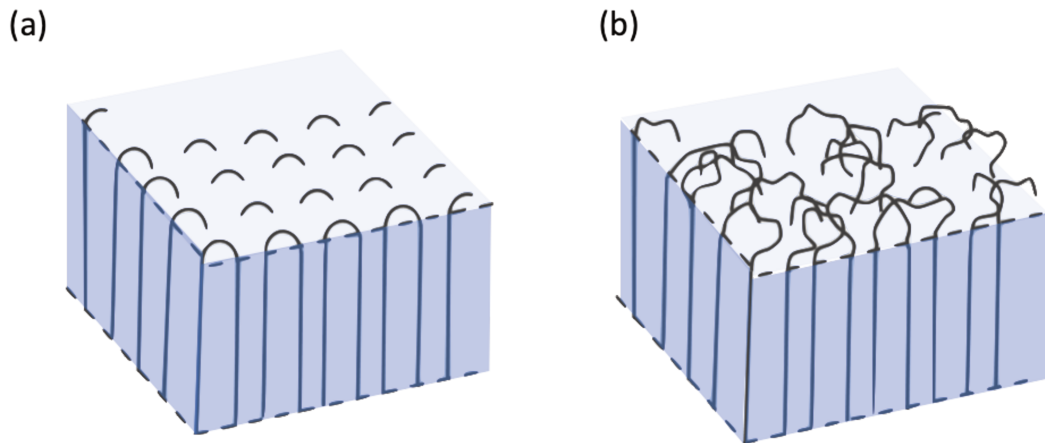


**Figure V.1:** Schematic views of a polymer crystalline lamella in (a) the adjacent re-entry and (b) the random switchboard models. [Reworked from <sup>8</sup>]

According to these two models, the polymer chains diffuse from the melt and fold in specific conformations, leading to the growth of the crystal lamella. The solidification model <sup>9</sup> depicted in [Figure V.2](#) assumes that there is no significant diffusion of the polymer chain segments, and that the crystal is rather formed from favorable conformations already existing in the melt close to the surface of the growing lamella.

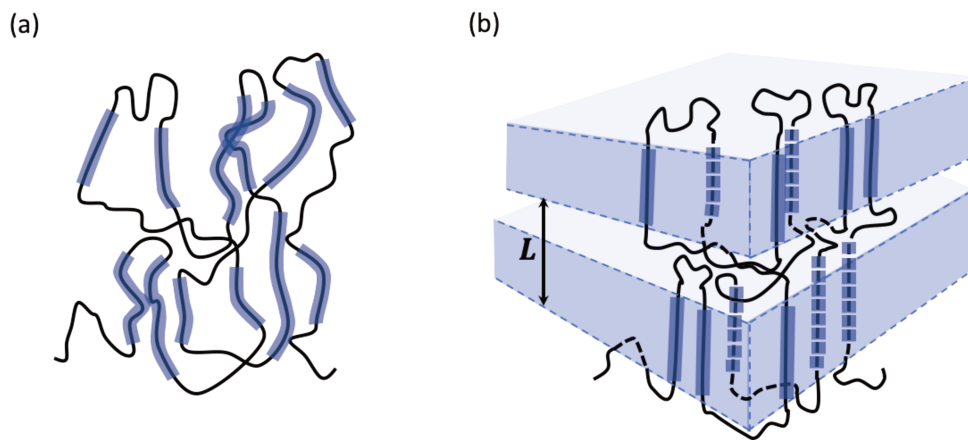


**Figure V.2:** Chain conformation (a) in the melt and (b) in the crystal according to the solidification model.

Spherulites are the largest microstructured entities formed during the solidification of a semi-crystalline polymer from the molten state (with sizes in the microscale). A spherulite can be approximately described as a spherical agglomerate consisting of monocrystalline radial lamellae, separated by amorphous zones ([Figure V.3](#)).

After homogenous or heterogeneous germination, the crystalline lamellae stack up while continuing to grow linearly; the microstructure then evolves to a spherical shape by a fan-like arrangement of curved crystallites <sup>10</sup>.

The growth of lamellae is essentially done by the folding and subsequent deposition of the macromolecular chains within the same crystalline lamella, but due to the typical size of the macromolecular chains (much bigger than the typical size of a lamella), any given macromolecule may as well belong to several adjacent lamellae. In this case, one or more portions of the macromolecules belong to the amorphous phase. This explains that, unlike systems consisting of atoms or small molecules, polymers generally cannot reach total crystallinity, for this would require an effort of arrangement impossible to achieve for very long chains. Due to the presence of interlamellar amorphous zones, spherulites are by nature semi-crystalline entities. After formation, each spherulite continues to grow in a spherical geometry until it comes into contact with a neighboring spherulite (confluence). A straight interface is then created and growth continues using the residual available amorphous volume, if its volume and thickness still allows folding and packing.

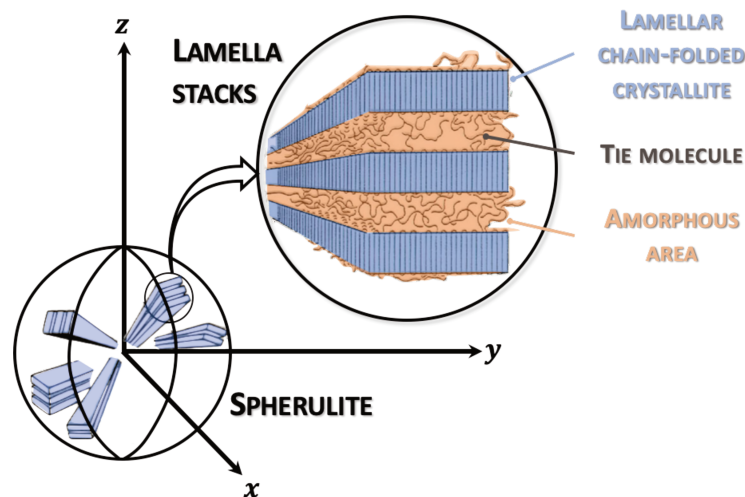


Figure V.3: Model of spherulitic structure. [Reworked from <sup>11</sup>]

### V.1.2. Other conditions of crystallization

In non-static crystallization conditions, i.e. in the presence of a flow or under any other kind of constraint, other microstructures can develop, such as mono-crystals with macroscopic size (crystallization from a dilute solution), crystallites with fringed micelles (crystallization under very high pressure) (Figure V.4), crystallites with aligned or even drawn chains, or the so-called shish-kebab structures (Figure V.5) (crystallization under deformation or flow-induced crystallization).

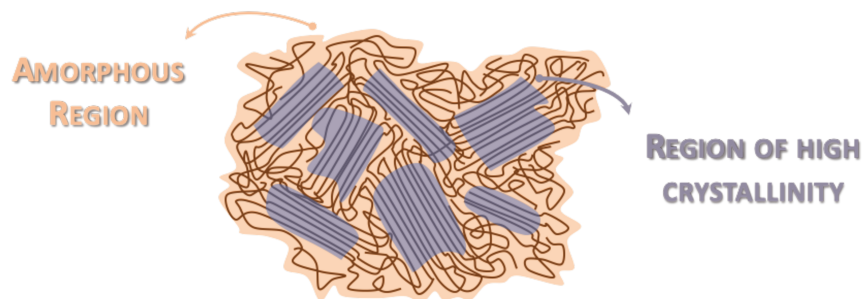


Figure V.4: Fringed micelles model. [Reworked from <sup>12]</sup>

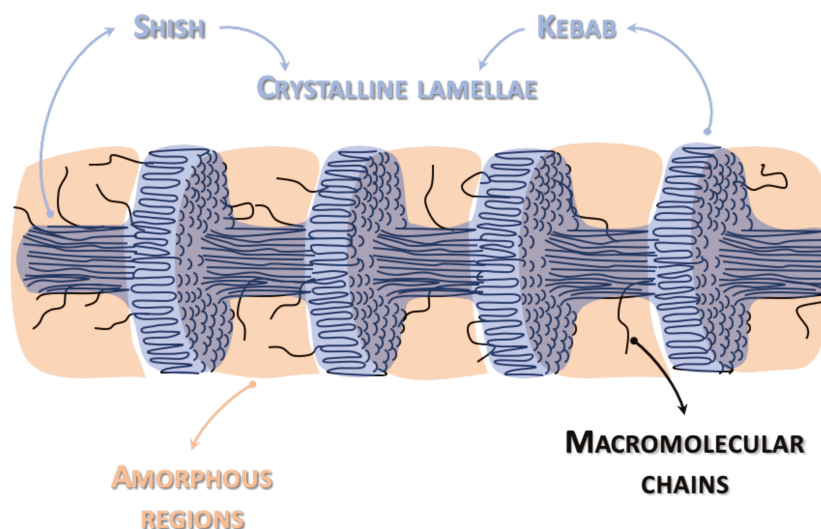


Figure V.5: Schematic illustration of the shish-kebab superstructures developed in semi-crystalline polymers under particular conditions. [Reworked from <sup>12]</sup>

The crystallization process leading to these microstructures includes several stages: germination, growth, and some secondary transformations (perfection of crystals, aging of the amorphous fractions). All of these stages are activated by crossing “free energy barriers”. Under static conditions, these free energy barriers depend on both the thermodynamic melting temperature and the degree of supercooling.

## V.2. Theory of germination and crystal growth

The crystallization of a polymer goes through different stages, including germination (formation of crystalline germs in the melt) and growth (development of primary crystals that build up into complex morphologies); sometimes, a further step of secondary crystallization occurs (perfection of defective primary crystals or growth of smaller crystals into the amorphous regions left after primary crystallization). The complete theory of germination-growth of polymer crystalline structures is presented in the works by Hoffman and Lauritzen<sup>13</sup>. According to thermodynamics, any spontaneous evolution of a system in conditions of constant pressure takes place by a diminution of its free energy  $g$ . The thermodynamic melting temperature  $T_m^0$  is determined as the intersection of the curves  $g_{liquid}(T)$  and  $g_{solid}(T)$  (Figure V.6). At  $T < T_m^0$ , the crystalline phase is more stable than the molten phase, and conversely at  $T > T_m^0$ .

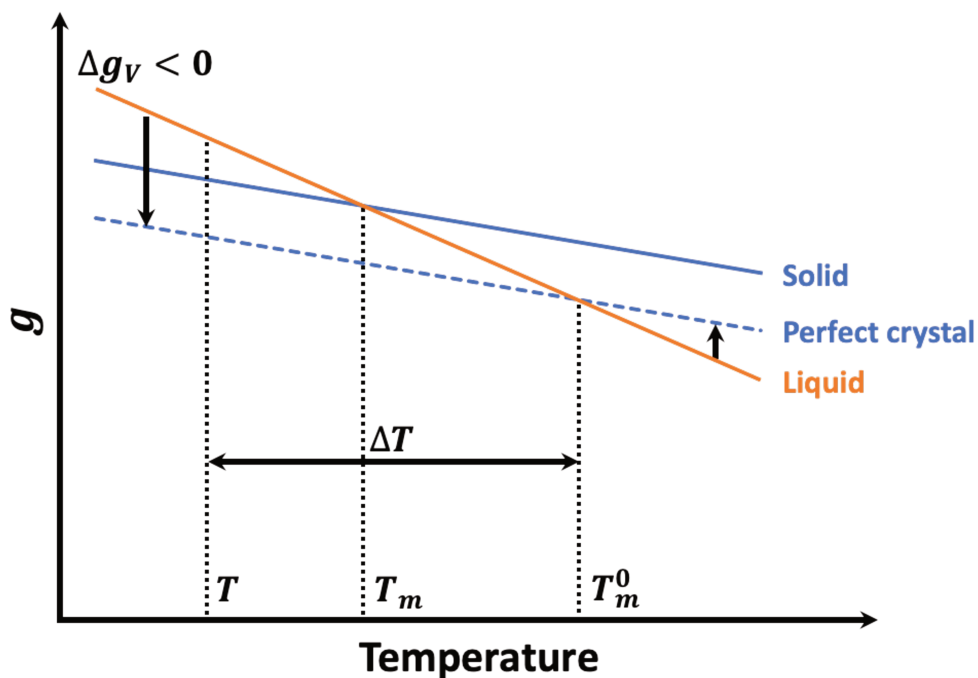


Figure V.6: Free energy  $g$  of a semi-crystalline polymer and thermodynamic melting temperature  $T_m^0$ .



### V.2.1. Germination

The formation of a germ results from two antagonistic mechanisms:

- a change in the free energy  $\Delta g_V$  associated with the transformation of a molten volume of polymer to a crystal. This term is proportional to the volume of the germ, is negative, and its absolute value increases as the supercooling  $\Delta T = T_m^0 - T$  increases;
- a change in the free enthalpy  $\Delta g_S$  associated with the molten-crystal interface formation. This term is proportional to the total interface area, and always positive.

The global change in the total free energy of the system during germination goes through a maximum, and is written as:

$$\Delta g = \Delta g_V + \Delta g_S \quad (\text{V.1})$$

As an example, let's consider the case of the formation of a spherical germ (characterized by a single dimensional parameter, the radius  $r$ ). The variation of free energy is shown in [Figure V.7](#). The germ is stable (and will survive until the growth stage) only if an augmentation of its size leads to a decrease of the free energy of the system. This condition is met for any point beyond the maximum value of  $\Delta g$ , or equivalently for  $r > r^*$  (critical radius). In the opposite case, the germ is unstable and has a limited lifetime. The higher the supercooling  $\Delta T$ , the smaller the critical radius, i.e., the formation of stable germs is statically favored as the supercooling degree increases.

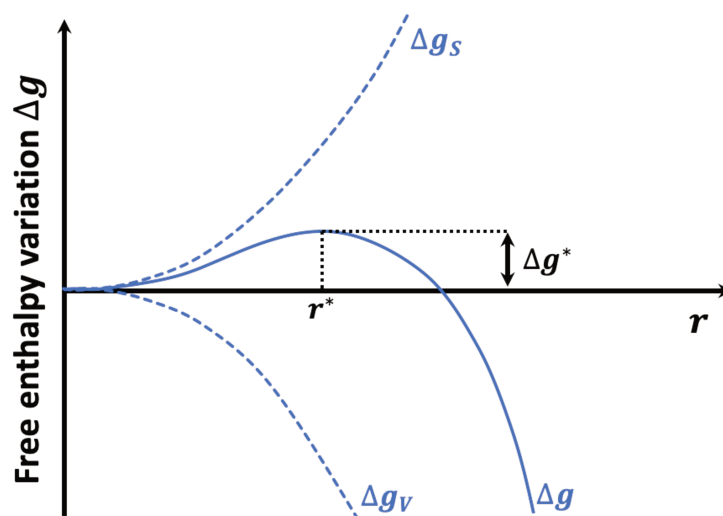


Figure V.7: Free enthalpy of formation of a spherical germ.

If germs are not spherical, several dimensional parameters should be considered, but the main variable governing the germination rate will still be the supercooling degree. A crystal germ may be constituted by the polymer itself. In this case, which is rare because it mainly happens for high supercooling degrees, the germination is homogeneous. The germ can also be constituted on a foreign body, in this case the germination is heterogeneous. Depending on the type of germination, different germ geometries are obtained: primary, secondary or tertiary.

- Primary germination

This is the first step in the formation of any crystalline entity. It can be heterogeneous, with the deposition of a segment of polymer chain onto a pre-existing substrate in the melt (catalyst residue, impurity, residual pre-existing crystalline structure...) or homogeneous (formation of a stable germ from the melt).

- Secondary germination (Figure V.8 (a))

It corresponds to the deposit of a segment of polymer chain onto the surface of a crystalline entity in order to start a new layer. It is intrinsically heterogeneous.

- Tertiary germination (Figure V.8 (b))

It corresponds to the deposit of a segment of polymer chain in the hollow space close to a "step" formed between the substrate and a secondary or tertiary germ (completion of a layer). It also is intrinsically heterogeneous.

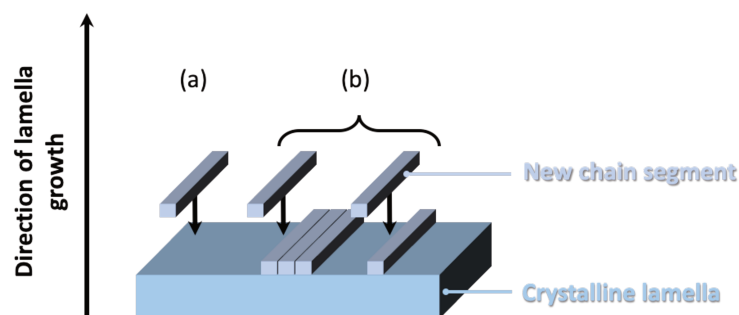


Figure V.8: Secondary and tertiary germinations.

The free energies associated with the formation of these different types of germs are not equal. For any given volume, the bigger is the area of the crystal-liquid interface to form, the more difficult will be the germination. So, primary germs will be less likely to form than secondary germs, and even less likely to form than tertiary germs.

## V.2.2. Growth

The growth of a crystalline lamella consists in the deposition of a secondary germ on a substrate followed by the completion of the crystal layer over the total width of the lamella by tertiary germination. The different growth rates sketched in Figure V.9 are noted as:

- $i$  rate of deposition of secondary germs
- $j$  rate of completion of the layer (i.e. rate of deposition of tertiaries germs)
- $G$  overall growth rate of the lamella

The growth rate of crystalline lamellae  $G$  can be expressed from these two parameters ( $i$  and  $j$ ), as a function of the growth regime.

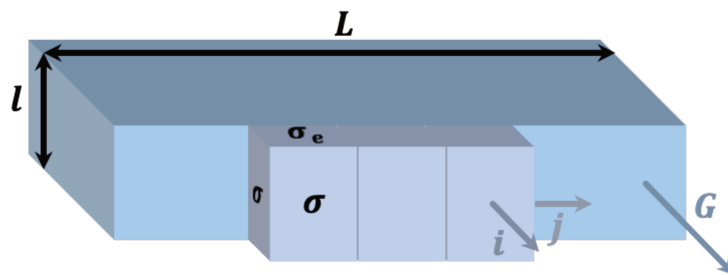


**Figure V.9: Schematization of different rates: rate of deposition of secondary germs ( $i$ ), rate of completion of the layer ( $j$ ) and the overall growth rate of the lamella ( $G$ ). [Reworked from <sup>14</sup>]**

$\sigma$ : lateral surface free energy;  $\sigma_e$ : fold surface free energy;  $L$ : length;  $l$ : thickness.

Three growth regimes can be evidenced (Figure V.10) according to the value of the supercooling degree, i.e. depending on the difference between the thermodynamic melting temperature  $T_m^0$  and the temperature at which crystallization occurs:

- Regime I ( $j \gg iL^2$ )

At low supercooling degrees, germination is difficult. Regime I is also called mononucleation because the rate of deposition secondary germs  $i$  is very low in comparison with the rate of completion a crystalline layer  $j$ . Each crystalline layer is completed before the deposition of a new secondary germ, thus the growth rate  $G$  is limited by the rate of deposition secondary germs ( $G \propto i$ ).

- Regime II ( $j \simeq iL^2$ )

For average values of the supercooling degree, the rate of deposition of secondary germs  $i$  and the rate of completion of a crystalline layer  $j$  are equivalent. The lamellae grow simultaneously along their width and their length. The growth rate goes as  $G \propto \sqrt{ij}$ .

- Regime III ( $j \ll iL^2$ )

For high supercooling degrees, the rate of deposition of secondary germs  $i$  is very high and the lamellae grow by the simultaneous deposition of several secondary germs on the same crystalline layer. The secondary germination governs the growth, whose rate goes as  $G \propto i$

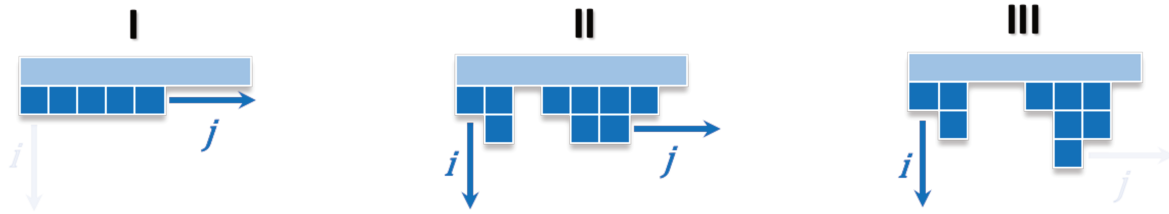


Figure V.10: Schematics of the three crystal growth regimes.

### V.2.3. The growth rate $G$

The total growth rate of the crystalline lamellae  $G$ , which is representative of the overall crystallization rate, is written as the product of a term related to the deposition of secondary and tertiary germs at the surface of the growing lamella, and a term related to the diffusion of the polymer chains from the melt:

$$G = G_0 \underbrace{\exp\left(-\frac{\Delta g_t}{RT}\right)}_{\text{Diffusion term}} \underbrace{\exp\left(-\frac{\Delta g^*}{k_B T}\right)}_{\text{Growth term}} \quad (\text{V.2})$$

Where  $G_0$  is a pre-exponential constant (independent of the temperature) and two exponential factors.

The first exponential factor is the diffusion (or transport) term, related to the transport of the macromolecular chains in the melt. This term is proportional to the characteristic rate of movement of the chains towards the surfaces of the growing crystalline lamellae;  $R$  is the gas constant and  $\Delta g_t$  is the activation energy governing the transport of macromolecular chains in the melt, frequently expressed by a semi-empirical law as:

$$\Delta g_t = \frac{U^* T}{T - T_\infty} \quad (\text{V.3})$$

Where  $U^*$  represents the activation energy of the displacement of the macromolecules within the melt and  $T_\infty$  is the temperature at which molecular movements becomes impossible ( $T_\infty = T_g - 30^\circ\text{C}$ ).

At  $T < T_\infty$ , the transport term is equal to zero and growth is disadvantaged. The second exponential factor is related to the deposition of germs on the surface of the growing lamella. In this term,  $k_B$  is the Boltzmann constant and  $\Delta g^*$  is the critical change in the free energy associated with the deposition of a germ (secondary or tertiary) on the substrate.  $\Delta g^*$  can be written as a function of the free energy  $\sigma$  of the crystal/melt interface, the free energy  $\sigma_e$  of the crystal folding surfaces, the molecular thickness  $b_0$ , and the transition free energy  $\Delta g_t$ :

$$\Delta g^* = \frac{j b_0 \sigma \sigma_e}{\Delta g_t} \quad (\text{V.4})$$

Where  $j$  is an integer that depends on the growth regime ( $j = 4$  for Regimes I and III,  $j = 2$  for Regime II).

By introducing the constant  $K_g$ , the previous equation can be rewritten as:

$$K_g = \frac{j b_0 \sigma \sigma_e T_m^0}{k_B \Delta h_m} \quad (\text{V.5})$$

Where  $\Delta h_m$  is the melting enthalpy per unit of volume.

The Hoffman-Lauritzen expression can therefore be obtained as:

$$G = G_0 \exp\left(\frac{-U^*}{R(T - T_\infty)}\right) \exp\left(\frac{-K_g}{fT\Delta T}\right) \quad (\text{V.6})$$

Where  $\Delta T$  is the supercooling temperature and  $f$  the correction factor defined by  $2T/(T_m^0 + T)$ .

The temperature dependence of the growth rate  $G$  is a curve approaching a Gaussian bell, as shown in [Figure V.11](#).

The Gaussian shape of the  $G = f(T)$  curve results from the competition of two mechanisms: the viscosity, which increases as temperature decreases and therefore slows the growth of crystallites near  $T_g$ , and the energy spent for nucleation, which becomes infinite as the temperature approaches  $T_m$ .

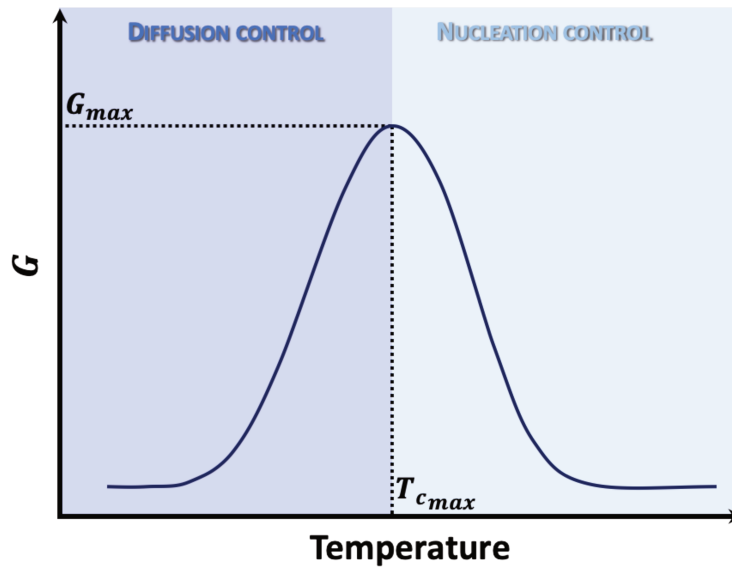


Figure V.11: Evaluation of the growth rate ( $G$ ) as function to the temperature.

At low and high supercooling degrees, the growth of the lamellae is slower either because the deposition of germs is thermodynamically disadvantaged (high temperatures), or because the diffusion of the polymer chains in the melt is slowed down due to an increase in viscosity (low temperatures). The temperature  $T_{cmax}$  corresponding to the maximum of the crystallization rate  $G_{max}$ , is of the order of  $(T_g + T_m)/2$ .

The Hoffman-Lauritzen's theory gives the temperature dependence of the growth rate measured by a microscope <sup>14</sup>.

Vyazovkin and Sbirrazzuoli <sup>15</sup> proposed a new equation to compute the Hoffman-Lauritzen's parameters from non-isothermal DSC data. This equation gives the temperature dependence of the effective activation energy of the growth rate as follow:

$$E_{\alpha}(T) = U^* \frac{T^2}{(T_c - T_{\infty})^2} + K_g R \frac{(T_m^0)^2 - T_c^2 - T_m^0 T_c}{(T_m^0 - T_c)^2 T_c} \quad (V.7)$$

Where  $E_{\alpha}$  is the effective activation energy,  $U^*$  is the activation energy of the segmental jump, which is associated with diffusion process,  $K_g$  is a parameter associated with the nucleation process,  $R$  is the gas constant,  $T_m^0$  is the equilibrium melting temperature,  $T_{\infty}$  is a hypothetical temperature where motion associated with viscous flow ceases and  $T_c$  is the crystallization temperature.

### V.3. The melting

As previously seen in [Chapter III](#), melting is a first-order thermodynamic transition. In semi-crystalline polymers, melting corresponds to the transition of ordered crystals to the disordered liquid state. The melting temperature  $T_m$  depends on the molecular weight, and increases when the degree of polymerization increases. Many parameters also influence  $T_m$ , such as the presence of additives or impurities, the presence of molecular defects, nodes and loops linked to chains entanglements, which result in a decrease of the order and then to a decrease of the melting temperature. The change in the degree of freedom which appears during melting is associated with melting entropy, which also depends on the molecular structure, and particularly on the rigidity of the polymer backbone. The Gibbs free energy associated to melting is given by:

$$\Delta G_m = \Delta H_m - T\Delta S_m \quad (\text{V.8})$$

Where  $\Delta H_m$  is the melting enthalpy and  $\Delta S_m$  is the melting entropy.

When the polymer reaches the melting temperature, the Gibbs free energy is equal to zero ( $\Delta G_m = 0$ ) and it is possible to define the melting temperature as:

$$T_m = \frac{\Delta H_m}{\Delta S_m} \quad (\text{V.9})$$

Where  $\Delta H_m$  is the enthalpy needed to break down the crystalline structure at constant  $T$  and  $P$ .

If the polymer chains are sufficiently long, this parameter becomes independent on the length.  $\Delta S_m > 0$  is related to the increase in disorder generally observed at melting. The value of  $T_m$  provides several information on the polymer behavior during melting. For a polymer having a fixed molecular weight, or a fixed volume, shorter chains lead to a more pronounced increase in the level of disorder  $\Delta S_m$ , therefore  $T_m$  is lower. If the polymer chains are highly connected to each other, the energy associated with the links increases, resulting in an increase of  $\Delta H_m$  and  $T_m$ . Finally, if the polymer chains have a low mobility in the liquid state, then the  $\Delta S_m$  value is lower and  $T_m$  is higher.

The thermodynamic melting temperature  $T_m^0$  is defined as the temperature where the free energy in the solid and the free energy in the liquid is the same.

In the case of semi-crystalline polymers, this condition corresponds at the intersection of the free energy curves for the perfect crystal of infinite dimensions and its amorphous counterpart. But the real solid is always semi-crystalline, and below  $T_m^0$  the amorphous phase is always present in (sometimes) significant proportion. Besides, the amorphous phase is by definition in a non-equilibrium state. In addition, polymers crystallize into thin lamellae for which the surface effects are no longer negligible and must be taken into account<sup>13</sup>. For these reasons, the real free energy of the solid is always greater than the one of the perfect crystal. As a result, the melting temperature  $T_m$  of a polymer is always lower than the thermodynamic melting temperature of the crystal. The Hoffman-Weeks method<sup>16</sup> allows to determine the value of  $T_m^0$  by an extrapolation procedure, as shown in Figure V.12. The melting temperature  $T_m$  is always greater than the crystallization temperature  $T_c$ , and the variation of  $T_m$  as a function of  $T_c$  is assumed to be linear according to the Hoffman-Lauritzen's theory. Consequently,  $T_m$  can never be lower than  $T_c$ , and the line defined by  $T_m$  represents the thermodynamic equilibrium condition between the crystal and the melt. The value of  $T_m^0$  is therefore obtained by the intersection between the extrapolated line  $T_m = f(T_c)$  and  $T_m = T_c$  line.

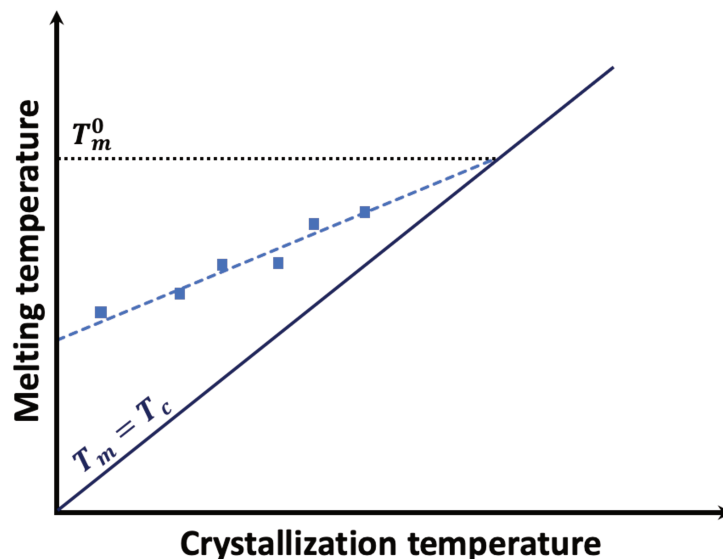


Figure V.12: Determination of the thermodynamic melting temperature  $T_m^0$  by the Hoffman-Weeks method.



## V.4. Global theories about crystallization kinetics

### V.4.1. Introduction

The so-called "global kinetic theories" describe the evolution of the transformation rate  $\alpha(T)$  as a function of time and temperature.  $\alpha(T)$  is a degree of conversion that represents the fraction of crystallized volume and is called the "conversion rate" or the "relative crystallinity".  $\alpha(T)$  is defined as the ratio of the crystallized volume fraction  $X_c$  on the crystallizable volume fraction  $X_\infty$ :

$$\alpha = \frac{X_c(t, T)}{X_\infty} \quad (\text{V.10})$$

$\alpha$  varies between 0 and 1, while  $X_\infty$  is always less than 1 and depends on the crystallization conditions.

The kinetic theories are based on the following general assumptions <sup>17,18</sup>:

- Potential germs are randomly and uniformly distributed in the melt; the growth of semi-crystalline entities starts instantly after activation of the germs: there is no induction time
- Potential germs can only disappear by activation or absorption by a growing semi-crystalline entity
- The geometry of growing semi-crystalline entities is imposed: spheres (3D growth), disks (2D) or sticks (1D)
- The collision of two growing entities blocks their growth: this implies that the geometry of each entity is conserved
- The total volume of polymer is constant during the transformation (isovolumic hypothesis)
- Secondary crystallization (subsequent and partial crystallization of the amorphous areas located between the lamellae of semi-crystalline entities) is not taken into account: the final crystallinity  $X_\infty$  of the spherulites is invariant during the transformation. This is a consequence of the isovolumic hypothesis: no crystallizable volume is created during the process

Two approaches have been typically used in the development of global theories of the crystallization kinetics: a geometric approach, which expresses the volume occupied by semi-crystalline entities, and a probabilistic approach, which calculates the probability that an element of volume is transformed. The main difference lies in the mathematical treatment, but the basic assumptions as well as the results are supposed to be identical. In this work, only the geometric approach was used.

#### V.4.2. Geometric approach

The geometric approach considers the free growth of crystalline entities having a simple geometry, and then applies a correction that take into account the reduction of available crystallizable volume (i.e. the fact that the growth of each entity is not free, but hindered by the contact with nearby growing entities). For a finite volume, a change in the transformation rate  $d\alpha$  can be written as a function of the change in the transformation rate for an infinite available volume  $d\alpha'$ :

$$d\alpha = (1 - \alpha)d\alpha' \quad (\text{V.11})$$

By specifying the dependence on time and then calculating the integral, the following expression is obtained:

$$\alpha(t) = 1 - \exp(-\alpha'(t)) \quad (\text{V.12})$$

where  $\alpha'$  represents the rate of fictive transformation that would be obtained by a free growth of crystallites.

This general relationship is the basis of all the Avrami's models, and can be extended to the simultaneous growth of several crystalline phases, assuming that each phase develops independently of the others, sharing with them the available volume <sup>19</sup>:

$$\alpha(t) = 1 - \exp\left(-\sum_i \alpha'_i(t)\right) \quad (\text{V.13})$$

### V.4.3. Isothermal conditions: the Avrami's theory

The Avrami-Evans' theory<sup>19-21</sup> allows to calculate the transformation rate with the additional hypothesis that crystallization occurs at a constant temperature. The frequency of germ activation  $q$  and the crystallite growth rate  $G$  are therefore constant. In these simplified conditions, the transformation rate can be written as:

$$\alpha(t) = 1 - \exp(-k_{Avrami}t^n) \quad (\text{V.14})$$

Where  $k_{Avrami}$  is the Avrami's constant depending on the temperature and the crystalline growth mode, and  $n$  is the Avrami's exponent depending on the growth mode (see [Table V.1](#)).

**Table V.1: Avrami's exponent of different modes of germination – growth**

Growth	Germination	
	Heterogeneous	Homogeneous
3D	$n = 3$	$n = 4$
2D	$n = 2$	$n = 3$
1D	$n = 1$	$n = 2$

### V.4.4. Cooling at a constant rate: the Ozawa's theory

Ozawa's theory<sup>22</sup> describes the kinetics of crystallization in the case of a constant cooling rate. The variation of the temperature causes a variation in the growth rate  $G$  and in the frequency of germ activation  $q$ . The theory makes the additional hypothesis that  $G$  and  $q$  vary in the same way with the temperature (isokinetic hypothesis):

$$\frac{G(T)}{q(T)} = cste \quad (\text{V.15})$$

The expression of the transformation rate is then written as:

$$\alpha(T) = 1 - \exp\left(-\frac{k_{Ozawa}(T)}{\phi^n}\right) \quad (\text{V.16})$$

Where  $\phi$  is the cooling rate (constant), and  $n$  is the Avrami's exponent.

## References

- (1) Carrega, M.; Agassant, J.; Biron, M. *Matériaux Industriels. Matériaux Polymères. Dunod Paris* **2000**.
- (2) Schlesinger, W.; Leeper, H. M. Gutta. I. Single Crystals of Alpha-Gutta. *Journal of Polymer Science* **1953**, *11* (3), 203–213.  
<https://doi.org/10.1002/pol.1953.120110302>.
- (3) Keller, A. The Spherulitic Structure of Crystalline Polymers. Part I. Investigations with the Polarizing Microscope. *Journal of Polymer Science* **1955**, *17* (84), 291–308.  
<https://doi.org/10.1002/pol.1955.120178414>.
- (4) Jaccodine, R. Observations of Spiral Growth Steps in Ethylene Polymer. *Nature* **1955**, *176* (4476), 305–306.
- (5) Storks, K. An Electron Diffraction Examination of Some Linear High Polymers | Journal of the American Chemical Society. *Journal of the American Chemical Society* **1938**, *60* (8), 1753–1761.
- (6) Flory, P. On the Morphology of the Crystalline State in Polymers | Journal of the American Chemical Society. *Journal of the American Chemical Society* **1962**, *84* (15), 2857–2867.
- (7) Fischer, E. W.; Lorenz, R. über Fehlorderungen in Polyäthylen-Einkristallen. *Kolloid-Z.u.Z.Polymer* **1963**, *189* (2), 97–110.  
<https://doi.org/10.1007/BF01499499>.
- (8) Lamellae\_Model.png  
[https://polymerdatabase.com/polymer%20physics/images/Lamellae\\_Model.png](https://polymerdatabase.com/polymer%20physics/images/Lamellae_Model.png)  
(accessed Jan 26, 2020).
- (9) Fischer, E. Ueber Die Hydrazinverbindungen. *Ann. Chem.* **1878**, *190*, 67–184.
- (10) Shonaike, G. O.; Advani, S. G.; Advani, S. G. Cure and Rubber Toughening of Vinyl Ester Resins <https://www.taylorfrancis.com/> (accessed Jan 26, 2020).  
<https://doi.org/10.1201/9780203492901-13>.
- (11) Núñez, E. CRYSTALLISATION OF STAR POLYESTERS WITH POLY( $\epsilon$ -CAPROLACTONE) ARMS - Approaching the Problem of Early Stages in Polymer Crystallisation., KTH, Stockholm, 2004.
- (12) Monnier, X. Molecular Dynamics in Complex Polymer Systems : From Anisotropy to Confinement Effects. phdthesis, Normandie Université, 2017.
- (13) Lauritzen, J.; Hoffman, J. D. Theory of Formation of Polymer Crystals with Folded Chains in Dilute Solution. *J. Res. Natl. Bur. Stand. A* **1960**, *64*, 73–102.
- (14) Hoffman, J. D.; Davis, G. T.; Lauritzen, J. I. The Rate of Crystallization of Linear Polymers with Chain Folding. In *Treatise on Solid State Chemistry: Volume 3 Crystalline and Noncrystalline Solids*; Hannay, N. B., Ed.; Springer US: Boston, MA, 1976; pp 497–614.  
[https://doi.org/10.1007/978-1-4684-2664-9\\_7](https://doi.org/10.1007/978-1-4684-2664-9_7).
- (15) Vyazovkin, S.; Sbirrazzuoli, N. Isoconversional Approach to Evaluating the Hoffman–Lauritzen Parameters ( $U^*$  and  $K_g$ ) from the Overall Rates of Nonisothermal Crystallization. *Macromolecular Rapid Communications* **2004**, *25* (6), 733–738.  
<https://doi.org/10.1002/marc.200300295>.
- (16) Hoffman, J. D.; Weeks, J. J. Melting Process and Equilibrium Melting Temperature of Polychlorotrifluoroethylene. In *Journal of Research of the National Bureau of Standards Section a-Physics and Chemistry*; 1962; p 13.

- (17) Koscher, E.; Fulchiron, R. Influence of Shear on Polypropylene Crystallization: Morphology Development and Kinetics. *Polymer* **2002**, *43* (25), 6931–6942.  
[https://doi.org/10.1016/S0032-3861\(02\)00628-6](https://doi.org/10.1016/S0032-3861(02)00628-6).
- (18) Poutot, G. Étude Des Transferts Thermiques Lors de La Cristallisation d'un Polymère Semi-Cristallin. thesis, Nantes, 2002.
- (19) Avrami, M. Kinetics of Phase Change. I General Theory. *J. Chem. Phys.* **1939**, *7* (12), 1103–1112.  
<https://doi.org/10.1063/1.1750380>.
- (20) Avrami, M. Kinetics of Phase Change. II Transformation-Time Relations for Random Distribution of Nuclei. *J. Chem. Phys.* **1940**, *8* (2), 212–224.  
<https://doi.org/10.1063/1.1750631>.
- (21) Avrami, M. Granulation, Phase Change, and Microstructure Kinetics of Phase Change. III. *The Journal of chemical physics* **1941**, *9* (2), 177–184.
- (22) Ozawa, T. Kinetics of Non-Isothermal Crystallization. *Polymer* **1971**, *12* (3), 150–158.  
[https://doi.org/10.1016/0032-3861\(71\)90041-3](https://doi.org/10.1016/0032-3861(71)90041-3).

# CHAPTER VI

---

## Crystallization Behavior of PEFs

### Content

Introduction .....	168
VI.1. Structural comparison between PET and 2,5-PEF.....	168
VI.1.1. $\alpha$ form of 2,5-PEF .....	170
VI.1.2. $\alpha'$ form of 2,5-PEF .....	171
VI.1.3. $\beta$ form of 2,5-PEF .....	171
VI.2. Comparison of PET and 2,5-PEF in terms of conformation.....	173
VI.3. Comparison of PET and 2,5-PEF in terms of thermal properties .....	174
VI.4. Study of the crystallization kinetics .....	175
VI.4.1. DSC analyses .....	175
VI.4.2. Crystallization kinetics.....	180
VI.4.3. Morphology and growth of spherulites .....	182
VI.5. Characterization of the amorphous phase during crystallization .....	187
VI.6. Influence of the position of the carbonyl group with respect to the furan ring on the crystal structure .....	189
Conclusion.....	192
References .....	193

## Introduction

Chapter IV, showed that the incorporation of a small amount of 2,4-FDCA DME in 2,5-FDCA-based polyesters is enough to significantly disturb the crystallization behavior of PEFs. This chapter shows some preliminary results evidencing the influence of the position of the carbonyl group on the crystallization kinetics for all the considered PEFs samples annealed both from the molten and the glassy state. Indeed, the crystallization behavior is an important aspect for both the production and application of thermoplastic aromatic polyesters. The isothermal crystallization kinetics were studied using Avrami's and Hoffman-Lauritzen's theories. A single set of Hoffman-Lauritzen parameters provides a linear relationship between the reference growth rate and the reciprocal molecular weight for catalyst-free PEFs. A particularly high activation energy for the segmental jump ( $U^*$ ) (related to diffusion processes) was found for PEF compared PET, which was attributed to more restricted conformational changes of PEF chains and therefore a limitation of the crystallization rate.

### VI.1. Structural comparison between PET and 2,5-PEF

The crystal structure commonly reported in the literature for PET was determined by Daubeny et al. <sup>1</sup> using X-ray diffraction measurements on drawn PET fibers. PET crystal structure is triclinic with dimensions  $a = 4.56 \text{ \AA}$ ,  $b = 5.94 \text{ \AA}$ ,  $c = 10.75 \text{ \AA}$ , and angles  $\alpha = 98.5^\circ$ ,  $\beta = 118^\circ$  and  $\gamma = 112^\circ$ . The unit cell hosts one PET repeating unit. The crystal density is  $1.455 \text{ g/cm}^3$ , whereas the amorphous density is  $1.335 \text{ g/cm}^3$  at ambient conditions.

The crystal structure of PEF was evaluated in an early study by Kazaryan and Medvedeva <sup>2</sup> using the same method that Daubeny and Bunn <sup>1</sup> used for PET. PEF crystal structure is also triclinic, with dimensions  $a = 5.75 \text{ \AA}$ ,  $b = 5.35 \text{ \AA}$ ,  $c = 20.10 \text{ \AA}$ , and angles  $\alpha = 133.3^\circ$ ,  $\beta = 90^\circ$  and  $\gamma = 112^\circ$ . The unit cell hosts two PEF repeating units, resulting in a crystal density of  $1.565 \text{ g/cm}^3$ . Mao et al. <sup>3</sup> characterized it by X-ray fiber diffraction combined with molecular modeling, and suggested an arrangement in the space group  $P2_1$  with a monoclinic unit cell having the following parameters  $a = 5.784 \text{ \AA}$ ,  $b = 6.780 \text{ \AA}$ ,  $c = 20.296 \text{ \AA}$  and  $\gamma = 103.3^\circ$ , and a calculated crystal density of  $1.562 \text{ g/cm}^3$ . Maini et al. <sup>4</sup> attributed this difference to the polymorphism of 2,5-PEF.

Some of the relationships between thermal and structural properties in 2,5-PEF have already been investigated, for instance to explain the complex behavior exhibited by this polyester during isothermal crystallization. Two phases, called  $\alpha'$  and  $\alpha$ , were identified by Stoclet et al.<sup>5</sup> Tsanatkis et al.<sup>6</sup>. They evidenced that the selected experimental conditions have an influence on the crystallization processes, the stability, and the eventual transformation of 2,5-PEF polymorphic crystalline structures. They also identified a new  $\beta$  phase obtained by solvent crystallization. The parameters of all the unit cells observed for 2,5-PEF are reported in Table VI.1<sup>4</sup>.

**Table VI.1: Polymorphic crystalline structures of 2,5-PEF and the corresponding structural data reported from<sup>4</sup>.**

Parameters	$\alpha$ form	$\alpha'$ form	$\beta$ form
Structure	Triclinic	Monoclinic	Monoclinic
$a$ (Å)	5.729	5.912	5.953
$b$ (Å)	7.89	6.913	6.600
$c$ (Å)	9.62	19.73	10.52
$\alpha$ (°)	98.1	90.0	90.0
$\beta$ (°)	65.1	90.0	107.0
$\gamma$ (°)	101.3	104.41	90.0
Volume (Å <sup>3</sup> )	385.85	780.84	394.30
$\rho_{crystal}$ (g/cm <sup>3</sup> )	1.567	1.549	1.482



### VI.1.1. $\alpha$ form of 2,5-PEF

The crystalline structure of the  $\alpha$  form observed in 2,5-PEF is displayed in Figure VI.1. The polymer chain is aligned moves away in opposite directions with respect to the furanic ring due to the orientation of the two ester groups. In particular, the backbone of the polymer chains is aligned in the  $c$  axis direction and lies roughly parallel to the  $(2\bar{5}0)$  plane (see Figure VI.1 (b) and (c)).

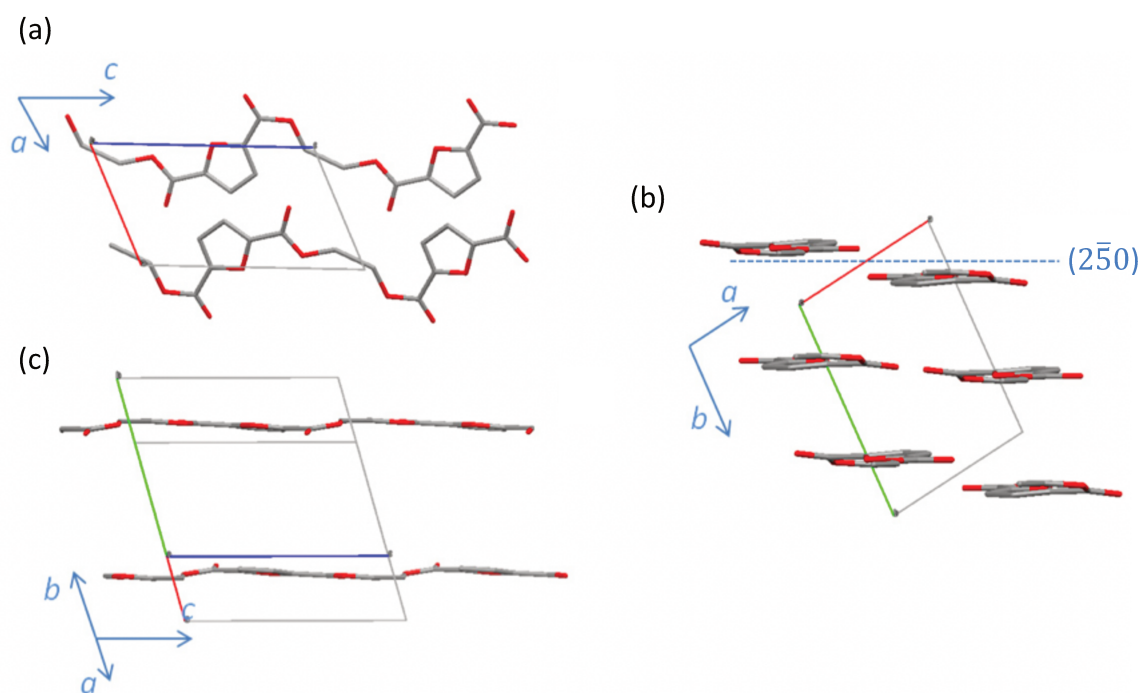


Figure VI.1: 3D views of the chain arrangements in the unit cell of the  $\alpha$  form of 2,5-PEF crystalline structures: (a) along the  $b$  axis; (b) projection onto the  $c$  axis; (c) view that shows chain sections. Oxygen atoms are in red. The Dotted line represents the intersection of the plane  $(2\bar{5}0)$  with the  $(a, b)$  plane. [Reproduced from <sup>4</sup>]

### VI.1.2. $\alpha'$ form of 2,5-PEF

The  $\alpha'$  form is the less stable crystalline form observed in 2,5-PEF. This pseudo monoclinic unit cell has a volume that is double compared to the  $\alpha$  form and hosts four repeating units belonging to two paired polymer chains. Each repeating unit is in a “trans” planar conformation in a  $2_1$  axis, as shown in Figure VI.2. The two polymer chains involved in the unit cell are parallel to the  $(a, c)$  planes staggered by  $3/12$  of the  $c$  axis in the chain direction and slightly bent.

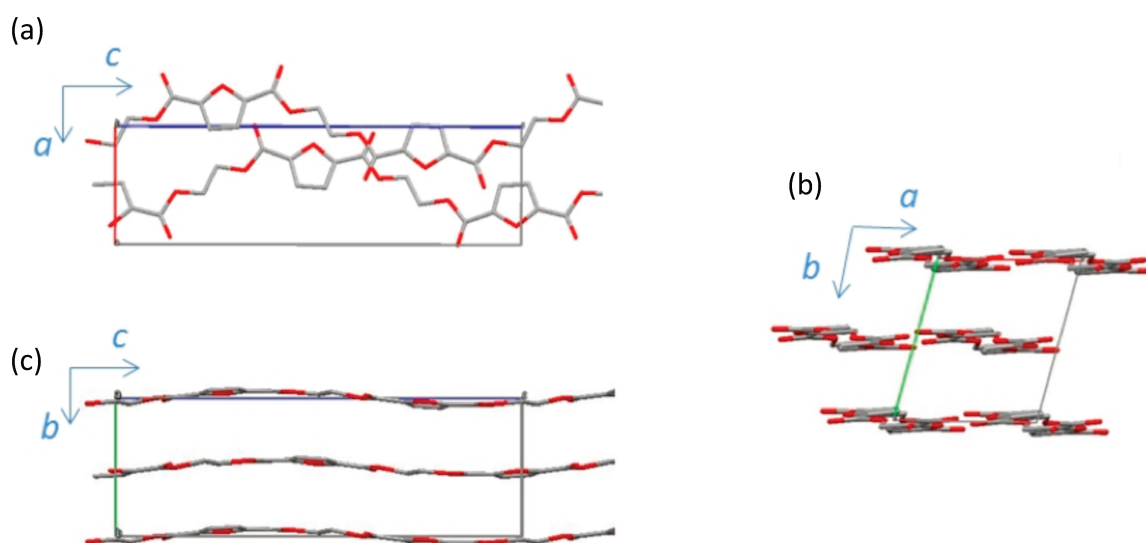
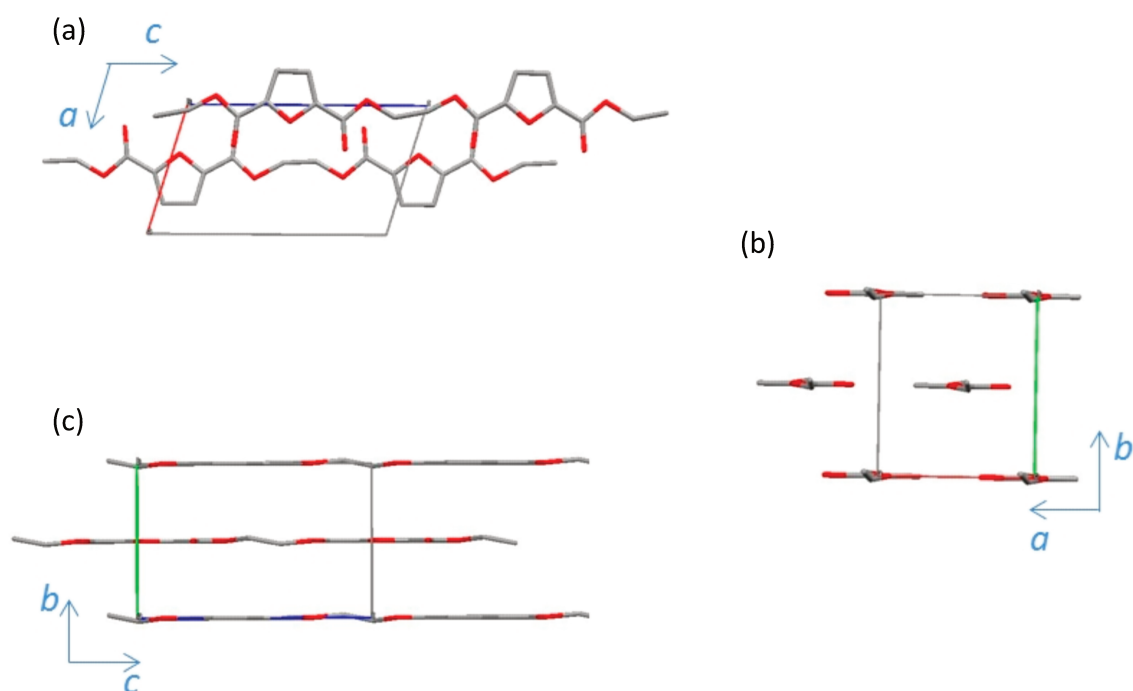


Figure VI.2: 3D views of the chain arrangement in the unit cell of the  $\alpha'$  form of 2,5-PEF crystalline structures: (a) projection onto the  $b$  axis; (b) along the  $c$  axis; (c) projection onto the  $a$  axis. [Reproduced from <sup>4</sup>]

### VI.1.3. $\beta$ form of 2,5-PEF

The crystal structure of the  $\beta$  form, which is generated by solvent-induced crystallization <sup>6</sup>, is displayed in Figure VI.3. Two planar molecules are contained in the monoclinic unit cell with a volume slightly bigger compared to the  $\alpha$  phase. Two flat chains lie parallel to the  $(a, c)$  plane, shifted by 0.4 units in the  $c$  axis direction.

The  $\beta$  form may be a good candidate for comparison with the structure of the strain-induced phase followed by in situ heat treatment, as reported by Stoclet et al. <sup>7</sup>.



**Figure VI.3:** 3D views of the chain arrangement in the unit cell of the  $\beta$  form of 2,5-PEF crystalline structures: (a) along the  $b$  axis; (b) projection onto the  $c$  axis; (c) projection onto the  $a$  axis. [Reproduced from <sup>4</sup>]

None of the crystalline structures observed for 2,5-PEF is isomorphous with respect to the crystal lattice of PET.

Besides, the dimensions of the unit cells are also different. Nevertheless, the chain packing in the  $\alpha$  form of 2,5-PEF is similar to the chain packing in the unit cell of PET <sup>4</sup>.

The presence of several polymorphs for 2,5-PEF, as compared to the fact that PET shows no polymorphism, could be associated with different factors, such as the intrinsic lower symmetry of the furan ring (5 atoms including one oxygen) with respect to the benzene ring (6 carbon atoms), which may generate different possible chain conformations, as well as the lower chain mobility due to the higher rigidity of the backbones containing a furanoate with respect to backbones containing a terephthalate <sup>8,9</sup>.

## VI.2. Comparison of PET and 2,5-PEF in terms of conformation

Araujo et al.<sup>9</sup> recently explored the chain conformation and dynamics of 2,5-PEF, both in the crystalline and amorphous regions, using a combination of vibrational spectroscopy and ab initio calculations. In the crystalline phase, the 2,5-PEF polymer chains arrange in an extended zig-zag arrangement. This strained  $\text{syn}^{\text{FDCA}}\text{trans}^{\text{EG}}$  conformation is unfeasible for single chains but advantageous as the chains arrange to form a crystal, since it enables the formation of an extensive array of C–H $\cdots$ O bonds which lock in place adjacent PEF segments. In the amorphous regions, the 2,5-PEF polymer chains tend to coil following a statistical distribution of possible microconformations, the most prevalent being the  $\text{anti}^{\text{FDCA}}\text{gauche}^{\text{EG}}$  helix. A significant energy difference separates the helical amorphous chain from the extended crystalline motif, almost 3 times the difference found for PET. This is why the crystallization temperature of 2,5-PEF is higher compared to PET, and the strain-induced crystallization requires higher stretching ratios. According to Araujo et al.<sup>9</sup>, the  $\alpha$  and  $\beta$  polymorphs are built from  $\text{syn}^{\text{FDCA}}\text{trans}^{\text{EG}}$  chains interlocked by C–H $\cdots$ O hydrogen bonds. The packing differences between the  $\alpha$  and  $\beta$  polymorphs reflect on the carbonyl stretching band profile, which can therefore be taken as a probe for the quick discrimination between 2,5-PEF polymorphs in highly crystalline samples. Araujo et al.<sup>9</sup> also showed, by recording Inelastic Neutron Scattering (INS) spectra, that the vibrational modes involving the furanic ring (the “ring flipping” mode) and the glycolic moiety (the “seesaw” mode) are related to a stiffer 2,5-PEF polymer chains, as compared to PET, which is a feature contributing to the lower gas permeability of 2,5-PEF.

### VI.3. Comparison of PET and 2,5-PEF in terms of thermal properties

Several values of the equilibrium enthalpy of melting can be found in the literature for PET ( $\Delta H_m^0 = 117.5$  J/g, 135.8 J/g, and 140 J/g)<sup>10,11</sup>. Groeninckx et al.<sup>12</sup> used the Hoffman-Weeks method to determine the equilibrium melting temperature  $T_m^0 = 290$  °C for PET crystals made of fully extended polymer chains, and demonstrated by WAXS and SAXS that the melting temperature increases only as a function of the lamellar thickening, because no alternative crystalline phases were formed. The same paper reported that fully annealed PET can reach a maximum degree of crystallinity of 60%. In a study on isothermal melt crystallization kinetics, the transition from primary to secondary crystallization was found to occur at 35-40% crystallinity, with a maximum rate of crystalline growth recorded at 175 °C<sup>13</sup>. However, many examples from the literature show how the crystal parameters and crystallization kinetics of PET can be influenced by catalyst residues and by the possible presence of co-monomers, which highlights the importance of the polymerization route on the observed behavior of the final polymer<sup>14,15</sup>.

Several values of the equilibrium enthalpy of melting have also been recently reported in the literature for 2,5-PEF ( $\Delta H_m^0 = 109$  J/g, 137 J/g, 140 J/g and 185 J/g)<sup>5,16-18</sup>. The theoretical melting temperature for 2,5-PEF crystals made of fully extended polymer chains has also been reported with different values ( $T_m^0 = 240, 247$  and 265 °C)<sup>19,20</sup>. Knoop et al.<sup>19</sup> presented some preliminary results about the crystallization kinetics of 2,5-PEF, and recorded a maximum rate of crystalline growth at 150 °C. On the basis of the Hoffman-Lauritzen's theory, Papageorgiou et al.<sup>17</sup> suggested a temperature of 165 °C. Clearly, a deeper investigation is required to elucidate the crystallization behavior and the characteristic temperature ranges for 2,5-PEF, especially because of the marked polymorphism reported for furan-based polyesters.

## VI.4. Study of the crystallization kinetics

### VI.4.1. DSC analyses

Studying the crystallization kinetics requires to monitor the development of crystals, i.e. to quantify the degree of crystallinity  $X_c$ , as a function of the crystallization time  $t_c$ . In the literature, Codou et al.<sup>20</sup> focused on the non-isothermal crystallization kinetics of 2,5-PEF by comparing the crystallization kinetics from the glassy and the molten state, they found that even if crystals show similar structures, different growth dynamics are observed. Stoclet et al.<sup>5</sup> focused in a first time, in isothermal crystallization from the two state with a variation of  $T_c$  and keeping  $t_c$  constant (1h) and a second time by keeping  $T_c$  constant (160 °C) with a variation of  $t_c$  but only from the molten state. In our case, DSC analyses were performed on PEFs samples crystallized at 140 °C both from the glassy and the molten state (by crossing or not the temperature zones where the nucleation is favored) during different annealing times ranging from 0 minutes to 7200 minutes, according to the protocols reported in [Figure VI.4](#).

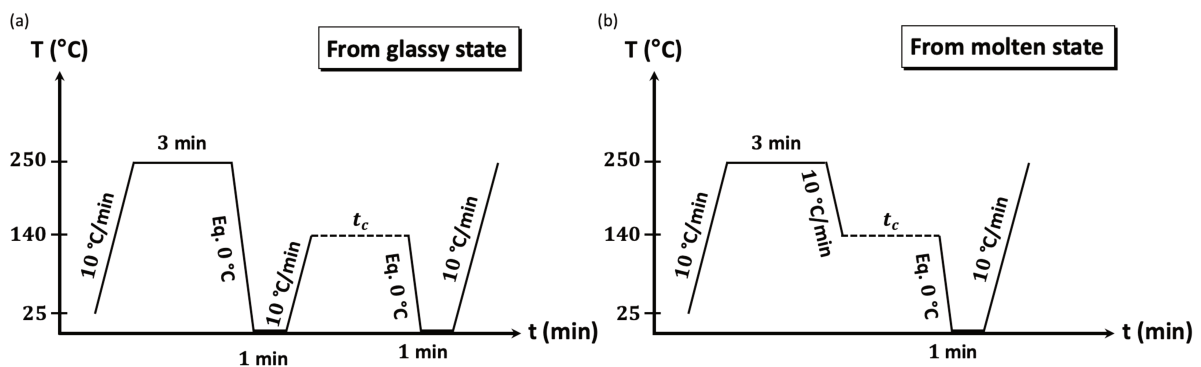


**Figure VI.4:** Schematic representation of the DSC protocols used for the analysis of PEFs crystallization kinetics from (a) the glassy state and (b) the molten state.

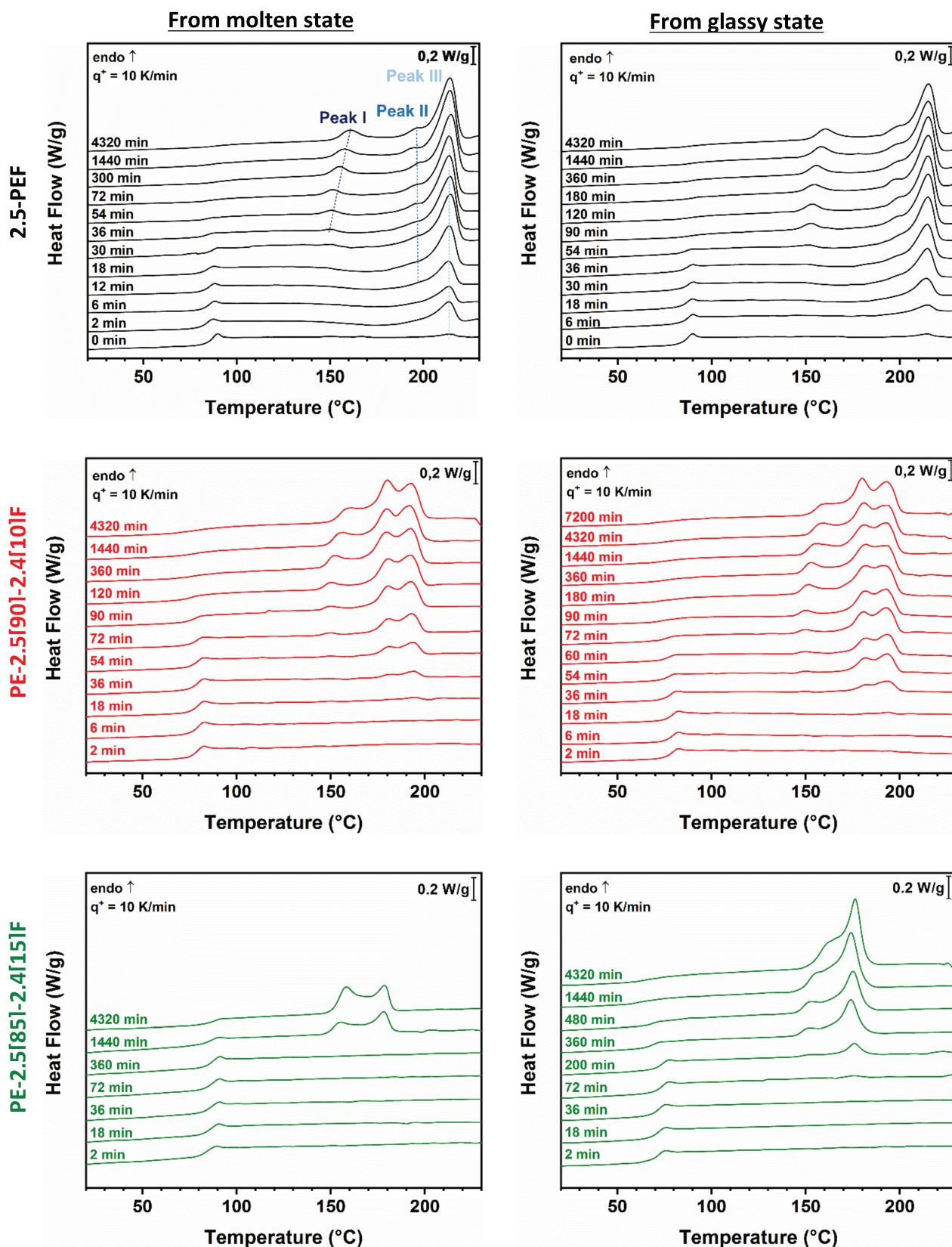
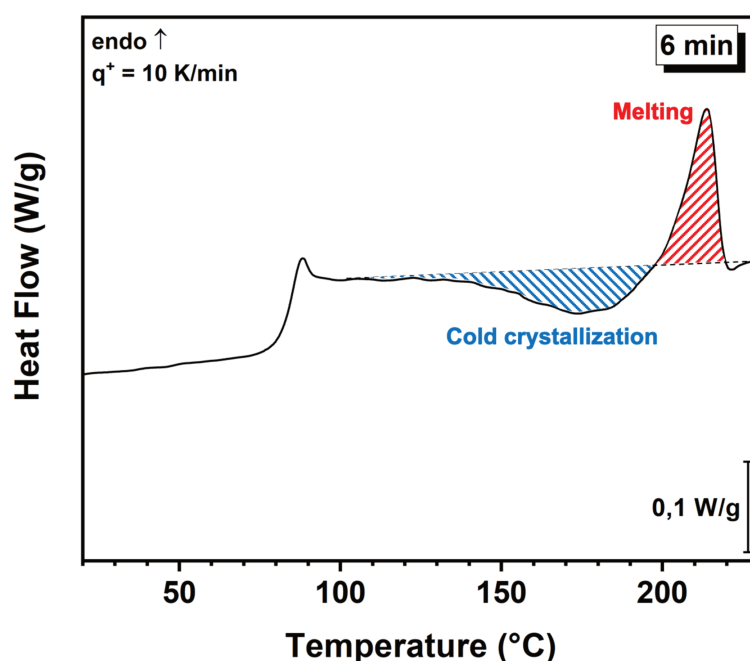


Figure VI.5: DSC thermograms recorded on 2,5-PEF (black), PE-2,5[90]-2,4[10]F (red) and PE-2,5[85]-2,4[15]F (green) from the molten state (on the left) and from the glassy state (on the right) after different crystallization times at 140 °C with a heating rate of 10 °C/min.

The results shown in Figure VI.5 reveal that three distinct behaviors are observed as a function of the annealing time, which can be distinguished by considering the evolution of the crystallinity (Figure VI.8). The first behavior is observed exclusively for 2,5-PEF at annealing times shorter than 10 minutes, and is characterized by the presence of both an exothermic and endothermic peak (see the zoom in Figure VI.6) whose respective areas increase with increasing crystallization time. The exothermic peak can be associated to cold crystallization and partially overlaps the endothermic peak associated with melting. The height of the heat capacity step at the glass transition suggests that the sample at  $T \sim 100$  °C is totally amorphous, indicating that no crystals were formed during the previous step of isothermal crystallization.



**Figure VI.6:** Zoom on one of the DSC thermograms of Figure IV.2, recorded with a heating rate of 10 °C/min for 2,5-PEF crystallized from the molten state during 6 minutes at 140 °C.

In the temperature region where melting is expected, only the highest temperature peak is observed (identified as peak III in Figure VI.5). The association of exothermic and endothermic peaks is not observed for PE-2,5[90]-2,4[10]F and PE-2,5[85]-2,4[15]F, which proves that both these samples remain amorphous in spite of the protocol for isothermal crystallization, and that even an increase in temperature does not allow the crystals formation during the heating scan. The second behavior is observed for annealing times ranging from 10 to 100 min for 2,5-PEF, and consist in a decrease in the area associated with cold crystallization as the crystallization time increases (Figure VI.7), while the area associated with the endothermic complex peaks keeps on increasing.



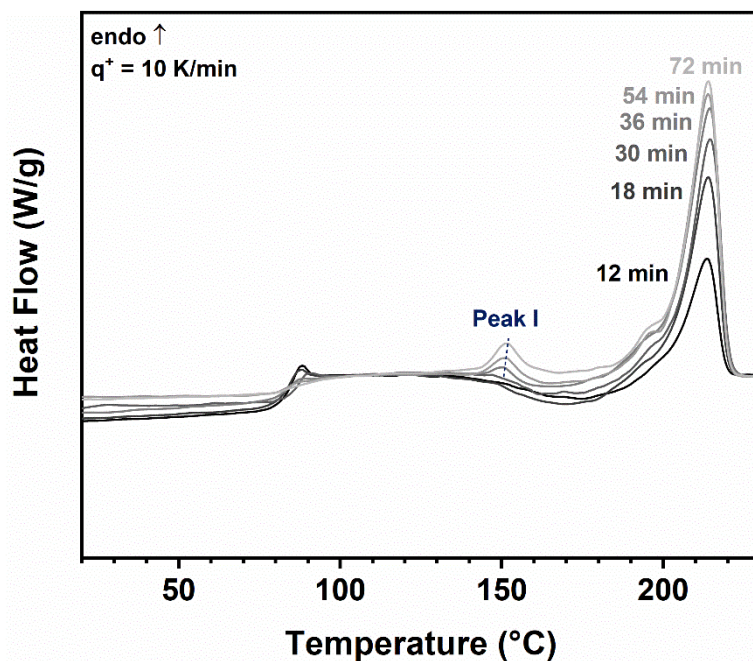


Figure VI.7: Zoom on some of the thermograms of Figure VI.5, recorded with a heating rate of 10 °C/min for 2,5-PEF crystallized from the molten state during 12 to 72 minutes at 140 °C.

For PE-2,5[90]-2,4[10]F, the second behavior is observed for annealing times ranging from approximately 30 to 300 min; for PE-2,5[85]-2,4[15]F, it is observed for annealing times ranging from approximately 100 to 1 000 min when the crystallization is performed from the glassy state, and approximately 1 000 to 10 000 min when the crystallization is performed from the molten state.

Furthermore, a small endothermic peak appears around 150 °C (denoted as peak I in Figure VI.5), whose area steadily increases with time while its position remains almost constant. Finally, for crystallization times above 100 min (2,5-PEF), 300 min (PE-2,5[90]-2,4[10]F), 1 000 min (PE-2,5[85]-2,4[15]F from the glassy state), and 10 000 min (PE-2,5[85]-2,4[15]F from the molten state), the area of the three endothermic peaks reaches a maximum value, indicating that the samples reached their maximum crystallinity.

The crystalline morphology of 2,5-PEF upon isothermal crystallization was reported as being spherulitic<sup>21</sup>, which was also confirmed in this work as shown later on (Figure VI.9).

Considering a standard nucleation-growth model for the description of the isothermal crystallization behavior of PEF, Stoclet et al.<sup>5</sup> described the crystallization behavior by distinguishing 3 regions:

- Region I, corresponding to nucleation;
- Region II, corresponding to crystal growth;
- Region III, characterized by a slight increase in crystallinity and accompanied by an evolution of the perfection degree of secondary crystals as the material reaches a crystallinity value of approximately 40%.

As the crystallization time increases, the heat capacity step at the glass transition  $\Delta c_p$  decreases in intensity (Figure VI.5 and VI.7), which means that a progressively smaller amount of sample undergoes the glass transition, the rest being consumed by the crystal growth during the annealing step. At the same time, the area below the crystallization peak decreases because the mass of sample available for cold crystallization upon heating is also reduced.

To explain the presence of multiple melting endotherms, several hypothesis can be made: of the crystallization process originated more than one crystallographic form (polymorphism); the crystals formed during the annealing step are not perfect and undergo a melting-crystallization-melting process during which the crystalline lamellae thicken and crystalline imperfections are fixed; if the polymer chains got stuck in the growing crystalline structure in a conformation which is unstable, upon heating there may be a change in orientation and/or conformation of the macromolecular segments within the lamellae; sometimes, complex melting behavior can be ascribed to a distribution of crystal sizes related to specific distributions of the molecular weight<sup>22-24</sup>. The most likely hypothesis is that none of these mechanisms alone can explain the presence of multiple endotherms, but a combination of several parameters that require further investigations<sup>25</sup>.

The thermal behavior observed during the melting of 2,5-PEF is complex and strongly depends on the crystallization temperature  $T_c$ . Stoclet et al.<sup>5</sup> suggested the existence of a critical value of  $T_c \approx 170$  °C where a major change in the crystallization mechanisms occurs. For crystallization at  $T_c < 170$  °C, the main melting peak has a double contribution (peaks II and III), whereas a single peak (peak II) is observed after crystallization at  $T_c \geq 170$  °C.

The observation of peaks II and III during melting may be due to the fact that in the low range of  $T_c$  the  $\alpha'$  form is formed, which is more defective than the  $\alpha$  form. The first peak (peak I) is observed only after crystallizations at  $T_c < 170$  °C, and at a temperature slightly above the crystallization temperature. As proposed by Papageorgiou et al.<sup>17</sup> and by analogy with PET<sup>25,26</sup>, its origin could be associated to the melting of secondary crystals, which are small and imperfect. These crystals have thinner lamellae due to the physical hindrance experienced during their formation because of a condition of lower mobility, and therefore melt at a lower temperature. By WAXD, Stoclet et al.<sup>5</sup> associate the Peaks II and III to a melting-recrystallization process and not to a crystal transformation (from the  $\alpha'$  form to the  $\alpha$  form) upon heating.

Regarding the influence of the position of the carbonyl group on the furan ring: as expected, when the ratio of 2,4-FDCA DME increases the time necessary (induction time) for the crystallization to occur in isothermal conditions increases. Concerning the position of the melting peaks: peak I remains relatively constant whatever the ratio of 2,5/2,4-FDCA DME, however when the ratio of 2,5-FDCA DME decreases peaks II and III are shifted to lower temperatures. For 2,5-PEF and PE-2,5[90]-2,4[10]F crystallized at 140 °C, the three peaks can be easily distinguished, revealing the presence of the  $\alpha'$  phase (disordered crystalline phase). However, in the case of PE-2,5[85]-2,4[15]F, only two endothermic peaks can be distinguished and likely attributed to a superposition of peaks I and II, that are quite close to peak III, or eventually to a modification of the crystalline form upon heating. This point will be further discussed later in the manuscript in the light of the structural characterizations.

#### VI.4.2. Crystallization kinetics

The crystalline fraction of a semi-crystalline polymer is generally calculated using the following equation:

$$X_c = \frac{\Delta H_m - \Delta H_{cc}}{\Delta H_m^0} \quad (\text{VI.1})$$

Where  $\Delta H_m$  is the enthalpy of melting measured by DSC,  $\Delta H_m^0$  is the equilibrium enthalpy of melting for of an ideal fully crystalline sample ( $\Delta H_m^0 = 140$  J/g for 2,5-PEF<sup>5</sup>) and  $\Delta H_{cc}$  is the enthalpy associated to cold crystallization measured by DSC.

The DSC curves detailed in the previous section, combined with the calculation of the crystallinity degree of each sample (Equation VI.1), allowed to build the curves representing the crystallization kinetics of all the considered PEFs samples, both from the glassy and the molten states. The obtained sigmoidal curves are presented in Figure VI.8.

The comparison of the crystallization kinetics can be done considering two parameters: the maximum crystallinity reached at the longest annealing times  $X_{c\ max}$  and the half-crystallization time  $t_{1/2}$  (i.e. the time required for the crystal to occupy half of the volume that can be eventually crystallized when the process has reached its maximum). These parameters are given in Table VI.2 for all the considered samples, for both the crystallization protocols (from the glassy and the molten states).

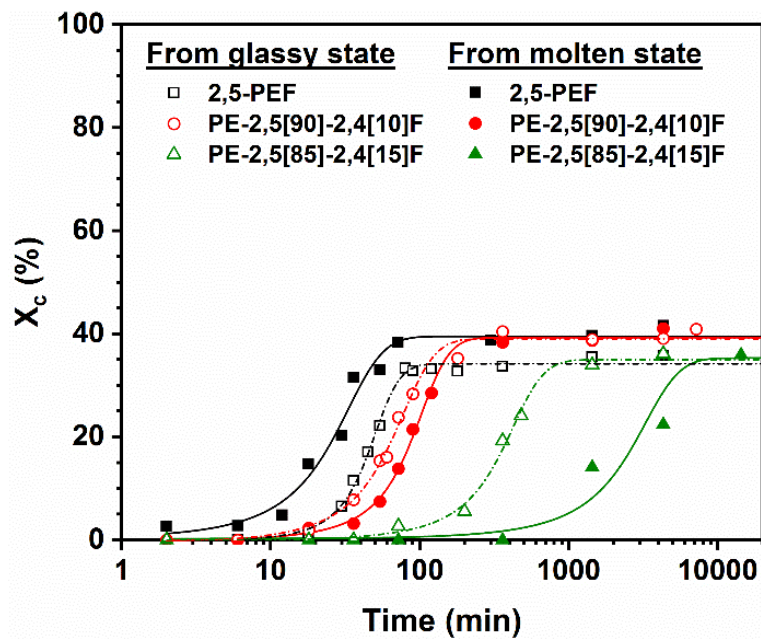


Figure VI.8: Evolution of crystallinity as a function of the annealing time for 2,5-PEF, PE-2,5[90]-2,4[10]F and PE-2,5[85]-2,4[15]F maintained in isothermal conditions at  $T_c = 140$  °C from the glassy state (hollow symbols) and from the molten state (filled symbols).

**Table VI.2: Maximum crystallinity degree ( $X_{c\ max}$ ) and half-crystallization time ( $t_{1/2}$ ) of PEFs samples after crystallization at 140 °C from the molten and the glassy states.**

	From molten state		From glassy state	
	$X_{c\ max}$ (%)	$t_{1/2}$ (min)	$X_{c\ max}$ (%)	$t_{1/2}$ (min)
2,5-PEF	39 ± 2	23 ± 5	34 ± 1	45 ± 2
PE-2,5[90]-2,4[10]F	39 ± 1	86 ± 3	39 ± 1	60 ± 5
PE-2,5[85]-2,4[15]F	35 ± 4	2326 ± 600	35 ± 1	337 ± 25

All the considered PEF samples reach a similar value of the maximum crystallinity degree for a given crystallization temperature, whatever their initial physical state (glassy vs. molten). The parameter making a difference between the considered PEF samples is the crystallization time that one should wait to reach  $X_{c\ max}$ . Obviously, the half crystallization time follows the same trend and increases when the amount of 2,4-FDCA-based isomers increases. 100 min is the time that one should wait to observe the beginning of crystallization (induction time) for PE-2,5[85]-2,4[15]F annealed at 140 °C. It is quite reasonable to assume that this difference is due to the asymmetry of 2,4-FDCA DME with respect to 2,5-FDCA DME, which is a sort of disadvantage for the polymer chains to align and fold, thus delaying (and eventually preventing) crystallization. Figure IV.5 also shows that PEF copolymers crystallize faster from the glassy state compared to the molten state. This difference is most likely due to germination, which is favored at low temperature and therefore is enhanced when the samples are cooled down to the glassy state and then heated up again to the cold-crystallization temperature range. For a deeper understanding, it could be interesting to study the evolution of crystallinity at different temperatures, both from the glassy and the molten states.

### VI.4.3. Morphology and growth of spherulites

The spherulitic growth of 2,5-PEF was also monitored by POM under isothermal conditions. The copolymers, however, develop spherulites that are too small to be observed by POM. Figure VI.9 shows a few pictures of the spherulites developed in 2,5-PEF during isothermal crystallization from the molten state.

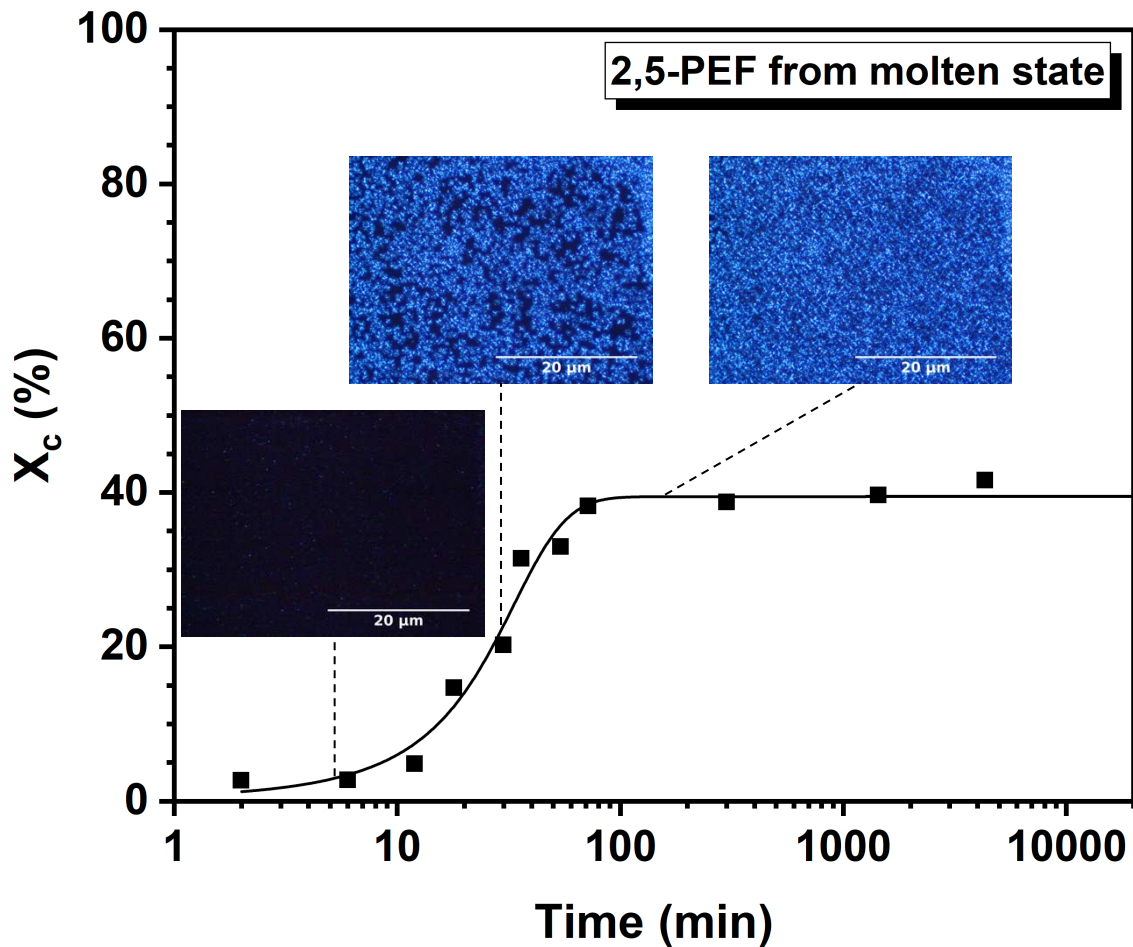


Figure VI.9: Crystallization kinetics of 2,5-PEF recorded by annealing the sample at 140 °C from the molten state. The inset pictures were taken by Polarizing Optical Microscopy at different crystallization times.

As the crystallization progresses, the crystallinity degree gradually increases as a result of a competition between germination and growth (the growth of the spherulites occurs simultaneously with the appearance of new spherulites). When the maximum crystallinity degree is reached, the spherulites percolate through the sample and occupy the entire field of view, but it does not look like they got to confluence. The average diameter of the spherulites was found to be very small (approximately 1  $\mu\text{m}$ ), whatever the selected crystallization temperature  $T_c$ . Figure VI.10 shows an example of the images used to estimate the isothermal spherulitic growth rate ( $G$ ) at different crystallization temperatures ( $T_c = 140, 150, 160$  and  $170$  °C).

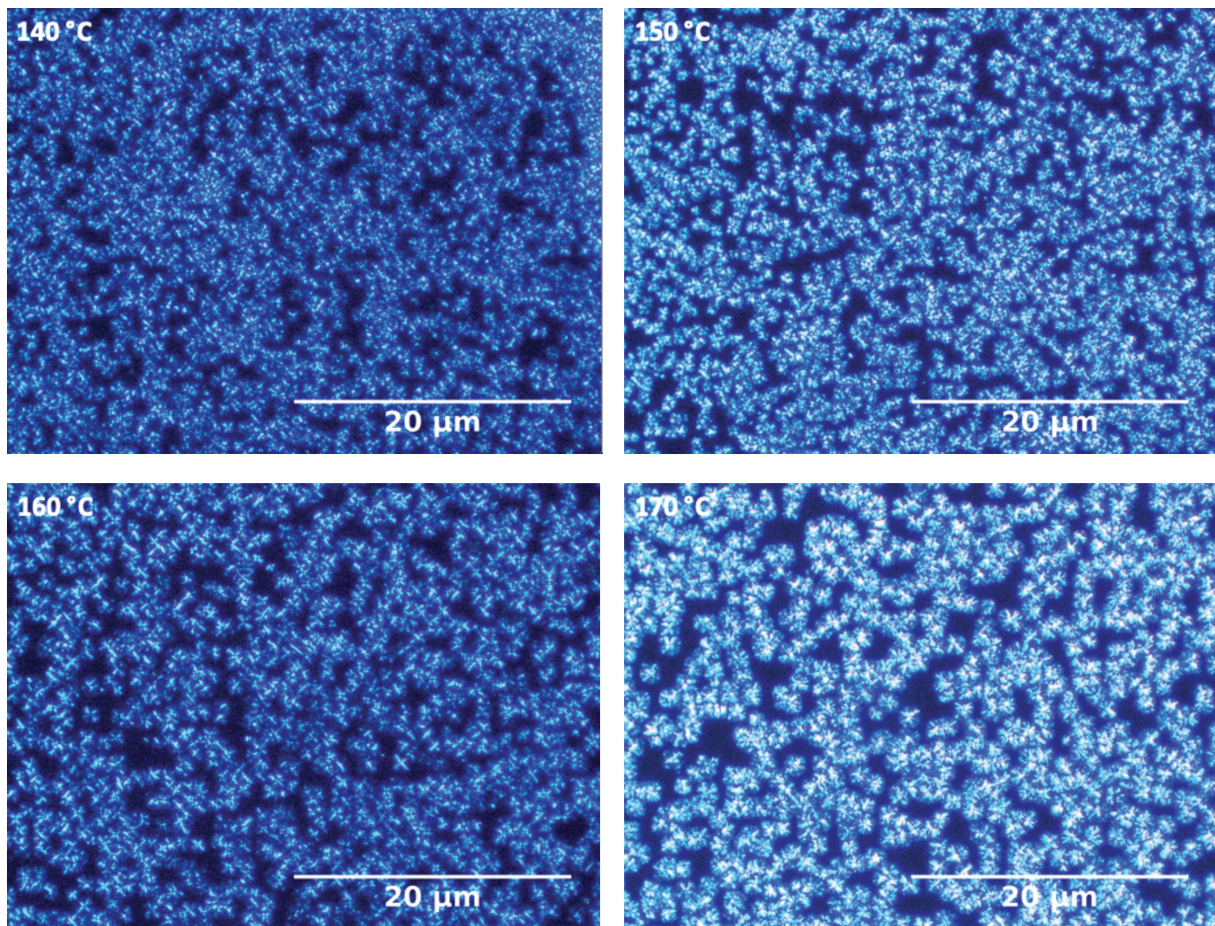
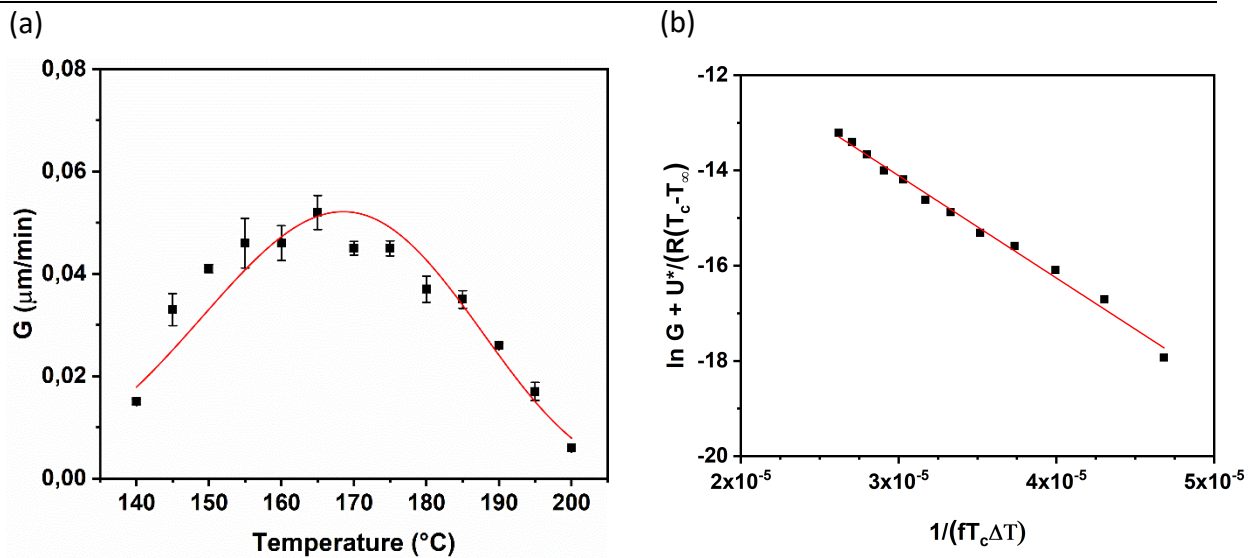


Figure VI.10: POM images showing the spherulites developed by 2,5-PEF at different crystallization temperatures ( $T_c=140, 150, 160$  and  $170$  °C). Crystallization was performed from the molten state.

By reiterating this method several times in isothermal conditions at different crystallization temperatures, the temperature dependence of the spherulitic growth rate  $G$  was obtained. Figure VI.11 (a) shows the typical bell-shaped curve  $G = f(T)$ , in total agreement with similar curves obtained for other synthetic polymers<sup>27</sup>. The maximum value of  $G$  is observed for a crystallization temperature close to  $170$  °C, in agreement with a previous work by van Berkel et al.<sup>18</sup>.



**Figure VI.11:** (a) Radial growth rate of spherulites ( $G$ ) developed by 2,5-PEF as a function of the crystallization temperature ( $T_c$ ), and (b) linearized Hoffmann-Lauritzen's equation for 2,5-PEF isothermally crystallized at different crystallization temperatures reached from the molten state.

The Hoffman-Lauritzen's theory (H-L theory) <sup>28</sup> was used to study the crystallization behavior of the 2,5-PEF (more details in [Chapter V](#)). The H-L theory states that the crystallization process can be described by three different growth regimes depending on the degree of supercooling ( $T_m - T_c$ ), where  $T_m$  and  $T_c$  are the melting and crystallization temperatures, respectively. In particular, the growth is supposed to progress through successive nucleation steps occurring on the surfaces of the growing crystals <sup>29</sup>. Regime I is typically observed when  $T_c$  is close to  $T_m$ . In this case, the growth rate  $G$  is proportional to the surface nucleation rate  $i$ , and the substrate completion rate  $g$  is higher than  $i$ . This means that any  $n^{\text{th}}$  layer of folded polymer chains is completed before the next  $(n + 1)^{\text{th}}$  layer is initiated. As  $T_c$  decreases with respect to  $T_m$ , a transition is observed from Regime I to Regime II. In Regime II,  $G$  is proportional to  $i^{1/2}$  and the rates  $g$  and  $i$  become comparable as a consequence of the rapid increase in the surface nucleation rate, itself associated with a higher degree of supercooling ( $T_m - T_c$ ). Several acts of nucleation take place at the same time and on the same crystalline surface, and the crystal growth proceeds even if a given layer of folded polymer chains is not yet completely filled. As  $T_c$  gets even lower with respect to  $T_m$ , another transition is observed from Regime II to Regime III. In Regime III, the growth rate  $G$  is controlled by  $i$  rather than by  $i^{1/2}$ . This means that there is a profusion of very small nuclei and the rate  $g$  is much lower or eventually nil. The growth front is extremely rough and irregular because of such an intensive



and multiple nucleation process. The H-L equation describes the radial growth rate of the spherulites as following:

$$G = G_0 e^{\left(\frac{-U^*}{R(T_c - T_\infty)}\right)} e^{\left(\frac{-K_g}{fT_c \Delta T}\right)} \quad (\text{VI.2})$$

Where  $G_0$  is an independent temperature constant,  $U^*$  is the activation energy for the transport phenomena of the crystallizable polymer segments,  $R = 8.314 \text{ J}/(\text{mol}\cdot\text{K})$  is the gas constant,  $T_c$  is the crystallization temperature,  $T_\infty$  is a hypothetical temperature where the molecular motions related to the viscous flow stop, defined as  $T_\infty = T_g - C$  ( in this case  $T_g = 82 \text{ }^\circ\text{C}$  ) and usually with  $C = 30 \text{ }^\circ\text{C}$ <sup>30</sup>,  $\Delta T = T_m^0 - T_c$  is the supercooling temperature with  $T_m^0$  is the equilibrium melting temperature determined from the Hoffman-Weeks routine as  $T_m^0 = 247 \text{ }^\circ\text{C}$ <sup>18</sup>,  $K_g$  is the nucleation constant and  $f$  is a parameter defined as:

$$f = 2T_c / (T_m^0 + T_c) \quad (\text{VI.3})$$

The software OriginPro 2018 was used for non-linear fittings of the experimental data, which provides the following values:  $U^* = 4\,865 \text{ J/mol}$  and  $K_g = 1.07 \times 10^5 \text{ K}^2$ .

By linearizing and rearranging the H-L equation, the following equation is obtained:

$$\ln(G) + \frac{U^*}{R(T_c - T_\infty)} = \ln(G_0) - \frac{K_g}{fT_c \Delta T} \quad (\text{VI.4})$$

By plotting  $\ln(G) + U^*/(R(T_c - T_\infty))$  as a function of  $1/(fT_c \Delta T)$  and by fixing  $U^* = 6\,270 \text{ J/mol}$  (typically taken as the universal value<sup>30</sup>), the nucleation constant is obtained from the slope ( $-K_g$ ) and the independent temperature constant is obtained from the intercept  $\ln(G_0)$ . **Figure VI.11 (b)** shows a single slope straight line which means that the growth regime is the same on the overall crystallization temperature range (140-200 °C). A value of  $2.15 \times 10^5 \text{ K}^2$  was obtained for the nucleation constant  $K_g$  and was in good agreement with the values obtained by Codou et al.<sup>20</sup> ( $3.16 \times 10^5 \text{ K}^2$ ) and van Berkel et al.<sup>18</sup> ( $2.8 \times 10^5 \text{ K}^2$ ) and PET values ( $K_g$  typically comprised ranging from  $1.9 \times 10^5$  to  $3.7 \times 10^5 \text{ K}^2$ <sup>26,31,32</sup>).

## VI.5. Characterization of the amorphous phase during crystallization

In most cases, semi-crystalline polymers cannot be described by a simple two-phase model associating an amorphous phase ( $X_{am}$ ) and a crystalline phase ( $X_c$ ), but is better described by a three-phase model dividing the amorphous phase into two amorphous fractions, the Mobile Amorphous Fraction (MAF) and the Rigid Amorphous Fraction (RAF). This approach has already been used by several authors to describe the microstructure of PET <sup>33–36</sup> and was recently applied by Stoclet et al. <sup>5</sup> to 2,5-PEF. In particular, the three phases generally admitted to describe the microstructure of semi-crystalline polymers have the following features:

- The MAF is defined as the amorphous fraction that relaxes at the glass transition and corresponds to the unconstrained amorphous polymer chains;
- The RAF is an amorphous fraction that cannot relax at the glass transition because it is constrained (by the crystals, for instance) and therefore devitrifies at temperatures generally comprised between  $T_g$  and  $T_m$ ;
- The crystalline phase is defined as usual, i.e. the fraction of polymer chains arranged in more or less regular structures in which the molecular mobility is dramatically reduced if not totally suppressed at  $T < T_m$ .

In general, the mobile amorphous fraction  $X_{am}$  is calculated from the value of  $\Delta C_p$  recorded at the glass transition using the following equation:

$$X_{am} = \frac{\Delta C_p}{\Delta C_p^0} \quad (\text{VI.5})$$

Where  $\Delta C_p$  is the heat capacity step at the glass transition for the semi-crystalline samples and  $\Delta C_p^0$  is the heat capacity step at the glass transition for the fully amorphous counterpart.

Whenever a discrepancy is observed leading to  $X_{am} + X_c < 1$  (with  $X_c$  calculated according to [Equation VI.1](#)), the calculations are adjusted by defining the rigid amorphous fraction as:

$$X_{ar} = 1 - (X_c + X_{am}) \quad (\text{VI.6})$$

Figure VI.12 shows the evolution of  $X_{am}$  and  $X_{ar}$  as a function of  $X_c$  for all the considered PEF samples crystallized both from the molten and the glassy state at the same crystallization temperature  $T_c = 140$  °C. It is clear that the increase in crystallinity is accompanied by the progressive formation of the rigid amorphous fraction.

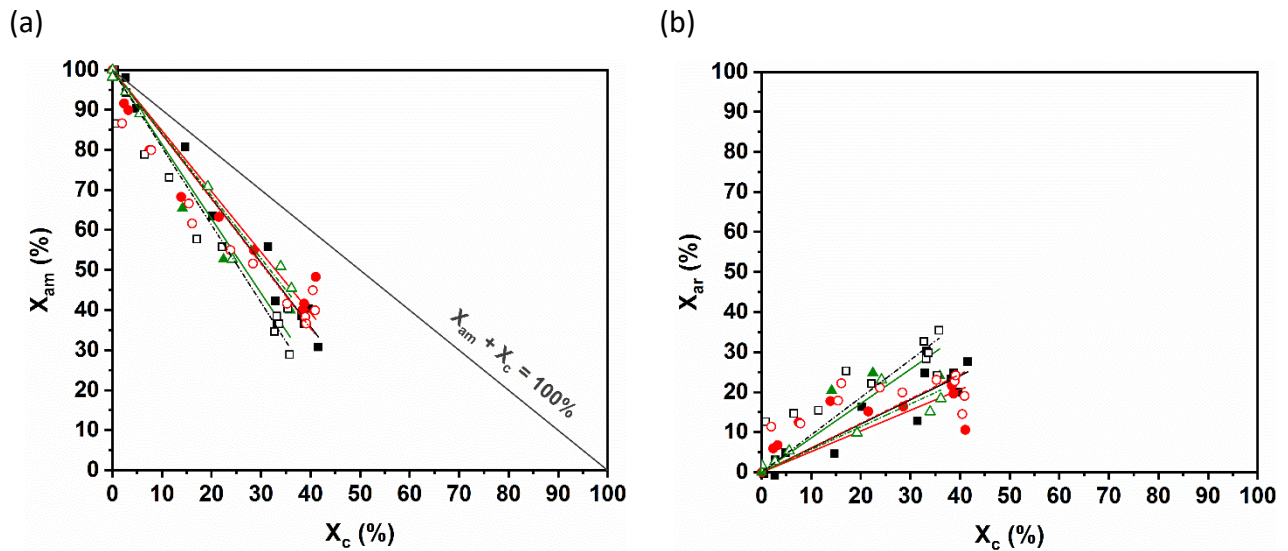


Figure VI.12: (a) Evolution of the mobile amorphous fraction ( $X_{am}$ ) and (b) the rigid amorphous fraction ( $X_{ar}$ ) as a function of the crystallinity ( $X_c$ ) for 2,5-PEF (black), PE-2,5[90]-2,4[10]F (red) and PE-2,5[85]-2,4[15]F (green) crystallized in isothermal conditions both from the glassy (hollow symbols) and the molten state (filled symbols).

It is noteworthy to point out that the crystallization process produces the same amount of crystals and constrained amorphous chains, for  $X_{am}$  and  $X_c$  both reach a maximum value of 35%). Similar results have already been reported for PET, for which a linear increase in  $X_{ar}$  with  $X_c$  was observed and explained by the fact that the polymer crystals confine the amorphous phase<sup>36</sup>. The presence of RAF, which is relatively stiffer in comparison with MAF, affect the properties of polymers. For example, previous studies showed that the RAF can be responsible of an increase in the elastic modulus like in PET<sup>33</sup>, Poly (1-Butene) (PB)<sup>37</sup>, Poly (Amide 6) (PA 6)<sup>38</sup> and Poly (Ethylene) (PE)<sup>39</sup> and can have a strong influence on the barrier properties like observed in PLA<sup>40,41</sup>.

## VI.6. Influence of the position of the carbonyl group with respect to the furan ring on the crystal structure

As previously detailed, 2,5-PEF chains can arrange in three different crystalline forms ( $\alpha$ ,  $\alpha'$  and  $\beta$ ), which can be distinguished thanks to WAXD experiments (Figure VI.13). The WAXD profiles for the  $\alpha$  and the  $\alpha'$  forms are very similar, the only difference being that the  $\alpha$  form shows sharper reflections as compared to the  $\alpha'$  form as well as an extra peak at  $2\theta = 19.3^\circ$  (obtained with a  $Cu_{K\alpha}$  radiation<sup>4</sup>). On the other hand, the  $\beta$  form exhibits five main reflections roughly positioned at the same angular values as the ones of the  $\alpha'$  form. However, they are much broader and have different relative intensities. There is also an additional low intensity reflection detectable around  $2\theta = 10^\circ$ <sup>4</sup>. Stoclet et al.<sup>5</sup> showed no significant influence of the crystallization pathway (from the molten or from the glassy state) on the intensity profile of WAXD results.

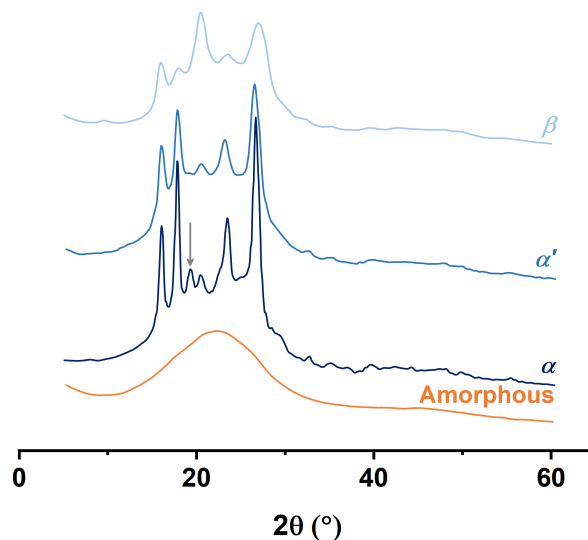


Figure VI.13: X-Ray diffraction patterns of 2,5-PEF reported by Maini et al.<sup>4</sup>.

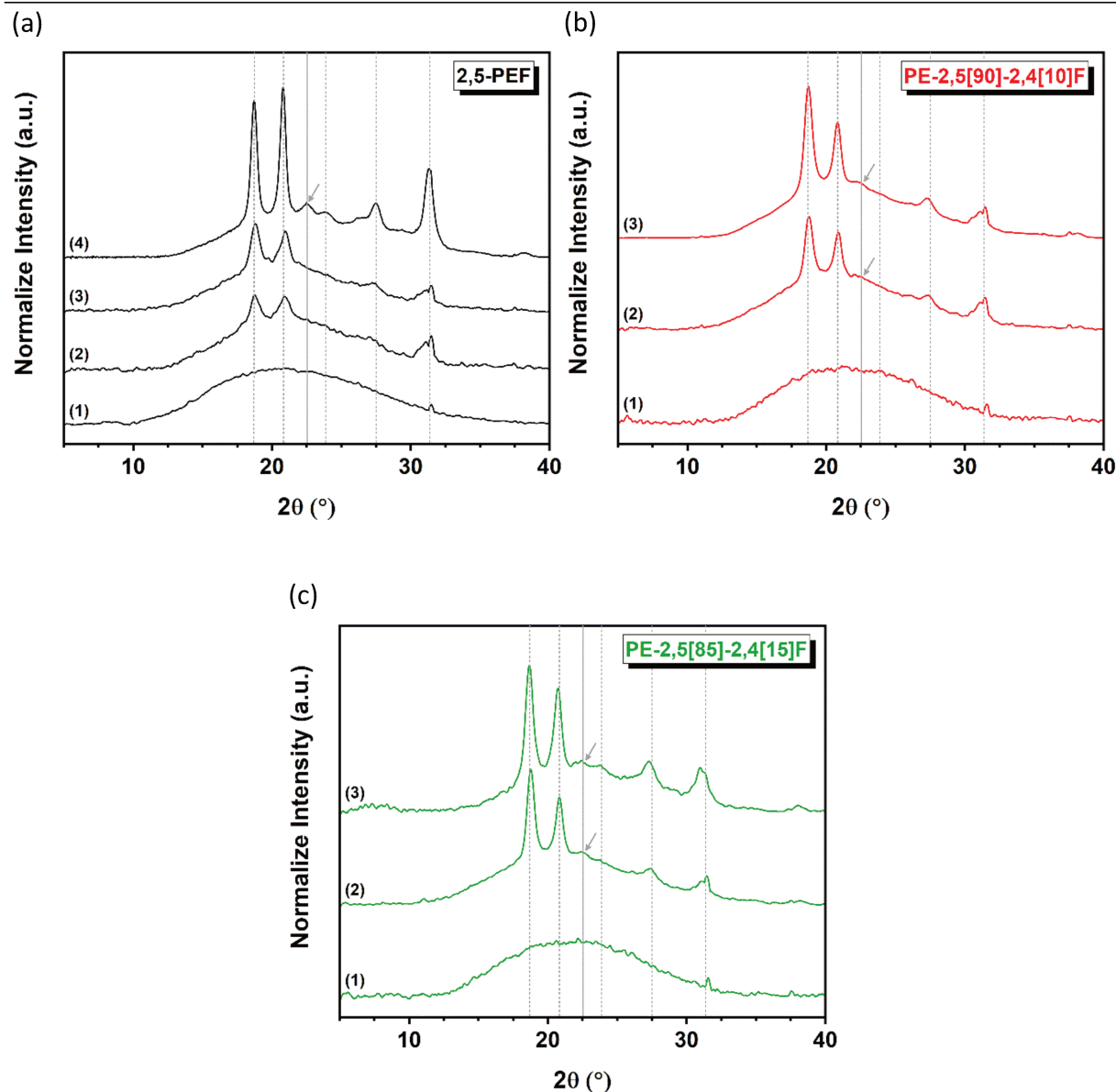


Figure VI.14: X-Ray diffraction patterns of (a) 2,5-PEF: (1) amorphous; (2)  $T_c = 140\text{ }^\circ\text{C}$  and  $t_c = 23\text{ min}$  from the molten state; (3)  $T_c = 140\text{ }^\circ\text{C}$  and  $t_c = 5\text{ h}$  from the molten state (4)  $T_c = 175\text{ }^\circ\text{C}$  and  $t_c = 45\text{ min}$  from the molten state; (b) PE-2,5[90]-2,4[10]F: (1) amorphous; (2)  $T_c = 140\text{ }^\circ\text{C}$  and  $t_c = 1\text{ h}26$  from the glassy state; (3)  $T_c = 140\text{ }^\circ\text{C}$  and  $t_c = 8\text{ h}20$  from the glassy state; (c) PE-2,5[85]-2,4[15]F: (1) amorphous; (2)  $T_c = 140\text{ }^\circ\text{C}$  and  $t_c = 38\text{ h}46$  from the molten state; (3)  $T_c = 140\text{ }^\circ\text{C}$  and  $t_c = 2\text{ j}2\text{ h}$  from the glassy state.

The integrated intensity profiles obtained for 2,5-PEF (Figure VI.14.a) are in agreement with the ones reported in the literature by other authors<sup>4,5,8,42,43</sup> and show the main diffraction peaks located at  $2\theta = 18.1^\circ$ ,  $2\theta = 20.9^\circ$ ,  $2\theta = 27.5^\circ$  and  $2\theta = 31.4^\circ$ . Compared to Figure VI.13, the peaks are shifted to higher degrees due to the different source used to generate the X-rays (Maini et al.<sup>4</sup> used  $\text{Cu}_{K\alpha}$  whereas the results in this work were obtained with  $\text{Co}_{K\alpha}$ ).

The WAXD analyses confirm that the crystalline form induced at  $T_c = 140$  °C (Figure VI.14.a (2) and (3)) differs from the one obtained at  $T_c = 175$  °C (Figure VI.14.a (4)). More specifically, the peak around  $2\theta = 22.5^\circ$  is not observed for 2,5-PEF at  $T_c = 140$  °C. Thus, the crystalline form grown during isothermal crystallization at  $T_c > 170$  °C is a reasonably “perfect” crystalline form of 2,5-PEF ( $\alpha$  form), whereas a slightly different (defective) form is grown at lower crystallization temperatures ( $\alpha'$  form).

The PE-2,5[90]-2,4[10]F (Figure VI.14.b) and PE-2,5[85]-2,4[15]F (Figure VI.14.c) samples crystallized at  $T_c = 140$  °C have a peak around  $2\theta = 22.5^\circ$ , therefore copolymers can also crystallize in the  $\alpha$  form. Looking at the DSC results reported in Figure VI.5 for PE-2,5[90]-2,4[10]F, three endothermic peaks are observed, which suggests that at the crystallization at  $T_c = 140$  °C produces both the  $\alpha$  and the  $\alpha'$  forms. In the case of PE-2,5[85]-2,4[15]F, only two peaks can be distinguished, which could correspond to the  $\alpha$  form of 2,5-PEF previously observed by Stoclet et al.<sup>5</sup> at lower crystallization temperature. One may conclude that, for this copolymer, two possibilities exist: either only the  $\alpha$  form is grown, or the two forms are grown as in the case of PE-2,5[90]-2,4[10]F, explaining the superposition of peaks I and II. As a perspective, it could be interesting to perform Fast Scanning Calorimetry (FSC) measurements because the use of fast scanning rates allows avoiding that the  $\alpha'$  form converts to the  $\alpha$  form. It would be even better if these measurements could be coupled with in situ DRX measurements as a function of the temperature.

To summarize, at  $T_c = 140$  °C, 2,5-PEF crystallizes in the  $\alpha'$  form, PE-2,5[90]-2,4[10]F crystallizes in the  $\alpha$  and  $\alpha'$  forms, and PE-2,5[85]-2,4[15]F crystallizes either exclusively in the  $\alpha$  form or in both.

The addition of 2,4-FDCA DME units into 2,5-FDCA DME based polymer chains can therefore be used to obtain the most stable crystalline phase typically observed for 2,5-PEF more easily and at lower crystallization temperatures.

## Conclusion

In this chapter, the influence of the position of the carbonyl group on the furan ring was evaluated in terms of crystallization behavior. The copolymerization of 2,5-FDCA DME units with 2,4-FDCA DME units leads to furan-based copolyesters with disturbed aptitude to crystallize (the copolymers are fully amorphous for 2,4-FDCA DME contents above 15%), a lower crystallinity rate (the half-crystallization time increases) but no significant decrease in the maximum crystallinity. The incorporation of 2,4-FDCA-based units into 2,5-PEF decreases the melting temperature (i.e. decreases the thickness of crystalline lamellae) and also increases the aptitude to form ordered crystals of 2,5-PEF.

## References

- (1) Daubeny, R. D. P.; Bunn, C. W.; Brown, C. J.; Bragg, W. L. The Crystal Structure of Polyethylene Terephthalate. *Proceedings of the Royal Society of London. Series A. Mathematical and Physical Sciences* **1954**, *226* (1167), 531–542.  
<https://doi.org/10.1098/rspa.1954.0273>.
- (2) Kazaryan, L. G.; Medvedeva, F. M. X-Ray Study of Poly (Ethylene Furan-2, 5-Dicarboxylate) Structure. *Vysokomol. Soedin. Ser. B Kratk. Soobshcheniya* **1968**, *10*, 305–306.
- (3) Mao, Y.; Bucknall, D. G.; Kriegel, R. M. Simultaneous WAXS/SAXS Study on Semi-Crystalline Poly(Ethylene Furanoate) under Uniaxial Stretching. *Polymer* **2018**, *143*, 228–236.  
<https://doi.org/10.1016/j.polymer.2018.04.018>.
- (4) Maini, L.; Gigli, M.; Gazzano, M.; Lotti, N.; Bikiaris, D. N.; Papageorgiou, G. Z. Structural Investigation of Poly(Ethylene Furanoate) Polymorphs. *Polymers* **2018**, *10* (3), 296.  
<https://doi.org/10.3390/polym10030296>.
- (5) Stoclet, G.; Gobius du Sart, G.; Yeniad, B.; de Vos, S.; Lefebvre, J. M. Isothermal Crystallization and Structural Characterization of Poly(Ethylene-2,5-Furanoate). *Polymer* **2015**, *72*, 165–176.  
<https://doi.org/10.1016/j.polymer.2015.07.014>.
- (6) Tsanaktsis, V.; Papageorgiou, D. G.; Exarhopoulos, S.; Bikiaris, D. N.; Papageorgiou, G. Z. Crystallization and Polymorphism of Poly(Ethylene Furanoate). *Crystal Growth & Design* **2015**, *15* (11), 5505–5512.  
<https://doi.org/10.1021/acs.cgd.5b01136>.
- (7) Stoclet, G.; Lefebvre, J. M.; Yeniad, B.; Gobius du Sart, G.; de Vos, S. On the Strain-Induced Structural Evolution of Poly(Ethylene-2,5-Furanoate) upon Uniaxial Stretching: An in-Situ SAXS-WAXS Study. *Polymer* **2018**, *134*, 227–241.  
<https://doi.org/10.1016/j.polymer.2017.11.071>.
- (8) Burgess, S. K.; Leisen, J. E.; Kraftschik, B. E.; Mubarak, C. R.; Kriegel, R. M.; Koros, W. J. Chain Mobility, Thermal, and Mechanical Properties of Poly(Ethylene Furanoate) Compared to Poly(Ethylene Terephthalate). *Macromolecules* **2014**, *47* (4), 1383–1391.  
<https://doi.org/10.1021/ma5000199>.
- (9) Araujo, C. F.; Nolasco, M. M.; Ribeiro-Claro, P. J. A.; Rudić, S.; Silvestre, A. J. D.; Vaz, P. D.; Sousa, A. F. Inside PEF: Chain Conformation and Dynamics in Crystalline and Amorphous Domains. *Macromolecules* **2018**, *51* (9), 3515–3526.  
<https://doi.org/10.1021/acs.macromol.8b00192>.
- (10) Jog, J. P. Crystallization of Polyethyleneterephthalate. *Journal of Macromolecular Science, Part C* **1995**, *35* (3), 531–553. <https://doi.org/10.1080/15321799508014598>.
- (11) Roland, C. M. High Temperature Crystallization of Poly(Ethylene Terephthalate). *Polymer Engineering & Science* **1991**, *31* (12), 849–854.  
<https://doi.org/10.1002/pen.760311202>.
- (12) Groeninckx, G.; Reynaers, H.; Berghmans, H.; Smets, G. Morphology and Melting Behavior of Semicrystalline Poly(Ethylene Terephthalate). I. Isothermally Crystallized PET. *J. Polym. Sci. Polym. Phys. Ed.* **1980**, *18* (6), 1311–1324.  
<https://doi.org/10.1002/pol.1980.180180612>.
- (13) Lin, S.-B.; Koenig, J. L. Spectroscopic Characterization of Solvent-Induced Crystallization of PET. *Journal of Polymer Science: Polymer Physics Edition* **1983**, *21* (8), 1539–1558.



- <https://doi.org/10.1002/pol.1983.180210820>.
- (14) Lawton, E. L. Nucleation of Crystallization of Polyester by Catalyst Remnants—a Review. *Polymer Engineering & Science* **1985**, *25* (6), 348–354.  
<https://doi.org/10.1002/pen.760250607>.
- (15) Hu, Y. S.; Hiltner, A.; Baer, E. Improving Oxygen Barrier Properties of Poly(Ethylene Terephthalate) by Incorporating Isophthalate. II. Effect of Crystallization. *Journal of Applied Polymer Science* **2005**, *98* (4), 1629–1642.  
<https://doi.org/10.1002/app.22214>.
- (16) Fosse, C.; Bourdet, A.; Ernault, E.; Esposito, A.; Delpouve, N.; Delbreilh, L.; Thiyagarajan, S.; Knoop, R. J. I.; Dargent, E. Determination of the Equilibrium Enthalpy of Melting of Two-Phase Semi-Crystalline Polymers by Fast Scanning Calorimetry. *Thermochimica Acta* **2019**, *677*, 67–78.  
<https://doi.org/10.1016/j.tca.2019.03.035>.
- (17) Papageorgiou, G. Z.; Tsanaktsis, V.; Bikiaris, D. N. Synthesis of Poly(Ethylene Furandicarboxylate) Polyester Using Monomers Derived from Renewable Resources: Thermal Behavior Comparison with PET and PEN. *Phys. Chem. Chem. Phys.* **2014**, *16* (17), 7946–7958.  
<https://doi.org/10.1039/C4CP00518J>.
- (18) van Berkel, J. G.; Guigo, N.; Kolstad, J. J.; Sipos, L.; Wang, B.; Dam, M. A.; Sbirrazzuoli, N. Isothermal Crystallization Kinetics of Poly (Ethylene 2,5-Furandicarboxylate). *Macromol. Mater. Eng.* **2015**, *300* (4), 466–474.  
<https://doi.org/10.1002/mame.201400376>.
- (19) Knoop, R. J. I.; Vogelzang, W.; van Haveren, J.; van Es, D. S. High Molecular Weight Poly(Ethylene-2,5-Furanoate); Critical Aspects in Synthesis and Mechanical Property Determination. *J. Polym. Sci. Part A: Polym. Chem.* **2013**, *51* (19), 4191–4199.  
<https://doi.org/10.1002/pola.26833>.
- (20) Codou, A.; Guigo, N.; van Berkel, J.; de Jong, E.; Sbirrazzuoli, N. Non-Isothermal Crystallization Kinetics of Biobased Poly(Ethylene 2,5-Furandicarboxylate) Synthesized via the Direct Esterification Process. *Macromol. Chem. Phys.* **2014**, *215* (21), 2065–2074.  
<https://doi.org/10.1002/macp.201400316>.
- (21) Papageorgiou, G. Z.; Papageorgiou, D. G.; Terzopoulou, Z.; Bikiaris, D. N. Production of Bio-Based 2,5-Furan Dicarboxylate Polyesters: Recent Progress and Critical Aspects in Their Synthesis and Thermal Properties. *European Polymer Journal* **2016**, *83*, 202–229.  
<https://doi.org/10.1016/j.eurpolymj.2016.08.004>.
- (22) Okazaki, I.; Wunderlich, B. Reversible Local Melting in Polymer Crystals. *Macromol. Rapid Commun.* **1997**, *18* (4), 313–318.  
<https://doi.org/10.1002/marc.1997.030180407>.
- (23) HOBBS, S.; SY, H.; CF, P. MULTIPLE MELTING IN POLY (BUTYLENE TEREPHTHALATE). *MULTIPLE MELTING IN POLY (BUTYLENE TEREPHTHALATE)* **1975**.
- (24) Medellin-Rodriguez, F. J.; Phillips, P. J.; Lin, J. S.; Campos, R. The Triple Melting Behavior of Poly(Ethylene Terephthalate): Molecular Weight Effects. *Journal of Polymer Science Part B: Polymer Physics* **1997**, *35* (11), 1757–1774.  
[https://doi.org/10.1002/\(SICI\)1099-0488\(199708\)35:11<1757::AID-POLB9>3.0.CO;2-P](https://doi.org/10.1002/(SICI)1099-0488(199708)35:11<1757::AID-POLB9>3.0.CO;2-P).

- (25) Kong, Y.; Hay, J. N. Multiple Melting Behaviour of Poly(Ethylene Terephthalate). *Polymer* **2003**, *44* (3), 623–633.  
[https://doi.org/10.1016/S0032-3861\(02\)00814-5](https://doi.org/10.1016/S0032-3861(02)00814-5).
- (26) Lu, X. F.; Hay, J. N. Isothermal Crystallization Kinetics and Melting Behaviour of Poly(Ethylene Terephthalate). *Polymer* **2001**, *42* (23), 9423–9431.  
[https://doi.org/10.1016/S0032-3861\(01\)00502-X](https://doi.org/10.1016/S0032-3861(01)00502-X).
- (27) Hannay, N. B. *Treatise on Solid State Chemistry: Volume 3 Crystalline and Noncrystalline Solids*; Springer US: Boston, MA, 1976.
- (28) Hoffman, J. D.; Frolen, L. J.; Ross, G. S.; Lauritzen, J. I. Growth-Rate of Spherulites and Axialites from Melt in Polyethylene Fractions-Regime-1 and Regime-2 Crystallization. *Journal of Research of the National Bureau of Standards Section a-Physics and Chemistry* **1975**, *79* (6), 671–699.
- (29) Mark, J.; Ngai, K.; Graessley, W.; Mandelkern, L.; Samulski, E.; Wignall, G.; Koenig, J. *Physical Properties of Polymers*; Cambridge University Press, 2004.
- (30) Hoffman, J. D.; Davis, G. T.; Lauritzen, J. I. The Rate of Crystallization of Linear Polymers with Chain Folding. In *Treatise on Solid State Chemistry: Volume 3 Crystalline and Noncrystalline Solids*; Hannay, N. B., Ed.; Springer US: Boston, MA, 1976; pp 497–614.  
[https://doi.org/10.1007/978-1-4684-2664-9\\_7](https://doi.org/10.1007/978-1-4684-2664-9_7).
- (31) Vyazovkin, S.; Sbirrazzuoli, N. Isoconversional Approach to Evaluating the Hoffman–Lauritzen Parameters ( $U^*$  and  $K_g$ ) from the Overall Rates of Nonisothermal Crystallization. *Macromolecular Rapid Communications* **2004**, *25* (6), 733–738.  
<https://doi.org/10.1002/marc.200300295>.
- (32) Chan, T. W.; Isayev, A. I. Quiescent Polymer Crystallization: Modelling and Measurements. *Polymer Engineering & Science* **1994**, *34* (6), 461–471.  
<https://doi.org/10.1002/pen.760340602>.
- (33) Di Lorenzo, M. L.; Righetti, M. C.; Cocca, M.; Wunderlich, B. Coupling between Crystal Melting and Rigid Amorphous Fraction Mobilization in Poly(Ethylene Terephthalate). *Macromolecules* **2010**, *43* (18), 7689–7694.  
<https://doi.org/10.1021/ma101035h>.
- (34) Hamonic, F.; Prevosto, D.; Dargent, E.; Saiter, A. Contribution of Chain Alignment and Crystallization in the Evolution of Cooperativity in Drawn Polymers. *Polymer* **2014**, *55* (12), 2882–2889.  
<https://doi.org/10.1016/j.polymer.2014.04.030>.
- (35) Righetti, M. C.; Laus, M.; Di Lorenzo, M. L. Rigid Amorphous Fraction and Melting Behavior of Poly(Ethylene Terephthalate). *Colloid Polym Sci* **2014**, *292* (6), 1365–1374.  
<https://doi.org/10.1007/s00396-014-3198-8>.
- (36) Arnoult, M.; Dargent, E.; Mano, J. F. Mobile Amorphous Phase Fragility in Semi-Crystalline Polymers: Comparison of PET and PLLA. *Polymer* **2007**, *48* (4), 1012–1019.  
<https://doi.org/10.1016/j.polymer.2006.12.053>.
- (37) Di Lorenzo, M. L.; Righetti, M. C. The Three-Phase Structure of Isotactic Poly(1-Butene). *Polymer* **2008**, *49* (5), 1323–1331.  
<https://doi.org/10.1016/j.polymer.2008.01.026>.
- (38) Kolesov, I.; Androsch, R. The Rigid Amorphous Fraction of Cold-Crystallized Polyamide 6. *Polymer* **2012**, *53* (21), 4770–4777.  
<https://doi.org/10.1016/j.polymer.2012.08.017>.

- (39) Martín, S.; Expósito, M. T.; Vega, J. F.; Martínez-Salazar, J. Microstructure and Properties of Branched Polyethylene: Application of a Three-Phase Structural Model. *Journal of Applied Polymer Science* **2013**, *128* (3), 1871–1878.  
<https://doi.org/10.1002/app.38290>.
- (40) Guinault, A.; Sollogoub, C.; Ducruet, V.; Domenek, S. Impact of Crystallinity of Poly(Lactide) on Helium and Oxygen Barrier Properties. *European Polymer Journal* **2012**, *48* (4), 779–788.  
<https://doi.org/10.1016/j.eurpolymj.2012.01.014>.
- (41) Delpouve, N.; Stoclet, G.; Saiter, A.; Dargent, E.; Marais, S. Water Barrier Properties in Biaxially Drawn Poly(Lactic Acid) Films. *J. Phys. Chem. B* **2012**, *116* (15), 4615–4625.  
<https://doi.org/10.1021/jp211670g>.
- (42) Jiang, M.; Liu, Q.; Zhang, Q.; Ye, C.; Zhou, G. A Series of Furan-Aromatic Polyesters Synthesized via Direct Esterification Method Based on Renewable Resources. *J. Polym. Sci. A Polym. Chem.* **2012**, *50* (5), 1026–1036.  
<https://doi.org/10.1002/pola.25859>.
- (43) Gandini, A.; Silvestre, A. J. D.; Neto, C. P.; Sousa, A. F.; Gomes, M. The Furan Counterpart of Poly(Ethylene Terephthalate): An Alternative Material Based on Renewable Resources. *J. Polym. Sci. A Polym. Chem.* **2009**, *47* (1), 295–298.  
<https://doi.org/10.1002/pola.23130>.

## Conclusions and Prospects

The aim of this work was to study the properties of new biopolyesters based on FuranDiCarboxylic Acid (FDCA) as a function of the positional isomerism of their repeating unit, i.e. the position of the carbonyl group on the furan ring. The study focused on the two main isomers of FDCA, i.e. 2,5-FDCA that is currently used to obtain Poly (Ethylene-2,5-Furanoate) (2,5-PEF), and 2,4-FDCA, which can be used to obtain Poly (Ethylene-2,4-Furanoate) (2,4-PEF) with extremely slow crystallization kinetics.

This work was articulated in two main sections:

The first section consisted in the study of the samples in their amorphous form. The investigations allowed to evaluate the molecular mobility as a function of the position of the carbonyl group on the furan ring, and how this affects the relaxation dynamics at the glass transition. This section considered the homopolymers, 2,5-PEF and 2,4-PEF, as well as a family of copolymers obtained by combining different amounts of 2,5- and 2,4-FDCA-based repeating units.

The second sections allowed to evaluate the ability to crystallize of the samples by combining X-ray diffraction and thermal analysis. The kinetics of crystallization both from the molten and the glassy state were evaluated, because they provide important information for manufacturers, such as the maximum percentage of crystallinity that can be reached in specific temperature conditions, as well as the time necessary to reach half of the crystallization process.

Regarding the thermal properties, a gap of 10 °C was observed between 2,5-PEF and 2,4-PEF, both in terms of degradation temperature and glass transition temperature. However, the most interesting results were obtained for the copolymers. The 2,5/2,4 ratio does not significantly affect these temperatures ( $T_d$  and  $T_g$  of the copolymers are closer to the values obtained for 2,5-PEF), however the presence of a slight amount of 2,4 repeating units is enough to significantly disrupt the crystallization of the copolymers as compared to 2,5-PEF.

Besides, the incorporation of 2,4 repeating units induces significant modifications in the amorphous phase: the local motions are slower, and the cooperativity associated to the glass transition is also reduced.

The crystallization behavior is also affected by the position of the carbonyl group on the furan ring. Indeed, the addition of 2,4 repeating units changed the ability to crystallize, and with as little as 15% of 2,4-isomers the copolymer becomes non-crystallizable. The copolymerization of 2,5-FDCA DME with 2,4-FDCA DME leads, in the case of the copolyesters, to a decrease in the crystallinity rate (revealed as an increase in the half-crystallization time  $t_{1/2}$ ) with no significant decrease of crystallinity. Furthermore, the incorporation of 2,4-FDCA-based repeating units into 2,5-PEF decreases the melting temperatures (i.e. decreases the thickness of crystalline lamellae) and increases the aptitude to form stable crystals of 2,5-PEF.

As a prospect, to complete the analyses already performed, it would be interesting to go deeper thanks to other experimental techniques. A measurement of the free volume in the series of samples based on both 2,5- and 2,4-FDCA could be done by Positron Annihilation Lifetime Spectroscopy (PALS). Indeed, free volume is a key parameter to evaluate the relaxation processes, which require an activation volume (not only an activation energy) to occur.

Fast Scanning Calorimetry (FSC) could be also an interesting experimental technique to better evaluate the influence of positional isomerisms on the glass-forming ability of these materials (critical cooling rate to play around with the nucleation/growth mechanisms), as well as on the mechanisms of their physical aging. Indeed, due to the tremendously high scanning rate and a radical decrease in the size and mass of the sample (nanoscale), FSC allows to accelerate the kinetics of physical aging, providing key information to understand the molecular dynamics in the glassy state.

## Abbreviations List

$\overline{M}_n$ : Number-average molecular weights	$C_V^*$ : Complex specific heat capacity at constant volume
$\overline{M}_w$ : Weight-average molecular weights	$E^{(vib)}$ : Vibrational energy
$\vec{r}_\alpha(t)$ : Position of the atom $\alpha$ at the time $t$	$E^{(\alpha)}$ : Energy associated to the $\alpha$ relaxation
$\vec{\mu}_i$ : Dipole moment of the molecule $i$	$E_a$ : Activation energy
$\Delta C_p^0$ : Heat capacity step at the glass transition for the fully amorphous counterpart	$E_i$ : Possible energy states
$\Delta H_{cc}$ : Enthalpy associated to cold crystallization	$\vec{E}$ : Electric field
$\Delta H_m^0$ : Equilibrium enthalpy of melting for of an ideal fully crystalline sample	$f_T(\omega)$ : Spectral shape function of temperature fluctuations
$\Delta H_m$ : Melting enthalpy	$f_X(\omega)$ : Spectral shape function of polarization fluctuations
$\Delta h_m$ : Melting enthalpy per unit of volume	$g_K$ : Kirkwood correlation factor
$\Delta S_m$ : Melting entropy	$G_{max}$ : Maximum of the crystallization rate
$A_{HF}$ : Amplitude of the heat flow modulation	$G_T''(\omega)$ : Imaginary part of the complex temperature modulus
$A_\beta$ : Amplitude of the heating rate modulation	$I_S^*(\omega)$ : Current measured across the sample
$b_0$ : Molecular thickness	$J_S''(\omega)$ : Imaginary part of the complex entropy compliance
$C^*$ : Complex heat capacity	$K_{C_p}$ : Calibration factor
$C_0$ : Respective geometric (i.e. empty cell) capacity	$k_{Avrami}$ : Avrami's constant
$C_m^*$ : Measured capacity	$k_B$ : Boltzmann's constant
$C_p$ : Heat capacity	$k_{GT}$ : Gordon-Taylor parameter
$c_p$ : Specific heat capacity	$k_{KW}$ : Kwei parameter
$C_{RCP}$ : Heat capacity of the reference	$M''(\omega)$ : Imaginary part of the complex electric modulus
$C_{SCP}$ : Heat capacity of the sample	$M^*$ : Complex electric modulus
$C_{su}$ : Substrate capacity	

## Abbreviations List

---

$M_0$ : Molar mass	$T_f$ : Fictive temperature
$N_A$ : Avogadro number	$T_g$ : Glass transition temperature
$N_o$ : Number of polarized entities	$T_i$ : Initial temperature
$N_\alpha$ : Number of partial systems or structural entities in a CRR	$T_K$ : Kauzmann's temperature
$P_i$ : Instantaneous polarization	$T_m^0$ : Thermodynamic melting temperature
$P_i$ : Probability that the partial system is in the energy state	$T_m$ : Melting temperature
$P_o$ : Orientation polarization	$t_p$ : Polarization time
$\vec{P}$ : Polarization	$T_R$ : Reference temperature
$q_\alpha$ : Fixed charge localized on the atom $\alpha$	$T_r$ : Reference temperature
$R^*(\omega)$ : Resistivity	$T_S$ : Sample temperature
$R_{RCP}$ : Thermal resistance of the reference	$T_\alpha$ : Dynamic vitreous transition temperature
$R_{SCP}$ : Thermal resistance of the sample	$U^*$ : Activation energy of the displacement of the macromolecules within the melt
$S_{crystal}$ : Entropy of the crystals	$U^*(\omega)$ : Sinusoidal voltage
$S_{liquid}$ : Entropy of the equilibrium liquid	$X_\infty$ : Crystallizable volume fraction
$t_{1/2}$ : Half-crystallization time	$X_{am}$ : Mobile amorphous fraction
$T_{c\ max}$ : Temperature corresponding to the maximum of the crystallization rate	$X_{ar}$ : Rigid amorphous phase
$T_0$ : Fixed temperature (Heat flow calculation)	$X_{c\ max}$ : Maximum crystallinity degree
$T_0$ : Vogel temperature	$X_c$ : Crystalline fraction
$T_a$ : Aging temperature	$Z^*(\omega)$ : Complex electrical impedance
$t_a$ : Aging time	$\alpha_{HN}$ : Shape parameter describing the symmetric broadening factors of the dielectric spectra
$T_c$ : Crossover temperature	$\beta^-$ : Cooling rate
$T_c$ : Crystallization temperature	$\beta_{HN}$ : Shape parameters describing the asymmetric broadening factors of the dielectric spectra
$t_c$ : Crystallization time	$\beta_{KWW}$ : Stretch exponent
$T_{d\ 5\%}$ : Temperature at which a mass loss of 5% is observed	$\varepsilon''$ : Dielectric loss
$T_{d\ max}$ : Temperature corresponding to the maximum rate of mass loss	$\varepsilon^*$ : Complex dielectric permittivity
	$\varepsilon_\infty$ : Unrelaxed dielectric permittivity

---

$\varepsilon_0$ : Dielectric permittivity of vacuum	$\Delta g_V$ : Free energy associated with the transformation of a molten volume of polymer to a crystal
$\varepsilon_s^*$ : Complex permittivity of the sample	$\Delta h^*$ : Apparent activation energy
$\varepsilon_{su}^*$ : Complex permittivity of the substrate	$\Delta P^2(\omega)$ : Spectral densities of the polarization
$\kappa_T$ : Isothermal compressibility	$\Delta S^2(\omega)$ : Spectral density of entropy fluctuations
$\xi_\alpha$ : Cooperativity length	$\Delta S_c$ : Configurational entropy
$\sigma^*(\omega)$ : Electrical conductivity	$\Delta T^2(\omega)$ : Spectral density of temperature fluctuations
$\sigma_0$ : Ohmic conduction related to the mobile charge carriers	$\Delta T$ : Supercooling
$\sigma_e$ : Free energy of the crystal folding surfaces	$\Delta\varepsilon$ : Dielectric relaxation strength
$\tau_{CC}$ : Cole-Cole relaxation time	$^1\text{H}$ : Proton
$\tau_{CD}$ : Cole Davidson relaxation time	2,4-PEF: Poly (Ethylene-2,4-Furandicarboxylate)
$\tau_D$ : Debye relaxation time	2,5-FDCA DME: Dimethyl-2,5-furandicarboxylate
$\tau_{max}$ : Relaxation time associated to the maximum of the relaxation peak	2,5-PEF: Poly (Ethylene-2,5-Furandicarboxylate)
$\phi_{eq}(T)$ : Equilibrium value of the property	$A$ : Amplitude temperature
$\phi_{NR}$ : Non-reversing heat flow	ATR: Attenuated Total Reflectance
$\phi_R$ : Reversing heat flow	$C$ : Heat capacity
$\chi''(\omega)$ : Imaginary part of dielectric susceptibility	$C'$ : In-phase component of the heat capacity
$\chi^*$ : Dielectric susceptibility	$C''$ : Out-phase component of the heat capacity
$\omega$ : Angular frequency	$C(\omega)$ : Capacitance
$\mu$ : Dipole moment	CC: Cole-Cole
$\varphi$ : Phase shift between the applied voltage and the measured current	CD: Cole-Davidson
$\Delta c_p$ : Specific heat capacity step	$\text{CHCl}_3$ : Chloroform
$\Delta E^2(\omega)$ : Spectral densities of the local electric field	$\text{CO}_2$ : Carbon dioxide
$\Delta g_S$ : Free enthalpy associated with the molten-crystal interface formation	
$\Delta g_t$ : Transition free energy	

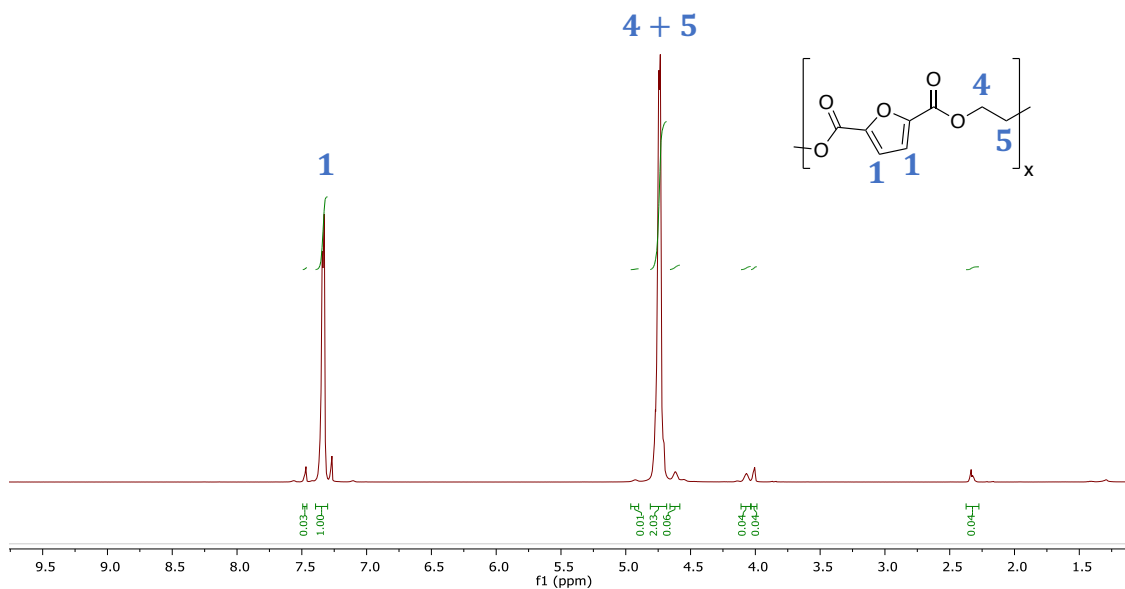
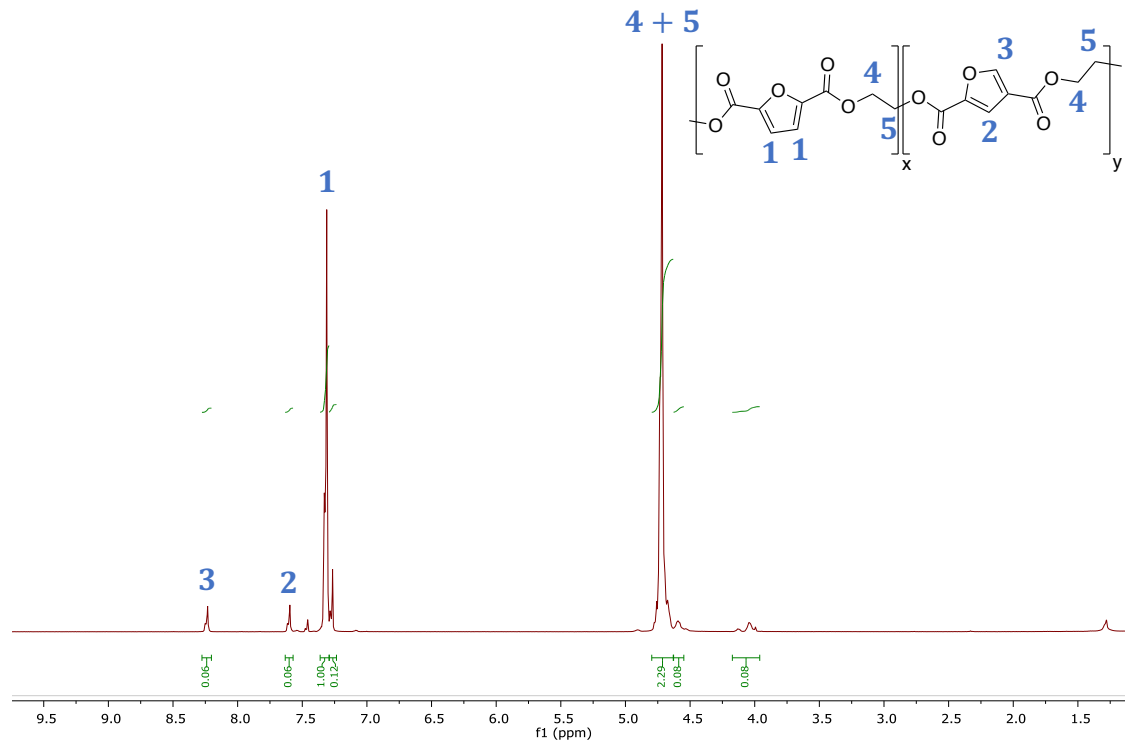


## Abbreviations List

---

CRR: Cooperative Rearranging Regions	HMF: 5-(HydroxyMethyl)-2-Furaldehyde
$d$ : Spacing between successive diffracting planes	HN: Havriliak-Negami
DMA: Dynamic Mechanical Analysis	$i$ : Rate of deposition of secondary germs
DMF: DiMethyl-2,5-Furandicarboxylate	$j$ : Rate of completion of the layer
DMSO: Deuterated dimethylsulfoxide	KWW: Kohlrausch-Williams-Watts
DMT: DiMethyl Terephthalate	$L$ : Natural logarithmic ratio between the maximum and minimum rates of degradation
DRS: Dielectric Relaxation Spectroscopy	LA: Levulinic Acid
DSC: Differential Scanning Calorimetry	$m$ : fragility index
$d\alpha$ : Transformation rate	MAF: Mobile Amorphous Fraction
$d\alpha'$ : Transformation rate for an infinite available volume	MDS: Molecular Dynamics Simulations
$E(\omega)$ : Electric field	MEG: Methyl Ethyl Glycol
EG: Ethylene Glycol	MT-DSC: Modulated Temperature Differential Scanning Calorimetry
EL: Ethyl Levulinate	MTGA: Modulated ThermoGravimetric Analysis
EMF: 5-EthoxyMethylFurfural	$n$ : Avrami's exponent
$f$ : Correction factor	$n$ : Order of diffraction
$f$ : frequency	$N_2$ : Dinitrogen
$F$ : Onsager factor	NMR: Nuclear Magnetic Resonance
$f(\alpha)$ : Kinetic expression	PA 6: Poly (Amide 6)
FA: 2-Furoic Acid	PB: Poly (1-Butene)
FA: Formic Acid	PBF: Poly (Butylene Furandicarboxylate)
FDCA: FuranDiCarboxylic Acid	PE: Poly (Ethylene)
FSC: Fast Scanning Calorimetry	PEN: Poly (Ethylene Naphthalate)
FTIR: Fourier-Transform Infrared Spectroscopy	PET: Poly (Ethylene Terephthalate)
$G$ : Gibbs Free energy	PLA: Poly (Lactid Acid)
$G$ : Overall growth rate of the lamella	POM: Polarized Optical Microscopy
$g(r)$ : Radial distribution function	PPF: Poly (Propylene Furandicarboxylate)
GPC: Gel Permeation Chromatography	PS: Poly (Styrene)
gVL: $\gamma$ -ValeroLactone	PVC: Poly (Vinyl Chloride)
$H$ : Specific enthalpy	

$Q$ : Heat transfer	$\delta T$ : Mean temperature fluctuation
$q$ : Kwei parameter proportional to the number of specific intermolecular interactions	$\eta$ : Viscosity
$r$ : Interatomic distance	$\theta$ : Diffraction angle
$r$ : Radius	$\lambda$ : Wavelength of the incident X-ray beam
$R$ : Thermal resistance (Ohm's law)	$\sigma$ : Free energy of the crystal/melt interface
$R$ : Universal gas constant	$\tau$ : Relaxation time
RAF: Rigid Amorphous Fraction	$\phi$ : Heat flow
$S$ : Specific entropy	$\phi$ : Property
SAXS: Small-Angle X-ray Scattering	
$T$ : Temperature	
TGA: ThermoGravimetric Analysis	
TNM: Tool-Narayanaswamy-Moynihan	
TPA: TerePhthalic Acid	
TSDC: Thermo-Stimulated Depolarization Currents	
$V$ : Specific volume	
VFT: Vogel-Fulcher-Tammann	
WAXD: Wide Angle X-ray Diffraction	
WAXS: Wide-Angle X-ray Scattering	
XRD: X-Ray Diffraction	
$Z$ : Pre-exponential factor	
$\alpha$ : Coefficient of expansion (Chapter III)	
$\alpha$ : Fraction of sample	
$\alpha(T)$ : Ratio of the crystallized volume fraction on crystallizable volume fraction	
$\alpha'$ : Rate of fictive transformation that would be obtained by a free growth of crystallites	
$\beta$ : Scanning rate	

Annex A:  $^1\text{H}$  RMN SpectraFigure A.1:  $^1\text{H}$  NMR spectrum of Poly(1,2-ethylene-2,5-furandicarboxylate) (2,5-PEF).Figure A.2:  $^1\text{H}$  NMR spectrum of Poly(1,2-ethylene-2,5[[90]-2,4[10]-furandicarboxylate) (PE-2,5[90]-2,4[10]-F).

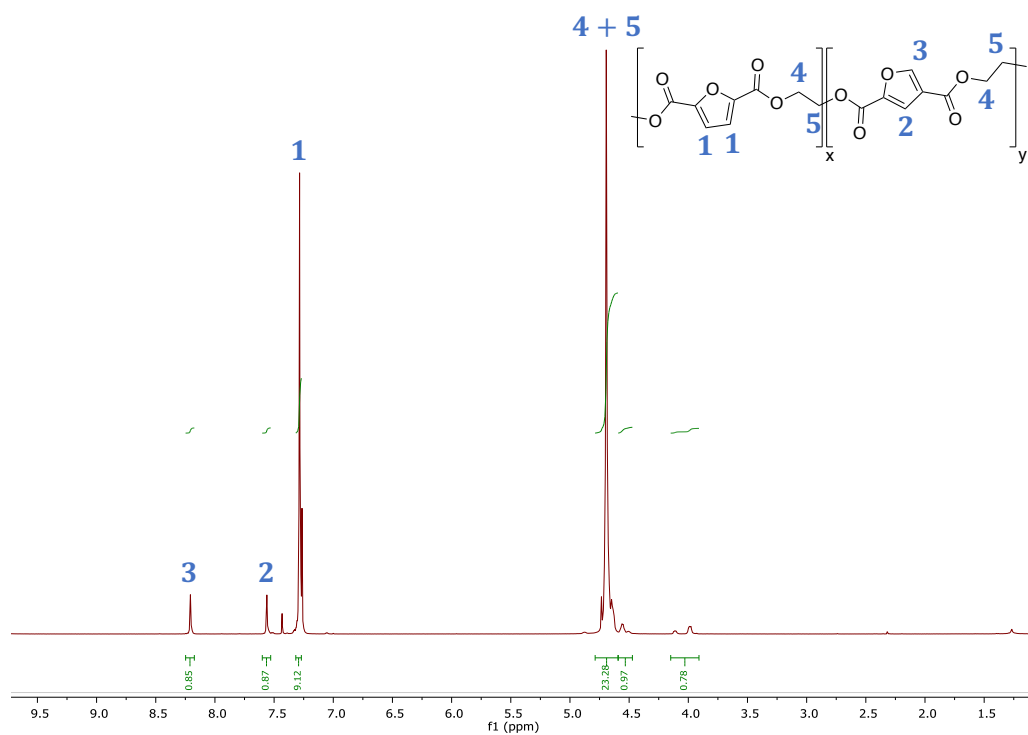


Figure A.3: <sup>1</sup>H NMR spectrum of Poly(1,2-ethylene-2,5[[85]-2,4[15]-furandicarboxylate) (PE-2,5[85]-2,4[15]-F).

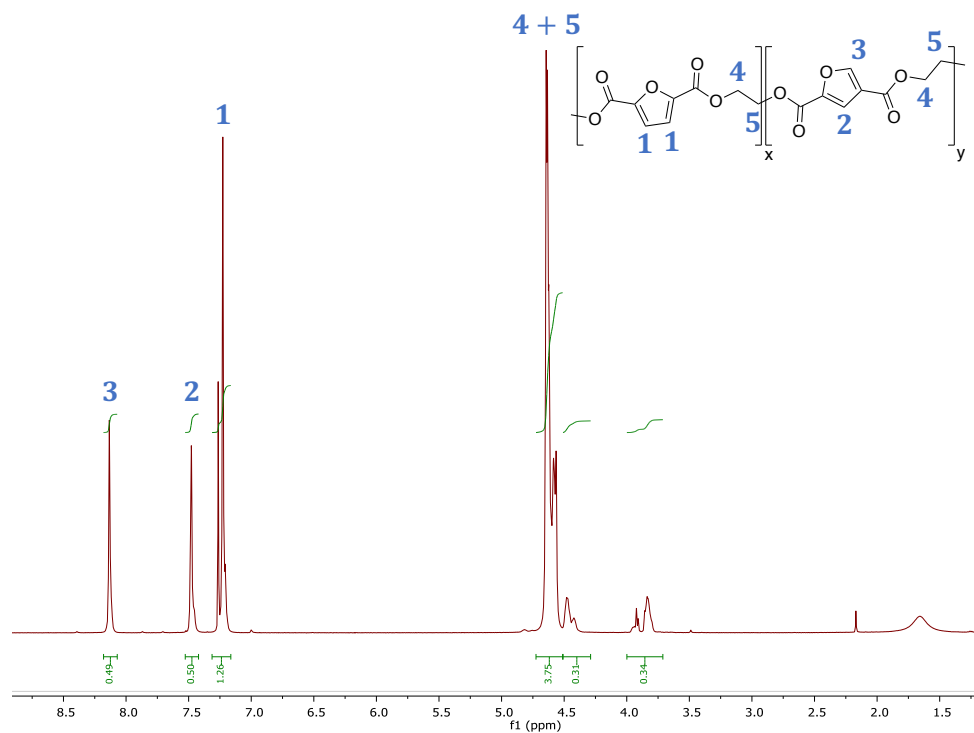


Figure A.4: <sup>1</sup>H NMR spectrum of Poly(1,2-ethylene-2,5[[50]-2,4[50]-furandicarboxylate) (PE-2,5[50]-2,4[50]-F).

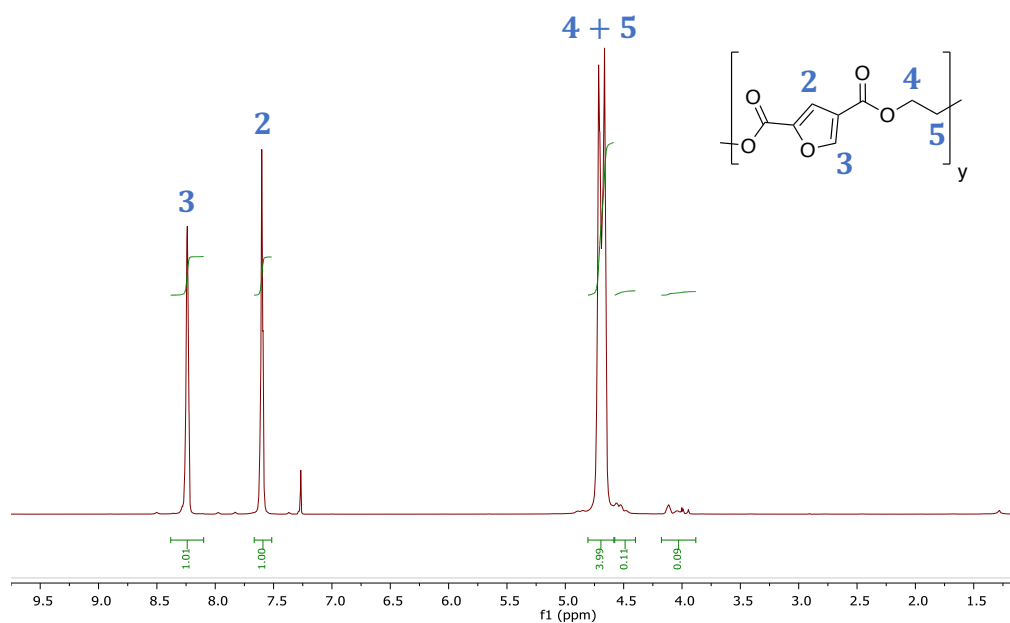


Figure A.5:  $^1\text{H}$  NMR spectrum of Poly (1,2-ethylene-2,4-furandicarboxylate) (2,4-PEF).

## Annex B: MDS Calculation

Molecular Dynamics Simulation (MDS) was performed by the University of Lille only on 2,4-PEF and 2,5-PEF. These two samples were studied in the molten state at  $T = 500$  K using the DL\_POLY<sup>1,2</sup> package and GAFF<sup>3</sup> force field to model the intra- and intermolecular interactions. The equations of motion were integrated using the Verlet leapfrog algorithm, with a time step of 1 fs, and bond lengths were constrained by means of the SHAKE algorithm. Cubic periodic boundary conditions were applied. For each compound, a disordered configuration of  $N = 30$  chains of 7 repeating units was generated. Each chain was therefore composed of  $N_a = 138$  atoms. A Lennard-Jones potential was employed to represent van der Waals interactions. For the electrostatic interactions, a pairwise damped shifted method developed by Wolf<sup>4</sup> was used. Fixed charges located on each atom were directly obtained from an ab initio computation using the Gaussian program<sup>5</sup> with the method HF/6-31G\* RESP recommended for GAFF. The same cutoff radius of 10 Å was used for both van der Waals and Coulombic interactions. Thermalization was carried in isobaric–isothermal NPT ensemble at a pressure of  $P = 1.0$  bar. The Nose–Hoover thermostat and barostat relaxation times were chosen as 0.2 and 2.0 ps, respectively. In these conditions, the duration of the simulations were 100 and 250 ns for 2,4-PEF and 2,5-PEF, respectively.

## References

- (1) Smith, W.; Forester, T. R.; Todorov, I. T. The DL\_POLY Classic User Manual. TFC, STFC Daresbury Laboratory, Daresbury, Warrington, Cheshire, WA4 4AD, United Kingdom 2012.
- (2) Computational Collaboration Project No 5 - Software for simulation of condensed phases. | CCP5 Computer Simulations of Condensed Phases <https://www.ccp5.ac.uk/software> (accessed Jan 28, 2020).
- (3) Wang, J.; Wolf, R. M.; Caldwell, J. W.; Kollman, P. A.; Case, D. A. Development and Testing of a General Amber Force Field. *J. Comput. Chem.* **2004**, 25 (9), 1157–1174. <https://doi.org/10.1002/jcc.20035>.
- (4) Wolf, D.; Keblinski, P.; Phillpot, S. R.; Eggebrecht, J. Exact Method for the Simulation of Coulombic Systems by Spherically Truncated, Pairwise R–1 Summation. *The Journal of Chemical Physics* **1999**, 110 (17), 8254–8282. <https://doi.org/10.1063/1.478738>.
- (5) Frisch, M.; Trucks, G. W.; Schlegel, H. B.; Scuseria, G. E.; Robb, M. A.; Cheeseman, J. R.; Scalmani, G.; Barone, V.; Mennucci, B.; Petersson, G. A. Gaussian 09, Revision D. 01. Gaussian, Inc., Wallingford CT 2009.

## Annex C: Scientific Communications

### Publications

1. Bourdet, A.; Esposito, A.; Thiyagarajan, S.; Delbreilh, L.; Affouard, F.; Knoop, R. J. I.; Dargent, E. Molecular Mobility in Amorphous Biobased Poly(Ethylene 2,5-Furandicarboxylate) and Poly(Ethylene 2,4-Furandicarboxylate). *Macromolecules* **2018**, *51* (5), 1937–1945. <https://doi.org/10.1021/acs.macromol.8b00108>.
2. Fosse, C.; Bourdet, A.; Ernault, E.; Esposito, A.; Delpouve, N.; Delbreilh, L.; Thiyagarajan, S.; Knoop, R. J. I.; Dargent, E. Determination of the Equilibrium Enthalpy of Melting of Two-Phase Semi-Crystalline Polymers by Fast Scanning Calorimetry. *Thermochimica Acta* **2019**, *677*, 67–78. <https://doi.org/10.1016/j.tca.2019.03.035>.
3. Thiyagarajan, S.; Meijlink, M. A.; Bourdet, A.; Vogelzang, W.; Knoop, R. J. I.; Esposito, A.; Dargent, E.; van Es, D. S.; van Haveren, J. Synthesis and Thermal Properties of Bio-Based Copolyesters from the Mixtures of 2,5- and 2,4-Furandicarboxylic Acid with Different Diols. *ACS Sustainable Chem. Eng.* **2019**, *acssuschemeng.9b04463*. <https://doi.org/10.1021/acssuschemeng.9b04463>.

### Oral communications

1. Bourdet, A.; Esposito, A.; Thiyagarajan, S.; Delbreilh, L.; Schammé, B.; Knoop, R. J.I.; Dargent, E. “Characterization of biobased polyesters derived from furandicarboxylic acid isomers in function of the repeating unit structure: Comparison with other polyesters”, **1ere journée du département Système Desordonnés et Polymères, GPM (June 26, 2017), Saint-Etienne-du-Rouvray, France**
2. Bourdet, A.; Esposito, A.; Thiyagarajan, S.; Delbreilh, L.; Schammé, B.; Tognetti, V., Affouard, F. ; Knoop, R. J.I.; Dargent, E. “Etude de la cinétique de cristallisation et de la dynamique moléculaire du poly(éthylène-2,5-furandicarboxylate) biosourcé”, **Journées de Calorimétrie et d’Analyse Thermique JCAT49 (may 22-25, 2018), Saint-Etienne, France**

3. Bourdet, A.; Esposito, A.; Thiyagarajan, S.; Delbreilh, L.; Schammé, B.; Tognetti, V., Affouard, F. ; Knoop, R. J.I.; Dargent, E. "Relations structure/propriétés physiques de polymères à base d'acide furandicarboxylique obtenu de la biomasse", **2ème Journée Scientifique du Département Systèmes Désordonnés et Polymères: SDP2 (Sept 05, 2018), Saint-Etienne-du-Rouvray, France**
4. Esposito, A.; Delpouve, N.; Delbreilh, L.; Dargent, E. "How Can Molecular Mobility Unveil The Limits And Potentialities Of Biopolymers?" **International conference on Biopolymers and Bioplastics, Exploring the advancements and frontiers in the field of Biopolymers, March 04-06, 2019, Baltimore, MD 21090, USA**
5. Bourdet, A.; Esposito, A.; Thiyagarajan, S.; Delbreilh, L.; Garda, MR.; Knoop, R. J.I.; Dargent, E. "Thermal properties and molecular mobility of a new generation of furanic copolyester", **7th International Conference on Biobased and Biodegradable Polymers, June 2019, Stockholm, Sweden**
6. Esposito, A.; Thiyagarajan, S.; Delpouve, N.; Delbreilh, L.; Dargent, E. "How Can Molecular Mobility Unveil The Limits And Potentialities Of Biopolymers?" **7th International Conference on Biobased and Biodegradable Polymers, June 2019, Stockholm, Sweden**
7. Bourdet, A.; Esposito, A.; Thiyagarajan, S.; Delbreilh, L.; Knoop, R. J.I.; Dargent, E. "Molecular Mobility in Amorphous Biobased poly(ethylene furanoate): the effect of positional isomerism" **27 World Forum on Advanced Materials Polychar, oct 2019, Naples, Italy**



## Poster communications

1. Bourdet, A.; Esposito, A.; Thiyagarajan, S.; Delbreilh, L.; Knoop, R. J.I.; Dargent, E. “Dielectric relaxation in amorphous poly (ethylene-2,5-furanoate): Comparison with other polyesters”, **6th International Conference on Biobased and Biodegradable Polymers BIOPOL2017 (Sept 11-13, 2017), Mons, Belgium**
2. Bourdet, A.; Esposito, A.; Thiyagarajan, S.; Delbreilh, L.; Garda, MR.; Knoop, R. J.I.; Dargent, E. “Propriétés thermiques et mobilité moléculaire d’une nouvelle génération de copolyesters à base d’acide furandicarboxylique”, **50èmes Journées de Calorimétrie et d’Analyse Thermique: JCAT50 (June 03-05, 2019), Saint-Valéry en Caux, France (*Best poster price*)**

# Molecular Mobility in Amorphous Biobased Poly(ethylene 2,5-furandicarboxylate) and Poly(ethylene 2,4-furandicarboxylate)

Aurélie Bourdet,<sup>†</sup> Antonella Esposito,<sup>\*,†,‡,§</sup> Shanmugam Thiyagarajan,<sup>‡</sup> Laurent Delbreilh,<sup>†,§</sup> Frédéric Affouard,<sup>§</sup> Rutger J. I. Knoop,<sup>‡</sup> and Eric Dargent<sup>†</sup>

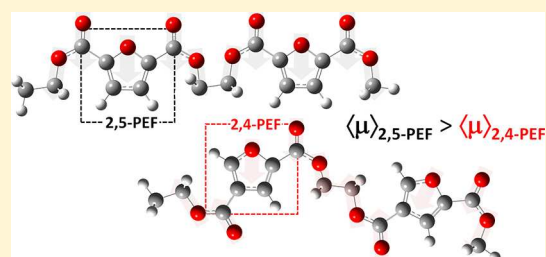
<sup>†</sup>Groupe de Physique des Matériaux, Normandie Univ, UNIROUEN Normandie, INSA Rouen, CNRS, 76000 Rouen, France

<sup>‡</sup>Wageningen Food & Biobased Research, P.O. Box 17, 6700 AA Wageningen, The Netherlands

<sup>§</sup>UMET, UMR CNRS 8207, Université Lille 1, 59655 Villeneuve d'Ascq, France

## Supporting Information

**ABSTRACT:** Among all the emergent biobased polymers, poly(ethylene 2,5-furandicarboxylate) (2,5-PEF) seems to be particularly interesting for packaging applications. This work is focused on the investigation of the relaxation dynamics and the macromolecular mobility in totally amorphous 2,5-PEF as well as in the less studied poly(ethylene 2,4-furandicarboxylate) (2,4-PEF). Both biopolymers were investigated by differential scanning calorimetry and dielectric relaxation spectroscopy in a large range of temperatures and frequencies. The main parameters describing the relaxation dynamics and the molecular mobility in 2,5-PEF and 2,4-PEF, such as the glass transition temperature, the temperature dependence of the  $\alpha$  and  $\beta$  relaxation times, the fragility index, and the apparent activation energy of the secondary relaxation, were determined and discussed. 2,5-PEF showed a higher value of the dielectric strength as compared to 2,4-PEF and other well-known polyesters, such as poly(ethylene terephthalate), which was confirmed by molecular dynamics simulations. According to the Angell's classification of glass-forming liquids, amorphous PEFs behave as stronger glass-formers in comparison with other polyesters, which may be correlated to the packing efficiency of the macromolecular chains and therefore to the free volume and the barrier properties.



## INTRODUCTION

The demand for sustainable alternatives to fossil resources is increasingly motivating both the scientific and industrial communities to pay attention to any polymer that may be obtained from renewable resources.<sup>1–6</sup> As a consequence, the number of polymers that are partially or entirely based on renewable resources, and that are already (or soon will be) commercialized, is increasing very fast. 2,5-Furandicarboxylic acid (2,5-FDCA), a monomer obtained from vegetal feedstock, can be used to synthesize poly(ethylene 2,5-furandicarboxylate) (2,5-PEF).<sup>7–12</sup> 2,5-PEF is nowadays considered as the most promising sustainable alternative to poly(ethylene terephthalate) (PET), as it exhibits improved mechanical and barrier properties, which is essential to process lightweight beverage packaging.<sup>4,13,14</sup> O<sub>2</sub>, CO<sub>2</sub>, and H<sub>2</sub>O permeability in 2,5-PEF is decreased by a factor 11,<sup>15</sup> 19,<sup>16</sup> and 2.8,<sup>17,18</sup> respectively, as compared to PET.<sup>5</sup> Recent studies provided information on the iso- and nonisothermal crystallization kinetics of 2,5-PEF.<sup>11,12,19–23</sup> The growth of crystalline structures within a polymer induces a progressive reduction of the amorphous phase. In most systems, the presence of crystals considerably modifies the molecular motions in the amorphous phase. The three-phase model and the concept of cooperative rearranging regions (CRR) were used by Codou et al.<sup>24</sup> to explain the incomplete decoupling between the crystalline and the

amorphous phases in 2,5-PEF as compared to PET. The motional processes in amorphous 2,5-PEF have been recently examined by Burgess et al.<sup>25</sup> and compared to those occurring in PET. The authors proved that the furan ring-flipping in 2,5-PEF is limited as compared to the benzene ring-flipping in PET, thus leading to slower chain mobility and a significant reduction in oxygen diffusion. A recent study on the molecular dynamics of semicrystalline 2,5-PEF was done by Dimitriadis et al.<sup>26</sup> In this study, they combined dielectric relaxation spectroscopy (DRS) and differential scanning calorimetry (DSC) in order to quantify the molecular mobility in each microstructural fraction. However, the molecular-scale motions in 2,5-PEF have not been completely investigated, yet they could greatly help explaining the macroscopic behavior of these polymers, as already reported for other biopolyesters.<sup>27</sup>

Thiyagarajan et al.<sup>28</sup> recently reported that depending on the conditions for the Henkel-type disproportionation reaction, not only the 2,5-isomer (2,5-FDCA) is formed (70%) but also the 2,4-isomer (2,4-FDCA) (30%) and the 3,4-isomer (3,4-FDCA) (<5%). They also pointed out for the first time the remarkable effects of the position of the carboxylic group on the furan ring

Received: January 17, 2018

Revised: February 10, 2018

Published: February 23, 2018

in such a series of FDCA isomers. In terms of symmetry, 2,4-FDCA is the least symmetrical diacid. A comparison made in terms of the dipole moment  $D$  obtained by simulation, and the projected angle between the C1–C2 bond and the C5–C6 bond, leads to the conclusion that contrary to the common belief and the general trend observed in the literature, the 2,5-FDCA isomer is more similar to isophthalic acid (IPA) rather than to terephthalic acid (TA), the latter being closer to the 2,4-FDCA.<sup>28</sup> As such, the polymer that should be compared to PET is 2,4-PEF rather than 2,5-PEF. From the point of view of the thermal properties, the glass transition temperature  $T_g$  of 2,4-PEF is 6 °C lower than that of 2,5-PEF. Furthermore, 2,4-PEF is completely amorphous (no melting point was observed during DSC scans up to 250 °C). 2,4-FDCA was also found to have a higher thermal stability with respect to the other FDCA polyesters. To the best of our knowledge, the work performed by Thiyagarajan et al.<sup>29</sup> is the only study dealing with the physical properties of 2,4-PEF. However, these materials are clearly worth a deeper investigation. This work aims to characterize the intrinsic mobility of the amorphous phase of 2,5-PEF and 2,4-PEF and is therefore focused on these biopolyesters in their totally amorphous state. A comparison is done between 2,5-PEF and 2,4-PEF in order to observe the consequence of the isomeric substitution on the relaxation behavior of the amorphous phase, on both a local and a delocalized level. The experimental investigations were performed by DRS and then supplemented by theoretical results obtained by molecular dynamics simulations (MDS). 2,5-PEF and 2,4-PEF were also compared to well-known polyesters, such as poly(ethylene terephthalate–glycol) (PETg) (which can be considered as the amorphous counterpart of PET)<sup>30</sup> and poly(lactid acid) (PLA).<sup>31</sup> These terms of comparison were selected in order to highlight the weaknesses and strengths of PEFs with respect to the actual references (both petroleum-based and biobased) for packaging solutions with specific barrier properties.

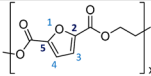
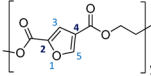
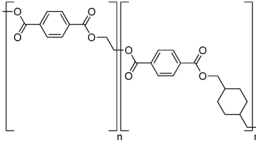
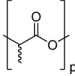
## EXPERIMENTAL SECTION

**Materials and Methods.** Poly(ethylene 2,5-furandicarboxylate) (2,5-PEF) and poly(ethylene 2,4-furandicarboxylate) (2,4-PEF) homopolyesters were synthesized by using dimethyl furandicarboxylate with 1,2-ethylene glycol in the presence of titanium(IV) isopropoxide as catalyst. The detailed polymerization procedure was described in a previous publication.<sup>28</sup>

Table 1 reports the repeating units of the obtained polymers, along with the weight-average molecular weight ( $\bar{M}_w$ ) and the number-average molecular weight ( $\bar{M}_n$ ) determined by gel permeation chromatography, as compared to the reference polyesters (PETg and PLA). PETg can be considered as the amorphous counterpart of PET because it has a considerably lower ability to crystallize;<sup>32</sup> the selected (EASTAR copolyester 6763, Eastman Chem. Co.) is a grade obtained with cyclohexanedimethanol, ethylene glycol, and terephthalic acid in a molar ratio 1:2:3. The reference biopolyester selected for comparison is a grade of PLA (4042D, NatureWorks LLC) including 4.3% D-lactic acid isomers; the presence of D-lactic acid interferes with polymer crystallization, increasing the chances to get a substantially amorphous PLA.<sup>33</sup> Prior to characterization, all the freshly prepared samples were dried for 3 days at  $T_g + 15$  °C (i.e., 95 °C) to remove any residual solvents used during the synthesis.

**Differential Scanning Calorimetry (DSC).** DSC thermograms were recorded on a Q2000 DSC (TA Instruments) equipped with a RCS90 intracooler. The dried samples (about 3 mg) were encapsulated in standard aluminum pans and stored in a desiccator over P<sub>2</sub>O<sub>5</sub> until measurement. Standard sapphires were used for energy calibration. Standard indium ( $T_m = 156.6$  °C,  $\Delta H_m = 28.66$  J g<sup>-1</sup>) and

**Table 1. Repeating Units, Weight-Average Molecular Weight ( $\bar{M}_w$ ), and Number-Average Molecular Weight ( $\bar{M}_n$ ) of 2,5-PEF and 2,4-PEF As Compared to PETg and PLA**

Samples	Repeating unit	$\bar{M}_w$ (kg mol <sup>-1</sup> )	$\bar{M}_n$ (kg mol <sup>-1</sup> )	Source
2,5-PEF		18.2	15.3	Synthesized
2,4-PEF		11.4	8.5	Synthesized
PETg		Not given	26.0	Eastman Chem. Co.
PLA		188.0	116.0	Nature Works LLC®

benzophenone ( $T_m = 48.0$  °C) were used for heat flow and temperature calibrations. The DSC cell was purged with a continuous flow of gaseous nitrogen (50 mL min<sup>-1</sup>). The samples in their fully amorphous state were analyzed with the following program: heating ramp from 0 to 250 °C at 10 K min<sup>-1</sup> to get to the molten state, isothermal step for 1 min at 250 °C for temperature homogenization in the melt, cooling ramp within the DSC at the highest achievable rate (ballistic quenching) down to 0 °C, followed by an isothermal step for 2 min at 0 °C for temperature stabilization, and finally a heating ramp until 250 °C at 10 K min<sup>-1</sup> for measurement.

**Dielectric Relaxation Spectroscopy (DRS).** DRS experiments were performed using interdigitated electrodes (IEs) (BDS1410-20-150, Novocontrol Technologies, with a sensor diameter of 20 mm, gold-plated copper combs, and an accuracy in loss factor equal to  $\tan \delta = 0.001$ ). The spacing between the comb fingers is 150 μm, and their thickness is 35 μm. Prior to sample deposition, each electrode was calibrated by measuring its respective geometric (empty cell) capacity  $C_0$  and substrate capacity  $C_{su}$  through the measurement of a standard material with known permittivity (mineral B oil, Vacuubrand). Assuming that the electric field penetrates only in the sample and the substrate, the measured capacity  $C_m^*$  is given by<sup>34</sup>

$$C_m^* = C_0(\epsilon_s^* + \epsilon_{su}^*) \quad (1)$$

where  $\epsilon_s^*$  and  $\epsilon_{su}^*$  are the complex permittivity of the sample and the substrate, respectively. The measurements were carried out in a frequency range of  $2 \times 10^6$ –0.1 Hz with an Alpha Analyzer (Novocontrol Technologies) allowing measurement of the complex impedance as a function of frequency. Nonisothermal dielectric spectra were collected over a wide temperature range (from –150 to 150 °C) with appropriate successive steps. Accurate temperature control was implemented using the Quatro system (Novocontrol Technologies) allowing a temperature stability of  $\pm 0.2$  °C. The dielectric relaxation curves were analyzed using the Havriliak–Negami (HN) complex function:<sup>35,36</sup>

$$\epsilon^* = \epsilon_\infty + \frac{\Delta\epsilon_{HN}}{[1 + (i\omega\tau_{HN})^{\alpha_{HN}}]^{\beta_{HN}}} \quad (2)$$

This formalism allows fitting the real ( $\epsilon'(\omega)$ ) and imaginary components ( $\epsilon''(\omega)$ ) of the complex dielectric permittivity ( $\epsilon^*(\omega)$ ) with the following equations:

$$\begin{aligned} \epsilon'(\omega) &= \epsilon_\infty + \Delta\epsilon_{HN} \\ &+ \frac{\cos(\beta_{HN}\varphi_{HN})}{\left(1 + 2\sin\left(\frac{\pi(1-\alpha_{HN})}{2}\right)(\omega\tau_{HN})^{\alpha_{HN}} + (\omega\tau_{HN})^{2\alpha_{HN}}\right)^{\beta_{HN}/2}} \end{aligned} \quad (3)$$

$$\varepsilon''(\omega) = \Delta\varepsilon_{\text{HN}} \frac{\sin(\beta_{\text{HN}}\varphi_{\text{HN}})}{\left(1 + 2 \sin\left(\frac{\pi(1-\alpha_{\text{HN}})}{2}\right)(\omega\tau_{\text{HN}})^{\alpha_{\text{HN}}} + (\omega\tau_{\text{HN}})^{2\alpha_{\text{HN}}}\right)^{\beta_{\text{HN}}/2}} \quad (4)$$

with

$$\varphi_{\text{HN}} = \arctan\left(\frac{(\omega\tau_{\text{HN}})^{\alpha_{\text{HN}}} \cos\left(\frac{\pi(1-\alpha_{\text{HN}})}{2}\right)}{1 + (\omega\tau_{\text{HN}})^{\alpha_{\text{HN}}} \sin\left(\frac{\pi(1-\alpha_{\text{HN}})}{2}\right)}\right) \quad (5)$$

where  $\omega$  is the angular position ( $\omega = 2\pi f$ ),  $\Delta\varepsilon_{\text{HN}}$  is the relaxation strength,  $\tau_{\text{HN}}$  is the relaxation time, and  $\alpha_{\text{HN}}$  and  $\beta_{\text{HN}}$  are the symmetric and asymmetric broadening factors. The side effects due to conductivity were treated by adding a contribution  $\sigma''_{\text{cond}} = \sigma_0/[\omega^s \varepsilon_0]$  to the dielectric loss, where  $\sigma_0$  is related to the specific direct current (dc) conductivity of the sample. The parameter  $s$  ( $0 < s \leq 1$ ) describes Ohmic ( $s = 1$ ) and non-Ohmic ( $s < 1$ ) contributions to conductivity. Two relaxation processes were observed in the experimental frequency window; therefore, a sum of two HN functions was used to fit the experimental data. The fitting procedure was applied to both the imaginary and real components of the signal in order to improve the accuracy of the resulting fitting parameters.

**Molecular Dynamics Simulations (MDS).** MDS of 2,4-PEF and 2,5-PEF in the molten state were performed at  $T = 500$  K using the DL\_POLY<sup>37,38</sup> package and GAFF<sup>39</sup> force field to model the intra- and intermolecular interactions. The equations of motion were integrated using the Verlet leapfrog algorithm, with a time step of 1 fs, and bond lengths were constrained by means of the SHAKE algorithm. Cubic periodic boundary conditions were applied. For each compound, a disordered configuration of  $N = 30$  chains of 7 repeating units was generated. Each chain was therefore composed of  $N_a = 138$  atoms. A Lennard-Jones potential was employed to represent van der Waals interactions. For the electrostatic interactions, a pairwise damped shifted method developed by Wolf<sup>40</sup> was used. Fixed charges located on each atom were directly obtained from an ab initio computation using the Gaussian program<sup>41</sup> with the method HF/6-31G\* RESP recommended for GAFF. The same cutoff radius of 10 Å was used for both van der Waals and Coulombic interactions. Thermalization was carried in isobaric–isothermal NPT ensemble at a pressure of  $P = 1.0$  bar. The Nosé–Hoover thermostat and barostat relaxation times were chosen as 0.2 and 2.0 ps, respectively. In these conditions, the duration of the simulations were 100 and 250 ns for 2,4-PEF and 2,5-PEF, respectively.

## RESULTS AND DISCUSSION

Conventional DSC analyses were performed on quenched 2,5-PEF and 2,4-PEF (Figure 1) to investigate any possible difference in their thermal behavior upon heating.

The parameters associated with the main thermal events, i.e., glass transition and melting, are reported in Table 2 and compared to the results that can be found in the literature for the reference polyesters, i.e., PETg and PLA. The glass transition temperature  $T_g$  of 2,4-PEF (72 °C) is 10 °C lower as compared to 2,5-PEF. These values are in agreement with those reported by Thiyagarajan et al.<sup>29</sup> The endothermic peak superimposed to the heat capacity step typical of the glass transition corresponds to the enthalpy recovery peak associated with physical aging and structural relaxation of the initial glasses and has been already observed in other studies.<sup>42,43</sup> Cold crystallization occurs only in 2,5-PEF, starting at approximately 160 °C and being closely followed by a melting peak, whose maximum is observed at approximately 215 °C. The enthalpies of cold crystallization and melting are equal, meaning that 2,5-PEF can be considered as fully amorphous prior to the DSC heating ramp. The peaks are weak (approximately 5 J g<sup>-1</sup>), confirming that 2,5-PEF has slower crystallization kinetics as

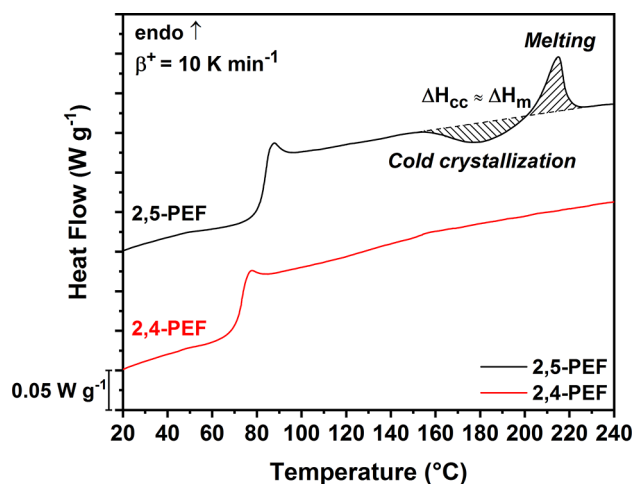


**Figure 1.** DSC thermograms obtained during the heating ramps (second scans) at 10 K min<sup>-1</sup> for amorphous 2,5-PEF and 2,4-PEF.

**Table 2.** Glass Transition Temperature ( $T_g$ ), Specific Heat Capacity Step at  $T_g$  ( $\Delta c_p$ ), and Melting Temperature ( $T_m$ ) of Amorphous 2,5-PEF and 2,4-PEF As Compared to Other Polyesters (PETg and PLA)

samples	$T_g$ (°C)	$\Delta c_p$ (J g <sup>-1</sup> K <sup>-1</sup> )	$T_m$ (°C)	$T_g/T_m$
2,5-PEF	82 ± 1	0.42 ± 0.03	215 ± 1	0.73
2,4-PEF	72 ± 1	0.42 ± 0.01		
PETg	80	0.30		
PLA	58	0.52	157 <sup>53</sup>	0.77

compared to other polyesters submitted to similar heating rates.<sup>44–46</sup> As for 2,4-PEF, only the glass transition and the corresponding structural relaxation peak were observed. A very long isothermal annealing (1 week at 140 °C, see Figure S1 in the Supporting Information) was performed, confirming that crystallization kinetics is extremely slow. The reason for the strong amorphous character of 2,4-PEF could likely be ascribed to the asymmetry of the 2,4-FDCA isomer, which disrupts any possible arrangement of the macromolecules. When compared to other polyesters (including semicrystalline PET), the gap between  $T_g$  and  $T_m$  is surprisingly small in 2,5-PEF ( $T_m - T_g = 215 - 82 = 133$  °C). Among all the polyesters mentioned in Table 2, 2,5-PEF has the highest value of  $T_g$  yet a value of  $T_m$  which is lower than PET, for which  $T_m - T_g = 243 - 73 = 170$  °C.<sup>25</sup> It is interesting to note that the equilibrium melting temperature of PEF is estimated to be 265 °C<sup>11</sup> or 226 °C,<sup>20,47</sup> while it is 280 °C<sup>48</sup> for PET. The relationship between  $T_m$  and  $T_g$  is discussed in the literature since the early 1950s; the empirical rule  $T_g/T_m \sim 2/3$ , also known as Beaman's rule,<sup>49</sup> applies to many polymers.<sup>50</sup> Later on, Lee and Knight<sup>51</sup> showed that the  $T_g/T_m$  ratio varies widely depending on the polymer. Van Krevelen<sup>52</sup> showed that a majority of polymers have a  $T_g/T_m$  ratio between 0.56 and 0.76, confirming that most of them have it equal to 2/3. In the case of 2,5-PEF, the  $T_g/T_m$  ratio is equal to 0.73 (see Table 2), which agrees with the proposed range.

The 3D plots of the dissipative signal ( $\varepsilon''(f,T)$ ) of the complex permittivity ( $\varepsilon^*(f,T)$ ) for both 2,5-PEF and 2,4-PEF are presented in Figure 2. Both of them show two complex relaxation processes. The first one ( $\beta$  relaxation) is recorded at low temperature and frequency and, as expected, shifts toward higher frequencies as the temperature increases. The second

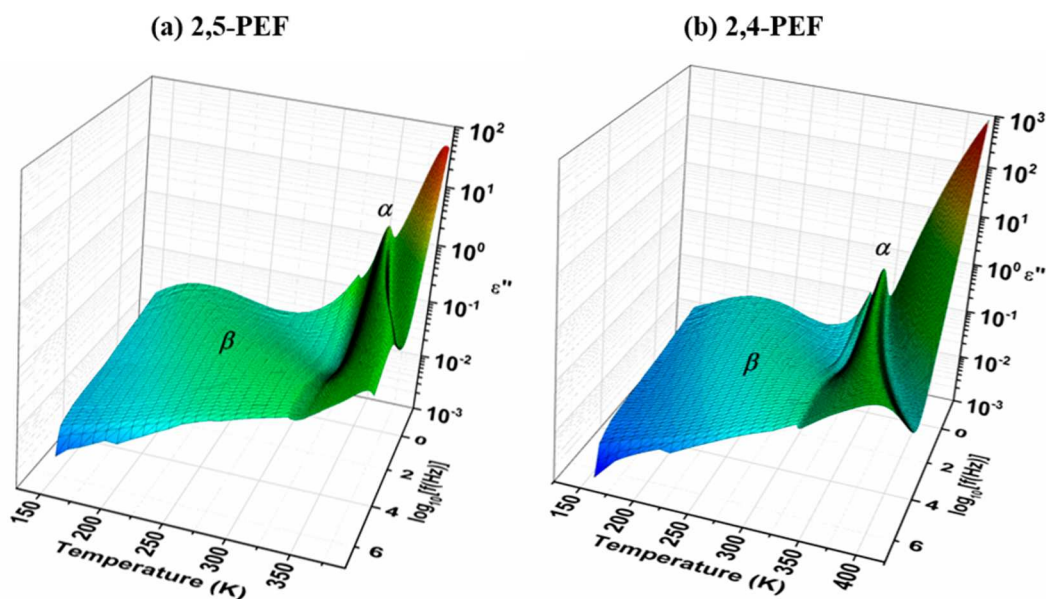


Figure 2. Imaginary part of the complex dielectric permittivity vs frequency and temperature for (a) amorphous 2,5-PEF and (b) amorphous 2,4-PEF.

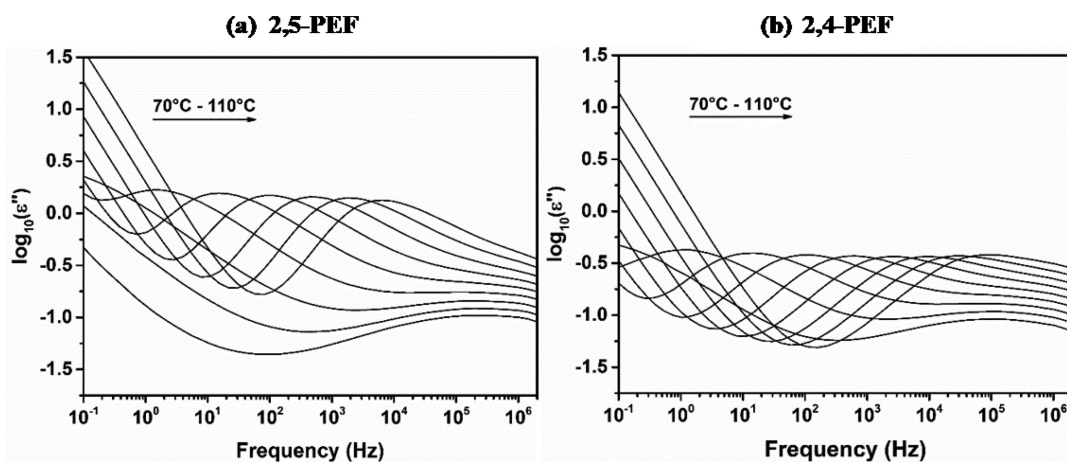


Figure 3. Dielectric loss spectra for (a) amorphous 2,5-PEF and (b) amorphous 2,4-PEF at several temperatures.

one ( $\alpha$  relaxation) is more intense, located at higher temperature and well separated from the  $\beta$  relaxation. At the highest temperatures (well above  $T_g$ ) and lowest frequencies, a classical increase in the dissipative signal ( $\epsilon''$ ) can be associated with the building up of conductivity phenomena.<sup>45</sup> The isothermal plots representing the dissipative signal vs frequency for both 2,5-PEF and 2,4-PEF at different temperatures are reported in Figure 3.

Figures 2 and 3 show that the same temperature dependence is observed for the main relaxation processes in both 2,5-PEF and 2,4-PEF, in that both the  $\alpha$  and  $\beta$  relaxations shift to higher frequencies but keep the same amplitude as the temperature increases. The evidence of a single  $\beta$  relaxation for both 2,5-PEF and 2,4-PEF is supported by the work of Dimitriadis et al.<sup>26</sup> on semicrystalline 2,5-PEF. This observation is interesting because most polyesters (PET,<sup>47,48</sup> PCT,<sup>47</sup> PEN,<sup>54</sup> PLA,<sup>55</sup> and PHAs<sup>45</sup>) are known to exhibit complex secondary relaxations including at least two contributions. A paper recently published by Soccio et al.<sup>56</sup> on biobased poly(butylene 2,5-furanoate) reports a broad  $\beta$  relaxation phenomenon that requires two processes to be described: a faster  $\beta_1$  relaxation associated with

the more mobile subunit (four  $-\text{CH}_2-$  of the aliphatic glycol connected to the C–O of the ester function) and a slower  $\beta_2$  relaxation due to the stiffer moiety (connection between the aromatic ring and the C=O of the ester function). In the case of 2,5-PEF and 2,4-PEF, the isothermal measurements of the  $\beta$  relaxation (Figure 3) could be analyzed using one symmetrical HN function (Cole–Cole function, eq 2). This analytical procedure, illustrated in Figure 4 for a temperature of 90 °C, can be extended to the measurements performed at different temperatures. The relaxation times  $\tau_{\text{max}}$  recorded for all the isothermal measurements for both the  $\alpha$  and  $\beta$  processes can then be plot in a relaxation map, as shown in Figure 5.

The values obtained for both 2,5-PEF and 2,4-PEF could then be fit by the following Arrhenius law:

$$\tau = \tau_{0,A} \exp\left(\frac{E_a}{RT}\right) \quad (6)$$

where  $E_a$  is the activation energy of the  $\beta$  relaxation,  $R$  is the gas constant, and  $\tau_{0,A}$  is a pre-exponential factor. The  $E_a$  values reported in Table 3 are close to the values provided by the literature for other polyesters (36–46 kJ mol<sup>-1</sup> for PLA,<sup>55</sup> 55 kJ

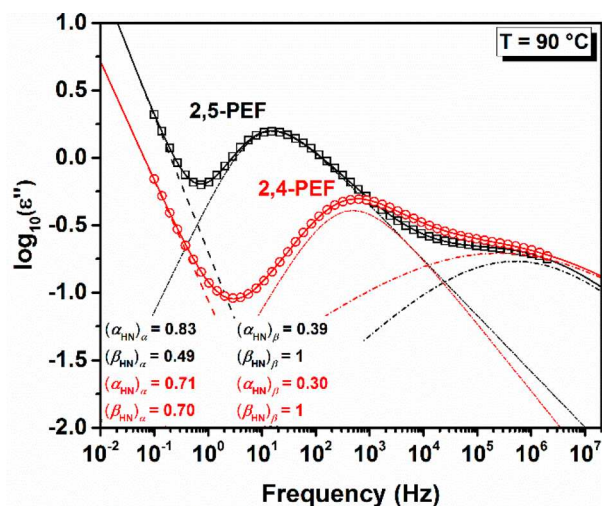


**Figure 4.** Illustration of the analytical procedure used to investigate the relaxation phenomena by fitting isothermal dielectric loss spectra (Figure 3) with a conductivity contribution and two Havriliak–Negami (HN) complex functions. The shape HN parameters for both the  $\alpha$  and  $\beta$  processes in amorphous 2,5-PEF and 2,4-PEF at  $90\text{ }^{\circ}\text{C}$  are also reported. This procedure allows obtaining the relaxation map in Figure 5.

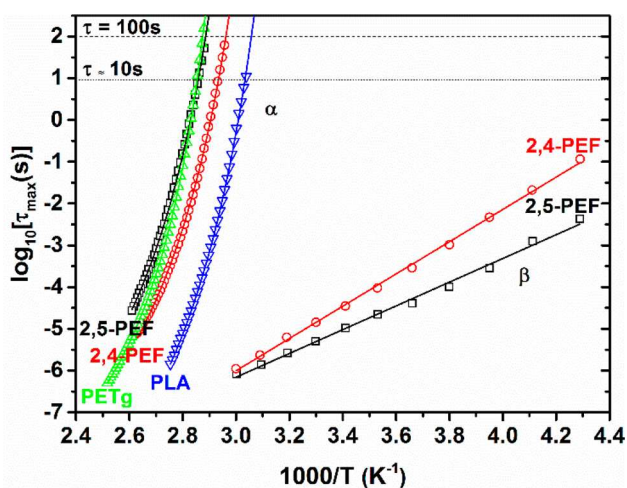


**Figure 5.** Relaxation map giving the temperature dependence of the relaxation time for both the  $\alpha$  and  $\beta$  processes in amorphous 2,5-PEF and 2,4-PEF as compared to PETg and PLA (the data for PETg and PLA have been reported from Rijal et al.<sup>58</sup>).

$\text{mol}^{-1}$  for PHBV,<sup>45</sup>  $79 \pm 10\text{ kJ mol}^{-1}$  for PET<sup>57</sup>) and can be associated with the local motions of the polar subunits. In particular, the  $E_a$  value obtained for 2,5-PEF is very close to the

value obtained by Dimitriadis et al.<sup>26</sup> on semicrystalline PEF ( $58\text{ kJ mol}^{-1}$ ). A higher value of  $E_a$  was found for the  $\beta$  relaxation of 2,4-PEF as compared to 2,5-PEF, which clearly originates from the differences in the chemical structure of the repeating units and not from the fitting procedure (the shape HN parameters for the  $\beta$  relaxation are similar in both 2,5-PEF and 2,4-PEF, and all the peaks could be fit by a single HN function; see Figure 4). Therefore, if the molecular structures are compared, one can deduce that having the carboxylic group in the 2,4-position on the furan ring reduces the molecular mobility of the local dipolar subunit with respect to having it in the 2,5-position.

The experimental data in the range of the  $\alpha$  relaxations could be fit by a Vogel–Tamman–Fulcher law (VFT) with the equation<sup>60–62</sup>

$$\tau_{\max} = \tau_0 \exp\left(\frac{DT_0}{T - T_0}\right) \quad (7)$$

where  $\tau_{\max}$  is the relaxation time at the maximum of the  $\alpha$  relaxation,  $D$  is a dimensionless parameter defined as the steepness strength,  $T_0$  is a reference temperature, and  $\tau_0$  is a pre-exponential factor. The relaxation map in Figure 5 shows that the  $\alpha$  relaxation of 2,5-PEF occurs at higher temperature as compared to the  $\alpha$  relaxation of 2,4-PEF. Conventionally, a relaxation time equal to 100 s is selected; in this case, the temperature read at a relaxation time equal to 10 s better relates to the calorimetric glass transition temperature obtained by MT-DSC with a period of 60 s<sup>63</sup> (Table 3). The literature provides several examples of dielectric values of the glass transition temperature that are in good agreement with the values obtained by thermal techniques, such as DSC or MT-DSC.<sup>64,65</sup>

The fragility index  $m$  was introduced by Angell<sup>59</sup> as a parameter to classify glass-formers on the basis of the temperature dependence of their structural relaxation:

$$m = \left. \frac{d \log(\tau_{\max})}{d\left(\frac{T_g}{T}\right)} \right|_{T=T_g} \quad (8)$$

where  $T_g/T$  is the temperature reduced with respect to the glass transition temperature  $T_g$ .

Small values of the fragility index  $m$  indicate an Arrhenius-like temperature dependence of the relaxation time (which is typical of “strong” supercooled liquids), i.e.,  $\log(\tau_{\max})(T)$  is quasi-linear in the whole  $T_g/T$  range. On the other hand, when  $\log(\tau_{\max})(T)$  strongly deviates from linearity, the corresponding glass-forming liquid is rather considered as “fragile”. The  $m$  values obtained for 2,5-PEF and 2,4-PEF (116 and 120,

**Table 3.** Values of the Glass Transition Temperature Obtained by DRS for  $\tau = 100$  and 10 s,  $D$  Is a Dimensionless Parameter from the VFT Fitting Equation,  $T_0$  Is a Reference Temperature,  $\tau_0$  Is the Relaxation Time Extrapolated at an Infinite Temperature,  $m$  Is the Fragility Index (Defined According to Angell<sup>59</sup>),  $\tau_{0,A}$  Is a Pre-exponential Factor in the Arrhenius Law, and  $E_a$  Is the Activation Energy of the  $\alpha$  Relaxation<sup>a</sup>

samples	$T_g(\tau = 100\text{ s})\text{ (}^{\circ}\text{C)}$	$T_g(\tau = 10\text{ s})\text{ (}^{\circ}\text{C)}$	$D$	$T_0\text{ (}^{\circ}\text{C)}$	$\log(\tau_0)\text{ (s)}$	$m$	$\log(\tau_{0,A})\text{ (s)}$	$E_a\text{ (kJ mol}^{-1}\text{)}$
2,5-PEF	73	77	4.46	32	−12	$116 \pm 10$	−15	56
2,4-PEF	65	68	4.32	25	−12	$120 \pm 5$	−17	75
PETg	75	77	3	44	−11	152		
PLA	54	54	5	17	−14	141		

<sup>a</sup>The data for PETg and PLA have been reported from Rijal et al.<sup>58</sup>

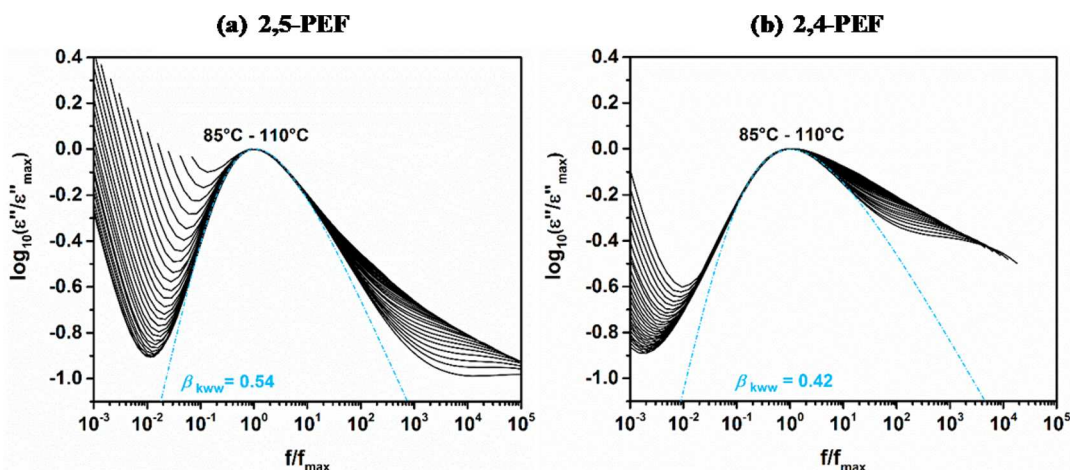


**Figure 6.** Master plots of (a) amorphous 2,5-PEF and (b) amorphous 2,4-PEF obtained by horizontally shifting at  $f = f_{\max}$  the isothermal spectra recorded from 85 to 110 °C.

respectively) are significantly lower compared to other polyesters (142 for PET,<sup>66</sup> 152 for PETg,<sup>58</sup> and 141 for PLA<sup>44</sup>) (Table 3). Such values correspond to “fragile” glass-formers, which is the behavior classically expected for macromolecules with extended van der Waals interactions or hydrogen bonds between chains.<sup>59,67</sup> In terms of fragility, rather than being close to PET, PETg, and PLA, PEF seems to be closer to other aliphatic polyesters, such as poly(butylene succinate) (PBS) ( $m = 125$ <sup>68</sup>) or poly(hydroxybutyrate-co-valerate) (PHBV) ( $m = 106$ <sup>45</sup>).

Many works investigate the relationships between the glass transition temperature, the fragility index, and the cooperativity in polymers. Sasaki et al.,<sup>69</sup> for instance, show that in PS derivatives the size of the cooperative rearranging regions (CRR) increases with increasing fragility. Recent investigations showed that  $m$  is a key parameter to evaluate the molecular arrangement and the relaxation dynamics of amorphous phases, for it is supposed to be strongly dependent on the packing efficiency of the macromolecules as well as on the stiffness of their backbone.<sup>27</sup> Indeed, the packing efficiency in glassy materials is related to the free volume, as it was pointed out that materials with lower fragility have less free volume.<sup>70</sup> The only difference between PEF and PET is in the composition of the aromatic ring. However, the stiffness of their backbones is similar, for their glass transition temperatures are pretty much the same (Table 3). It is therefore reasonable to admit that the packing efficiency is higher in PEF with respect to PET, that is to say, that less free volume can be found in PEF as compared to PET. This hypothesis perfectly correlates to the evidence of higher barrier properties reported for PEF in comparison with PET.<sup>15–18</sup>

The literature reports that the non-Debye relaxation behavior in the time domain ( $t$ ) is empirically described by the Kohlrausch–Williams–Watts (KWW) function as follows:<sup>71</sup>

$$\phi(t) = e^{-(t/\tau_{\text{KWW}})^{\beta_{\text{KWW}}}} \quad (9)$$

where  $\phi(t)$  is the correlation function,  $\beta_{\text{KWW}}$  ( $0 < \beta_{\text{KWW}} \leq 1$ ) is a stretching parameter, and  $\tau_{\text{KWW}}$  is the relaxation time for  $\beta_{\text{KWW}} = 1$ . The stretching parameter  $\beta_{\text{KWW}}$  allows comparing any asymmetrical broadening behavior of the relaxation process at short times (e.g., high frequencies) with the exponential decay corresponding to a Debye relaxation with  $\beta_{\text{KWW}} = 1$ . The

HN parameters (eqs 2–5) are correlated with  $\beta_{\text{KWW}}$  as follows:<sup>72</sup>

$$\log\left(\frac{\tau_{\text{HN}}}{\tau_{\text{KWW}}}\right) \approx 2.6(1 - \beta_{\text{KWW}})^{0.5} e^{(-3\beta_{\text{KWW}})} \quad (10)$$

with a good approximation of eq 10 given by

$$\beta_{\text{KWW}} = (\alpha_{\text{HN}}\beta_{\text{HN}})^{0.813} \quad (11)$$

The master plots reported in Figure 6 were obtained by shifting the spectra recorded at different temperatures (from 85 to 110 °C with a step of 1 °C) in order to superimpose them onto a reference spectrum (at 90 °C) and can be used to graphically visualize the stretching parameter  $\beta_{\text{KWW}}$ . This graphical procedure allows ascertaining whether temperature plays an active role in the shape of the structural relaxation process, which would have resulted in different distributions of the relaxation times at different temperatures. The values of  $\beta_{\text{KWW}}$  experimentally found for 2,5-PEF and 2,4-PEF (0.54 and 0.42, respectively) are in agreement with the values obtained by eq 11 ( $0.48 \pm 0.02$  for 2,5-PEF and  $0.56 \pm 0.07$  for 2,4-PEF) and also with the values previously reported for PETg ( $\beta_{\text{KWW}} \approx 0.40$ )<sup>73</sup> and PLA ( $\beta_{\text{KWW}} \approx 0.35$ ).<sup>74</sup>

When fitting the experimental data with the HN function (eq 2), the dielectric strength  $\Delta\epsilon_\alpha$  is also obtained, which was defined (according to the generalized form of the Debye’s theory) by Onsager, Fröhlich, and Kirkwood as<sup>75</sup>

$$\Delta\epsilon = \frac{1}{3\epsilon_0} G_{\text{K}} \frac{\mu^2 N}{k_{\text{B}} T V} \quad (12)$$

where  $\epsilon_0$  is the vacuum permittivity,  $G_{\text{K}}$  is the Kirkwood correlation factor,  $\mu^2$  is the time-correlation function of the total dipole moment,  $k_{\text{B}}$  is Boltzmann’s constant,  $T$  is the temperature, and  $N/V$  is the volume density of dipoles. The temperature dependence of the dielectric strength  $\Delta\epsilon_\alpha$  can be plotted in the  $\alpha$  relaxation’s temperature range, as reported in Figure 7 for amorphous 2,5-PEF, 2,4-PEF, PETg, and PLA. In general, the dielectric strength decreases as temperature increases.<sup>74,75</sup>

Figure 7 shows that the temperature dependence of  $\Delta\epsilon_\alpha$  for both 2,5-PEF and 2,4-PEF has the same (negative) slope, which is significantly higher when compared to others polyesters. This is a remarkable result that deserves to be pointed out and that

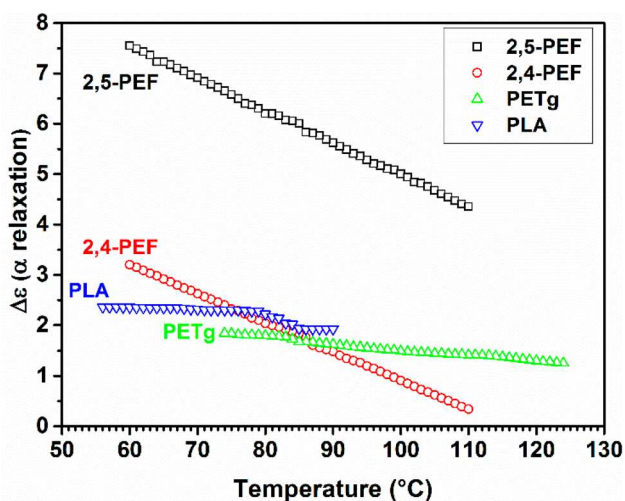


**Figure 7.** Dielectric strength ( $\Delta\epsilon_\alpha$ ) as a function of temperature for amorphous 2,5-PEF, 2,4-PEF, PETg, and PLA in the  $\alpha$  relaxation's temperature range (the data for PETg and PLA have been extracted from Rijal et al.<sup>58</sup>).

required MDS for further investigation. The individual dipole moment of a given polymer chain at a time  $t$  can be calculated by MDS according to the expression

$$\vec{\mu}(t) = \sum_{\alpha=1}^{N_a} q_\alpha \vec{r}_\alpha(t) \quad (13)$$

where  $q_\alpha$  and  $\vec{r}_\alpha(t)$  are respectively the fixed charge localized on the atom  $\alpha$  and its position at the time  $t$ , and  $N_a$  is the number of atoms in the considered polymer chain.

The dipole moment distributions  $P(\mu)$  obtained by MDS runs on 2,5-PEF and 2,4-PEF polymer chains are shown in Figure 8. 2,5-PEF and 2,4-PEF polymer chains experience a broad range of dipole moments because of their intrinsic flexibility; besides, the average dipole moment of 2,4-PEF polymer chains is significantly lower with respect to the average dipole moment of 2,5-PEF polymer chains ( $\mu \approx 6.2$  and  $8.2$  D for 2,4-PEF and 2,5-PEF, respectively). Dipole correlations are

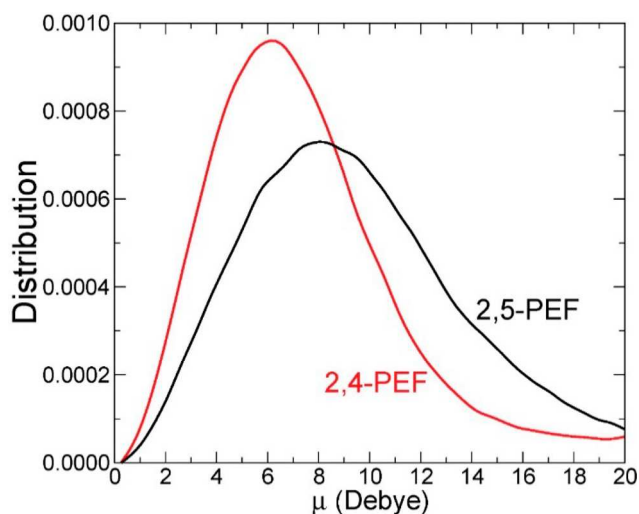


**Figure 8.** Distribution of the dipole moment for 2,5-PEF and 2,4-PEF polymer chains obtained from MDS.

well described by the so-called Kirkwood correlation factor  $G_K$  given by the relation

$$G_K = 1 + (N - 1) \langle \vec{\mu}_i \cdot \vec{\mu}_j \rangle / \langle \mu^2 \rangle \quad (14)$$

where  $\vec{\mu}_i$  is the dipole moment of the molecule  $i$  and  $\langle \vec{\mu}_i \cdot \vec{\mu}_j \rangle$  indicates an average over distinct pairs of molecules ( $i \neq j$ ). The Kirkwood correlation factor accounts for the orientational correlation of neighboring dipoles. In this study,  $G_K \approx 1$  has been computed for both 2,4-PEF and 2,5-PEF systems, suggesting no specific correlation between dipoles. Based on both  $\mu$  and  $G_K$  values and on the expression of the dielectric strength defined in eq 9, it is thus possible to propose that the significant difference in the dielectric strength obtained between 2,4-PEF and 2,5-PEF mostly originates from the different values found for the average dipole moment, which is higher for 2,5-PEF polymer chains with respect to 2,4-PEF polymer chains.

## CONCLUSIONS

Different techniques were used to investigate PEFs and compare them with well-known polymers belonging to the same family (polyesters). The comparison between 2,5-PEF and 2,4-PEF indicates that PEFs properties may be highly affected by the position of the carbonyl group on the furan ring. In particular, DSC showed that the effects on the capability of the polymer chains to crystallize is dramatic, most likely because the asymmetry in the 2,4-FDCA disrupts the crystallization. This work benefited from DRS sensitivity to further investigate the dielectric properties of PEFs and their consequences on molecular mobility. The local  $\beta$  relaxations were found to be quite different in 2,5-PEF and 2,4-PEF, suggesting that PEFs with an asymmetrical position of the carbonyl group on the furan ring require more time to relax with respect to their symmetrical counterparts. The investigations about the structural  $\alpha$  relaxation revealed that 2,5-PEF and 2,4-PEF both behave as “fragile” glass-forming systems, which is typical of most polymers. MDS performed on oligomers (30 chains of 7 repeating units) provided evidence that 2,5-PEF has a higher value of the average dipole moment  $\mu$  with respect to 2,4-PEF, which correlates with the higher dielectric strength  $\Delta\epsilon_\alpha$  measured by DRS.

## ASSOCIATED CONTENT

### Supporting Information

The Supporting Information is available free of charge on the ACS Publications website at DOI: 10.1021/acs.macromol.8b00108.

Figure S1: DSC thermograms obtained after 1 week annealing at 140 °C with a heating ramp at 10 K min<sup>-1</sup> for 2,4-PEF (PDF)

## AUTHOR INFORMATION

### Corresponding Author

\*(A.E.) E-mail [antonella.esposito@univ-rouen.fr](mailto:antonella.esposito@univ-rouen.fr).

### ORCID

Antonella Esposito: 0000-0003-0507-1417

Laurent Delbreilh: 0000-0002-9322-7153

### Notes

The authors declare no competing financial interest.



## ACKNOWLEDGMENTS

The authors thank the Région Normandie and the European FEDER for their financial support through the SCAMPI project. The authors acknowledge the use of the facilities of the CRI (Villeneuve d'Ascq, France) where calculations were carried out.

## REFERENCES

- (1) Belgacem, M. N.; Gandini, A. *Monomers, Polymers and Composites from Renewable Resources*; Elsevier: 2011.
- (2) Wilsens, C. H. R. M.; Noorder, B. A. J.; Rastogi, S. Aromatic Thermotropic Polyesters Based on 2,5-Furandicarboxylic Acid and Vanillic Acid. *Polymer* **2014**, *55* (10), 2432–2439.
- (3) Gubbels, E.; Jasinska-Walc, L.; Koning, C. E. Synthesis and Characterization of Novel Renewable Polyesters Based on 2,5-Furandicarboxylic Acid and 2,3-Butanediol. *J. Polym. Sci., Part A: Polym. Chem.* **2013**, *51* (4), 890–898.
- (4) Wu, J.; Eduard, P.; Thiyagarajan, S.; Jasinska-Walc, L.; Rozanski, A.; Guerra, C. F.; Noorder, B. A. J.; van Haveren, J.; van Es, D. S.; Koning, C. E. Semicrystalline Polyesters Based on a Novel Renewable Building Block. *Macromolecules* **2012**, *45* (12), 5069–5080.
- (5) Konstantopoulou, M.; Terzopoulou, Z.; Nerantzaki, M.; Tsagkalias, J.; Achilias, D. S.; Bikiaris, D. N.; Exarhopoulos, S.; Papageorgiou, D. G.; Papageorgiou, G. Z. Poly(Ethylene Furanoate-Co-Ethylene Terephthalate) Biobased Copolymers: Synthesis, Thermal Properties and Cocrystallization Behavior. *Eur. Polym. J.* **2017**, *89*, 349–366.
- (6) Matos, M.; Sousa, A. F.; Fonseca, A. C.; Freire, C. S. R.; Coelho, J. F. J.; Silvestre, A. J. D. A New Generation of Furanic Copolyesters with Enhanced Degradability: Poly(Ethylene 2,5-Furandicarboxylate)-Co-Poly(Lactic Acid) Copolyesters. *Macromol. Chem. Phys.* **2014**, *215* (22), 2175–2184.
- (7) Sherman, L. M. Coca-Cola Debuts First 100% Biobased PET Bottle; <http://www.ptonline.com/blog/post/coca-cola-debuts-first-100-biobased-pet-bottle> (accessed June 15, 2017).
- (8) Gandini, A.; Lacerda, T. M.; Carvalho, A. J. F.; Trovatti, E. Progress of Polymers from Renewable Resources: Furans, Vegetable Oils, and Polysaccharides. *Chem. Rev.* **2016**, *116* (3), 1637–1669.
- (9) Sousa, A. F.; Matos, M.; Freire, C. S. R.; Silvestre, A. J. D.; Coelho, J. F. J. New Copolyesters Derived from Terephthalic and 2,5-Furandicarboxylic Acids: A Step Forward in the Development of Biobased Polyesters. *Polymer* **2013**, *54* (2), 513–519.
- (10) de Jong, E.; Dam, M. A.; Sipos, L.; Gruter, G.-J. M. Furandicarboxylic Acid (FDCA), A Versatile Building Block for a Very Interesting Class of Polyesters. In *Biobased Monomers, Polymers, and Materials*; ACS Symposium Series; *ACS Symp. Ser.* **2012**, *1105*, 1–13.
- (11) Papageorgiou, G. Z.; Tsanaktsis, V.; Bikiaris, D. N. Synthesis of Poly(Ethylene Furandicarboxylate) Polyester Using Monomers Derived from Renewable Resources: Thermal Behavior Comparison with PET and PEN. *Phys. Chem. Chem. Phys.* **2014**, *16* (17), 7946–7958.
- (12) Knoop, R. J. I.; Vogelzang, W.; van Haveren, J.; van Es, D. S. High Molecular Weight Poly(Ethylene-2,5-Furanoate); Critical Aspects in Synthesis and Mechanical Property Determination. *J. Polym. Sci., Part A: Polym. Chem.* **2013**, *51* (19), 4191–4199.
- (13) Gandini, A.; Silvestre, A. J. D.; Neto, C. P.; Sousa, A. F.; Gomes, M. The Furan Counterpart of Poly(Ethylene Terephthalate): An Alternative Material Based on Renewable Resources. *J. Polym. Sci., Part A: Polym. Chem.* **2009**, *47* (1), 295–298.
- (14) Pellis, A.; Haernvall, K.; Pichler, C. M.; Ghazaryan, G.; Breinbauer, R.; Guebitz, G. M. Enzymatic Hydrolysis of Poly(Ethylene Furanoate). *J. Biotechnol.* **2016**, *235*, 47–53.
- (15) Burgess, S. K.; Karvan, O.; Johnson, J. R.; Kriegel, R. M.; Koros, W. J. Oxygen Sorption and Transport in Amorphous Poly(Ethylene Furanoate). *Polymer* **2014**, *55* (18), 4748–4756.
- (16) Burgess, S. K.; Kriegel, R. M.; Koros, W. J. Carbon Dioxide Sorption and Transport in Amorphous Poly(Ethylene Furanoate). *Macromolecules* **2015**, *48* (7), 2184–2193.
- (17) Burgess, S. K.; Mikkilineni, D. S.; Yu, D. B.; Kim, D. J.; Mubarak, C. R.; Kriegel, R. M.; Koros, W. J. Water Sorption in Poly(Ethylene Furanoate) Compared to Poly(Ethylene Terephthalate). Part 1: Equilibrium Sorption. *Polymer* **2014**, *55* (26), 6861–6869.
- (18) Burgess, S. K.; Mikkilineni, D. S.; Yu, D. B.; Kim, D. J.; Mubarak, C. R.; Kriegel, R. M.; Koros, W. J. Water Sorption in Poly(Ethylene Furanoate) Compared to Poly(Ethylene Terephthalate). Part 2: Kinetic Sorption. *Polymer* **2014**, *55* (26), 6870–6882.
- (19) Codou, A.; Guigo, N.; van Berkel, J.; de Jong, E.; Sbirrazzuoli, N. Non-Isothermal Crystallization Kinetics of Biobased Poly(Ethylene 2,5-Furandicarboxylate) Synthesized via the Direct Esterification Process. *Macromol. Chem. Phys.* **2014**, *215* (21), 2065–2074.
- (20) Stoclet, G.; Gobius du Sart, G.; Yeniad, B.; de Vos, S.; Lefebvre, J. M. Isothermal Crystallization and Structural Characterization of Poly(Ethylene-2,5-Furanoate). *Polymer* **2015**, *72*, 165–176.
- (21) van Berkel, J. G.; Guigo, N.; Kolstad, J. J.; Sipos, L.; Wang, B.; Dam, M. A.; Sbirrazzuoli, N. Isothermal Crystallization Kinetics of Poly(Ethylene 2,5-Furandicarboxylate). *Macromol. Mater. Eng.* **2015**, *300* (4), 466–474.
- (22) Guigo, N.; van Berkel, J.; de Jong, E.; Sbirrazzuoli, N. Modelling the Non-Isothermal Crystallization of Polymers: Application to Poly(Ethylene 2,5-Furandicarboxylate). *Thermochim. Acta* **2017**, *650*, 66–75.
- (23) Mao, Y.; Kriegel, R. M.; Bucknall, D. G. The Crystal Structure of Poly(Ethylene Furanoate). *Polymer* **2016**, *102*, 308–314.
- (24) Codou, A.; Moncel, M.; van Berkel, J. G.; Guigo, N.; Sbirrazzuoli, N. Glass Transition Dynamics and Cooperativity Length of Poly(Ethylene 2,5-Furandicarboxylate) Compared to Poly(Ethylene Terephthalate). *Phys. Chem. Chem. Phys.* **2016**, *18* (25), 16647–16658.
- (25) Burgess, S. K.; Leisen, J. E.; Kraftschik, B. E.; Mubarak, C. R.; Kriegel, R. M.; Koros, W. J. Chain Mobility, Thermal, and Mechanical Properties of Poly(Ethylene Furanoate) Compared to Poly(Ethylene Terephthalate). *Macromolecules* **2014**, *47* (4), 1383–1391.
- (26) Dimitriadis, T.; Bikiaris, D. N.; Papageorgiou, G. Z.; Floudas, G. Molecular Dynamics of Poly(Ethylene-2,5-Furanoate) (PEF) as a Function of the Degree of Crystallinity by Dielectric Spectroscopy and Calorimetry. *Macromol. Chem. Phys.* **2016**, *217* (18), 2056–2062.
- (27) Esposito, A.; Delpouve, N.; Causin, V.; Dhotel, A.; Delbreilh, L.; Dargent, E. From a Three-Phase Model to a Continuous Description of Molecular Mobility in Semicrystalline Poly(Hydroxybutyrate-Co-Hydroxyvalerate). *Macromolecules* **2016**, *49* (13), 4850–4861.
- (28) Thiyagarajan, S.; Pukin, A.; van Haveren, J.; Lutz, M.; Van Es, D. S. Concurrent Formation of Furan-2,5- and Furan-2,4-Dicarboxylic Acid: Unexpected Aspects of the Henkel Reaction. *RSC Adv.* **2013**, *3* (36), 15678–15686.
- (29) Thiyagarajan, S.; Vogelzang, W.; Knoop, R. J. I.; Frissen, A. E.; van Haveren, J.; van Es, D. S. Biobased Furandicarboxylic Acids (FDCA): Effects of Isomeric Substitution on Polyester Synthesis and Properties. *Green Chem.* **2014**, *16* (4), 1957–1966.
- (30) Couderc, H.; Delbreilh, L.; Saiter, A.; Grenet, J.; De Souza, N.; Saiter, J. M. Relaxation in Poly(Ethylene Terephthalate Glycol)/Montmorillonite Nanocomposites Studied by Dielectric Methods. *J. Non-Cryst. Solids* **2007**, *353* (47), 4334–4338.
- (31) Delpouve, N.; Delbreilh, L.; Stoclet, G.; Saiter, A.; Dargent, E. Structural Dependence of the Molecular Mobility in the Amorphous Fractions of Polylactide. *Macromolecules* **2014**, *47* (15), 5186–5197.
- (32) Hamonic, F.; Prevosto, D.; Dargent, E.; Saiter, A. Contribution of Chain Alignment and Crystallization in the Evolution of Cooperativity in Drawn Polymers. *Polymer* **2014**, *55* (12), 2882–2889.
- (33) Delpouve, N.; Saiter, A.; Dargent, E. Cooperativity Length Evolution during Crystallization of Poly(Lactic Acid). *Eur. Polym. J.* **2011**, *47* (12), 2414–2423.
- (34) Schaumburg, G. Novocontrol Introduces High Quality Low Cost Interdigitated Comb Electrodes. *Dielectr. Newsl.* **2006**, *22*, 5–7.

- (35) Havriliak, S.; Negami, S. A Complex Plane Analysis of  $\alpha$ -Dispersions in Some Polymer Systems. *J. Polym. Sci., Part C: Polym. Symp.* **1966**, *14* (1), 99–117.
- (36) Havriliak, S.; Negami, S. A Complex Plane Representation of Dielectric and Mechanical Relaxation Processes in Some Polymers. *Polymer* **1967**, *8*, 161–210.
- (37) Smith, W.; Forester, T. R.; Todorov, I. T. *The DL\_POLY Classic User Manual*; TFC, STFC Daresbury Laboratory: Daresbury, Warrington, Cheshire, WA4 4AD, United Kingdom, 2012.
- (38) Computational Collaboration Project No 5-Software for simulation of condensed phases. CCP5 Computer Simulations of Condensed Phases; <http://www.ccp5.ac.uk/software> (accessed Jan 12, 2018).
- (39) Wang, J.; Wolf, R. M.; Caldwell, J. W.; Kollman, P. A.; Case, D. A. Development and Testing of a General Amber Force Field. *J. Comput. Chem.* **2004**, *25* (9), 1157–1174.
- (40) Wolf, D.; Keblinski, P.; Phillpot, S. R.; Eggebrecht, J. Exact Method for the Simulation of Coulombic Systems by Spherically Truncated, Pairwise R<sup>-1</sup> Summation. *J. Chem. Phys.* **1999**, *110* (17), 8254–8282.
- (41) Frisch, M.; Trucks, G. W.; Schlegel, H. B.; Scuseria, G. E.; Robb, M. A.; Cheeseman, J. R.; Scalmani, G.; Barone, V.; Mennucci, B.; Petersson, G. A.; et al. *Gaussian 09*, Revision D. 01; Gaussian, Inc.: Wallingford, CT, 2009.
- (42) Delbreilh, L.; Dargent, E.; Grenet, J.; Saiter, J.-M.; Bernès, A.; Lacabanne, C. Study of Poly(Bisphenol A Carbonate) Relaxation Kinetics at the Glass Transition Temperature. *Eur. Polym. J.* **2007**, *43* (1), 249–254.
- (43) Delbreilh, L.; Negahban, M.; Benzohra, M.; Lacabanne, C.; Saiter, J. M. Glass Transition Investigated by a Combined Protocol Using Thermostimulated Depolarization Currents and Differential Scanning Calorimetry. *J. Therm. Anal. Calorim.* **2009**, *96* (3), 865–871.
- (44) Arnoult, M.; Dargent, E.; Mano, J. F. Mobile Amorphous Phase Fragility in Semi-Crystalline Polymers: Comparison of PET and PLLA. *Polymer* **2007**, *48* (4), 1012–1019.
- (45) Crétois, R.; Delbreilh, L.; Dargent, E.; Follain, N.; Lebrun, L.; Saiter, J. M. Dielectric Relaxations in Polyhydroxyalkanoates/Organoclay Nanocomposites. *Eur. Polym. J.* **2013**, *49* (11), 3434–3444.
- (46) Groeninckx, G.; Reynaers, H.; Berghmans, H.; Smets, G. Morphology and Melting Behavior of Semicrystalline Poly(Ethylene Terephthalate). I. Isothermally Crystallized PET. *J. Polym. Sci., Polym. Phys. Ed.* **1980**, *18* (6), 1311–1324.
- (47) Sperling, L. H. Multicomponent Polymeric Materials. In *Introduction to Physical Polymer Science*; John Wiley & Sons, Inc.: 2005; pp 687–756.
- (48) Okazaki, I.; Wunderlich, B. Reversible Local Melting in Polymer Crystals. *Macromol. Rapid Commun.* **1997**, *18* (4), 313–318.
- (49) Beaman, R. G. Relation between (Apparent) Second-Order Transition Temperature and Melting Point. *J. Polym. Sci.* **1952**, *9* (5), 470–472.
- (50) Askadskii, A. A. *Computational Materials Science of Polymers*; Cambridge Int Science Publishing: 2003.
- (51) Lee, W. A.; Knight, G. J. Ratio of the Glass Transition Temperature to the Melting Point in Polymers. *Br. Polym. J.* **1970**, *2* (1), 73–80.
- (52) van Krevelen, D. W.; te Nijenhuis, K. *Properties of Polymers: Their Correlation with Chemical Structure; Their Numerical Estimation and Prediction from Additive Group Contributions*; Elsevier: 2009.
- (53) Cao, X.; Mohamed, A.; Gordon, S. H.; Willett, J. L.; Sessa, D. J. DSC Study of Biodegradable Poly(Lactic Acid) and Poly(Hydroxy Ester Ether) Blends. *Thermochim. Acta* **2003**, *406* (1), 115–127.
- (54) Kim, H.-S.; Yang, H.-S.; Kim, H.-J.; Kattan, M. Relaxations IN Amorphous and Semi-Crystalline Polyesters. *J. Therm. Anal. Calorim.* **2004**, *76* (2), 379–394.
- (55) Starkweather, H. W.; Avakian, P.; Fontanella, J. J.; Wintersgill, M. C. Internal Motions in Polylactide and Related Polymers. *Macromolecules* **1993**, *26* (19), 5084–5087.
- (56) Soccio, M.; Martínez-Tong, D. E.; Alegría, A.; Munari, A.; Lotti, N. Molecular Dynamics of Fully Biobased Poly(Butylene 2,5-Furanoate) as Revealed by Broadband Dielectric Spectroscopy. *Polymer* **2017**, *128*, 24.
- (57) Mackintosh, A. R.; Liggat, J. J. Dynamic Mechanical Analysis of Poly(Trimethylene Terephthalate)—A Comparison with Poly(Ethylene Terephthalate) and Poly(Ethylene Naphthalate). *J. Appl. Polym. Sci.* **2004**, *92* (5), 2791–2796.
- (58) Rijal, B.; Delbreilh, L.; Saiter, A. Dynamic Heterogeneity and Cooperative Length Scale at Dynamic Glass Transition in Glass Forming Liquids. *Macromolecules* **2015**, *48* (22), 8219–8231.
- (59) Angell, C. A. Spectroscopy Simulation and Scattering, and the Medium Range Order Problem in Glass. *J. Non-Cryst. Solids* **1985**, *73* (1), 1–17.
- (60) Vogel, H. Z. *Law Relat. Viscosity Liq. Temp. Vogel Hans Phys. Z.* **1921**, *22*, 645–646.
- (61) Tammann, G.; Hesse, W. Die Abhängigkeit Der Viscosität von Der Temperatur Bie Unterkühlten Flüssigkeiten. *Z. Für Anorg. Allg. Chem.* **1926**, *156* (1), 245–257.
- (62) Fulcher, G. S. Analysis of Recent Measurements of the Viscosity of Glasses. *J. Am. Ceram. Soc.* **1925**, *8* (6), 339–355.
- (63) Saiter, J. M.; Grenet, J.; Dargent, E.; Saiter, A.; Delbreilh, L. Glass Transition Temperature and Value of the Relaxation Time at T<sub>g</sub> in Vitreous Polymers. *Macromol. Symp.* **2007**, *258* (1), 152–161.
- (64) Leonardi, A.; Dantras, E.; Dandurand, J.; Lacabanne, C. Dielectric Relaxations in PEEK by Combined Dynamic Dielectric Spectroscopy and Thermally Stimulated Current. *J. Therm. Anal. Calorim.* **2013**, *111* (1), 807–814.
- (65) Soto Puente, J. A.; Rijal, B.; Delbreilh, L.; Fatyeyeva, K.; Saiter, A.; Dargent, E. Segmental mobility and glass transition of poly(ethylene-vinyl acetate) copolymers: Is there a continuum in the dynamic glass transitions from PVAc to PE? *Polymer* **2015**, *76*, 213–219.
- (66) Dargent, E.; Bureau, E.; Delbreilh, L.; Zumailan, A.; Saiter, J. M. Effect of Macromolecular Orientation on the Structural Relaxation Mechanisms of Poly(Ethylene Terephthalate). *Polymer* **2005**, *46* (9), 3090–3095.
- (67) Bouthegourd, E.; Esposito, A.; Lourdin, D.; Saiter, A.; Saiter, J. M. Size of the cooperative rearranging regions versus fragility in complex glassy systems: influence of the structure and the molecular interactions. *Phys. B* **2013**, *425*, 83–89.
- (68) Charlon, S.; Delbreilh, L.; Dargent, E.; Follain, N.; Soulestin, J.; Marais, S. Influence of Crystallinity on the Dielectric Relaxations of Poly(Butylene Succinate) and Poly[(Butylene Succinate)-Co-(Butylene Adipate)]. *Eur. Polym. J.* **2016**, *84*, 366–376.
- (69) Sasaki, T.; Ichimura, M.; Irie, S. Correlation between Fragility and Cooperativity in Segmental Dynamics of Glass-Forming Para-Substituted Polystyrenes. *Polym. J.* **2015**, *47* (10), 687–694.
- (70) Matsuoka, S. Entropy, Free Volume, and Cooperative Relaxation. *J. Res. Natl. Inst. Stand. Technol.* **1997**, *102* (2), 213–228.
- (71) Williams, G.; Watts, D. C. Non-Symmetrical Dielectric Relaxation Behaviour Arising from a Simple Empirical Decay Function. *Trans. Faraday Soc.* **1970**, *66* (0), 80–85.
- (72) Alvarez, F.; Alegria, A.; Colmenero, J. Relationship between the Time-Domain Kohlrausch-Williams-Watts and Frequency-Domain Havriliak-Negami Relaxation Functions. *Phys. Rev. B: Condens. Matter Mater. Phys.* **1991**, *44* (14), 7306.
- (73) Massa, D. J.; O'Reilly, J. M.; Perchak, D. R.; Gillmor, J. R. Physical Aging, Coreset Curl, and Stress Relaxation of PETG Polyester, 2000.
- (74) Mano, J. F.; Gómez Ribelles, J. L.; Alves, N. M.; Salmerón Sanchez, M. Glass Transition Dynamics and Structural Relaxation of PLLA Studied by DSC: Influence of Crystallinity. *Polymer* **2005**, *46* (19), 8258–8265.
- (75) Schönhals, A.; Kremer, F. Analysis of Dielectric Spectra. In *Broadband Dielectric Spectroscopy*; Kremer, P. D. F., Schönhals, P.-D. D. A., Eds.; Springer: Berlin, 2003; pp 59–98.
- (76) Yin, H.; Napolitano, S.; Schönhals, A. Molecular Mobility and Glass Transition of Thin Films of Poly(Bisphenol A Carbonate). *Macromolecules* **2012**, *45* (3), 1652–1662.



## Determination of the equilibrium enthalpy of melting of two-phase semi-crystalline polymers by fast scanning calorimetry



Clément Fosse<sup>a</sup>, Aurélie Bourdet<sup>a</sup>, Estève Ernault<sup>a</sup>, Antonella Esposito<sup>a,\*</sup>, Nicolas Delpouve<sup>a</sup>, Laurent Delbreilh<sup>a</sup>, Shanmugam Thiyagarajan<sup>b</sup>, Rutger J.I. Knoop<sup>b</sup>, Eric Dargent<sup>a</sup>

<sup>a</sup> Normandie Univ, UNIROUEN Normandie, INSA Rouen, CNRS, Groupe de Physique des Matériaux, 76000 Rouen, France

<sup>b</sup> Wageningen Food & Biobased Research, P.O. Box 17, 6700 AA Wageningen, the Netherlands

### ARTICLE INFO

#### Keywords:

Fast scanning calorimetry  
Rigid amorphous fraction  
Enthalpy of melting  
PEF  
PBF

### ABSTRACT

The equilibrium enthalpy of melting  $\Delta H_m^0$  [ $\text{J}\cdot\text{g}^{-1}$ ] is an extrapolated thermodynamic quantity attributed to crystallizable macromolecules and widely used to characterize polymers in their semi-crystalline state, for it allows estimating the degree of crystallinity by direct comparison with the enthalpy of melting obtained from differential scanning calorimetry.  $\Delta H_m^0$  is typically obtained by cross-comparing the results obtained by at least two techniques. This work proposes a simplified experimental protocol to determine  $\Delta H_m^0$  by the use of Fast Scanning Calorimetry (FSC). This approach applies to any crystallizable polymer for which a specific microstructure can be obtained (i.e. a two-phase semi-crystalline microstructure with a negligible amount of rigid amorphous fraction) and that can also be quenched to its fully amorphous state. Such a two-phase microstructure can be obtained on nanoscale samples through an annealing process performed in situ on the FSC sensor at crystallization temperatures as close as possible to the melting temperature. The enthalpy of melting is then evaluated from the two-phase model for different crystallization times (i.e. different crystallinities) and the  $\Delta H_m^0$  is obtained by extrapolating the data to the 100% crystalline state. This procedure was applied on samples whose  $\Delta H_m^0$  values are already available in the literature, but also on more recent biobased polyesters whose thermal properties are still under investigations.

### 1. Introduction

Since polymers can crystallize to different extents but never entirely, an extrapolated value of enthalpy, the so-called equilibrium enthalpy of melting  $\Delta H_m^0$  [ $\text{J}\cdot\text{g}^{-1}$ ], can be theoretically defined as the enthalpy that would be obtained from the melting peak of one gram of a 100% crystalline sample. According to its own definition, this information is not directly accessible because polymers are made of macromolecules which are way too big to perfectly fold and entirely fit in a regularly repeated crystal lattice; it is however essential to give an estimate of  $\Delta H_m^0$ , for it allows estimating the degree of crystallinity of a semi-crystalline polymer by direct comparison with the enthalpy of melting measured by DSC for any given semi-crystalline microstructure. The debate is still open on the method used to determine  $\Delta H_m^0$ , and probably because the method may be different from a research group to another, the values of  $\Delta H_m^0$  found in the literature are sometimes diverging, as shown in Table 1 for a selection of polymers. In addition,

some polymers are subjected to polymorphism; to our knowledge, so far only Righetti and co-workers [1] took it into account for the calculation of  $\Delta H_m^0$  in the case of poly(lactic acid). Besides, new polymers are continuously synthesized, such as polyfuranates [2] and many other polyesters, and a value of  $\Delta H_m^0$  will certainly have to be found for each of them to make preliminary characterizations complete [3,4]. It is therefore of great interest to find a method that is robust and efficient to determine the equilibrium enthalpy of melting for semi-crystalline polymers, which would eventually help closing the debate or at least provide further elements for discussion.

Even if some authors estimated the equilibrium enthalpy of melting through methods such as the Flory equation [36] or density measurements [9,34], the value of  $\Delta H_m^0$  for most crystallizable polymers has been more traditionally determined by generating different microstructures with an increasing degree of crystallinity, and then cross-comparing the results of microstructural characterizations performed by at least two techniques, such as XRD and DSC [1,27–30,32–35]. On

\* Corresponding author.

E-mail addresses: [clement.fosse@univ-rouen.fr](mailto:clement.fosse@univ-rouen.fr) (C. Fosse), [aurelie.bourdet@univ-rouen.fr](mailto:aurelie.bourdet@univ-rouen.fr) (A. Bourdet), [esteve.ernault@univ-rouen.fr](mailto:esteve.ernault@univ-rouen.fr) (E. Ernault), [antonella.esposito@univ-rouen.fr](mailto:antonella.esposito@univ-rouen.fr) (A. Esposito), [nicolas.delpouve1@univ-rouen.fr](mailto:nicolas.delpouve1@univ-rouen.fr) (N. Delpouve), [laurent.delbreilh@univ-rouen.fr](mailto:laurent.delbreilh@univ-rouen.fr) (L. Delbreilh), [shanmugam.thiyagarajan@wur.nl](mailto:shanmugam.thiyagarajan@wur.nl) (S. Thiyagarajan), [rutger.knoop@wur.nl](mailto:rutger.knoop@wur.nl) (R.J.I. Knoop), [eric.dargent@univ-rouen.fr](mailto:eric.dargent@univ-rouen.fr) (E. Dargent).

<https://doi.org/10.1016/j.tca.2019.03.035>

Received 29 November 2018; Received in revised form 26 March 2019; Accepted 27 March 2019

0040-6031/ © 2019 Elsevier B.V. All rights reserved.

**Table 1**Values of the equilibrium enthalpy of melting  $\Delta H_m^0$  [J·g<sup>-1</sup>] found in the literature for a selection of crystallizable polymers.

Polymer	Abbreviation	$\Delta H_m^0$ [J·g <sup>-1</sup> ]
Poly(ethylene)	PE	289 [5], 282 [6], 307 [7], 281 [8]
Isotactic poly(styrene)	iso-PS	86 [9], 80 [10], 96 [11]
Isotactic poly(propylene)	iso-PP	63 [12], 260 [9], 234 [13], 183 [14], 65 [15], 147 [16], 188 [17], 138 [18]
Polyamide 6	PA6	188 [19], 155 [20]
Poly(ethylene terephthalate)	PET	140 [21], 125 [22]
Poly(butylene terephthalate)	PBT	145 [23], 141 [24]
Poly(L-lactic acid)	PLLA	135 [25], 91 [26], 146 [27], 96 [28], 143 ( $\alpha$ -crystals) [1], 107 ( $\alpha'$ -crystals) [1], $\Delta H_m^0(T) = 20.9 + 0.74T - 0.0011T^2$ [J·g <sup>-1</sup> ] for the $\alpha'$ -form and $\Delta H_m^0(T) = 45.7 + 0.74T - 0.0011T^2$ [J·g <sup>-1</sup> ] for the $\alpha$ -form [1]
Poly(phenylene sulfide)	PPS	80 [29], 146 [30], 112 [31]
Poly(ethylene 2,5-furandicarboxylate)	PEF	137 [32], 140 [33], 185 [34]
Poly(butylene 2,5-furandicarboxylate)	PBF	129 [35]

one side, XRD provides an overall apparent degree of crystallinity that is calculated as a ratio of areas, i.e. the area corresponding to the sharper (crystalline) peaks divided by the total area of the pattern (crystalline peaks plus amorphous halo). On the other side, DSC provides the enthalpy [J·g<sup>-1</sup>] associated to the melting process of the percentage of polymer crystals previously quantified by XRD. A linear regression of several experimental points collected by this method on samples with different crystallinities allows extrapolating the values of enthalpy of melting to the ideal case of a 100% crystalline polymer. Most of the time, the degree of crystallinity  $X_c$  is obtained from XRD patterns, the enthalpy of melting  $\Delta H_m$  is estimated from DSC curves, and the equilibrium enthalpy of melting  $\Delta H_m^0$  is calculated according to Eq. (1).

$$\Delta H_m^0 = \Delta H_m^{DSC} / X_c^{XRD} \quad (1)$$

Sometimes other techniques, such as infrared [8,37–40] or Raman spectroscopy [41–46], are used to quantify the overall percentage of crystallinity to be compared to the value of enthalpy of melting obtained by DSC, but the use of XRD cross-compared to DSC is by far the most common. In a recent study about PLA, Righetti et al. [1] used XRD patterns cross-compared to conventional DSC to obtain the equilibrium enthalpy of melting as a function of temperature rather than a single extrapolated value. Recently, Cebe et al. [8] proposed a method for determining the equilibrium enthalpy of melting from Fast Scanning Calorimetry (FSC). This method requires the measurement of the enthalpy of melting plotted against the product of the sample mass times its crystallinity for several samples having variable masses and/or crystallinities; in this case,  $\Delta H_m^0$  is deduced from the slope of the plot, expected to be linear, representing  $\Delta H_m$  [J] vs. ( $m \cdot X_c$ ). This method is interesting for it has two major advantages: (1) it allows determining the equilibrium enthalpy of melting for samples that degrade right after melting and therefore can be hardly characterized by conventional DSC [47–50], and (2) it reduces the uncertainties that could be reproached to conventional DSC, because melting/recrystallization processes are observed at standard heating conditions [49–51] but largely suppressed at higher heating rates [52–56]. According to the authors, this method would reduce errors and can be applied to all types of polymers, copolymers, and blends regardless of their degree of crystallinity. In a paper dealing with the heat capacity of poly(trimethylene terephthalate), Pyda et al. [57] raised the question about the possibility of correlating the heat capacity at the glass transition  $\Delta C_p|_{T=T_g}$  [J·g<sup>-1</sup>·mol<sup>-1</sup>] to the heat of fusion  $\Delta H_f$  [kJ·mol<sup>-1</sup>] obtained by calorimetry on the same sample subjected to different thermal treatments (as received, partially quenched, quenched, crystallized isothermally, annealed, after cooling with 10 K·min<sup>-1</sup>) and therefore with different microstructures and crystallinities. They compared the experimental results to the values predicted on the basis of the ATHAS Data Bank [21] and observed that the extrapolated value of the heat of fusion, which was used as a control over the measured values of heat capacity, was in accord with an extrapolation of the experimental points only

when the corresponding microstructure contained little or no rigid amorphous content. The thing is, when it comes to the microstructural description of semi-crystalline polymers, in most cases the two-phase model is better replaced by a more complex three-phase model [58,59], which involves an additional “phase” to explain the connection between the ordered and disordered domains, the so-called rigid amorphous fraction (RAF). As such, the RAF should be considered as an interphase, rather than a phase, for it usually forms within the amorphous phase and involves all the entangled macromolecular segments that are too disordered to be part of a crystalline domain, yet too constrained by the nearby crystals to relax as freely as the mobile amorphous fraction (MAF). The appearance of a RAF is highly probable, for it is due to the length of the polymer chains, which is intrinsically much larger than the lamellar thickness [60,61]. The amount of RAF can vary from a polymer to another, sometimes reaching up to 40% [62]. Quite intuitively, the amount of RAF is expected to decrease if crystals grow bigger and the macromolecular segments get less entangled [59,61,63,64]. Several studies have shown how the RAF can be used to explain some macroscopic properties of semi-crystalline materials [65–71] and understand their behavior [56], which in turns means that controlling the amount of RAF is a key parameter for tailoring the performance of semi-crystalline polymers – almost as much as controlling the global amount, the size and the regularity of the crystalline domains. As pointed out by previous works on the establishment of the RAF [59,61,63,64], the connection between the amorphous and the crystalline domains can be evidenced either during [58,63,72,73] or after the crystallization process [58,59,63,64,73]. Moreover, the amount of RAF depends on the crystallization conditions (thermal treatment [57,74], time and temperature of crystallization [56], thickness [75], mechanical treatments [76,77]). If it is possible to control the amount of RAF by adjusting and carefully controlling the experimental conditions for crystallization, with a suitable set of crystallization parameters it should be possible to eventually create semi-crystalline microstructures in which almost no RAF is formed.

As previously mentioned, the equilibrium enthalpy of melting  $\Delta H_m^0$  may be calculated according to Eq. (1) where  $X_c$  is an estimation of the crystallinity degree obtained from XRD patterns, and the enthalpy of melting  $\Delta H_m$  is calculated from DSC curves. On one side, being part of the amorphous phase, the RAF is expected to contribute to the amorphous halo [78], which should be carefully subtracted to obtain  $X_c^{XRD}$ . On the other side, the presence of RAF is known to be responsible for a progressive change in the baseline of the DSC curves [58,79], which also leads to either overestimate or underestimate  $\Delta H_m^{DSC}$ , depending on the choice of the baseline and of the temperature range selected for integration. As a consequence, the cross-comparison of  $X_c^{XRD}$  with  $\Delta H_m^{DSC}$  is subjected to large uncertainties on the estimation of  $\Delta H_m^0$ . Besides, and most importantly, as for any other cross-comparison method, the assumption has to be made that two samples prepared in different ways, having different dimensions, and measured with two different techniques, actually represent the same system. From an

experimental point of view, the RAF is distinguished from the MAF as it does not contribute to the heat capacity change at the glass transition [80,81]. Due to its highly constrained behavior, the “relaxation” of the RAF requires more energy to be accomplished with respect to the relaxation of the MAF, therefore its contribution to the increase in the heat capacity occurs at higher temperatures, contributing to a slight but continuous change in the DSC baseline over the entire temperature range of devitrification [58,79]. In general, the development of a significant amount of RAF is associated to the growth of irregular crystalline domains [56,73,82,83] that are potentially subjected to crystalline reorganization. As a consequence, most of the time the error made on the estimation of  $\Delta H_m^{DSC}$  is not only related to the devitrification of the RAF and the choice of a good baseline used to integrate the melting peak, but also to the eventual reorganization (melting/recrystallization) of small and imperfect crystal boundaries [58]. In this case, performing DSC measurements at conventional heating rates (up to  $20 \text{ K} \cdot \text{min}^{-1}$ ) exposes to the risk of introducing an additional source of error in the estimation of  $\Delta H_m^{DSC}$ . FSC is the only experimental technique able to reduce and eventually suppress any contribution due to melting/recrystallization, as shown by Prof. Schick’s pioneer work [53–55]. FSC measurements can only be performed if the size of the samples is decreased to nanoscale, within a range of thickness  $1\text{--}10 \mu\text{m}$  [84]; Nassar et al. [75] recently observed that crystallizing nanoscale samples in which the polymer thickness is reduced to a few nanometers dramatically reduces the chances of developing RAF, even when the temperature selected for isothermal crystallization does not necessarily favor phase decoupling.

This work aims at (1) using FSC to estimate the equilibrium enthalpy of melting of several crystallizable polymers, such as poly(ethylene terephthalate) (PET), poly(L-lactic acid) (PLLA), poly(phenylene sulfide) (PPS), poly(ethylene 2,5-furandicarboxylate) (PEF) and poly(butylene 2,5-furandicarboxylate) (PBF), and (2) discussing the results in comparison with the literature and the most common method that uses DSC cross-compared with XRD.

## 2. Materials and methods

### 2.1. Materials

Commercial grades of poly(ethylene terephthalate) (PET), poly(L-lactic acid) (PLLA) and poly(phenylene sulfide) (PPS) were purchased in the form of pellets, with the exception of PET that was purchased as a film. Poly(ethylene 2,5-furandicarboxylate) (PEF) and poly(butylene 2,5-furandicarboxylate) (PBF) were synthesized in the laboratories of the Wageningen Food and Biobased Research (FBR), The Netherlands. PEF was synthesized according to the procedure reported in [2]. PBF was obtained by melt polymerization of dimethyl-furan-dicarboxylic acid (DMFDCA) with 1,4-butanediol using  $\text{Ti}(\text{O}-i\text{-Pr})_4$  as a catalyst. The synthesized polymer was subjected to solid-state post-condensation (SSPC) and then used without further purification. All the samples were dried prior to measurement: PET and PLLA were dried at  $T_g + 10^\circ\text{C}$  for at least 4 h, whereas PPS, PEF and PBF were stored in a desiccator with  $\text{P}_2\text{O}_5$  for at least 24 h. The list of samples used in this study is reported in Table 2. Nanoscale samples were crystallized in situ on Fast Scanning Calorimetry (FSC) sensors and subsequently characterized by FSC. Bulk

samples were crystallized in an oven and then characterized by wide-angle X-Ray Diffractometry (XRD), Differential Scanning Calorimetry (DSC), Modulated-Temperature DSC (MT-DSC) and FSC.

### 2.2. Fast Scanning Calorimetry (FSC)

FSC measurements were performed using a Flash-DSC 1 calorimeter (Mettler-Toledo) equipped with a HUBER TC100 intracooler. Prior to use, each MultiSTAR UFS 1 MEMS empty chip was conditioned and corrected according to the manufacturer’s procedure. Temperature calibration was performed according to the procedures reported in the literature [85]. The dynamic thermal lag corresponds to half the distance between the glass transition temperatures measured at the same heating and cooling rates; the static thermal lag corresponds to a third of the distance between the onset melting temperatures of two indium samples, one placed on top of the polymer sample and the other directly placed on the reference [86]. The dynamic thermal lag  $\Delta T_D$  (which depends on the selected heating and cooling rates) was measured at  $\beta^+ = |\beta^-| = 1000 \text{ K} \cdot \text{s}^{-1}$  and found to be less than 4 K. As for the static thermal lag  $\Delta T_S$  (which mostly depends on the sample thickness), values less than 2 K were ensured by preparing samples with thickness of  $10 \pm 3 \mu\text{m}$ , as recommended by Toda et al. [84] to prevent thermal gradients, and in agreement with the findings previously reported in the literature for different polymers [87–89]. The thickness of the samples was estimated from the determined mass, the literature value of density, and the area measured by optical microscopy, as previously done by Toda et al. [84]. A constant nitrogen flow of  $20 \text{ mL} \cdot \text{min}^{-1}$  was used to purge the measurement cell. Prior to in situ crystallization, the samples were quenched to their reference amorphous state by performing five heating/cooling steps at a rate of  $1000 \text{ K} \cdot \text{s}^{-1}$  over a temperature range going from  $-60^\circ\text{C}$  to the melt in order to ensure that any previous thermo-mechanical history was erased. The mass of the FSC samples used for this study ranged between 27 and 251 ng. The mass values were estimated using Eq. (2):

$$m = \Delta C_{p_{am}}^{FSC} [J \cdot K^{-1}] / \Delta C_{p_{am}}^{MT-DSC} [J \cdot g^{-1} \cdot K^{-1}] \quad (2)$$

Where  $\Delta C_{p_{am}}^{FSC} [J \cdot K^{-1}]$  is the heat capacity step at the glass transition estimated from FSC curves ( $\beta^+ = 1000 \text{ K} \cdot \text{s}^{-1}$ ) and  $\Delta C_{p_{am}}^{MT-DSC} [J \cdot g^{-1} \cdot K^{-1}]$  is the heat capacity step at the glass transition obtained by a MT-DSC scan of the quenched reference bulk samples (heating rate  $\beta^+ = 2 \text{ K} \cdot \text{min}^{-1} \approx 0.033 \text{ K} \cdot \text{s}^{-1}$ ).

### 2.3. Modulated-Temperature Differential Scanning Calorimetry (MT-DSC)

MT-DSC measurements were carried out on a DSC Q100 (TA Instruments) using the Tzero technology. Temperature, energy and heat capacity calibrations were performed with indium and sapphire standards. All the thermal treatments and characterizations were done under a constant nitrogen flow of  $50 \text{ mL} \cdot \text{min}^{-1}$  to prevent any oxidative degradation of the samples. The mass of MT-DSC bulk samples ranged between 5 and 10 mg. The modulated-temperature heating ramps were designed using a heat-only protocol, starting from  $-70^\circ\text{C}$  and reaching a temperature that ensures the complete melting of each sample, with a heating rate of  $2 \text{ K} \cdot \text{min}^{-1}$ , a modulating amplitude of  $\pm 0.318 \text{ K}$  and a period of 60 s, as recommended in [90], to prevent reversible

Table 2

List of samples along with their number-average molecular weight ( $M_n$ ), weight-average molecular weight ( $M_w$ ), polydispersity index ( $M_w/M_n$ ), grade and source.

Sample	$M_n$ [ $\text{g} \cdot \text{mol}^{-1}$ ]	$M_w$ [ $\text{g} \cdot \text{mol}^{-1}$ ]	$M_w/M_n$	Grade, Source
PET	31 000	62 000	2.00	Carolex, France
PLLA	53 000	97 000	1.80	PLI005, Natureplast, France
PPS	n.a.	n.a.	n.a.	FORTRON 0214, Celanese, France
PEF	11 500	18 000	1.60	Wageningen FBR, The Netherlands
PBF	36 000	74 500	2.07	Wageningen FBR, The Netherlands

crystallization during melting. MT-DSC was used to determine the heat capacity step at the glass transition for the quenched bulk samples  $\Delta C_{p_{am}}^{MT-DSC} [J \cdot g^{-1} \cdot K^{-1}]$ , which is further needed to estimate the mass of FSC nanoscale samples according to Eq. (2).

#### 2.4. Differential Scanning Calorimetry (DSC)

DSC measurements were made on a DSC TA2920 (TA Instruments). Energy and temperature calibrations were carried out using an indium standard. All the characterizations were done after ballistic cooling to  $-20\text{ }^\circ\text{C}$ , with a heating rate of  $20\text{ K} \cdot \text{min}^{-1}$  under a constant nitrogen flow of  $50\text{ mL} \cdot \text{min}^{-1}$  to prevent any oxidative degradation of the samples. The mass of DSC bulk samples ranged between 5 and 10 mg. DSC was used to estimate the enthalpy of melting  $\Delta H_m$  of bulk samples to be used in Eq. (1).

#### 2.5. Wide-angle X-Ray Diffractometry (XRD)

XRD spectra were recorded at room temperature on (16 mm x 16 mm) samples by a Bruker D8 X-ray diffractometer in the angular range  $2\theta = 5\text{--}40^\circ$ , with a step of  $0.05^\circ$  and a counting time of 1 s/step, using a Co K $\alpha$  radiation ( $\lambda = 2.29\text{ \AA}$ ). The patterns were obtained by subtracting the background signal and averaging at least three spectra recorded on the same spot of the sample. XRD patterns were then exploited with different fitting methods (multi-peak fitting with Gaussian or Pearson functions) by two different operators to have an estimation of the uncertainties on the calculation of the apparent degree of crystallinity  $X_c^{XRD}$ . This value was determined as a ratio of areas, i.e. the area corresponding to the crystalline peaks divided by the total area of the pattern (crystalline peaks plus amorphous halo), and used in Eq. (1).

#### 2.6. Sample preparation and thermal treatments

In order to create a microstructure with a reduced amount of RAF, nanoscale samples were crystallized in situ on FSC sensors using selected conditions of temperature and time.

##### 2.6.1. Choice of the crystallization temperature $T_c$

The samples were melted, cooled down to a temperature within the crystallization temperature range, held in isothermal conditions for a constant crystallization time (60 minutes), cooled down to  $-60\text{ }^\circ\text{C}$  with a cooling rate of  $1000\text{ K} \cdot \text{s}^{-1}$  (the same rate used for measurements), and then heated again to observe the melting endotherm. This protocol was repeated at progressively increasing temperatures (the increase was done by steps of  $5\text{ }^\circ\text{C}$ ) and the crystallization temperature  $T_c$  was selected as the highest temperature at which the crystallization induction time was shorter than the isothermal time (i.e. crystallization started within a time  $\leq 60$  minutes). The choice of 60 minutes results from a compromise between a reasonable crystallization time and a sufficiently high crystallization temperature for crystal perfection.

##### 2.6.2. Preparation of maximum crystallized nanoscale samples

A cycle of isothermal crystallizations was performed on each sample at the selected temperature  $T_c$  for progressively increasing durations until a microstructure was formed that showed no further increase in the melting peak, i.e. until the crystallinity degree reached its maximum. The corresponding time was taken as  $t_c^{max}$ .

##### 2.6.3. Preparation of maximum crystallized bulk samples to be compared to nanoscale samples

The results obtained by FSC on nanoscale samples were compared to the results obtained by more conventional techniques (XRD, DSC and MT-DSC), which require bigger samples. To this purpose, semi-crystalline bulk samples were also prepared by melting the polymer samples between two Teflon sheets, then quickly transferring the assembly to an

oven previously set at the selected crystallization temperature  $T_c$  and holding the isothermal conditions for a crystallization time at least equal to  $t_c^{max}$ . Maximum crystallized bulk samples were obtained by holding the selected crystallization temperature  $T_c$  for a crystallization time varying between 2 and 5 h. The fully amorphous counterparts were obtained by melting the samples between two Teflon sheets, followed by quenching in cold water.

#### 2.7. Determination of the equilibrium enthalpy of melting ( $\Delta H_m^0$ )

Eq. (1) gives a good estimate of  $\Delta H_m^0$  only if the same microstructure can be obtained by two different techniques (e.g. DSC and XRD) and the corresponding results (i.e.  $\Delta H_m^{DSC}$  and  $X_c^{XRD}$ ) are available for cross-comparison. With the value of  $\Delta H_m^0$ , the degree of crystallinity  $X_c$  of a semi-crystalline polymer can be determined by performing a single DSC run and applying the following equation [91,92]:

$$X_c = \Delta H_m^{DSC} / \Delta H_m^0 \quad (3)$$

Where  $\Delta H_m^{DSC}$  is the enthalpy of melting obtained by integration of the melting endothermic peak. Cebe et al. [8] recently applied Eq. (1) to FSC experiences and rewrote it as follows:

$$\Delta H_m^{FSC}(T_m)[J] = \Delta H_m^0(T_m)[J \cdot g^{-1}] * (mass [g] * X_c) \quad (4)$$

With  $X_c$  obtained either by combining FSC results with information found in the literature (i.e. the heat of fusion of 100% crystal at  $T_m$  and the specific heat capacity at a given temperature, judiciously chosen) [8] and/or by a different experimental technique (through independent measurements performed on similarly treated samples – under the assumption that uniform thermal treatment would result in uniform crystallinity, whatever the size of the sample and the experimental technique).

According to Eq. (4), the value of  $\Delta H_m^0$  can be determined if the sample mass, degree of crystallinity and enthalpy of melting are known, i.e.  $\Delta H_m^0$  can be directly deduced from the slope of a plot representing the enthalpy of melting  $\Delta H_m^{FSC}$  as a function of ( $mass [g] * X_c$ ). When the conditions for a two-phase model are fulfilled, the degree of crystallinity  $X_c$  can be directly estimated from the ratio between the heat capacity change at the glass transition of a crystallized sample ( $\Delta C_{p_{cryst}}$ ) and the value previously found for its fully amorphous counterpart ( $\Delta C_{p_{am}}$ ) as follows:

$$X_c^{2ph} = 1 - (\Delta C_{p_{cryst}} / \Delta C_{p_{am}}) \quad (5)$$

If the works of Cebe et al. [8] (using FSC) and Pyda et al. [26,57] (correlating the enthalpy of melting and the heat capacity change at the glass transition in two-phase microstructures) are merged, Eqs. (1), (4) and (5) can be combined as:

$$\Delta H_m^{FSC}(T_m)[J \cdot g^{-1}] = -(\Delta H_m^0(T_m)[J \cdot g^{-1}] / \Delta C_{p_{am}}^{FSC} [J \cdot g^{-1} \cdot K^{-1}]) * \Delta C_{p_{cryst}}^{FSC} [J \cdot g^{-1} \cdot K^{-1}] + \Delta H_m^0(T_m) [J \cdot g^{-1}] \quad (6)$$

$\Delta H_m^0$  can therefore be calculated from the intercept of a plot representing the enthalpy of melting  $\Delta H_m^{FSC}(T_m)[J \cdot g^{-1}]$  versus the heat capacity step at the glass transition  $\Delta C_{p_{cryst}}^{FSC} [J \cdot g^{-1} \cdot K^{-1}]$ .  $\Delta H_m^{FSC}$  is obtained by integrating the endothermic peak observed on the FSC curves normalized to the sample mass (according to Eq. (2)) with a linear baseline going from the end of the glass transition up to the melt.  $\Delta C_{p_{cryst}}^{FSC}$  is obtained by extrapolating the baselines of the FSC curves in the glassy/solid state ( $T < T_g$ ) and in the liquid state ( $T > T_g$ ) through the glass transition  $T_g$  (read as the midpoint of the heat capacity step), and calculating the difference between  $baseline_{liquid}^{FSC}|_{T=T_g}$  and  $baseline_{solid}^{FSC}|_{T=T_g}$ . Values equivalent to a change in the heat capacity are obtained from the values of heat flow [mW] by conversion to [J] and normalization to the sample mass [g].

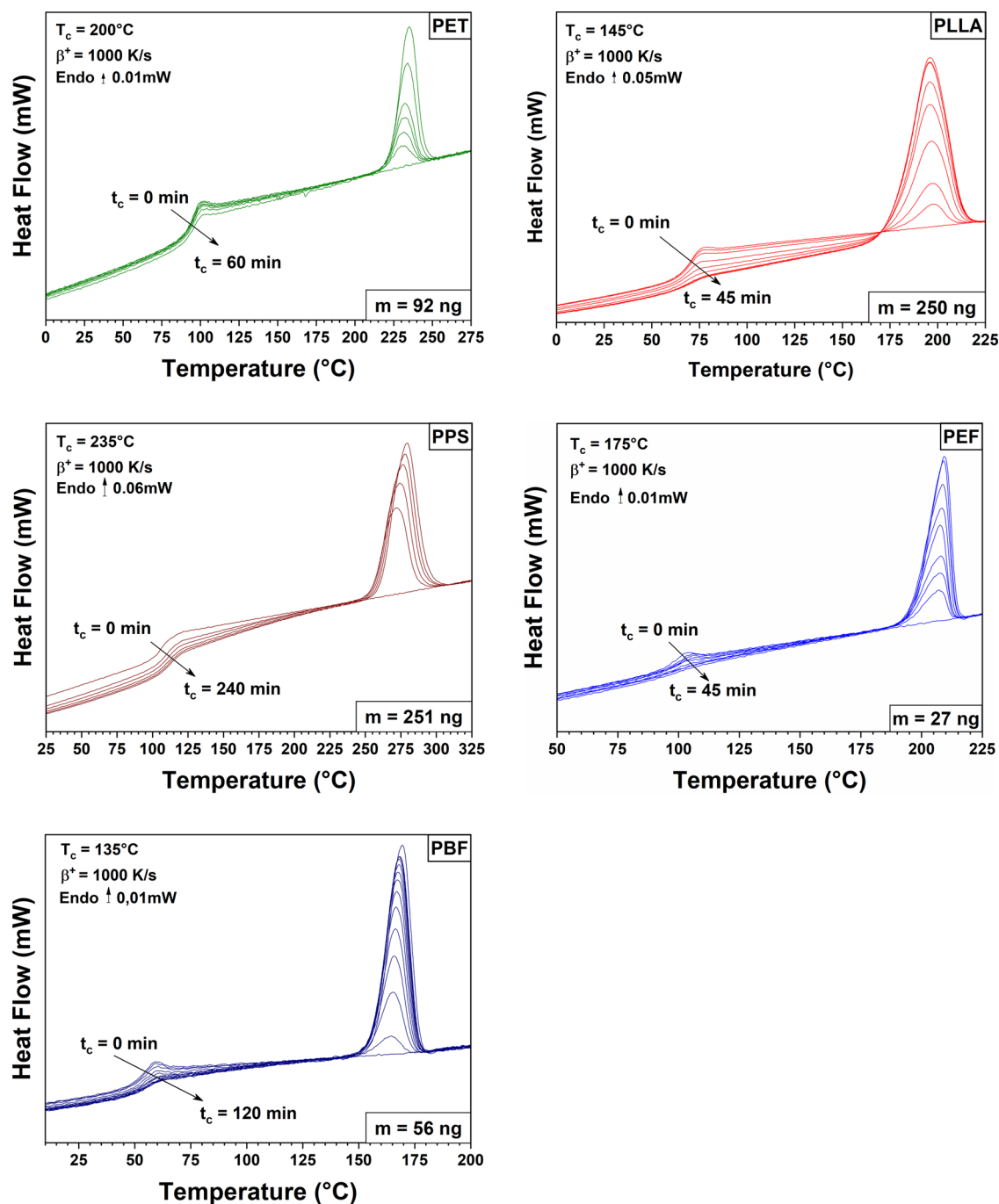


Fig. 1. FSC curves recorded upon heating at  $\beta^+ = 1000 \text{ K s}^{-1}$  on nanoscale samples of PET, PLLA, PPS, PEF and PBF after in situ isothermal crystallization from the melt at the crystallization temperature  $T_c$  during different crystallization times  $t_c$ .

### 3. Results and discussion

Fig. 1 shows the FSC curves recorded on nanoscale samples upon heating at  $\beta^+ = 1000 \text{ K s}^{-1}$  after in situ isothermal crystallization from the melt at the crystallization temperature  $T_c$  during different crystallization times  $t_c$  followed by cooling down to  $-60^\circ\text{C}$  at  $\beta^- = 1000 \text{ K s}^{-1}$ . Some of the samples investigated in this study are known to be potentially subjected to the formation of a metastable crystalline phase (PLLA [1,93], PEF [34,94] and PBF [95]). A special care was given to the selection of  $T_c$  so that only the most stable crystalline phase was formed. In the case of PLLA, for instance, the crystallization from the melt at temperatures higher than  $130^\circ\text{C}$  leads to the formation of  $\alpha$  crystals (helical chain segments aligned in an

orthorhombic unit cell), whereas at temperatures lower than  $100^\circ\text{C}$  the formation of conformationally disordered  $\alpha'$  crystals is observed [1]. The presence of metastable crystalline phases increases the risk of crystalline reorganization, which in turn affects the calculation of the enthalpy of melting. For this reason, PLLA samples were crystallized at  $T_c = 145^\circ\text{C}$ . For similar reasons,  $T_c$  was set at  $175^\circ\text{C}$  in the case of PEF and  $135^\circ\text{C}$  in the case of PBF (whose thresholds between different crystalline phases were found at  $170^\circ\text{C}$  [94] and  $130^\circ\text{C}$  [95], respectively).

The first encouraging evidence is that in Fig. 1 all the samples show a single and relatively sharp melting peak, excluding the possibility of a melting/recrystallization process during heating, which would have been typical of polymorphism or crystalline reorganization and is

usually revealed by an exothermic signal partially or entirely overlapping the melting endotherm (as observed, for instance, in PLA [96–99]). As the crystallization time increases, the intensity of the melting endotherm increases. Since no cold crystallization occurs during the heating ramp, the values of  $\Delta H_m^{FSC}$  obtained by integrating the endothermic peaks in Fig. 1 can be reliably and exclusively associated to the melting of the crystalline domains progressively created during the previous isothermal treatments. For some polymers (e.g. for PET and PPS), the maximum of the melting endotherm slightly shifts to higher temperatures as the crystallization time increases, suggesting that the crystallization progresses and the crystalline lamellae grow thicker, in agreement with the Gibbs-Thomson equation [100].

One may also note that the baseline of the FSC curves in Fig. 1 slightly changes as the crystallinity of the samples increases. This dependence is observed in the solid state (from the glassy state up to the onset of melting) but never observed in the molten state, and is particularly visible when the sample mass is relatively large (e.g. for PLLA and PPS). These changes may be due to some interfacial effects associated with stress transfers between the polymer sample and the SiN membrane of the sensor. Stress transfers could be the consequence of a mismatch in the thermal conductivity of the polymer sample and the SiN membrane of the sensor, but also to the shrinkage related to crystallization. The second hypothesis is most likely because the shrinkage of a polymer sample is expected to be proportional to the extent of crystallization, proportional to the sample mass and only visible when the sample is semi-crystalline (in the molten state the polymer is supposed to relax). These effects are not due to a sample mass change, because precautions were taken to make sure that the mass of polymer in contact with the sensor remained constant during the whole experimental protocol.

XRD scans were recorded on maximum crystallized bulk samples to confirm that the crystalline phases grown during the isothermal crystallization at  $T_c$  are the most stable ones (Fig. 2), which is consistent with the information previously reported in the literature about PLA [1,93], PEF [34] and PBF [95]. The XRD patterns in Fig. 2 were also used to estimate the apparent degree of crystallinity [101], a method that requires a careful subtraction of the amorphous halo. In this work, all the samples maximum crystallized in the bulk showed a complex amorphous halo that required two Gaussian peaks for fitting. Huo et al. [78] have already pointed out that the presence of RAF affects XRD patterns; being part of the amorphous phase, the RAF is expected to be included in the amorphous halo along with the MAF. The literature reports that the amorphous halo of PET can be deconvoluted in two Gaussian contributions [102]: the first one attributed to the interchain distances perpendicular to the plans of aligned aromatic rings, the second one attributed to the interchain distances within the plane of the aligned aromatics rings. Similarly to PET, two Gaussian contributions were used to deconvolute the amorphous halos of PLLA and PPS according to information reported in the literature [103,104]. As for PEF and PBF, two Gaussian contributions were also used, even if no information is reported in the literature.

Fig. 3 shows the values of the enthalpy of melting  $\Delta H_m^{FSC}$  plotted against the values of the heat capacity step at the glass transition in the semi-crystalline samples  $\Delta C_{p_{cryst}}^{FSC}$ , both measured on the FSC curves reported in Fig. 1.

According to its definition,  $\Delta H_m^0$  could be straightforwardly calculated with the datasets reported in Fig. 3, provided that the hypothesis of a two-phase microstructure is verified. Indeed, the comparison between the values of  $\Delta H_m$  (with respect to its reference  $\Delta H_m^0$ ) and  $\Delta C_{p_{cryst}}$  (with respect to its reference  $\Delta C_{p_{am}}$ ) obtained from the same DSC curve is generally used to discuss the pertinence of a two-phase model to describe the microstructure of semi-crystalline polymers. Whenever a discrepancy is revealed in the information provided by  $\Delta H_m$  (crystalline fraction  $X_c$  calculated according to Eq. (3)) and  $\Delta C_{p_{cryst}}$  (residual amorphous fraction relaxing at the glass transition), a three-phase model is adopted in the place of Eq. (5) and the RAF is introduced to

solve the discrepancy.

$$1 = X_c^{3ph} + (\Delta C_{p_{cryst}} / \Delta C_{p_{am}}) + X_{RAF} \quad (7)$$

Nassar et al. [75] recently reported that growing crystals in a nanoscale confined environment reduces the development of RAF, even when the temperature conditions are supposed to favor the connections between the crystalline domains and the surrounding amorphous phase. The samples used in FSC experiments are intrinsically nanoscale (the biggest weighs 250 ng), which may eventually help limiting the formation of RAF for similar reasons, i.e. for a sort of finite-size effect. With this being said, the choice of a two-phase model to determine the degree of crystallinity using Eq. (5) applied to FSC curves sounds encouraging. Besides, the experimental conditions used in this study for crystallization were designed to minimize the development of RAF, and the fact that the baselines of the FSC curves in Fig. 1 look quite straight in the temperature range between the glass transition and the melt, suggests that a two-phase model could actually apply to all the semi-crystalline microstructures obtained by in situ isothermal crystallization on nanoscale samples. The literature reports that the amount of RAF formed during the crystallization process typically decreases as the size and thermal stability of the crystalline phase increases [61], and it is well known that the size and thermal stability of the crystalline lamellae increases with the crystallization temperature [105]. The literature also reports that the development of RAF is typically associated to an increase in the glass transition temperature (revealing a mobility restriction of the RAF on the MAF) [106], as well as a modification of its shape (due to a different distribution of the relaxation times, revealing a stronger coupling between phases) [56]. These modifications of the glass transition, especially when associated to the development of irregular crystalline domains melting over an extended temperature range, would make it impossible to distinguish the microstructural information conveyed by the heat capacity change as a function of temperature (baseline) and the melting endotherm, respectively. None of these modifications were observed in the FSC curves recorded for this study.

When Eq. (6) is used to fit the data in Fig. 3, the linear regression gives a slope that corresponds to  $\Delta H_m^0(T_m) [J \cdot g^{-1}] / \Delta C_{p_{app}}^{FSC} [J \cdot g^{-1} \cdot K^{-1}]$  and an intercept that directly provides the value of  $\Delta H_m^0$ . The dispersion of the experimental values around the linear fit (grey hatched areas in Fig. 3) corresponds to  $\pm 5\%$  uncertainty on the estimation of the degree of crystallinity. If this uncertainty were introduced in the calculation, the value of  $\Delta H_m^0$  would be affected by an uncertainty of  $\pm 10 J \cdot g^{-1}$  (which is acceptable when compared to the error introduced by a wrong estimation of the enthalpy of melting, e.g. in the case of crystalline reorganization during DSC measurement ramps at conventional heating rates). Indeed, there are several possible sources of uncertainties, and the scattering in the values of  $\Delta H_m^0$  found in the literature is quite explicit, as illustrated by the grey horizontal areas in Fig. 3 covering all the values previously reported in Table 1. One of the main sources of uncertainty in determining the equilibrium enthalpy of melting by this method, is due to the fact that this is an extrapolative method. It is quite difficult to obtain a polymer with a highly crystalline microstructure for which the two-phase assumption can be assuredly made. Most of the polymers investigated in this paper have a degree of crystallinity that barely reaches 30%. For these polymers, the uncertainty associated with the slope of the  $\Delta H_m$  vs  $\Delta C_p$  plots is much relevant. This being said, the values of  $\Delta H_m^0$  obtained in this study fall in the same range as the values previously reported in the literature by several authors, as illustrated by the grey areas in Fig. 3. In the case of PET, for instance, for which no substantial divergences are found in the literature, the FSC protocol provides a value of  $138 J \cdot g^{-1}$ , which is in agreement with the value previously obtained by Wunderlich and Androsch ( $140 J \cdot g^{-1}$ ) [21,61]. As a consequence, when it comes to relatively new polymers for which no data are found in the literature, such as PEF and PBF, one may assume that this method provides at least a



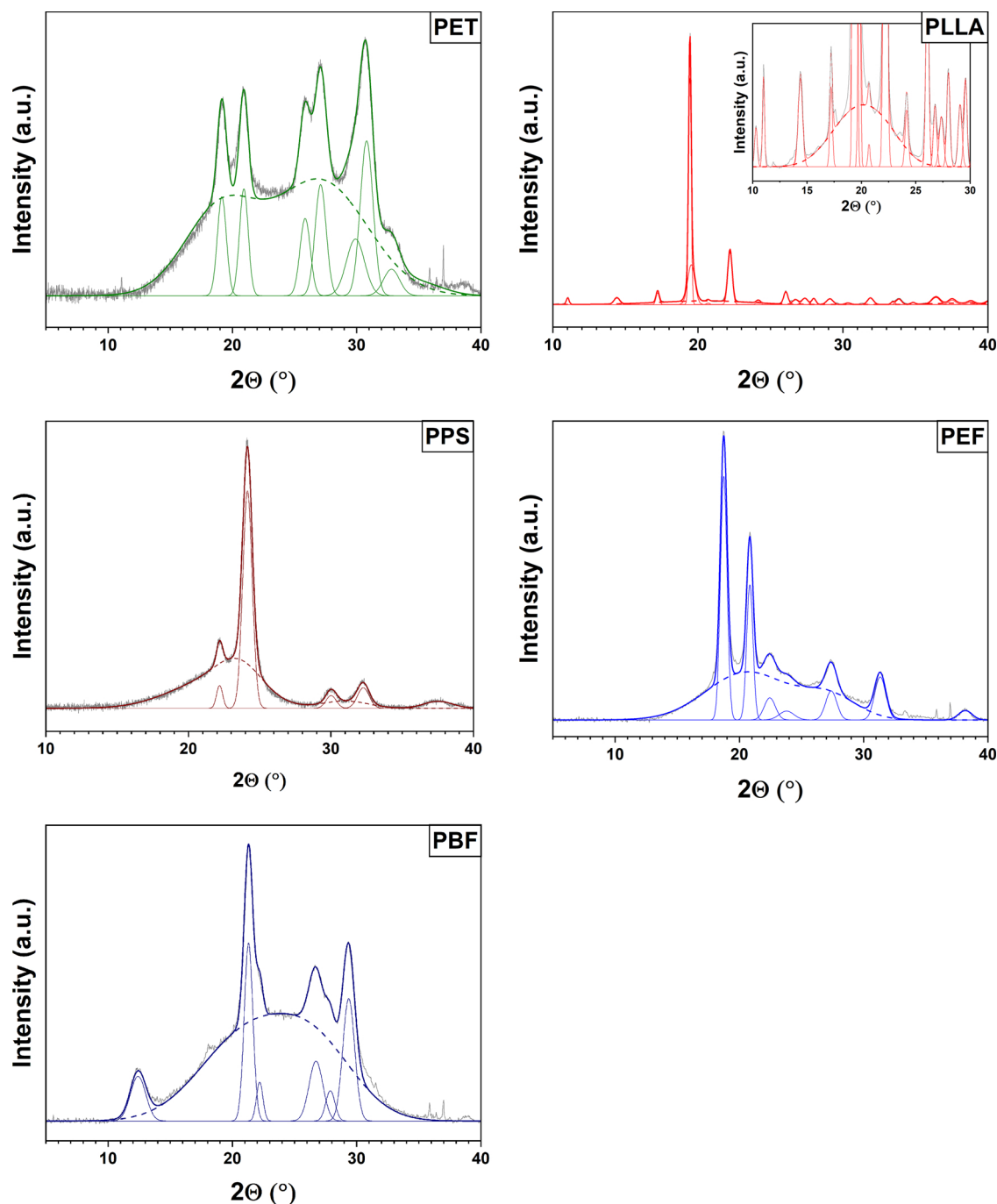


**Fig. 2.** XRD patterns recorded at room temperature on maximum crystallized bulk samples of PET, PLLA, PPS, PEF and PBF after isothermal crystallization from the melt at the crystallization temperature  $T_c$  (solid lines). The raw data are in grey. The thick solid lines represent the fitting result. Thinner solid and dashed lines are also reported to represent the crystalline and amorphous contributions to each pattern (multi-peak fitting with Gaussian functions). The amorphous halos were fitted by two Gaussian peaks; the dashed lines represent the sum of the peaks used for fitting. In the case of PLLA, an inset with suitable rescaling is provided to better visualize the amorphous halo.

preliminary estimation of  $\Delta H_m^0$  that is fairly reliable, yet debatable if different values are successively found by other experimental techniques. Table 3 summarizes the experimental conditions used for the in situ isothermal crystallization performed on the FSC sensors, as well as the main outcomes of the crystallization process measured by FSC on the maximum crystallized nanoscale samples (exploitation of Fig. 1) and the corresponding values of  $\Delta H_m^0$ .

The experimental procedure proposed in this work can be compared to the ones commonly found in the literature that are based on the cross-comparison of two different techniques. PET is a good example to

illustrate the possible sources of uncertainty when different methods are used to estimate  $\Delta H_m^0$ . The XRD patterns recorded on maximum crystallized bulk samples (Fig. 2) were used to calculate the apparent degree of crystallinity  $X_{Cmax}^{XRD}$ . The value obtained for PET is  $37 \pm 5\%$ . Ruland method (based on the conservation of the total scattered intensity by a set of atoms, independent on their structural order) could have been used to obtain the absolute degree of crystallinity [101], but most of the works reported in the literature use the method based on the ratio of areas. When Eq. (1) is used to cross-compare  $X_{Cmax}^{XRD}$  with the enthalpy of melting measured by conventional DSC, a value of  $162 \text{ J} \cdot \text{g}^{-1}$

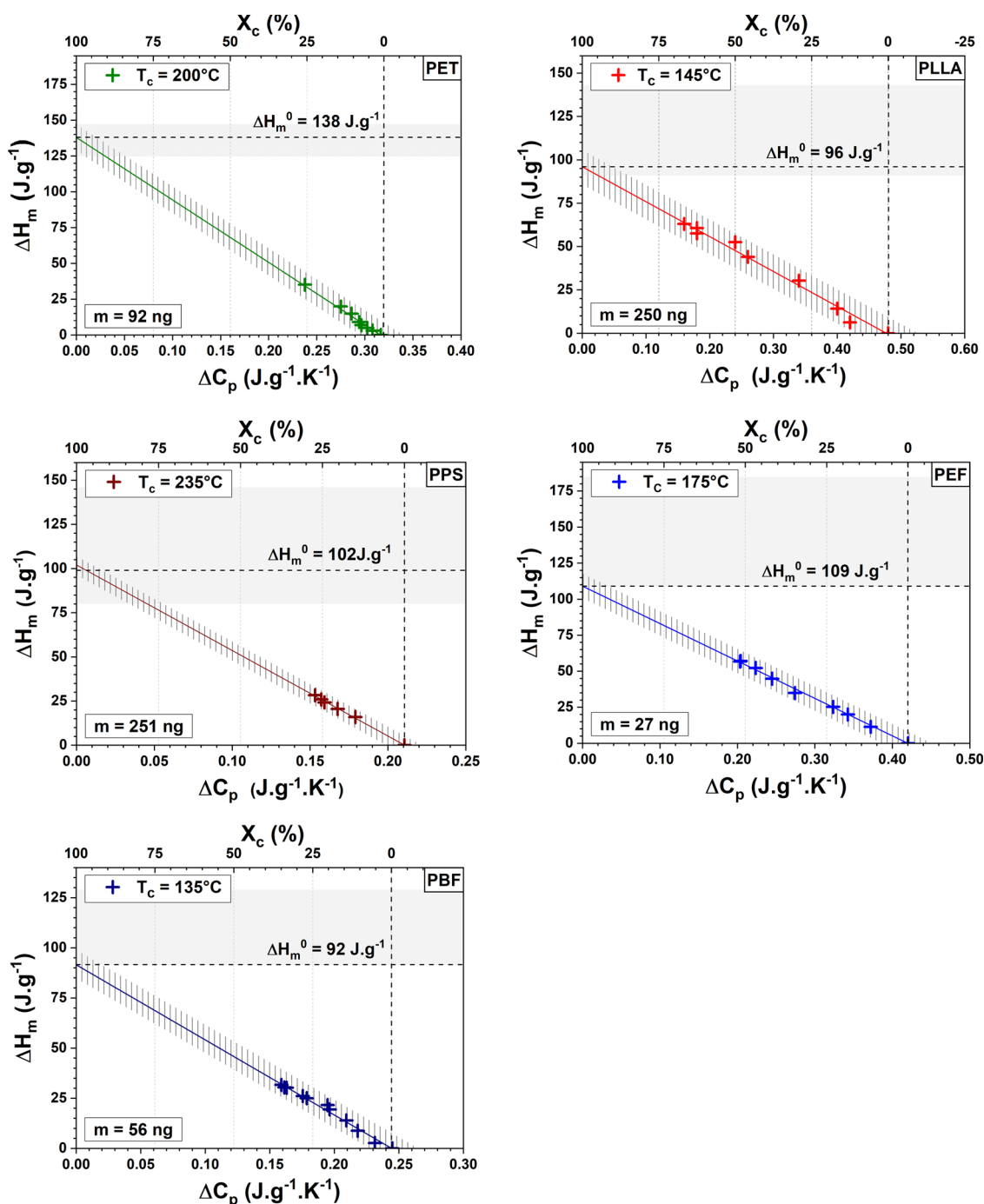


**Fig. 3.** Enthalpy of melting vs. heat capacity change at the glass transition obtained from FSC curves normalized to the sample mass and the heating rate (Fig. 1) for nanoscale samples of PET, PLLA, PPS, PEF and PBF crystallized in situ at the crystallization temperature  $T_c$  for different crystallization times  $t_c$ . The linear regression of the experimental data (solid lines) extrapolated to  $X_c = 100\%$  and  $\Delta C_p = 0 \text{ J.g}^{-1}.\text{K}^{-1}$  reveals the equilibrium enthalpy of melting  $\Delta H_m^0$  under the assumption of a two-phase model. The grey hatched areas around the solid lines represent the uncertainty of  $\pm 5\%$  on the estimation of the apparent degree of crystallinity. The grey horizontal areas represent the domain covered by the values of  $\Delta H_m^0$  that can be found in the literature (Table 1) plus the values obtained in this work.

is obtained. When FSC results are used instead of DSC in Eq. (1), the cross-comparison with  $X_{Cmax}^{XRD}$  provides a value of  $165 \text{ J.g}^{-1}$ . These values are quite different with respect to the values found in the literature ( $140 \text{ J.g}^{-1}$  [21],  $125 \text{ J.g}^{-1}$  [22], Table 1), independently on the technique used to measure the enthalpy of melting. The value obtained by the FSC method is much closer to the values of the literature ( $138 \text{ J.g}^{-1}$ ). Comparing different values of  $\Delta H_m^0$  is definitely a multifactor problem that requires a deeper understanding of both the advantages and drawbacks of the experimental procedures used to obtain them. The

differences may be acceptable or very large, depending on the nature of the sample (some polymers crystallize faster, easier and more regularly than other polymers, generating different amounts of RAF), on the design of the experimental protocol used for crystallization (which includes the size of the sample and the crystallization conditions, i.e. the crystallization temperature and time), as well as on the calculation procedure. Since  $\Delta H_m^0$  is estimated by extrapolating the experimental data (crystallinity degree  $X_c$  vs. enthalpy of melting  $\Delta H_m$ ) obtained on samples with different crystallinity degrees, it is mandatory to ensure

**Table 3**

Crystallization temperature ( $T_c$ ) and crystallization time ( $t_c^{max}$ ) selected to reach the maximum crystallinity degree during in situ isothermal crystallization aiming to reduce coupling between phases.  $T_g$  and  $T_m$  are the glass transition temperature and the melting temperature of the maximum crystallized nanoscale samples measured by FSC. The equilibrium enthalpy of melting  $\Delta H_m^0$  was obtained according to Eq. (6) based exclusively on FSC results. For comparison's purposes, the crystallinities of maximum crystallized bulk and nanoscale samples, which were obtained by XRD and FSC respectively, are also reported ( $X_{C_{max}}^{XRD}$  and  $X_{C_{max}}^{FSC}$ ).

Sample	$T_c$ [°C]	$t_c^{max}$ [min]	$T_g$ [ ± 1 °C]	$T_m$ [ ± 1 °C]	$\Delta H_m^0$ [ ± 10 J·g <sup>-1</sup> ]	$X_{C_{max}}^{XRD}$ [ ± 5%]	$X_{C_{max}}^{FSC}$ [ ± 5%]
PET	200	60	92	235	138	37	25
PLLA	145	45	68	196	96	82	67
PPS	235	240	108	279	102	39	27
PEF	175	45	96	210	109	52	52
PBF	135	120	51	169	92	33	30

the accuracy on the calculation of these quantities. In general, techniques such as XRD and DSC are used to cross-compare the results obtained on bulk samples crystallized in controlled conditions. Bulk samples are subjected to bigger thermal gradients, resulting in less controlled crystallization conditions and less regular microstructures. Besides, using conventional DSC to determine the enthalpy of melting of semi-crystalline polymers expands the level of uncertainty because of crystalline reorganization that is sometimes observed during the heating ramps, and that is hardly distinguished from the baseline drift related to the devitrification of the RAF. Using FSC improves the accuracy of measurement thanks to the extremely fast heating rates, which exclude any possible crystalline reorganization and suppress the effects eventually due to polymorphism. Last but not least, in suitable and controlled crystallization conditions, FSC allows the concomitant measurement of  $X_{MAF} = 1 - X_c$  and  $\Delta H_m$ , considerably reducing the uncertainties due to the cross-comparison of samples whose microstructures are not necessarily the same because of sampling heterogeneities. The main source of uncertainty for the FSC method proposed here is related to the fact that  $\Delta H_m^0$  is estimated under the assumption that a two-phase microstructure is obtained during the in situ crystallization protocol. For this reason, an accurate selection of the crystallization temperature  $T_c$  should be done with the purpose of growing regular crystalline domains with reduced connections between phases, i.e. with a negligible amount of RAF.

Among the samples shown in Fig. 1, PLLA and PPS are the ones with the largest masses (~250 ng). Sample mass and crystallization temperature are two parameters that possibly affect the results of FSC measurements and the following data treatment. However, it is quite difficult to distinguish how these parameters respectively contribute to the combined uncertainty on  $\Delta H_m^0$  because it is very hard to prepare several FSC sensors with samples having exactly the same mass and shape, and placed exactly in the same position on the membrane. Fig. 4 shows the results obtained on smaller samples of PLLA and PPS (58 ng and 94 ng respectively) at higher crystallization temperatures (149 °C and 243 °C respectively) with respect to Fig. 1.

The  $\Delta H_m$  vs  $\Delta C_p$  plots reveal that, for these polymers, the extrapolated value of  $\Delta H_m^0$  is indeed quite dependent on the sample mass and/or on the choice of  $T_c$ . Further studies are required to evaluate the influence of these parameters. It should be reminded that all extrapolative methods have intrinsic limitations that are sources of uncertainties, and this is particularly true when the extrapolation is done on a large range of values starting with few points unevenly distributed (the case of PPS crystallized at 243 °C is a good example). From this point of view, the extrapolation done on the basis of FSC measurements is neither better nor worse than any other extrapolative method, but

provides values in agreement with the literature. Besides, there are polymers (such as PET) that are quite insensitive to the choice of a different crystallization temperature. The same PET sample was crystallized at three different temperatures (190 °C, 200 °C, and 210 °C) and the values of  $\Delta H_m^0$  obtained (141 J·g<sup>-1</sup>, 138 J·g<sup>-1</sup> and 133 J·g<sup>-1</sup> respectively) are quite similar and in perfect agreement with the literature (140 J·g<sup>-1</sup> [21] and 125 J·g<sup>-1</sup> [22]) (Fig. 5).

Other samples may be more sensitive to the choice of  $T_c$ , especially if they have peculiar crystallization features such as polymorphism. PLLA, for instance, exhibits several types of crystal modifications ( $\alpha$ ,  $\alpha'$ ,  $\beta$ , and  $\gamma$  phases) that are sometimes difficult to isolate, even if the crystallization temperature is accurately selected. The  $\Delta H_m$  vs  $\Delta C_p$  plots reported in Fig. 4 (bottom) suggest that PLLA is extremely sensitive to the choice of  $T_c$ . Table 3 reported a value of  $\Delta H_m^0 = 96 \pm 10$  J·g<sup>-1</sup> for PLLA crystallized at  $T_c = 145$  °C, but a much different value is obtained for  $T_c = 149$  °C ( $\Delta H_m^0 = 134 \pm 10$  J·g<sup>-1</sup>). None of these values is in disagreement with the literature, because Pyda et al. [26] and Kalish et al. [28] reported values of 91 J·g<sup>-1</sup> (at  $T_c = 145$  °C) and 96 J·g<sup>-1</sup> (at  $T_c = 150$  °C) respectively, whereas Miyata et al. [25] and Badrinayan et al. [27] reported values of 135 J·g<sup>-1</sup> and 146 J·g<sup>-1</sup> respectively; the most accurate approach seems to be the one proposed by Righetti et al. [1], which suggests to take into account the temperature dependence of  $\Delta H_m^0$ .

These preliminary results indicate that polymers are not equally sensitive to parameters such as the sample mass and the crystallization temperature. As potential sources of uncertainty on the extrapolated value of the equilibrium enthalpy of melting, these parameters definitely deserve further investigations. As a perspective, it would also be interesting to measure the crystallinity degree by recording XRD patterns directly on the FSC sensor, according to the technical solutions proposed by Ivanov, Cavallo, Vlassak and their-coworkers [85,99,107,108], who worked out some feasible solutions to combine XRD with FSC.

#### 4. Conclusions

This work shows that the equilibrium enthalpy of melting  $\Delta H_m^0$  can be determined by fast scanning calorimetry (FSC), provided that suitable crystallization conditions are selected to reduce the connection between phases. The metrological concept relies, as usual, on the characterization of samples having microstructures with different degrees of crystallinity and the extrapolation of the experimental data to the theoretical situation of a 100% crystalline polymer. Contrarily to the methods commonly found in the literature, which are based on the cross-comparison of different experimental techniques (such as XRD and DSC) performed on different samples, this method is only calorimetric and significantly reduces the uncertainties related to (1) thermal gradients (FSC measurements are performed on nanoscale samples), (2) polymorphism and/or crystalline reorganization (FSC ramps are recorded at very high heating rates), and (3) sample heterogeneities (all the information required to calculate  $\Delta H_m^0$  is obtained from the same curve, recorded on the same sample). This method applies to any crystallizable polymer that is quenchable and for which a two-phase microstructure with a negligible amount of rigid amorphous fraction and reduced connections between phases is obtained under controlled crystallization conditions. The protocol of isothermal crystallization is performed in situ on nanoscale samples placed on the FSC sensor. The optimization of the crystallization parameters (temperature and time) should be preliminarily done according to the selected samples, especially for polymers that are subjected to polymorphism and/or particularly sensitive to the choice of the crystallization temperature. This method was used to estimate the equilibrium enthalpy of melting  $\Delta H_m^0$  of well-known polymers, such as PET and PPS, as well as of more recent biopolymers, such as PLLA, PEF and PBF.

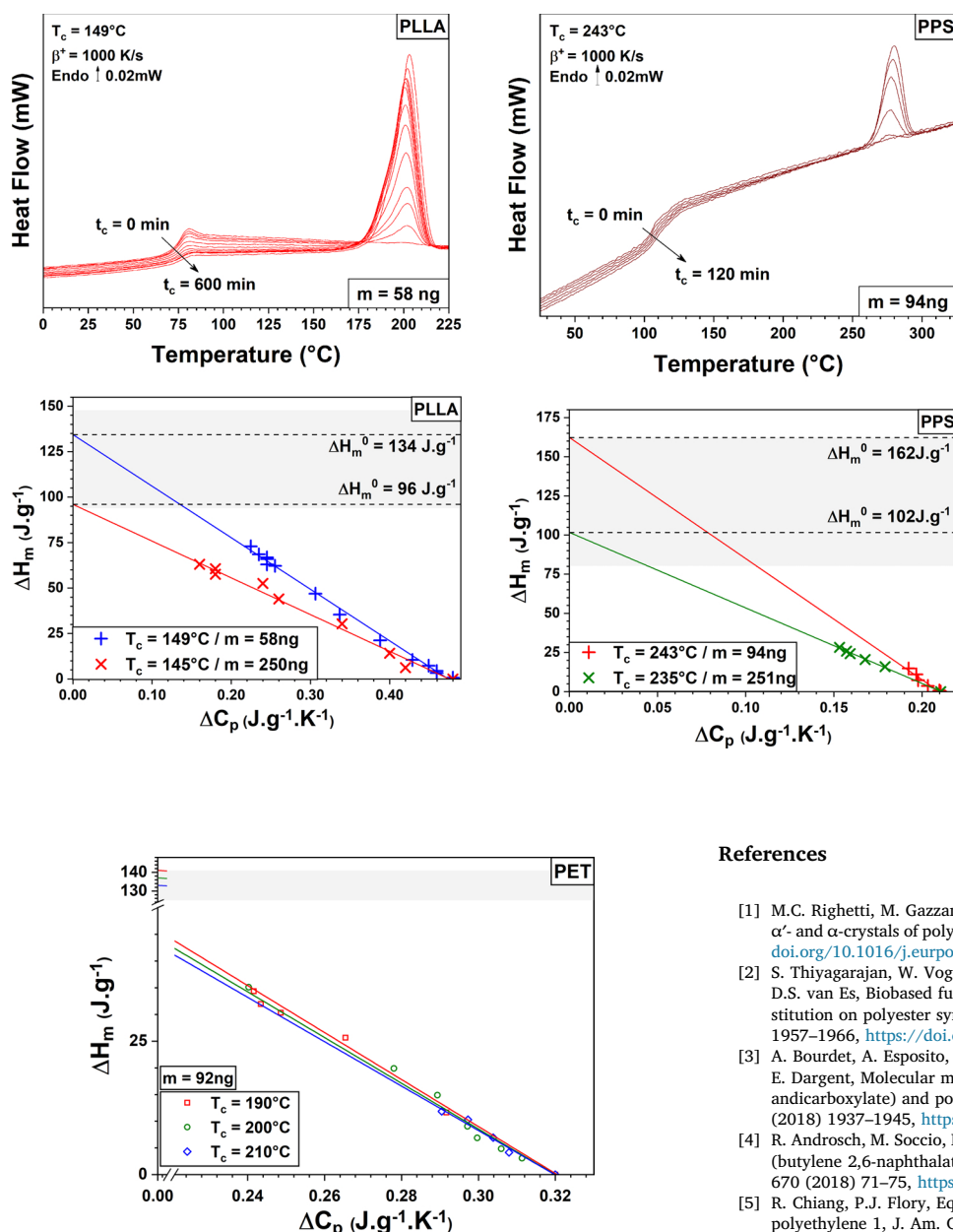


**Fig. 5.** Extrapolation based on the FSC measurements on a nanoscale sample of PET (92 ng) isothermally crystallized from the melt at three different crystallization temperatures (190 °C, 200 °C and 210 °C) during different crystallization times. The linear regression (solid lines) of the experimental data (crosses) extrapolated to  $X_c = 100\%$  and  $\Delta C_p = 0 \text{ J}\cdot\text{g}^{-1}\cdot\text{K}^{-1}$  provides a values of  $\Delta H_m^0 = 137 \pm 4 \text{ J}\cdot\text{g}^{-1}$ . The grey horizontal area represents the domain covered by the values of  $\Delta H_m^0$  found in the literature (Table 1) (For interpretation of the references to colour in this figure legend, the reader is referred to the web version of this article).

## Acknowledgments

The authors thank the Région Normandie and the European FEDER for their financial support through the SCAMPI project (Aurélien Bourdet's PhD program) and the FARM Rin Recherche project (Estève Ernault's post-doc position), as well as the French Ministère de l'Enseignement Supérieur et de la Recherche for the financial support for Clément Fosse's PhD program. The authors also thank Dr Benoît Vieille for providing PPS pellets.

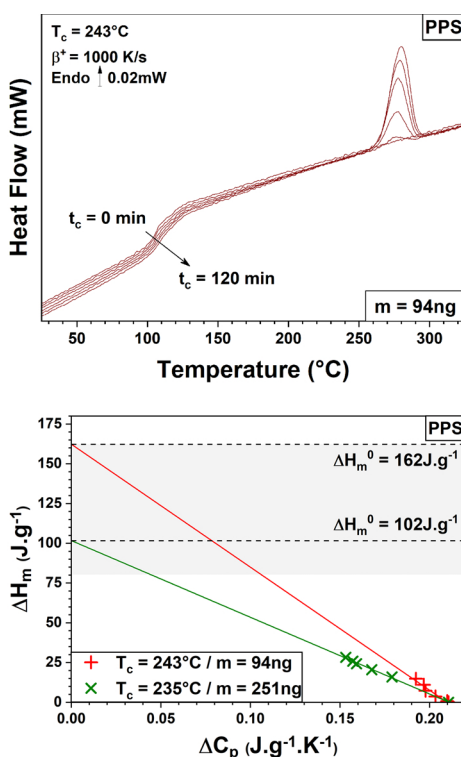


**Fig. 4.** (top) FSC curves recorded upon heating at  $\beta^* = 1000 \text{ K}\cdot\text{s}^{-1}$  on nanoscale samples of PLLA and PPS after in situ isothermal crystallization from the melt at two different crystallization temperatures (145 °C and 149 °C for PLLA, 235 °C and 243 °C for PPS) during different crystallization times. Smaller samples were used with respect to Fig. 1 (58 ng vs. 250 ng for PLLA, 94 ng vs. 251 ng for PPS). (bottom) Enthalpy of melting vs. heat capacity change at the glass transition obtained from the FSC curves normalized to the sample mass and to the heating rate. The linear regression (solid lines) of the experimental data (crosses) extrapolated to  $X_c = 100\%$  and  $\Delta C_p = 0 \text{ J}\cdot\text{g}^{-1}\cdot\text{K}^{-1}$  reveals the equilibrium enthalpy of melting  $\Delta H_m^0$  under the assumption of a two-phase model. The grey horizontal areas represent the domain covered by the values of  $\Delta H_m^0$  that can be found in the literature (Table 1) plus the values obtained in this work.

## References

- [1] M.C. Righetti, M. Gazzano, M.L. Di Lorenzo, R. Androsch, Enthalpy of melting of  $\alpha'$ - and  $\alpha$ -crystals of poly(L-lactic acid), *Eur. Polym. J.* 70 (2015) 215–220, <https://doi.org/10.1016/j.eurpolymj.2015.07.024>.
- [2] S. Thiagarajan, W. Vogelzang, R.J.I. Knoop, A.E. Frissen, J. van Haverenab, D.S. van Es, Biobased furandicarboxylic acids (FDCA): effects of isomeric substitution on polyester synthesis and properties, *Green Chem.* 16 (2014) 1957–1966, <https://doi.org/10.1039/c3gc42184h>.
- [3] A. Bourdet, A. Esposito, S. Thiagarajan, L. Delbreilh, F. Affouard, R.J.I. Knoop, E. Dargent, Molecular mobility in amorphous biobased poly(ethylene 2,5-furandicarboxylate) and poly(ethylene 2,4-furandicarboxylate), *Macromolecules* 51 (2018) 1937–1945, <https://doi.org/10.1021/acs.macromol.8b00108>.
- [4] R. Androsch, M. Soccio, N. Lotti, D. Cavallo, C. Schick, Cold-crystallization of poly(butylene 2,6-naphthalate) following Ostwald's rule of stages, *Thermochim. Acta* 670 (2018) 71–75, <https://doi.org/10.1016/j.tca.2018.10.015>.
- [5] R. Chiang, P.J. Flory, Equilibrium between crystalline and amorphous phases in polyethylene 1, *J. Am. Chem. Soc.* 83 (1961) 2857–2862, <https://doi.org/10.1021/ja01474a017>.
- [6] B. Wunderlich, C.M. Cormier, Heat of fusion of polyethylene. *Journal of polymer science part A-2, J. Polym. Sci.: Polym. Phys. Ed.* 5 (1967) 987–988, <https://doi.org/10.1002/pol.1967.160050514>.
- [7] C.M.L. Atkinson, M.J. Richardson, Thermodynamic properties of ideally crystalline polyethylene, *Trans. Faraday Soc.* 65 (1969) 1764, <https://doi.org/10.1039/tf9696501764>.
- [8] P. Cebe, D. Thomas, J. Merfeld, B.P. Partlow, D.L. Kaplan, R.G. Alamo, A. Wurm, E. Zhuravlev, C. Schick, Heat of fusion of polymer crystals by fast scanning calorimetry, *Polymer* 126 (2017) 240–247, <https://doi.org/10.1016/j.polymer.2017.08.042>.
- [9] F. Danusso, G. Gianotti, Fusion enthalpy and entropy of isotactic polypropylene, *Eur. Polym. J.* 4 (1968) 165–171, [https://doi.org/10.1016/0014-3057\(68\)90018-9](https://doi.org/10.1016/0014-3057(68)90018-9).
- [10] R. Dedeurwaerder, J.F.M. Oth, Enthalpie et entropie de fusion du polystyrène isotactique, *J. Chim. Phys.* 56 (1959) 940–945, <https://doi.org/10.1051/jcp/1959560940>.
- [11] I. Abu-Isa, M. Dole, Specific heat of synthetic high polymers. XII. Atactic and isotactic polystyrene 1, *J. Phys. Chem.* 69 (1965) 2668–2675, <https://doi.org/10.1021/j100892a031>.
- [12] G. Gee, *London Proceedings of the Chemical Society 1957*, Proceedings of the Chemical Society (1957) 111.
- [13] J.R. Schaeffgen, Estimation of the heat and entropy of fusion of some polyhydrocarbons, *J. Polym. Sci.* 38 (1959) 549–552, <https://doi.org/10.1002/pol.1959.1203813427>.
- [14] S. Newman, On the characterization of stereoregular polymers. II. Polypropylene, *J. Polym. Sci.* 47 (1960) 111–137, <https://doi.org/10.1002/pol.1960.1204714911>.

- [15] B. Ke, Characterization of polyolefins by differential thermal analysis, *J. Polym. Sci.* 42 (1960) 15–23, <https://doi.org/10.1002/pol.1960.1204213903>.
- [16] R.W. Wilkinson, M. Dole, Specific heat of synthetic high polymers. X. Isotactic and atactic polypropylene, *J. Polym. Sci.* 58 (1962) 1089–1106, <https://doi.org/10.1002/pol.1962.1205816668>.
- [17] E. Passaglia, H.K. Kevorkian, Specific heat of atactic and isotactic polypropylene and the entropy of the glass, *J. Appl. Phys.* 34 (1963) 90–97, <https://doi.org/10.1063/1.1729095>.
- [18] J.G. Fatou, Melting temperature and enthalpy of isotactic polypropylene, *Eur. Polym. J.* 7 (1971) 1057–1064, [https://doi.org/10.1016/0014-3057\(71\)90138-8](https://doi.org/10.1016/0014-3057(71)90138-8).
- [19] P. Marx, C.W. Smith, A.E. Worthington, M. Dole, Specific heat of synthetic high polymers. IV. Polycaprolactam, *J. Phys. Chem.* 59 (1955) 1015–1019, <https://doi.org/10.1021/j150532a005>.
- [20] S. Gogolewski, A. Pennings, Crystallization of polyamides under elevated pressure: 2. Pressure-induced crystallization of nylon-6 (polycapramide) from the melt, *Polymer* 16 (1975) 673–679, [https://doi.org/10.1016/0032-3861\(75\)90075-0](https://doi.org/10.1016/0032-3861(75)90075-0).
- [21] M. Pyda, ATLAS Data Bank 2019.
- [22] H.F. Mark, et al. (Ed.), *Encyclopedia of Polymer Science and Engineering*, vol. 12, John Wiley and Sons, New York, 1985p. 226.
- [23] A. Conix, R. Van Kerpel, Crystallization behavior and melting properties of *m*-phenylene group containing polyesters, *J. Polym. Sci.* 40 (1959) 521–532, <https://doi.org/10.1002/pol.1959.1204013720>.
- [24] K.-H. Illers, Heat of fusion and specific volume of poly(ethylene terephthalate) and poly(butylene terephthalate), *Colloid Polym. Sci.* 258 (1980) 117–124, <https://doi.org/10.1007/BF01498267>.
- [25] T. Miyata, T. Masuko, Crystallization behaviour of poly(L-lactide), *Polymer* 39 (1998) 5515–5521, [https://doi.org/10.1016/S0032-3861\(97\)10203-8](https://doi.org/10.1016/S0032-3861(97)10203-8).
- [26] M. Pyda, R. Bopp, B. Wunderlich, Heat capacity of poly(lactic acid), *J. Chem. Thermodyn.* 36 (2004) 731–742, <https://doi.org/10.1016/j.jct.2004.05.003>.
- [27] P. Badrinarayanan, K.B. Dowdy, M.R. Kessler, A comparison of crystallization behavior for melt and cold crystallized poly (L-Lactide) using rapid scanning rate calorimetry, *Polymer* 51 (2010) 4611–4618, <https://doi.org/10.1016/j.polymer.2010.08.014>.
- [28] J.P. Kalish, K. Aou, X. Yang, S.L. Hsu, Spectroscopic and thermal analyses of  $\alpha'$  and  $\alpha$  crystalline forms of poly(L-lactic acid), *Polymer* 52 (2011) 814–821, <https://doi.org/10.1016/j.polymer.2010.12.042>.
- [29] S.Z.D. Cheng, Z.Q. Wu, B. Wunderlich, Glass transition and melting behavior of poly(thio-1,4-phenylene), *Macromolecules* 20 (1987) 2802–2810, <https://doi.org/10.1021/ma00177a028>.
- [30] E. Maemura, M. Cakmak, J.L. White, Characterization of crystallinity and orientation in Poly-*p*-Phenylene sulfide, *Int. Polym. Process.* 3 (1988) 79–85, <https://doi.org/10.3139/217.880079>.
- [31] P. Huo, P. Cebe, Effects of thermal history on the rigid amorphous phase in poly(phenylene sulfide), *Colloid Polym. Sci.* 270 (1992) 840–852, <https://doi.org/10.1007/BF00657728>.
- [32] G.Z. Papageorgiou, V. Tsanakis, D.N. Bikiaris, Synthesis of poly(ethylene furandicarboxylate) polyester using monomers derived from renewable resources: thermal behavior comparison with PET and PEN, *Phys. Chem. Chem. Phys.* 16 (2014) 7946–7958, <https://doi.org/10.1039/C4CP00518J>.
- [33] G. Stoclet, G. Gobius du Sart, B. Yeniad, S. de Vos, J.M. Lefebvre, Isothermal crystallization and structural characterization of poly(ethylene-2,5-furanoate), *Polymer* 72 (2015) 165–176, <https://doi.org/10.1016/j.polymer.2015.07.014>.
- [34] J.G. van Berkel, N. Guigo, J.J. Kolstad, L. Sipos, B. Wang, M.A. Dam, N. Sbirrazzuoli, Isothermal Crystallization Kinetics of Poly (Ethylene 2,5-Furandicarboxylate): Isothermal Crystallization Kinetics of Poly (Ethylene 2,5-Furandicarboxylate), *Macromol. Mater. Eng.* 300 (2015) 466–474, <https://doi.org/10.1002/mame.201400376>.
- [35] G.Z. Papageorgiou, V. Tsanakis, D.G. Papageorgiou, S. Exarhopoulos, M. Papageorgiou, D.N. Bikiaris, Evaluation of polyesters from renewable resources as alternatives to the current fossil-based polymers. Phase transitions of poly(butylene 2,5-furan-dicarboxylate), *Polymer* 55 (2014) 3846–3858, <https://doi.org/10.1016/j.polymer.2014.06.025>.
- [36] E.W. Fischer, H.J. Sterzel, G. Wegner, Investigation of the structure of solution grown crystals of lactide copolymers by means of chemical reactions, *Colloid Polym. Sci.* 251 (11) (1973) 980–990, <https://doi.org/10.1007/BF01498927>.
- [37] T. Okada, L. Mandelkern, Effect of morphology and degree of crystallinity on the infrared absorption spectra of linear polyethylene, *J. Polym. Sci. Part A-2 Polym. Phys.* 5 (1967) 239–262, <https://doi.org/10.1002/pol.1967.160050201>.
- [38] X. Hu, D. Kaplan, P. Cebe, Determining beta-sheet crystallinity in fibrous proteins by thermal analysis and infrared spectroscopy, *Macromolecules.* 39 (2006) 6161–6170, <https://doi.org/10.1021/ma0610109>.
- [39] C.E. Miller, B.E. Eichinger, Determination of crystallinity and morphology of fibrous and bulk poly(ethylene terephthalate) by near-infrared diffuse reflectance spectroscopy, *Appl. Spectrosc.* 44 (1990) 496–504, <https://doi.org/10.1366/0003702904086173>.
- [40] S.-F. Yao, X.-T. Chen, H.-M. Ye, Investigation of structure and crystallization behavior of poly(butylene succinate) by Fourier transform infrared spectroscopy, *J. Phys. Chem. B* 121 (2017) 9476–9485, <https://doi.org/10.1021/acs.jpcc.7b07954>.
- [41] B.H. Stuart, Polymer crystallinity studied using Raman spectroscopy, *Vib. Spectrosc.* 10 (1996) 79–87, [https://doi.org/10.1016/0924-2031\(95\)00042-9](https://doi.org/10.1016/0924-2031(95)00042-9).
- [42] A. Nielsen, D. Batchelder, R. Pyrz, Estimation of crystallinity of isotactic polypropylene using Raman spectroscopy, *Polymer* 43 (2002) 2671–2676, [https://doi.org/10.1016/S0032-3861\(02\)00053-8](https://doi.org/10.1016/S0032-3861(02)00053-8).
- [43] F. Rull, A.C. Prieto, J.M. Casado, F. Sobron, H.G.M. Edwards, Estimation of crystallinity in polyethylene by Raman spectroscopy, *J. Raman Spectrosc.* 24 (1993) 545–550, <https://doi.org/10.1002/jrs.1250240813>.
- [44] L.S. Taylor, G. Zografi, The quantitative analysis of crystallinity using FT-Raman spectroscopy, *Pharm. Res.* 15 (5) (1998) 755–761, <https://doi.org/10.1023/A:1011979221685>.
- [45] G.R. Strobl, W. Hagedorn, Raman spectroscopic method for determining the crystallinity of polyethylene, *J. Polym. Sci.: Polym. Phys. Ed.* 16 (1978) 1181–1193, <https://doi.org/10.1002/pol.1978.180160704>.
- [46] K. Schenzel, S. Fischer, E. Brendler, New method for determining the degree of cellulose I crystallinity by means of FT raman spectroscopy, *Cellulose* 12 (2005) 223–231, <https://doi.org/10.1007/s10570-004-3885-6>.
- [47] P. Cebe, X. Hu, D.L. Kaplan, E. Zhuravlev, A. Wurm, D. Arbeiter, C. Schick, Beating the heat - fast scanning melts silk Beta sheet crystals, *Sci. Rep.* 3 (2013) 1130, <https://doi.org/10.1038/srep01130>.
- [48] Y. Corvis, A. Wurm, C. Schick, P. Espeau, Vitreous state characterization of pharmaceutical compounds degrading upon melting by using fast scanning calorimetry, *J. Phys. Chem. B* 119 (2015) 6848–6851, <https://doi.org/10.1021/acs.jpcc.5b03041>.
- [49] J.A.S. Puente, A. Esposito, F. Chivrac, E. Dargent, Effects of size and specific surface area of boron nitride particles on the crystallization of bacterial poly(3-hydroxybutyrate-co-3-hydroxyvalerate), *Macromol. Symp.* 328 (2013) 8–19, <https://doi.org/10.1002/masy.2013050601>.
- [50] J.A.S. Puente, A. Esposito, F. Chivrac, E. Dargent, Effect of boron nitride as a nucleating agent on the crystallization of bacterial poly(3-hydroxybutyrate), *J. Appl. Polym. Sci.* 128 (2013) 2586–2594, <https://doi.org/10.1002/app.38182>.
- [51] Y. Kong, J.N. Hay, The measurement of the crystallinity of polymers by DSC, *Polymer* 43 (2002) 3873–3878, [https://doi.org/10.1016/S0032-3861\(02\)00235-5](https://doi.org/10.1016/S0032-3861(02)00235-5).
- [52] A. Toda, R. Androsch, C. Schick, Insights into polymer crystallization and melting from fast scanning chip calorimetry, *Polymer* 91 (2016) 239–263, <https://doi.org/10.1016/j.polymer.2016.03.038>.
- [53] A.A. Minakov, D.A. Mordvintsev, C. Schick, Melting and reorganization of poly(ethylene terephthalate) on fast heating (1000 K/s), *Polymer* 45 (2004) 3755–3763, <https://doi.org/10.1016/j.polymer.2004.03.072>.
- [54] S. Adamovsky, A. Minakov, C. Schick, Scanning microcalorimetry at high cooling rate, *Thermochim. Acta* 403 (2003) 55–63, [https://doi.org/10.1016/S0040-6031\(03\)00182-5](https://doi.org/10.1016/S0040-6031(03)00182-5).
- [55] F. De Santis, S. Adamovsky, G. Titomanlio, C. Schick, Scanning nanocalorimetry at high cooling rate of isotactic polypropylene, *Macromolecules* 39 (2006) 2562–2567, <https://doi.org/10.1021/ma052525n>.
- [56] A. Esposito, N. Delpouve, V. Causin, A. Dhotel, L. Delbreilh, E. Dargent, From a three-phase model to a continuous description of molecular mobility in Semicrystalline Poly(hydroxybutyrate-co-hydroxyvalerate), *Macromolecules* 49 (2016) 4850–4861, <https://doi.org/10.1021/acs.macromol.6b00384>.
- [57] M. Pyda, A. Boller, J. Grebowicz, H. Chuah, B.V. Lebedev, B. Wunderlich, Heat capacity of poly(trimethylene terephthalate), *J. Polym. Sci. Part B: Polym. Phys.* 36 (1998) 2499–2511, [https://doi.org/10.1002/\(SICI\)1099-0488\(199810\)36:14<2499::AID-POLB4>3.0.CO;2-O](https://doi.org/10.1002/(SICI)1099-0488(199810)36:14<2499::AID-POLB4>3.0.CO;2-O).
- [58] B. Wunderlich, Reversible crystallization and the rigid amorphous phase in semicrystalline macromolecules, *Prog. Polym. Sci.* 28 (2003) 383–450, [https://doi.org/10.1016/S0079-6700\(02\)00085-0](https://doi.org/10.1016/S0079-6700(02)00085-0).
- [59] H. Chen, P. Cebe, Vitrification and devitrification of rigid amorphous fraction of PET during quasi-isothermal cooling and heating, *Macromolecules* 42 (2009) 288–292, <https://doi.org/10.1021/ma802104a>.
- [60] B. Wunderlich, A. Mehta, Macromolecular nucleation, *J. Polym. Sci.: Polym. Phys. Ed.* 12 (1974) 255–263, <https://doi.org/10.1002/pol.1974.180120203>.
- [61] R. Androsch, B. Wunderlich, The link between rigid amorphous fraction and crystal perfection in cold-crystallized poly(ethylene terephthalate), *Polymer* 46 (2005) 12556–12566, <https://doi.org/10.1016/j.polymer.2005.10.099>.
- [62] M. Arnould, E. Dargent, J.F. Mano, Mobile amorphous phase fragility in semicrystalline polymers: comparison of PET and PLLA, *Polymer* 48 (2007) 1012–1019, <https://doi.org/10.1016/j.polymer.2006.12.053>.
- [63] C. Schick, A. Wurm, A. Mohammed, Formation and disappearance of the rigid amorphous fraction in semicrystalline polymers revealed from frequency dependent heat capacity, *Thermochim. Acta* 396 (2003) 119–132, [https://doi.org/10.1016/S0040-6031\(02\)00526-9](https://doi.org/10.1016/S0040-6031(02)00526-9).
- [64] M.C. Righetti, E. Tombari, M. Angiuli, M.L.D. Lorenzo, Enthalpy-based determination of crystalline, mobile amorphous and rigid amorphous fractions in semicrystalline polymers, *Thermochim. Acta* 462 (2007) 15–24, <https://doi.org/10.1016/j.tca.2007.06.003>.
- [65] A. Guinault, C. Sollogoub, V. Ducruet, S. Domenek, Impact of crystallinity of poly(lactide) on helium and oxygen barrier properties, *Eur. Polym. J.* 48 (2012) 779–788, <https://doi.org/10.1016/j.eurpolymj.2012.01.014>.
- [66] T.L. Nguyen, F. Bédoui, P.-E. Mazeran, M. Guignon, Mechanical investigation of confined amorphous phase in semicrystalline polymers: case of PET and PLA, *Polym. Eng. Sci.* 55 (2015) 397–405, <https://doi.org/10.1002/pen.23896>.
- [67] S. Martín, M.T. Expósito, J.F. Vega, J. Martínez-Salazar, Microstructure and properties of branched polyethylene: Application of a three-phase structural model, *J. Appl. Polym. Sci.* 128 (2013) 1871–1878, <https://doi.org/10.1002/app.38290>.
- [68] B.G. Olson, J. Lin, S. Nazarenko, A.M. Jamieson, Positron annihilation lifetime spectroscopy of poly(ethylene terephthalate): contributions from rigid and mobile amorphous fractions, *Macromolecules* 36 (2003) 7618–7623, <https://doi.org/10.1021/ma034813u>.
- [69] M. Drieskens, R. Peeters, J. Mullens, D. Franco, P.J. Lemstra, D.G. Hristova-Bogaerds, Structure versus properties relationship of poly(lactic acid). I. Effect of crystallinity on barrier properties, *J. Polym. Sci. Part B: Polym. Phys.* 47 (2009)

- 2247–2258, <https://doi.org/10.1002/polb.21822>.
- [70] I. Kolesov, R. Androsch, The rigid amorphous fraction of cold-crystallized polyamide 6, *Polymer* 53 (2012) 4770–4777, <https://doi.org/10.1016/j.polymer.2012.08.017>.
- [71] S. Fernandes Nassar, A. Guinault, N. Delpouve, V. Divry, V. Ducruet, C. Sollogoub, S. Domenek, Multi-scale analysis of the impact of polylactide morphology on gas barrier properties, *Polymer* 108 (2017) 163–172, <https://doi.org/10.1016/j.polymer.2016.11.047>.
- [72] C. Schick, A. Wurm, A. Mohamed, Vitrification and devitrification of the rigid amorphous fraction of semicrystalline polymers revealed from frequency-dependent heat capacity, *Colloid Polym. Sci.* 279 (2001) 800–806, <https://doi.org/10.1007/s003960100507>.
- [73] M.C. Righetti, D. Prevosto, E. Tombari, Time and temperature evolution of the rigid amorphous fraction and differently constrained amorphous fractions in PLLA, *Macromol. Chem. Phys.* 217 (2016) 2013–2026, <https://doi.org/10.1002/macp.201600210>.
- [74] M.C. Righetti, E. Tombari, Crystalline, mobile amorphous and rigid amorphous fractions in poly(L-lactic acid) by TMDSC, *Thermochim. Acta* 522 (2011) 118–127, <https://doi.org/10.1016/j.tca.2010.12.024>.
- [75] S.F. Nassar, S. Domenek, A. Guinault, G. Stoclet, N. Delpouve, C. Sollogoub, Structural and dynamic heterogeneity in the amorphous phase of poly(L,L-lactide) confined at the nanoscale by the coextrusion process, *Macromolecules* 51 (2018) 128–136, <https://doi.org/10.1021/acs.macromol.7b02188>.
- [76] F. Hamonic, V. Miri, A. Saiter, E. Dargent, Rigid amorphous fraction versus oriented amorphous fraction in uniaxially drawn polyesters, *Eur. Polym. J.* 58 (2014) 233–244, <https://doi.org/10.1016/j.eurpolymj.2014.06.014>.
- [77] D.F. Miranda, C. Yin, S. Zhang, J. Runt, Fluoropolymer microstructure and dynamics: influence of molecular orientation induced by uniaxial drawing, *Polymer* 91 (2016) 211–221, <https://doi.org/10.1016/j.polymer.2016.03.057>.
- [78] P. Huo, P. Cebe, Effects of thermal history on the rigid amorphous phase in poly(phenylene sulfide), *Colloid Polym. Sci.* 270 (1992) 840–8852, <https://doi.org/10.1007/BF00657728>.
- [79] A.A. Minakov, A. Wurm, C. Schick, Superheating in linear polymers studied by ultrafast nanocalorimetry, *Eur. Phys. J. E.* 23 (2007) 43–53, <https://doi.org/10.1140/epje/i2007-10173-8>.
- [80] J. Mencil, B. Wunderlich, Heat capacity hysteresis of semicrystalline macromolecular glasses, *J. Polym. Sci. Polym. Lett. Ed.* 19 (1981) 261–264, <https://doi.org/10.1002/pol.1981.130190506>.
- [81] Q. Ma, G. Georgiev, P. Cebe, Constraints in semicrystalline polymers: using quasi-isothermal analysis to investigate the mechanisms of formation and loss of the rigid amorphous fraction, *Polymer* 52 (2011) 4562–4570, <https://doi.org/10.1016/j.polymer.2011.08.006>.
- [82] M. Kanchanasopa, E. Manias, J. Runt, Solid-state microstructure of poly(L-lactide) and L-Lactide/meso-Lactide random copolymers by atomic force microscopy (AFM), *Biomacromolecules* 4 (2003) 1203–1213, <https://doi.org/10.1021/bm034063w>.
- [83] C. Santa Cruz, N. Stribeck, H.G. Zachmann, F.J. Baltá Calleja, Novel aspects in the structure of polyethylene terephthalate As revealed by means of small-angle X-ray scattering, *Macromolecules* 24 (1991) 5980–5990, <https://doi.org/10.1021/ma00022a013>.
- [84] A. Toda, M. Konishi, An evaluation of thermal lags of fast-scan microchip DSC with polymer film samples, *Thermochim. Acta* 589 (2014) 262–269, <https://doi.org/10.1016/j.tca.2014.05.038>.
- [85] C. Schick, V. Mathot (Eds.), *Fast Scanning Calorimetry*, Springer International Publishing, Rostock, Germany, 2016, <https://doi.org/10.1007/978-3-319-31329-0>.
- [86] J.E.K. Schawe, Measurement of the thermal glass transition of polystyrene in a cooling rate range of more than six decades, *Thermochim. Acta* 603 (2015) 128–134, <https://doi.org/10.1016/j.tca.2014.05.025>.
- [87] J.E.K. Schawe, Description of thermal relaxation of polystyrene close to the thermal glass transition, *J. Polym. Sci. Part B: Polym. Phys.* 36 (1998) 2165–2175, [https://doi.org/10.1002/\(SICI\)1099-0488\(19980915\)36:12<2165::AID-POLB14>3.0.CO;2-Y](https://doi.org/10.1002/(SICI)1099-0488(19980915)36:12<2165::AID-POLB14>3.0.CO;2-Y).
- [88] A. Dhotel, B. Rijal, L. Delbreilh, E. Dargent, A. Saiter, Combining Flash DSC, DSC and broadband dielectric spectroscopy to determine fragility, *J. Therm. Anal. Calorim.* 121 (2015) 453–461, <https://doi.org/10.1007/s10973-015-4650-9>.
- [89] X. Monnier, A. Saiter, E. Dargent, Vitrification of PLA by fast scanning calorimetry: Towards unique glass above critical cooling rate? *Thermochim. Acta* 658 (2017) 47–54, <https://doi.org/10.1016/j.tca.2017.10.019>.
- [90] A.A. Lacey, D.M. Price, M. Reading, *Theory and practice of modulated temperature differential scanning calorimetry*, *Modulated Temperature Differential Scanning Calorimetry*, Springer, 2006, pp. 1–81.
- [91] V.B.F. Mathot, Temperature dependence of some thermodynamic functions for amorphous and semi-crystalline polymers, *Polymer* 25 (1984) 579–599, [https://doi.org/10.1016/0032-3861\(84\)90025-9](https://doi.org/10.1016/0032-3861(84)90025-9).
- [92] V.B.F. Mathot, *Thermal characterization of states of matter*, in: V.B.F. Mathot (Ed.), *Calorimetry and Thermal Analysis of Polymers*, Hanser/Gardner Publications, Cincinnati, OH USA, 1994.
- [93] J. Zhang, Y. Duan, H. Sato, H. Tsuji, I. Noda, S. Yan, Y. Ozaki, Crystal modifications and thermal behavior of poly(L-lactic acid) revealed by infrared spectroscopy, *Macromolecules* 38 (2005) 8012–8021, <https://doi.org/10.1021/ma051232r>.
- [94] L. Martino, N. Guigo, J.G. van Berkel, J.J. Kolstad, N. Sbirrazzuoli, Nucleation and self-nucleation of bio-based poly(ethylene 2,5-furandicarboxylate) probed by fast scanning calorimetry, *Macromol. Mater. Eng.* 301 (2016) 586–596, <https://doi.org/10.1002/mame.201500418>.
- [95] J. Ma, X. Yu, J. Xu, Y. Pang, Synthesis and crystallinity of poly(butylene 2,5-furandicarboxylate), *Polymer* 53 (2012) 4145–4151, <https://doi.org/10.1016/j.polymer.2012.07.022>.
- [96] M.L. Di Lorenzo, Calorimetric analysis of the multiple melting behavior of poly(L-lactic acid), *J. Appl. Polym. Sci.* 100 (2006) 3145–3151, <https://doi.org/10.1002/app.23136>.
- [97] P. Pan, W. Kai, B. Zhu, T. Dong, Y. Inoue, Polymorphous crystallization and multiple melting behavior of poly(L-lactide): molecular weight dependence, *Macromolecules* 40 (2007) 6898–6905, <https://doi.org/10.1021/ma071258d>.
- [98] M. Yasuniwa, S. Tsubakihara, Y. Sugimoto, C. Nakafuku, Thermal analysis of the double-melting behavior of poly(L-lactic acid), *J. Polym. Sci. Part B: Polym. Phys.* 42 (2004) 25–32, <https://doi.org/10.1002/polb.10674>.
- [99] A.P. Melnikov, M. Rosenthal, A.I. Rodygin, D. Doblas, D.V. Anokhin, M. Burghammer, D.A. Ivanov, Re-exploring the double-melting behavior of semirigid-chain polymers with an in-situ combination of synchrotron nano-focus X-ray scattering and nanocalorimetry, *Eur. Polym. J.* 81 (2016) 598–606, <https://doi.org/10.1016/j.eurpolymj.2015.12.031>.
- [100] G.W.H. Höhne, Another approach to the Gibbs-Thomson equation and the melting point of polymers and oligomers, *Polymer* 43 (2002) 4689–4698, [https://doi.org/10.1016/S0032-3861\(02\)00305-1](https://doi.org/10.1016/S0032-3861(02)00305-1).
- [101] A. Seidel, *Characterization and Analysis of Polymers*, John Wiley & Sons, 2008, p. 755.
- [102] N.S. Murthy, S.T. Correale, H. Minor, Structure of the amorphous phase in crystallizable polymers: poly(ethylene terephthalate), *Macromolecules* 24 (1991) 1185–1189, <https://doi.org/10.1021/ma00005a033>.
- [103] J.F. Mano, Structural evolution of the amorphous phase during crystallization of poly(L-lactic acid): a synchrotron wide-angle X-ray scattering study, *J. Non-Cryst. Solids* 353 (2007) 2567–2572, <https://doi.org/10.1016/j.jnoncrysol.2007.04.022>.
- [104] N.S. Murthy, H. Minor, General procedure for evaluating amorphous scattering and crystallinity from X-ray diffraction scans of semicrystalline polymers, *Polymer* 31 (1990) 996–1002, [https://doi.org/10.1016/0032-3861\(90\)90243-R](https://doi.org/10.1016/0032-3861(90)90243-R).
- [105] J.D. Hoffman, Regime III crystallization in melt-crystallized polymers: the variable cluster model of chain folding, *Polymer* 24 (1983) 3–26, [https://doi.org/10.1016/0032-3861\(83\)90074-5](https://doi.org/10.1016/0032-3861(83)90074-5).
- [106] I. Okazaki, B. Wunderlich, Modulated differential scanning calorimetry in the glass transition region, V. Activation energies and relaxation times of poly(ethylene terephthalate), *J. Polym. Sci. Part B: Polym. Phys.* 34 (1996) 2941–2952, [https://doi.org/10.1002/\(SICI\)1099-0488\(199612\)34:17<2941::AID-POLB7>3.0.CO;2-T](https://doi.org/10.1002/(SICI)1099-0488(199612)34:17<2941::AID-POLB7>3.0.CO;2-T).
- [107] M. van Drongelen, T. Meijer-Vissers, D. Cavallo, G. Portale, G.V. Poel, R. Androsch, Microfocus wide-angle X-ray scattering of polymers crystallized in a fast scanning chip calorimeter, *Thermochim. Acta* 563 (2013) 33–37, <https://doi.org/10.1016/j.tca.2013.04.007>.
- [108] D. Baeten, V.B.F. Mathot, T.F.J. Pijpers, O. Verkinderen, G. Portale, P. Van Puyvelde, B. Goderis, Simultaneous synchrotron WAXD and fast scanning (Chip) calorimetry: on the (Isothermal) crystallization of HDPE and PA11 at high supercoolings and cooling rates up to 200 °C s<sup>-1</sup>, *Macromol. Rapid Commun.* 36 (2015) 1184–1191, <https://doi.org/10.1002/marc.201500081>.

# Synthesis and Thermal Properties of Bio-Based Copolyesters from the Mixtures of 2,5- and 2,4-Furandicarboxylic Acid with Different Diols

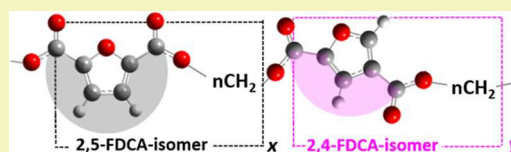
Shanmugam Thiyagarajan,<sup>\*,†</sup> Michael A. Meijlink,<sup>†</sup> Aurélie Bourdet,<sup>†,‡</sup> Willem Vogelzang,<sup>†</sup> Rutger J. I. Knoop,<sup>†</sup> Antonella Esposito,<sup>\*,‡</sup> Eric Dargent,<sup>‡</sup> Daan S. van Es,<sup>†</sup> and Jacco van Haveren<sup>†</sup>

<sup>†</sup>Wageningen Food and Biobased Research, Bornse Weiland 9, 6708 WG Wageningen, Netherlands

<sup>‡</sup>Groupe de Physique des Matériaux, Normandie Univ, UNIROUEN, INSA Rouen, CNRS, 76000 Rouen, France

## Supporting Information

**ABSTRACT:** Recent works highlighted how interesting are the properties of furan-based polyesters. Most of the attention has been focused on the homopolyester obtained with 2,5-furandicarboxylic acid and ethylene glycol, but other possibilities exist, which could help in tuning the final properties by carefully selecting the nature and proportion of the initial building blocks. This work reports the synthesis and properties (thermal stability, activation energy for thermal decomposition, glass transition temperature, and aptitude to crystallize) of three series of polyesters obtained by combining various amounts of two isomers of furandicarboxylic acid with different linear aliphatic diols, such as ethylene glycol, 1,3-propanediol, and 1,4-butanediol. This approach provided homopolymers and copolymers with high molecular weights, good thermal stability, broad processing windows, and a thermal behavior that can be tuned both in terms of glass transition temperature and crystallinity. In most cases, the mixtures of 2,5- and 2,4-isomers obtained during the Henkel disproportionation reaction can be directly used to synthesize furan-based copolyesters with good properties without the downstream processing typically performed to separate the isomers prior to polymerization, which may considerably reduce the time and costs for biomass valorization.



**KEYWORDS:** FDCA isomers, MT-TGA, activation energy, mixing law, Henkel reaction

## INTRODUCTION

Furandicarboxylic acid (FDCA) is a bio-based building block that has received tremendous attention since the time it appeared as a promising alternative for various petroleum-based monomers, in particular, for terephthalic acid (TA), to synthesize polymers that are suitable for several applications.<sup>1</sup> Polyesters derived from 2,5-FDCA, which is a symmetrical molecule, have properties comparable to TA-based analogues.<sup>2–5</sup> In terms of gas barrier properties, the performance of poly(ethylene-2,5-furandicarboxylate) (2,5-PEF) has been found to be even superior to poly(ethylene-terephthalate) (PET), which is obtained from ethylene glycol (EG) and TA.<sup>6–9</sup> This premise prompted several researchers to explore the potential properties of 2,5-FDCA-based polymers in various application areas.<sup>10–13</sup> Evidence has been recently reported about the structure–property relationship of three isomers of FDCA, that is, 2,5-furandicarboxylic acid (2,5-FDCA), 2,4-furandicarboxylic acid (2,4-FDCA), and 3,4-furandicarboxylic acid (3,4-FDCA), which are simultaneously formed in a one-pot Henkel-type disproportionation reaction.<sup>4,14</sup> The position of the carboxylic group on the furan ring has no influence on the reactivity of these isomers, as proven by the fact that all of them equally lead to high-molecular weight homopolyesters.<sup>4</sup> However, thermal analysis revealed that the homopolyester derived from 2,4-FDCA, that is, poly(ethylene-2,4-furandicarboxylate) (2,4-PEF), even if it is

amorphous, has a glass transition temperature that is very similar to that of 2,5-PEF and PET, which are both semicrystalline. These results encourage us to further investigate the potential properties of different copolyesters derived from a mixture of 2,5- and 2,4-FDCA isomers. Given that the selectivity of the Henkel reaction to the formation of 3,4-FDCA is not significant (yield of <5%),<sup>14</sup> in this study, the 3,4-isomer is not investigated. Various ratios of the isomers 2,5- and 2,4-FDCA were used in combination with different linear aliphatic diols, such as ethylene glycol (EG), 1,3-propanediol (PDO), and 1,4-butanediol (BDO), to synthesize a brand new family of copolyesters (Scheme 1). Two approaches were used to obtain mixtures of 2,5- and 2,4-FDCA isomers: (i) physical mixtures (the isomers were isolated and then physically mixed on purpose, i.e., with specific ratios of 2,4-FDCA and 2,5-FDCA), and (ii) Henkel mixtures (two mixtures were directly obtained from the Henkel reaction,<sup>14</sup> i.e., mixture A and mixture B, and they were used without further processing). Dimethyl esters of FDCA were synthesized and then purified to monomer grade as described in a previous publication.<sup>14</sup> The copolyesters were then synthesized similar to the homopolyesters,<sup>4</sup> that is, by

**Received:** August 1, 2019

**Revised:** October 11, 2019

**Published:** October 21, 2019

Scheme 1. Synthesis of 2,5-/2,4-FDCA Monomers and Their Copolyesters

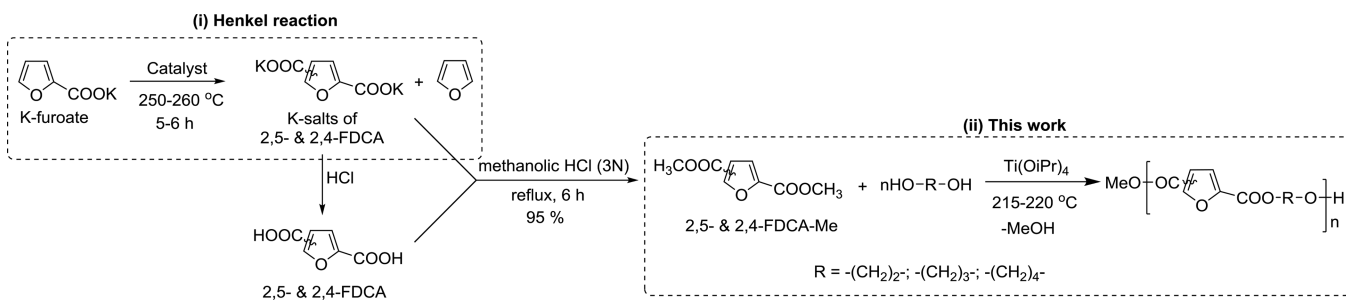


Table 1. Results of the Synthesis of Copolyesters from FDCA Isomers (2,5- and 2,4-FDCA) and Three Different Linear Glycols (EG, PDO, and BDO)

entry	code	2,5-FDCA:2,4-FDCA (mol %)		GPC <sup>c</sup>			yield <sup>g</sup> (%)	appearance <sup>h</sup>
		charged ratio	found ratio ( <sup>1</sup> H NMR)	$\overline{M}_n$ (g/mol) <sup>d</sup>	$\overline{M}_w$ (g/mol) <sup>e</sup>	$\mathcal{D}^f$		
ethylene glycol (EG)								
1	2,5-PEF	100:00	100:00	19,100	34,200	1.8	91	opaque
2	PE-2,5[95]-2,4[05]-F	95:05	95:05	20,600	36,200	1.8	89	translucent
3	PE-2,5[90]-2,4[10]-F	90:10	90:10	21,100	40,600	1.9	92	translucent
4	PE-2,5[85]-2,4[15]-F	85:15	85:15	22,000	39,900	1.8	93	translucent
5	PE-2,5[75]-2,4[25]-F	75:25	75:25	18,900	35,700	1.9	84	translucent
6	PE-2,5[50]-2,4[50]-F	50:50	50:50	30,200	57,400	1.9	87	translucent
7	PE-2,5[25]-2,4[75]-F	25:75	25:75	15,200	31,800	2.0	92	translucent
8	2,4-PEF	00:100	00:100	21,200	39,700	1.9	88	translucent
9	PEF-2,5/2,4[H.M-A]	mixture A <sup>a</sup>	68:32	14,500	28,300	1.9	85	translucent
10	PEF-2,5/2,4[H.M-B]	mixture B <sup>b</sup>	86:14	13,600	26,600	2.0	87	translucent
1,3-propanediol (PDO)								
11	2,5-PPF	100:00	100:00	36,300	64,100	1.8	89	opaque
12	PP-2,5[50]-2,4[50]-F	50:50	50:50	29,000	51,100	1.8	91	translucent
13	2,4-PPF	00:100	00:100	21,600	42,100	2.0	92	translucent
14	PPF-2,5/2,4[H.M-A]	mixture A <sup>a</sup>	74:26	28,000	58,500	2.0	88	translucent
15	PPF-2,5/2,4[H.M-B]	mixture B <sup>b</sup>	86:14	27,100	55,600	2.1	85	translucent
1,4-butanediol (BDO)								
16	2,5-PBF	100:00	100:00	21,400	55,400	2.5	90	opaque
17	PB-2,5[50]-2,4[50]-F	50:50	50:50	27,800	57,300	2.0	92	translucent
18	2,4-PBF	00:100	00:100	21,800	36,800	1.7	93	opaque
19	PBF-2,5/2,4[H.M-A]	mixture A <sup>a</sup>	72:28	53,400	112,500	2.1	87	translucent
20	PBF-2,5/2,4[H.M-B]	mixture B <sup>b</sup>	86:14	28,000	53,911	1.9	89	translucent

<sup>a</sup>Actual mixture obtained from the disproportionation reaction using CdI<sub>2</sub> as a catalyst.<sup>14</sup> <sup>b</sup>Actual mixture obtained from the disproportionation reaction using ZnCl<sub>2</sub> as a catalyst.<sup>14</sup> Feed and incorporation ratios are the same. <sup>c</sup>Gel permeation chromatography performed on crude samples using hexafluoroisopropanol (HFIP) as a solvent. <sup>d</sup>( $\overline{M}_n$ ) is the number-average molecular weight. <sup>e</sup>( $\overline{M}_w$ ) is the weight-average molecular weight. <sup>f</sup> $\mathcal{D}$  is the dispersity, i.e., a measure of how spread is the molar-mass distribution. <sup>g</sup>Isolated yield (crude). <sup>h</sup>Appearance of the crude polyester in the reactor.

melt polycondensation, and were obtained in excellent isolated yields (Table 1). This work reports the preliminary results obtained on these samples by thermogravimetric analysis (TGA), modulated-temperature TGA (MT-TGA), and differential scanning calorimetry (DSC).

Scheme 1 illustrates (i) the synthesis of dimethyl esters of 2,5-FDCA and 2,4-FDCA via the Henkel reaction and (ii) the synthesis of copolyesters derived from dimethyl esters of 2,5-FDCA and 2,4-FDCA isomers. The catalyst used, the ratio of isomers obtained, and their separation/purification procedures related to Henkel reaction are described in a previous publication.<sup>14</sup>

## RESULTS AND DISCUSSION

The series of samples based on EG was investigated more in detail (eight copolyesters compared to the homopolyesters 2,5-

PEF and 2,4-PEF) due to the increasing interest in trying to substitute PET with renewable 2,5-PEF for a range of commercial applications, whereas the series of samples based on PDO and BDO were limited (three copolyesters compared to the corresponding homopolyesters) to reduce the consumption of 2,4-FDCA, which, at the moment, is only available on a lab scale. The three series of samples are presented in Table 1 along with the main results of the synthesis. Characterizations by nuclear magnetic resonance (<sup>1</sup>H NMR and <sup>13</sup>C NMR) and Fourier transform infrared spectroscopy (FTIR) were performed to confirm the structure of the synthesized polymers (the data are reported in the Experimental Section). The number-average and weight-average molecular weights ( $\overline{M}_n$  and  $\overline{M}_w$ ) obtained by gel permeation chromatography (GPC) show that all the copolyesters synthesized in this work have reasonably high



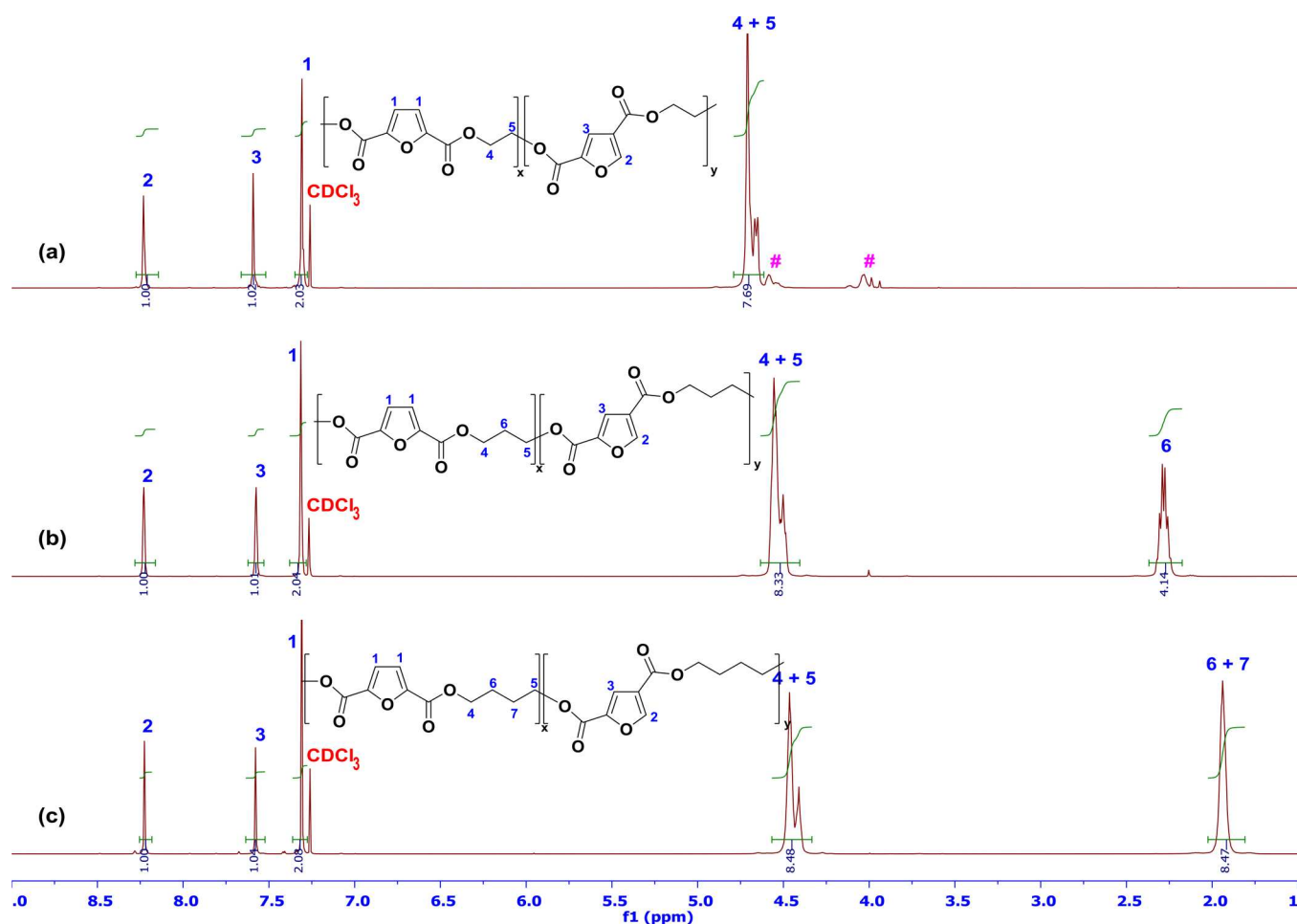


**Figure 1.**  $^1\text{H}$  NMR spectra of the 50:50 mixture of 2,5/2,4-FDCA isomers with (a) EG, (b) PDO, and (c) BDO in  $\text{CDCl}_3$  + TFA-d. The pink symbol (#) in (a) indicates the presence of DEG groups.

molecular weights with values of the dispersity ( $\mathcal{D}$ ) ranging between 1.7 and 2.5. 2,5-PEF was obtained with a molecular weight of 19,100 g/mol. The incorporation of 5 to 15 mol % 2,4-FDCA resulted in a steady increase in the molecular weight of up to 22,000 g/mol (Table 1, entries 1–4). The use of a physical mixture containing 50:50 mol % of 2,5/2,4-FDCA isomers further enhanced this effect, and the molecular weight reached 30,200 g/mol (Table 1, entry 6). A similar trend has also been reported in a very recent publication where the copolymerization of 50:50 mixtures of 2,4-FDCA Me and dimethyl terephthalate with EG produced a higher molecular weight compared to other combinations.<sup>15</sup> However, a drop in the molecular weight was observed when 25 mol % 2,4-FDCA was incorporated in the reactor (Table 1, entry 5), giving a similar value to that of 2,5-PEF. The symmetrical situation is similar because introducing 75 mol % 2,4-FDCA (which leaves 25 mol % 2,5-FDCA) in the reactor also resulted in a drop in the molecular weight from 21,200 g/mol obtained for 2,4-PEF to 15,200 g/mol (Table 1, entries 7 and 8). It is still unclear whether the results obtained with these particular ratios (25:75 and 75:25 mol %) are systematic and what could be the reasons for them. Besides preparing physical mixtures on purpose, two Henkel mixtures of the two isomers (so-called because they can be directly obtained from the Henkel reaction) were also used for the polymerization, which resulted in slightly lower molecular weights as compared to the physical mixtures having similar compositions (Table 1, entries 9 and

10). All the copolyesters listed in Table 1 were obtained in the form of translucent samples after cooling down from the melt, suggesting that the incorporation of the 2,4-isomer, even at the lowest amount, significantly disrupts the crystallization of the polymer chains. This is consistent with the results previously reported in the literature for which the homopolymer obtained with 2,4-FDCA is totally amorphous, whereas the homopolymer obtained with 2,5-FDCA is semicrystalline.<sup>4,16</sup> Besides, 2,4-FDCA seems to be the isomer that disrupts crystallinity the best because the homopolymer obtained with 3,4-FDCA was also found to be intrinsically semicrystalline.<sup>4</sup> In the series of samples obtained with PDO, a significant difference is observed in the molecular weight of the two homopolyesters, that is, 2,5-PPF and 2,4-PPF (Table 1, entries 11 and 13), and the copolyesters obtained with both the physical mixture and the Henkel mixtures resulted in molecular weights that are intermediate between the extreme values of the series (Table 1, entries 12, 14, and 15). Similar to the series of samples based on EG, all the copolyesters obtained with PDO have the appearance of translucent materials. In the series of samples obtained with BDO, the physical mixture of 50:50 mol % and the Henkel mixture B provided similar values of molecular weights ( $\bar{M}_n \approx 28,000$  g/mol) (Table 1, entries 17 and 20), whereas the Henkel mixture A provided a remarkably two-fold higher molecular weight ( $\bar{M}_n = 53,400$  g/mol) (Table 1, entry 19). In most cases, as for the samples in the BDO series, the

**Table 2.** Thermal Stability of Copolyesters from FDCA Isomers (2,5- and 2,4-FDCA) and Three Different Linear Glycols (EG, PDO, and BDO)

entry	code	TGA <sup>a</sup>		MT-TGA <sup>d</sup>			
		T <sub>5%</sub> <sup>b</sup> (°C)	T <sub>max</sub> <sup>c</sup> (°C)	T <sub>5%</sub> <sup>b</sup> (°C)	T <sub>max</sub> <sup>c</sup> (°C)	E <sub>a</sub> <sup>e</sup> (kJ mol <sup>-1</sup> )	log Z <sup>f</sup> (min <sup>-1</sup> )
ethylene glycol (EG)							
1	2,5-PEF	339	411	315 ± 3	390 ± 1	190 ± 25	14 ± 2
2	PE-2,5[95]-2,4[05]-F	328	411	334 ± 2	383 ± 2	198 ± 33	15 ± 3
3	PE-2,5[90]-2,4[10]-F	341	413	339 ± 4	390 ± 3	208 ± 30	15 ± 3
4	PE-2,5[85]-2,4[15]-F	338	411	345 ± 8	392 ± 3	185 ± 31	13 ± 2
5	PE-2,5[75]-2,4[25]-F	336	414	335 ± 2	389 ± 2	190 ± 25	13 ± 2
6	PE-2,5[50]-2,4[50]-F	331	411	334 ± 2	386 ± 4	191 ± 30	13 ± 3
7	PE-2,5[25]-2,4[75]-F	344	426	350 ± 2	399 ± 2	208 ± 23	15 ± 2
8	2,4-PEF	345	429	350 ± 2	405 ± 1	198 ± 10	14 ± 4
9	PEF-2,5/2,4[H.M-A]	339	404	344 ± 2	393 ± 2	195 ± 12	14 ± 3
10	PEF-2,5/2,4[H.M-B]	348	411	348 ± 5	411 ± 5	195 ± 35	14 ± 5
1,3-propanediol (PDO)							
11	2,5-PPF	330	405	343 ± 2	368 ± 2	167 ± 35	12 ± 3
12	PP-2,5[50]-2,4[50]-F	333	406	338 ± 2	374 ± 2	170 ± 18	12 ± 2
13	2,4-PPF	342	415	334 ± 2	376 ± 2	158 ± 26	11 ± 2
14	PPF-2,5/2,4[H.M-A]	332	401	342 ± 2	374 ± 2	176 ± 22	14 ± 2
15	PPF-2,5/2,4[H.M-B]	330	402	341 ± 2	373 ± 2	167 ± 37	15 ± 3
1,4-butanediol (BDO)							
16	2,5-PBF	304	367	304 ± 2	329 ± 2	151 ± 10	12 ± 1
17	PB-2,5[50]-2,4[50]-F	320	389	312 ± 2	343 ± 2	142 ± 19	11 ± 1
18	2,4-PBF	328	402	324 ± 2	368 ± 2	182 ± 09	13 ± 2
19	PBF-2,5/2,4[H.M-A]	327	396	331 ± 2	363 ± 2	190 ± 20	14 ± 3
20	PBF-2,5/2,4[H.M-B]	314	395	323 ± 2	365 ± 2	163 ± 16	12 ± 1

<sup>a</sup>Thermogravimetric analysis performed under N<sub>2</sub> on the final products with a heating rate of 10 °C min<sup>-1</sup>. <sup>b</sup>Temperature at which a weight loss of 5% is observed. <sup>c</sup>Temperature corresponding to the maximum rate of weight loss. <sup>d</sup>Modulated-temperature thermogravimetric analysis performed under N<sub>2</sub> on the final products after drying in a desiccator with P<sub>2</sub>O<sub>5</sub> with an overall heating rate of 2 °C min<sup>-1</sup>. <sup>e</sup>Average value of the activation energy for thermal degradation ± the difference between the upper and lower bounds of its fluctuations as a function of temperature. <sup>f</sup>Z is a pre-exponential factor.

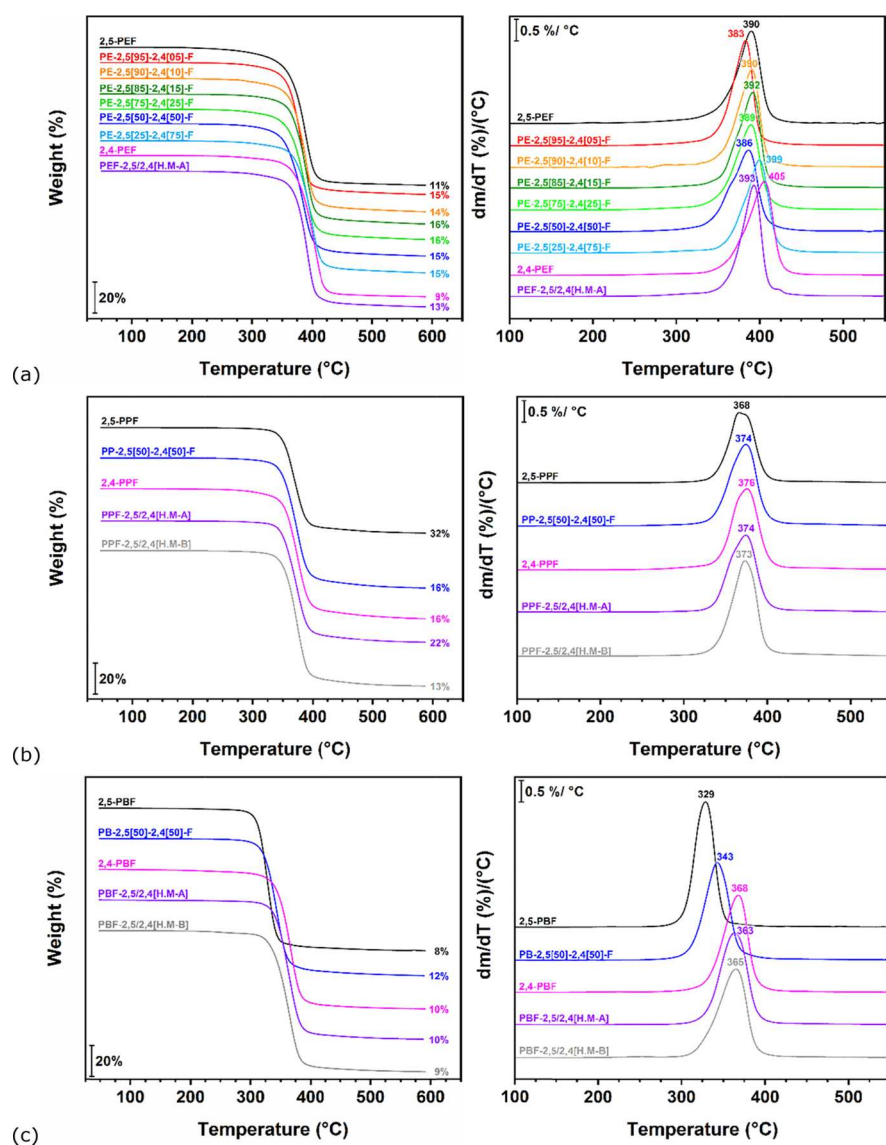
values of molecular weight obtained for the copolyesters are higher compared to the molecular weights of the corresponding homopolyesters (Table 1, entries 16 and 18). More interestingly, the use of Henkel mixtures provided higher molecular weights compared to the use of physical mixtures, in particular, in the PDO and BDO series, suggesting that there may be no need for the downstream processing (DSP) typically performed to separate the isomers prior to polymerization.

Figure 1 depicts the representative <sup>1</sup>H NMR spectra of the copolyesters obtained with a physical mixture of 2,5- and 2,4-isomers (50:50 mol %) with EG, PDO, and BDO (<sup>13</sup>C NMR spectra are given in the Supporting Information). The feed and incorporation ratios of the two FDCA isomers were found to be identical in all the synthesized copolyesters. The sum of the integrals corresponding to the two symmetrical protons (H1) in the 2,5-isomer is equal to the sum of the integrals corresponding to the two unsymmetrical protons (H2 and H3) in the 2,4-isomer, confirming that an equal incorporation ratio of the two FDCA isomers was achieved in the final polymers. The <sup>1</sup>H NMR spectrum of PE-2,5[50]-2,4[50]-F (Figure 1) shows one broad multiplet representing the -CH<sub>2</sub>- groups (H4 and H5) adjacent to the oxygen atom in the linear glycols. The multiplet pattern arises from the condensation of each linear glycol with the unsymmetrical carboxylic esters in the mixture of 2,5- and 2,4- isomers.

Consistently with previous observations, the formation of diethylene glycol (DEG) is observed in the samples belonging to the EG series. As the DEG content may significantly affect

the physical and thermal properties of the synthesized polymers (the higher the DEG content, the lower the glass transition temperature T<sub>g</sub>), the incorporation of DEG in all the PEF samples was also estimated (Table S1 in the Supporting Information). The DEG content ranges from 2 to 6%, which is reasonably compared to the values found in the literature.<sup>4</sup> In general, a DEG content of approximately 3 to 4% is observed in 2,5-PEF, whereas in the copolyesters, the DEG content is reduced to 1–3%.<sup>4,17</sup> For the moment, it is not possible to say whether the DEG content is the only parameter that can possibly affect the glass transition temperature and how this parameter would combine with other parameters such as the molecular weights. The <sup>1</sup>H NMR spectra of all the samples in the EG, PDO, and BDO series are given in the Supporting Information.

The thermal stability of the samples was preliminarily evaluated by conventional TGA measurements performed under gaseous N<sub>2</sub> with a heating rate of 10 °C min<sup>-1</sup> (curves reported in the Supporting Information; results are reported in Table 2). A preliminary TGA scan is necessary to make sure that the synthesized polymer is stable in the temperature range targeted for the subsequent DSC scans. Previous works showed that the thermal stability of polyesters obtained with different aliphatic diols depends on the length of the aliphatic segment. In particular, in a recent review, Papageorgiou et al.<sup>18</sup> reported relevant information about the thermal degradation of furanoate polyesters along with their decomposition mechanisms; however, they did not provide any information about the activation energy for thermal degradation. In this work, the



**Figure 2.** MT-TGA signals and derivative curves recorded for the homo- and copolyesters synthesized using 2,5/2,4-FDCA and (a) EG, (b) PDO, and (c) BDO, recorded from 30 to 600 °C with an overall heating rate of 2 °C min<sup>-1</sup>, an amplitude modulation of ±5 °C, and a period of 200 s under a constant flow of gaseous N<sub>2</sub>.

products of the synthesis were then dried, stored in a desiccator with P<sub>2</sub>O<sub>5</sub>, and further characterized by modulated-temperature TGA. MT-TGA allows us to obtain not only the mass loss as a function of temperature but also the kinetic parameters associated to the mass loss,<sup>19–21</sup> that is, the activation energy  $E_a$  as a function of the mass loss and therefore of temperature (Figures S41–S43 in the [Supporting Information](#)). More information about MT-TGA is provided in the [Supporting Information](#). Both TGA and MT-TGA showed that all the samples have similar degradation behaviors when the temperature is increased under gaseous nitrogen, whatever may be the ratio of the FDCA isomers or the length of the glycol unit. In particular, they are stable up to 250 °C (mass losses: <1 wt %), which allows quite broad processing windows; their thermal decomposition occurs between 300 and 450 °C, and the residual masses range between 9 and 16% for the samples in the EG series (PEFs), between 13 and 32% for the samples in the PDO series (PPFs), and between 8 and 12% for the samples in the BDO series (PBFs) ([Figure 2](#)). The decomposition mechanisms leading to the thermal degradation

of furanoate polyesters has been already extensively discussed by Papageorgiou et al.<sup>18</sup> and Terzopoulou et al.,<sup>22</sup> who characterized several furanic polyesters and their terephthalate equivalents by performing TGA measurements under a N<sub>2</sub> atmosphere and evidenced that, in all cases, the main decomposition mechanism is  $\beta$ -hydrogen scission. In particular, Terzopoulou et al.<sup>22</sup> investigated the decomposition mechanism of polyesters based on 2,5-furandicarboxylic acid and aliphatic diols with medium- and long-chain methylene groups and confirmed that all polyesters decompose in a similar way. Decomposition takes place mainly via  $\beta$ -hydrogen bond scission and less extensively by homolytic scission; the number of methylene groups of the parent diol monomer in the repeating unit seems to not affect the decomposition mechanism of the polyesters.

In [Table 2](#),  $T_{\max}$  is the temperature of degradation corresponding to the maximum of the derivative curves  $d(\text{weight})/d(\text{temperature})$  (%/°C) and  $T_{5\%}$  is the temperature corresponding to a weight loss of 5% as determined by either TGA (heating rate: 10 °C min<sup>-1</sup>) or MT-TGA (overall heating

**Table 3. Thermal Properties of Copolyesters from FDCA Isomers (2,5- and 2,4-FDCA) and Three Different Linear Glycols (EG, PDO, and BDO)**

entry	code	first heating				second heating			
		$T_g^a$ (°C)	$\Delta C_p^b$ (J g <sup>-1</sup> K <sup>-1</sup> )	$T_m^c$ (°C)	$\Delta H_m^d$ (J g <sup>-1</sup> )	$T_g^a$ (°C)	$\Delta C_p^b$ (J g <sup>-1</sup> K <sup>-1</sup> )	$T_m^c$ (°C)	$\Delta H_m^d$ (J g <sup>-1</sup> )
ethylene glycol (EG)									
1	2,5-PEF	81.4 ± 0.6	0.39 ± 0.08	215 ± 1	5 ± 2	82.4 ± 1.8	0.42 ± 0.06	215 ± 1	4 ± 2
2	PE-2,5[95]-2,4[05]-F	81.8 ± 0.6	0.44 ± 0.06	205 ± 1	0.3 ± 0.2	81.9 ± 0.6	0.46 ± 0.04	203 ± 1	0.2 ± 0.1
3	PE-2,5[90]-2,4[10]-F	83.7 ± 1.0	0.43 ± 0.12	n.o. <sup>e</sup>	n.o. <sup>e</sup>	83.3 ± 1.5	0.42 ± 0.08	n.o. <sup>e</sup>	n.o. <sup>e</sup>
4	PE-2,5[85]-2,4[15]-F	82.0 ± 1.4	0.36 ± 0.04	n.o. <sup>e</sup>	n.o. <sup>e</sup>	81.8 ± 2.0	0.40 ± 0.06	n.o. <sup>e</sup>	n.o. <sup>e</sup>
5	PE-2,5[75]-2,4[25]-F	81.3 ± 0.6	0.40 ± 0.04	n.o. <sup>e</sup>	n.o. <sup>e</sup>	81.8 ± 0.6	0.43 ± 0.04	n.o. <sup>e</sup>	n.o. <sup>e</sup>
6	PE-2,5[50]-2,4[50]-F	74.7 ± 0.6	0.36 ± 0.04	n.o. <sup>e</sup>	n.o. <sup>e</sup>	75.7 ± 0.6	0.39 ± 0.06	n.o. <sup>e</sup>	n.o. <sup>e</sup>
7	PE-2,5[25]-2,4[75]-F	73.4 ± 0.6	0.40 ± 0.04	n.o. <sup>e</sup>	n.o. <sup>e</sup>	74.0 ± 0.6	0.42 ± 0.04	n.o. <sup>e</sup>	n.o. <sup>e</sup>
8	2,4-PEF	72.9 ± 1.0	0.36 ± 0.08	n.o. <sup>e</sup>	n.o. <sup>e</sup>	72.6 ± 0.8	0.42 ± 0.06	n.o. <sup>e</sup>	n.o. <sup>e</sup>
9	PEF-2,5/2,4[H.M-A]	75.0 ± 0.6	0.39 ± 0.08	n.o. <sup>e</sup>	n.o. <sup>e</sup>	74.8 ± 0.6	0.44 ± 0.04	n.o. <sup>e</sup>	n.o. <sup>e</sup>
10	PEF-2,5/2,4[H.M-B]	78.0 ± 1.0	0.38 ± 0.08	n.o. <sup>e</sup>	n.o. <sup>e</sup>	76.0 ± 1.0	0.40 ± 0.08	n.o. <sup>e</sup>	n.o. <sup>e</sup>
1,3-propanediol (PDO)									
11	2,5-PPF	51.8 ± 0.6	0.40 ± 0.04	175 ± 1	11 ± 1	51.7 ± 0.6	0.41 ± 0.04	175 ± 1	8 ± 2
12	PP-2,5[50]-2,4[50]-F	47.8 ± 0.6	0.37 ± 0.04	n.o. <sup>e</sup>	n.o. <sup>e</sup>	50.4 ± 0.6	0.37 ± 0.04	n.o. <sup>e</sup>	n.o. <sup>e</sup>
13	2,4-PPF	40.2 ± 0.6	0.40 ± 0.04	n.o. <sup>e</sup>	n.o. <sup>e</sup>	40.7 ± 0.6	0.41 ± 0.04	n.o. <sup>e</sup>	n.o. <sup>e</sup>
14	PPF-2,5/2,4[H.M-A]	48.7 ± 0.6	0.40 ± 0.04	n.o. <sup>e</sup>	n.o. <sup>e</sup>	52.1 ± 0.6	0.39 ± 0.06	n.o. <sup>e</sup>	n.o. <sup>e</sup>
15	PPF-2,5/2,4[H.M-B]	50.0 ± 0.6	0.39 ± 0.04	n.o. <sup>e</sup>	n.o. <sup>e</sup>	53.0 ± 0.6	0.39 ± 0.04	n.o. <sup>e</sup>	n.o. <sup>e</sup>
1,4-butanediol (BDO)									
16	2,5-PBF	31.1 ± 0.6	0.37 ± 0.04	170 ± 1	41 ± 1	37.6 ± 0.6	0.30 ± 0.04	170 ± 1	42 ± 2
17	PB-2,5[50]-2,4[50]-F	33.7 ± 0.6	0.28 ± 0.04	n.o. <sup>e</sup>	n.o. <sup>e</sup>	35.4 ± 0.6	0.28 ± 0.04	n.o. <sup>e</sup>	n.o. <sup>e</sup>
18	2,4-PBF	29.4 ± 0.6	0.36 ± 0.08	n.o. <sup>e</sup>	n.o. <sup>e</sup>	33.3 ± 0.6	0.36 ± 0.04	n.o. <sup>e</sup>	n.o. <sup>e</sup>
19	PBF-2,5/2,4[H.M-A]	33.1 ± 0.6	0.36 ± 0.04	n.o. <sup>e</sup>	n.o. <sup>e</sup>	36.3 ± 0.6	0.36 ± 0.04	n.o. <sup>e</sup>	n.o. <sup>e</sup>
20	PBF-2,5/2,4[H.M-B]	30.8 ± 0.6	0.34 ± 0.04	153 ± 2	32 ± 1	33.5 ± 0.6	0.35 ± 0.04	152 ± 2	28 ± 3

<sup>a</sup>Midpoint glass transition temperature measured upon heating after melt-quenching (average of 5 samples). <sup>b</sup>Heat capacity step at the glass transition estimated on the basis of the normalized heat flow measured upon heating by DSC (average of 5 samples). <sup>c</sup>Melting temperature measured at the maximum of the melting endotherm. <sup>d</sup>Enthalpy of melting calculated by integrating the melting endotherm. <sup>e</sup>Not observed.

rate: 2 °C min<sup>-1</sup>). The dispersion of the experimental data and the uncertainties of measurement were evaluated by characterizing five samples per batch. In some cases, the incorporation of 2,4-FDCA into 2,5-FDCA-based polyesters increases the thermal stability, as shown by the values of  $T_{5\%}$  recorded by MT-TGA. In the EG series (entries 1–8), for instance,  $T_{5\%}$  is recorded at its minimum (315 °C) for 2,5-PEF and its maximum (350 °C) for 2,4-PEF, and the values found for the copolyesters are intermediate. Similar trends were observed for the copolymers in the PDO and BDO series (Table 2, entries 11–13 and 16–18, respectively) when a physical mixture of the two isomers was used; in some cases, the thermal stability obtained with the Henkel mixtures was even higher compared to the thermal stability of the corresponding homopolymers (Table 2, entries 14–15 and 19–20).

Figure 2 shows the MT-TGA curves (on the left) and their derivative curves (on the right) recorded for the samples in the EG, PDO, and BDO series. As previously mentioned, the samples were characterized by MT-TGA to obtain the temperature dependence of the activation energy (as shown by Figures S41–S43 in the Supporting Information). The  $E_a = f(\text{mass loss})$  curves are mostly flat (i.e., the degradation occurs in a single step) but present some fluctuations; the upper and lower bounds of such fluctuations were used to estimate the uncertainty on the values of  $E_a$  reported in Table 2. The average value of the activation energy obtained by MT-TGA for the thermal degradation under gaseous nitrogen is consistent with the values determined by the second step/ $n$ th-order model described by Tsanaktsis et al.<sup>23</sup> and intermediate between the values previously reported for PLA (110 kJ mol<sup>-1</sup><sup>24</sup> and 120 kJ mol<sup>-1</sup><sup>25</sup>) and PET (227 kJ mol<sup>-1</sup>

<sup>24</sup>). A trend can be evidenced when 2,5-PEF, 2,5-PPF, and 2,5-PBF are compared in terms of activation energy: the thermal stability decreases as the length of the aliphatic segment increases, that is, as the number of methylene groups in the diol used for the synthesis increases. This result is in total agreement with the decrease in  $T_{\text{max}}$  observed both by TGA (411 °C for 2,5-PEF, 405 °C for 2,5-PPF, and 367 °C for 2,5-PBF) and MT-TGA (390 ± 1 °C for 2,5-PEF, 368 ± 1 °C for 2,5-PPF, and 329 ± 1 °C for 2,5-PBF) (Table 3, entries 1, 11, and 16), and previously reported by Papageorgiou et al.<sup>18</sup> for FDCA-based polyesters (number of methylene groups = 2, 3, and 4). Similar to what happens in the polyesters obtained with terephthalic acid (polyethylene terephthalate (PET), polypropylene terephthalate (PPT), and polybutylene terephthalate (PBT)), in FDCA-based polyesters, the thermal stability depends on the ratio of aromatic/aliphatic segments in the repeating unit: the longer the aliphatic segment, the poorer the thermal stability. The incorporation of 2,4-FDCA has less impact on the activation energy for thermal degradation rather than the number of methylene groups in the monomer diol. This is particularly true for the samples in the EG and PDO series. However, the position isomerism on the furan ring seems to impact the degradation kinetics of the samples in the BDO series because the activation energy for 2,5-PBF was found to be significantly lower with respect to 2,4-PBF (Table 3, entries 16 and 18). Sometimes the copolyesters obtained with Henkel mixtures seem to be thermally more stable than the corresponding 2,5-FDCA-based homopolymers. Additional characterizations done with complementary techniques are probably necessary to elucidate whether

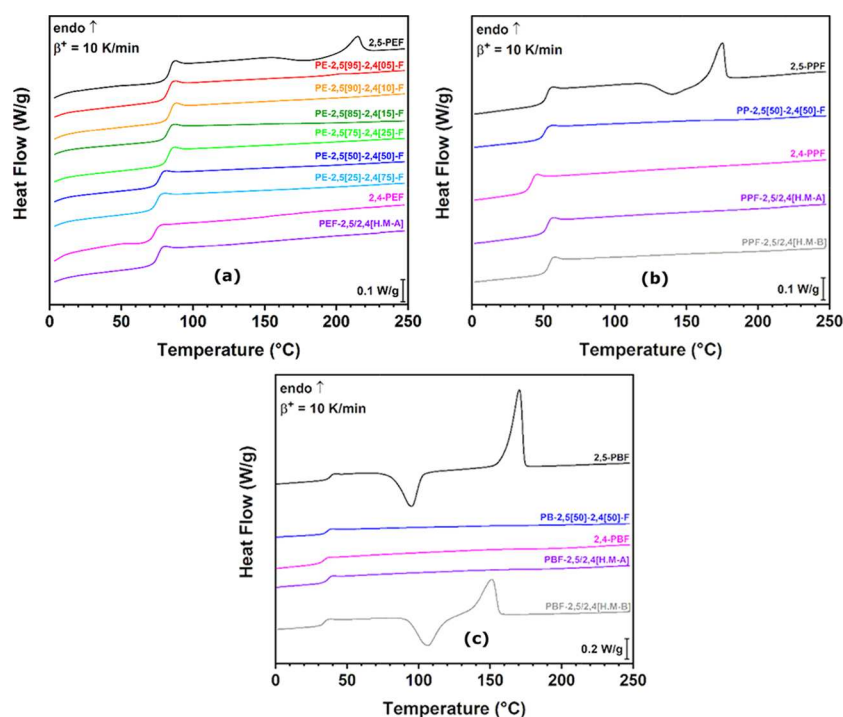


**Figure 3.** DSC curves recorded upon heating (second scans after melt-quenching) at  $10\text{ }^{\circ}\text{C min}^{-1}$  on the polyesters obtained from different proportions of 2,5- and 2,4-FDCA combined with (a) EG, (b) PDO, and (c) BDO.

positional isomerism could affect the mechanisms and kinetics of thermal degradation for these series of copolyesters.

DSC analyses were performed on the quenched samples of all the considered series of polyesters (Figure 3) to investigate any possible difference in their thermal behavior upon heating, including their aptitude to crystallize from the solid glassy state. The dispersion of the experimental data and the uncertainties of measurement were evaluated by characterizing five samples per batch. The parameters associated with the main thermal events observed during the heating ramps, that is, the midpoint glass transition temperature  $T_g$ , the heat capacity step at the glass transition temperature  $\Delta C_p$ , and the melting temperature  $T_m$ , are reported in Table 3.

Similar to the results obtained by TGA and MT-TGA, DSC also reveals a synergetic effect of the combination of the 2,4- and 2,5-isomers with respect to the glass transition temperature; however, this effect seems to be specific to the samples synthesized containing 5 to 15 mol % 2,4-FDCA, which is an intriguing result because they seem to have a  $T_g$  slightly higher than that of the homopolymer 2,5-PEF (Table 3, entries 1–4). The interpretation of this trend is tricky because the glass transition temperature of a polymer is affected by several parameters, which are not independent from each other and whose effects can eventually be compensated to different extents. Some of these parameters are strictly related to the chemical bonds as well as to their arrangement within the repeating unit, which are responsible for both the intra- and intermolecular interactions and therefore determine the flexibility of the polymer backbone, the local and overall dipole moment, the steric hindrance and the spacing between the polymer chains, the free volume available for molecular relaxations, etc.. Besides, the glass transition temperature also depends on the thermal treatment performed on the sample as well as on the cooling rate used to form the glass; therefore, it is important to consider both the first and second heating scans

prior to making any conclusions about the values of  $T_g$  for a series of samples. It is worth mentioning that, as previously said, one possible explanation could be found in the literature, which reports that the DEG content decreases when increasing the content of 2,5-FDCA that reacts with TA.<sup>17</sup> In this case, the effect on  $T_g$  could be enhanced by the incorporation of the 2,4-isomer because, in the copolymers, the DEG content is further reduced compared to the homopolymer 2,5-PEF. The  $T_g$  of the copolyesters containing 15 and 25 mol % the 2,4-isomer does not show any significant difference with respect to 2,5-PEF; however, the copolyesters containing higher contents of the 2,4-isomer (50 and 75 mol %) have a  $T_g$  that significantly drops, following a trend that is consistent with the  $T_g$  of the homopolymer 2,4-PEF (Table 3, entries 4–8).

Except for the sample with the lowest incorporation rate (5 mol % the 2,4-isomer) (Table 3, entry 2), all the copolyesters in the EG series seem to be unable to crystallize in the selected conditions. The DSC curves reported in Figure 3 show that cold crystallization and the corresponding melting peak can be clearly observed only for the homopolymer 2,5-PEF and no significant melting endotherm is observed for the copolyesters. Preliminary results obtained by wide-angle X-ray diffractometry (WAXD) performed at room temperature on some of the copolyesters in the EG series (results are given in the Supporting Information) also support the evidence that the incorporation of as little as 10 mol % the unsymmetrical 2,4-isomer is able to disrupt the crystallization of the 2,5-FDCA-based repeating units. Further investigations should be performed by DSC and WAXD after crystallization in different isothermal conditions to evaluate the crystallization kinetics, which would give a deeper insight into the aptitude to crystallize of these samples. As for the number of methylene groups in the diol used in the reaction with FDCA, it has a clear effect on the glass transition temperature. As expected, for a given isomer ratio (e.g., 50:50 mol %),  $T_g$  decreases as the

aliphatic glycolic subunits get longer (Table 3, entries 6, 12, and 17). This trend is also observed for the corresponding homopolymers (Table 3, entries 1, 11, and 16 for the 2,5-FDCA-based homopolyesters and entries 8, 13, and 18 for the 2,4-FDCA-based homopolyesters). In all cases (both homopolyesters and copolyesters), the biggest drop in  $T_g$  is observed when stepping from EG (a diol with two methylene groups) to PDO (a diol with three methylene groups); stepping to BDO, that is, using a diol with an extra methylene group, further decreases  $T_g$ , but the difference is much smaller. Besides, in the PDO series, the 50:50 physical mixture of the two FDCA isomers provided a copolyester with a  $T_g$  that is much higher compared to the average value expected on the basis of a simple mixing law, such as the Fox equation.<sup>26</sup> According to the values recorded during the second heating ramp, the average of the glass transition temperatures of the homopolyesters 2,5-PPF and 2,4-PPF should be 46.2 °C, whereas the  $T_g$  recorded for PP-2,5[50]-2,4[50]-F is 50.4 °C (Table 3, entries 11–13). The opposite is observed in the EG series where the 50:50 physical mixture of the two FDCA isomers provided copolyesters with a  $T_g$  that is much lower compared to the average value expected on the basis of Fox's mixing law (75.7 °C vs 77.5 °C) (Table 3, entries 1, 6, and 8). It would be interesting to better understand how the glass transition is modified by either selecting a specific ratio of the two FDCA isomers or by using a monomer diol with a given number of methylene groups.

As for the copolyesters obtained with the two Henkel mixtures in the DPO series, they have  $T_g$  values that are closer to 2,5-PPF rather than 2,4-PPF, suggesting that no significant effect is obtained on the glass transition temperature by the incorporation of the 2,4-isomer in the reactor (Table 3, entries 14 and 15). Eventually, their glass transition temperatures seem to be even slightly higher than 2,5-PPF, which is an intriguing result that needs to be confirmed by further studies. Whatever the reason for such behavior, the most important consequence is that, with respect to the glass transition, using purified 2,5-FDCA or a Henkel mixture for the synthesis provides polymers with similar behaviors. In the BDO series, the 50:50 physical mixture of the two FDCA isomers provides a copolyester with a  $T_g$  value that is approximately the average of the glass transition temperatures of the homopolyesters, at least according to the values recorded during the second heating ramp (Table 3, entries 16–18). As expected, all of the copolyesters in both the PDO and BDO series are fully amorphous, except the ones obtained with the Henkel mixture B in the BDO series for which a melting endotherm was observed at 152 °C (Figure 3c).

Considering the complex dependence of the glass transition temperature on the chemical composition and arrangement of the subunits for all these polyesters, the values of  $T_g$  reported in Table 3 were plotted as a function of the 2,5-FDCA DME content for all the polyesters in the EG, PDO, and BDO series and then fitted by different mixing laws (Figure 4). The first law used for fitting is the Fox equation,<sup>26</sup> which describes a weighted-average relationship between  $T_g$  and the mass fraction of each component:

$$\frac{1}{T_g} = \frac{x}{T_{g1}} + \frac{1-x}{T_{g2}} \quad (1)$$

where  $T_g$  is the glass transition temperature of the copolymer,  $T_{g1}$  and  $T_{g2}$  are the glass transition temperatures of each

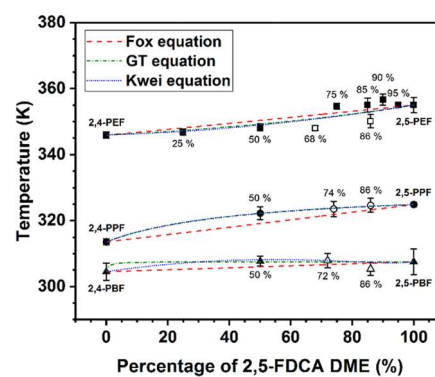


**Figure 4.** Values of the glass transition temperature  $T_g$  plotted against 2,5-FDCA DME content and fitted by Fox's, Gordon–Taylor's, and Kwei's equations. Solid symbols correspond to the copolyesters obtained with physical mixtures, whereas empty symbols correspond to the copolyesters obtained with Henkel mixtures.

homopolymer,  $x$  is the weight fraction of one of the isomers, and  $1-x$  is the weight fraction of the other isomer. Equation 1 is symmetric with respect to the weight fraction of each isomer and could help in predicting the properties of the copolyesters from the properties of the corresponding homopolyesters. Equation 2 proposed by Gordon and Taylor<sup>27</sup> was also used for fitting:

$$T_g = \frac{xT_{g1} + k_{GT}(1-x)T_{g2}}{x + k_{GT}(1-x)} \quad (2)$$

In this case,  $k_{GT}$  has to be evaluated from the experimental data and is incorporated into the simple weighted-average relation to better represent the eventual unequal contributions of each isomer to the final value of  $T_g$ . Finally, equation 3 proposed by Kwei<sup>28</sup> was used, which includes two additional parameters,  $k_{Kw}$  and  $q$ :

$$T_g = \frac{xT_{g1} + k_{Kw}(1-x)T_{g2}}{x + k_{Kw}(1-x)} + qx(1-x) \quad (3)$$

The  $q$  parameter is proportional to the number of specific intermolecular interactions eventually existing in the copolymer. This model is generally used to take into account dipole-driven intermolecular interactions, such as hydrogen bonding.<sup>28,29</sup>

The fitting results obtained with Fox's, Gordon–Taylor's, and Kwei's equations are shown in Figure 4, and the corresponding parameters are reported in Table 4. All the equations provide relatively good fitting results. Whatever may be the mixing law, the best fitting is obtained for the samples in

**Table 4.** Parameters Obtained by Fitting the Glass Transition Temperatures of Copolyesters from FDCA Isomers (2,5- and 2,4-FDCA) and Three Different Linear Glycols (EG, PDO, and BDO) with Fox's, Gordon–Taylor's, and Kwei's Equations

polymer	Fox		Gordon–Taylor		Kwei	
	$R^2$	$k_{GT}$	$R^2$	$k_{Kw}$	$q$	$R^2$
ethylene glycol (EG)	0.69	1.70	0.73	1.00	−5.98	0.73
1,3-propanediol (PDO)	0.84	0.31	1.00	0.32	0.12	1.00
1,4-butanediol (BDO)	0.22	0.01	0.48	9.31	13.33	0.57

the PDO series, whereas the worst fitting is obtained for the samples in the BDO series. Within each series of samples, the best fitting results are generally obtained with Kwei's equation, probably owing to the peculiar dielectric properties recently reported by Bourdet et al. for 2,5-PEF and 2,4-PEF.<sup>16</sup> In the EG and PDO series, the use of Gordon–Taylor's or Kwei's equation provides results that are equally good; however, the EG series has the highest value of  $k_{GT}$ , likely because the unequal contribution of each isomer is better evidenced in the series of copolymers having the highest ratio of furan rings to methylene groups. When it comes to Kwei's equation, the value of  $k_{Kw}$  is higher for the samples having an even number of methylene groups in the aliphatic glycolic subunit (EG and BDO series) and lower for the samples having an odd number of methylene groups (PDO series). Once again, this result is consistent with the even–odd effect experimentally evidenced on different properties by Soccio et al.<sup>30</sup> for a series of aliphatic poly(propylene dicarboxylate)s and subsequently confirmed by Papageorgiou et al.<sup>18</sup> for a series of bio-based 2,5-furan dicarboxylate polyesters with an increasing number of methylene groups in the monomer diol. The results obtained with Kwei's equation, compared to the values of  $T_g$  reported in Table 3, seem to suggest that the number of methylene groups in the selected diol and therefore the length of the aliphatic subunit in the repeating unit increase the flexibility of the backbone (as shown by the decrease in the glass transition temperature) but, at the same time, seem to favor the development of intermolecular dipole-driven interactions between the furan rings.

The recent work by Bourdet et al.<sup>16</sup> compared the homopolymers 2,5-PEF and 2,4-PEF in terms of molecular mobility and crystallization capability and showed how dramatic the influence of the position of the carboxylic groups with respect to the furan ring can be, not only on the average dipole moment but also on the ability to crystallize. At a heating rate of 10 °C/min, an amount of 2,4-FDCA DME units as little as 10 wt % is enough to make it impossible for the crystals to nucleate and grow upon heating from the glassy state. This proves that the incorporation of 2,4-FDCA-based repeating units is a highly efficient method for disrupting the crystallization of 2,5-FDCA-based units and represents a smart, sustainable, and relatively easy solution for controlling the crystallinity degree of PEFs whenever it significantly affects the targeted performances (transport properties, brittleness, and transparency). Based on the work by Bourdet et al.,<sup>16</sup> the use of the 2,4-isomer associated with the 2,5-isomer to obtain FDCA-based polyesters could proportionally affect the dipole moment of the macromolecules, whatever the glycolic unit may be. Interestingly, so far, no significant effects are observed on the heat capacity step at the glass transition temperature ( $\Delta C_p$ ) (values are reported in Table 3), which was found to be quite the same for all the considered polyesters. It would be interesting to evaluate the degree of influence of the intermolecular dipole-driven interactions (mostly related to positional isomerism on the furan ring) and the backbone's flexibility (strictly related to the number of methylene groups in the aliphatic glycolic subunit) on the molecular dynamics of these polyesters along with the subsequent physical properties (molecular relaxations, physical aging, etc.), the development of controlled microstructures, and the overall performance (mechanical properties, barrier properties, etc.).

## CONCLUSIONS

This work reports the successful synthesis of copolyesters by the melt polycondensation reaction using two isomers of furandicarboxylic acid (2,5- and 2,4-FDCA) with linear glycols having different lengths, which yielded polymers with reasonably high molecular weights, good thermal stability, and quite broad processing windows. The experimental results obtained on these samples show that the incorporation of 2,4-FDCA-based units into 2,5-PEF (and also into 2,5-PPF and 2,5-PBF) has a significant effect on the physical and thermal properties of the final products, in particular, on the glass transition temperature, on the aptitude to crystallize, and therefore on the melting behavior. For instance, an amount of 2,4-FDCA DME as little as 5–10 mol % was shown to be sufficient to completely disrupt the crystallization of the 2,5-FDCA-based repeating units when EG is used to obtain PEF. Interesting results are also obtained for the other furan-based polyesters considered in this study, which suggests that combining different proportions of the FDCA isomers with different types of diols is an interesting route to fine-tune polyesters with the desired properties for specific application areas. This work also shows that the mixture of FDCA isomers obtained from the Henkel disproportionation reaction can be directly used for the polymerization process and provides copolyesters that have similar properties compared to the ones derived from physical mixtures of different isomers, which proves the nonnecessity of time-consuming and expensive purification steps.

## EXPERIMENTAL SECTION

**Materials.** The dimethyl esters of 2,5- and 2,4-furandicarboxylate (FDCA) and their mixtures were obtained from the Henkel reaction. The experimental conditions, the catalyst used, the ratio of isomers obtained, and their separation/purification procedures are described in a previous publication.<sup>14</sup> All the other chemicals, that is, ethylene glycol (EG) (anhydrous, 99.8%, Sigma-Aldrich), 1,3-propanediol (PDO) ( $\geq 99.6\%$ , Sigma-Aldrich), 1,4-butanediol (BDO) ( $\geq 99\%$ , Sigma-Aldrich), titanium(IV) isopropoxide ( $\geq 97\%$ , Sigma-Aldrich), *o*-xylene (anhydrous, 97%, Sigma-Aldrich), trifluoroacetic acid (99%, Sigma-Aldrich), chloroform (Merck, p.a.), methanol (Merck, p.a.), chloroform-*d* (99.8 at. % D, Sigma-Aldrich), and trifluoroacetic acid-*d* (99%, Sigma-Aldrich), were used as received unless otherwise denoted.

**General Polycondensation Procedure for 2,5/2,4-FDCA-Me and Linear Diol Copolyesters.** Polycondensation reactions were conducted in 100 mL three-neck round-bottom flasks equipped with a mechanical overhead stirrer, an inlet for gaseous nitrogen, and a Liebig condenser. Dimethyl furandicarboxylate (1.5 g, 8.14 mmol) and diols (moles and ratios of each diol are given in Table 1) were charged into the reaction flask. The setup was placed under vacuum and purged with gaseous nitrogen, and this cycle was repeated three times. The polycondensation method involves two stages. During the first stage, the reaction was carried out under gaseous nitrogen to form oligomers. The reaction mixture was heated in a DrySyn at 125 °C for 15 min with constant stirring. After observing the complete melt of the mixture, the catalyst Ti(OiPr)<sub>4</sub> (0.10 mmol) in 2.5 mL of *o*-xylene was added into the flask under a continuous flow of nitrogen. The temperature was then increased to 160 °C, and the mixture was stirred for 12 h. Then, the temperature was finally increased to 215–220 °C for 1.5–2 h to complete the first stage of prepolymerization; after which, methanol and *o*-xylene were collected in the cooling flask. In the second stage of the polycondensation, vacuum was gradually applied (reaching 0.02 mbar) at 215–220 °C for 3 h to obtain high-molecular weight polyesters. After completion of the reaction, the mixture was cooled down to room temperature under a nitrogen atmosphere. The polymer was purified by dissolving it in 10 mL of a

chloroform/TFA mixture (6:1) and precipitated in 100 mL of methanol, filtered, and dried in vacuum at 40 °C for 12 h to yield a white powder.

**Methods for Characterization.** Fourier transform infrared (FTIR) spectra were obtained on a Varian Scimitar 1000 FTIR spectrometer equipped with a Pike MIRacle ATR Diamond/ZnSe single reflection plate and a DTSG detector. The measurement resolution was set at 4 cm<sup>-1</sup>, and the spectra were collected in the range of 4000–650 cm<sup>-1</sup> with 32 co-added scans. Nuclear magnetic resonance (NMR) spectra were recorded on a Bruker Advance III spectrometer operating at 400.17 MHz (<sup>1</sup>H) and 100.62 MHz (<sup>13</sup>C). The absolute molecular weight of the polyesters was determined by gel permeation chromatography (GPC) on a Viscotek HP-SEC system, VE-2001 GPC max (pump and auto sampler) equipped with TDA305 triple detector array (right-angle light scattering (RALS), low-angle light scattering (LALS), and refractive index (RI) detector and viscometer), a 2× GPC column (PSS, PFG, analytical, linear M), and a guard column, molecular range of 250–2.5 × 10<sup>6</sup> D (PMMA in HFIP). Data were calculated with OmniSECTM software (version 4.6). Hexafluoroisopropanol (HFIP) containing 0.02 M potassium trifluoroacetate was used as the eluent with a flow rate of 0.7 mL min<sup>-1</sup>. Control measurements were performed with EasiVial PMMA standards from Agilent. The thermal stability of the polyesters was determined by modulated-temperature thermogravimetric analysis (MT-TGA) by heating the samples from room temperature to 600 °C at 2 °C/min with a continuous amplitude modulation of ±5 °C and a period of 200 s under a continuous flow of gaseous nitrogen (25 mL/min). Prior to characterization, all the freshly prepared samples were dried for 3 days at *T<sub>g</sub>* + 15 °C (i.e., 95 °C for the samples in the EG series, 65 °C for the samples in the PDO series, and 55 °C for the samples in the BDO series) and stored in a desiccator over P<sub>2</sub>O<sub>5</sub> until measurement. Differential scanning calorimetry (DSC) curves were recorded on a power-compensation PerkinElmer Diamond DSC during temperature ramps from -60 to 230 °C at a heating and cooling rate of 10 °C min<sup>-1</sup>. A heat-flow Q2000 DSC (TA Instruments) equipped with a RCS90 intracooler was also used to characterize samples encapsulated in standard aluminum pans, previously melted at 240 °C in 2 min on the hot stage of a hydraulic manual press (SPECAC 25 T), and finally quenched on a cold metal plate. Standard sapphires were used for energy calibration, and standard indium (*T<sub>m</sub>* = 156.6 °C, Δ*H<sub>m</sub>* = 28.66 J/g) was used for heat flow and temperature calibrations. The DSC cell was purged with a continuous flow of gaseous nitrogen (50 mL/min). The samples in their fully amorphous state were analyzed with the following program: equilibrate at 0 °C for temperature stabilization followed by a heating ramp from 0 to 250 °C at 10 K min<sup>-1</sup> to reach the molten state and an isothermal step during 1 min at 250 °C for temperature homogenization in the melt then a cooling ramp at the highest achievable rate (ballistic quenching) down to 0 °C and an isothermal step during 2 min at 0 °C for temperature stabilization and finally a heating ramp until 250 °C at 10 K min<sup>-1</sup> for measurement.

**Poly(ethylene-2,5-furandicarboxylate) (2,5-PEF).** FTIR (neat): *v* = 3126, 2966, 1722, 1582, 1269, 1021, 969, 829, 763 cm<sup>-1</sup>; <sup>1</sup>H NMR (400 MHz, CDCl<sub>3</sub> + CF<sub>3</sub>COOD): δ = 7.3 (s, 2H), 4.7 (s, 4H) ppm; <sup>13</sup>C NMR (100 MHz, CDCl<sub>3</sub> + CF<sub>3</sub>COOD): δ = 159.5, 146.1, 121.1, 63.7 ppm.

**Polyethylene(2,5-[95]-2,4-[05]-furandicarboxylate) (PE-2,5[95]-2,4[05]-F).** FTIR (neat): *v* = 3128, 2965, 1717, 1581, 1265, 1221, 1130, 1019 cm<sup>-1</sup>; <sup>1</sup>H NMR (400 MHz, CDCl<sub>3</sub> + CF<sub>3</sub>COOD): δ = 8.21 (s, 1H), 7.57 (s, 1H), 7.28 (s, 2H), 4.70 (s, 8H) ppm; <sup>13</sup>C NMR (100 MHz, CDCl<sub>3</sub> + CF<sub>3</sub>COOD): δ = 158.8, 146.7, 119.8, 63.4.

**Polyethylene(2,5-[90]-2,4-[10]-furandicarboxylate) (PE-2,5[90]-2,4[10]-F).** FTIR (neat): *v* = 3125, 2963, 1718, 1582, 1265, 1222, 1132, 1020 cm<sup>-1</sup>; <sup>1</sup>H NMR (400 MHz, CDCl<sub>3</sub> + CF<sub>3</sub>COOD): δ = 8.28–8.20 (m, 1H), 7.63–7.57 (m, 1H), 7.32 (d, *J* = 7.3 Hz, 2H), 4.73 (d, *J* = 7.2 Hz, 8H) ppm; <sup>13</sup>C NMR (100 MHz, CDCl<sub>3</sub> + CF<sub>3</sub>COOD): δ = 159.3, 146.1, 120.0, 63.6.

**Polyethylene(2,5-[85]-2,4-[15]-furandicarboxylate) (PE-2,5[85]-2,4[15]-F).** FTIR (neat): *v* = 3124, 1719, 1582, 1265, 1222, 1132, 1020 cm<sup>-1</sup>; <sup>1</sup>H NMR (400 MHz, CDCl<sub>3</sub> + CF<sub>3</sub>COOD): δ = 8.21 (s,

1H), 7.56 (s, 1H), 7.28 (s, 2H), 4.79–4.59 (m, 8H) ppm; <sup>13</sup>C NMR (100 MHz, CDCl<sub>3</sub> + CF<sub>3</sub>COOD): δ = 158.8, 146.1, 119.8, 63.4.

**Polyethylene(2,5-[75]-2,4-[25]-furandicarboxylate) (PE-2,5[75]-2,4[25]-F).** FTIR (neat): *v* = 313, 2962, 1713, 1582, 1260, 1220, 1124, 1018 cm<sup>-1</sup>; <sup>1</sup>H NMR (400 MHz, CDCl<sub>3</sub> + CF<sub>3</sub>COOD): δ = 8.21 (s, 1H), 7.56 (s, 1H), 7.29 (s, 2H), 4.69 (s, 8H) ppm; <sup>13</sup>C NMR (100 MHz, CDCl<sub>3</sub> + CF<sub>3</sub>COOD): δ = 162.9, 159.0, 158.8, 151.9, 146.1, 120.2, 119.8, 118.3, 63.5, 63.4.

**Polyethylene(2,5-[50]-2,4-[50]-furandicarboxylate) (PE-2,5[50]-2,4[50]-F).** FTIR (neat): *v* = 3142, 2963, 1718, 1585, 1261, 1224, 1132, 1080 cm<sup>-1</sup>; <sup>1</sup>H NMR (400 MHz, CDCl<sub>3</sub> + CF<sub>3</sub>COOD): δ = 8.13 (s, 1H), 7.48 (s, 1H), 7.23 (s, 2H), 4.72–4.51 (m, 8H) ppm; <sup>13</sup>C NMR (100 MHz, CDCl<sub>3</sub> + CF<sub>3</sub>COOD): δ = 161.3, 157.5, 157.4, 150.6, 150.6, 146.4, 145.0, 120.5, 118.9, 117.5, 62.8, 62.7, 62.4.

**Polyethylene(2,5-[25]-2,4-[75]-furandicarboxylate) (PE-2,5[25]-2,4[75]-F).** FTIR (neat): *v* = 3145, 1720, 1589, 1259, 1195, 1134, 1079 cm<sup>-1</sup>; <sup>1</sup>H NMR (400 MHz, CDCl<sub>3</sub> + CF<sub>3</sub>COOD): δ = 8.22 (d, *J* = 2.6 Hz, 1H), 7.58 (t, *J* = 1.1 Hz, 1H), 7.30 (d, *J* = 1.3 Hz, 2H), 4.77–4.59 (m, 8H) ppm; <sup>13</sup>C NMR (100 MHz, CDCl<sub>3</sub> + CF<sub>3</sub>COOD): δ = 161.7, 157.8, 157.6, 150.7, 150.6, 144.8, 144.7, 143.2, 118.8, 118.5, 117.0, 62.2, 62.1, 61.8.

**Poly(ethylene-2,4-furandicarboxylate) (2,4-PEF).** FTIR (neat): *v* = 3142, 2960, 1726, 1591, 1264, 1080, 978, 868, 760 cm<sup>-1</sup>; <sup>1</sup>H NMR (400 MHz, CDCl<sub>3</sub> + CF<sub>3</sub>COOD): δ = 8.2 (s, 1H), 7.6 (s, 1H), 4.7 (d, 4H) ppm; <sup>13</sup>C NMR (100 MHz, CDCl<sub>3</sub> + CF<sub>3</sub>COOD): δ = 163.8, 160.0, 152.7, 144.8, 120.4, 118.8, 63.9, 63.6 ppm.

**Polyethylenefurandicarboxylate [Henkel Mixture A] (PEF-2,5/2,4[H.M-A]).** FTIR (neat): *v* = 3131, 2963, 1717, 1583, 1263, 1222, 1130, 1020 cm<sup>-1</sup>; <sup>1</sup>H NMR (400 MHz, CDCl<sub>3</sub> + CF<sub>3</sub>COOD): δ = 8.20 (s, 1H), 7.55 (s, 1H), 7.28 (s, 2H), 4.69 (s, 8H) ppm; <sup>13</sup>C NMR (100 MHz, CDCl<sub>3</sub> + CF<sub>3</sub>COOD): δ = 160.1, 159.7, 159.3, 158.8, 158.7, 146.2, 119.7, 115.7, 112.9, 63.4, 63.4.

**Polyethylenefurandicarboxylate [Henkel Mixture B] (PEF-2,5/2,4[H.M-B]).** FTIR (neat): *v* = 3129, 2964, 1720, 1582, 1265, 1222, 1132, 1020 cm<sup>-1</sup>; <sup>1</sup>H NMR (400 MHz, CDCl<sub>3</sub> + CF<sub>3</sub>COOD): δ = 8.21 (s, 1H), 7.56 (s, 1H), 7.29 (s, 13H), 4.70 (s, 27H) ppm; <sup>13</sup>C NMR (100 MHz, CDCl<sub>3</sub> + CF<sub>3</sub>COOD): δ = 160.5, 160.0, 159.6, 159.2, 158.8, 146.2, 119.8, 115.7, 112.9, 63.4, 47.1.

**Poly(propylene-2,5-furandicarboxylate) (2,5-PPF).** FTIR (neat): *v* = 3121, 2950, 1723, 1581, 1272, 1035, 967, 828, 765 cm<sup>-1</sup>; <sup>1</sup>H NMR (400 MHz, CDCl<sub>3</sub> + CF<sub>3</sub>COOD): δ = 7.5 (s, 2H), 4.7 (t, 4H), 2.4 (q, 2H) ppm; <sup>13</sup>C NMR (100 MHz, CDCl<sub>3</sub> + CF<sub>3</sub>COOD): δ = 154.6, 141.0, 114.6, 57.8, 22.0 ppm.

**Polypropylene(2,5-[50]-2,4-[50]-furandicarboxylate) (PP-2,5[50]-2,4[50]-F).** FTIR (neat): *v* = 3136, 2964, 1710, 1583, 1258, 1222, 1125, 1074, 1018 cm<sup>-1</sup>; <sup>1</sup>H NMR (400 MHz, CDCl<sub>3</sub> + CF<sub>3</sub>COOD): δ = 8.23 (s, 1H), 7.58 (s, 1H), 7.31 (s, 2H), 4.87–4.29 (m, 8H), 2.28 (h, *J* = 6.5 Hz, 4H) ppm; <sup>13</sup>C NMR (100 MHz, CDCl<sub>3</sub> + CF<sub>3</sub>COOD): δ = 163.8, 159.8, 159.7, 151.9, 146.2, 144.7, 120.3, 119.7, 118.1, 63.0, 62.4, 27.4.

**Poly(propylene-2,4-furandicarboxylate) (2,4-PPF).** FTIR (neat): *v* = 3143, 2958, 1718, 1590, 1260, 1076, 978, 827, 760 cm<sup>-1</sup>; <sup>1</sup>H NMR (400 MHz, CDCl<sub>3</sub> + CF<sub>3</sub>COOD): δ = 8.2 (s, 1H), 7.5 (s, 1H), 4.5 (m, 4H), 2.2 (m, 2H) ppm; <sup>13</sup>C NMR (100 MHz, CDCl<sub>3</sub> + CF<sub>3</sub>COOD): δ = 163.7, 159.8, 151.9, 144.7, 120.4, 118.4, 62.9, 62.4, 27.4 ppm.

**Polypropylenefurandicarboxylate [Henkel Mixture A] (PPF-2,5/2,4[H.M-A]).** FTIR (neat): *v* = 3128, 2964, 1710, 1582, 1263, 1220, 1124, 1078, 1018 cm<sup>-1</sup>; <sup>1</sup>H NMR (400 MHz, CDCl<sub>3</sub> + CF<sub>3</sub>COOD): δ = 8.22 (d, *J* = 2.4 Hz, 1H), 7.56 (d, *J* = 2.5 Hz, 1H), 7.28 (d, *J* = 15.3 Hz, 2H), 4.88–4.27 (m, 8H), 2.28 (h, *J* = 6.5 Hz, 4H) ppm; <sup>13</sup>C NMR (100 MHz, CDCl<sub>3</sub> + CF<sub>3</sub>COOD): δ = 162.0, 158.0, 144.7, 118.8, 118.1, 116.5, 61.3, 60.8, 25.8.

**Polypropylenefurandicarboxylate [Henkel Mixture B] (PPF-2,5/2,4[H.M-B]).** FTIR (neat): *v* = 3125, 2968, 1715, 1582, 1268, 1222, 1133, 1080, 1021 cm<sup>-1</sup>; <sup>1</sup>H NMR (400 MHz, CDCl<sub>3</sub> + CF<sub>3</sub>COOD): δ = 8.20 (d, *J* = 3.2 Hz, 1H), 7.54 (d, *J* = 3.2 Hz, 1H), 7.28 (s, 2H), 4.54 (t, *J* = 6.1 Hz, 8H), 2.27 (h, *J* = 7.3, 6.6 Hz, 4H) ppm; <sup>13</sup>C NMR (100 MHz, CDCl<sub>3</sub> + CF<sub>3</sub>COOD): δ = 160.3, 159.9, 159.5, 159.2, 146.3, 119.5, 115.7, 112.9, 62.8, 47.1, 27.5.



*Poly(butylene-2,5-furandicarboxylate) (2,5-PBF)*. FTIR (neat):  $\nu = 3120, 2965, 1730, 1579, 1274, 1023, 968, 824, 768 \text{ cm}^{-1}$ ;  $^1\text{H}$  NMR (400 MHz,  $\text{CDCl}_3 + \text{CF}_3\text{COOD}$ ):  $\delta = 7.3$  (s, 2H), 4.4 (m, 4H), 1.9 (m, 4H) ppm;  $^{13}\text{C}$  NMR (100 MHz,  $\text{CDCl}_3 + \text{CF}_3\text{COOD}$ ):  $\delta = 159.1, 145.3, 118.6, 65.3, 23.6$  ppm.

*Polybutylene(2,5-[50]-2,4-[50]-furandicarboxylate) (PB-2,5[50]-2,4[50]-F)*. FTIR (neat):  $\nu = 3143, 2958, 1711, 1583, 1262, 1128, 1075, 1019 \text{ cm}^{-1}$ ;  $^1\text{H}$  NMR (400 MHz,  $\text{CDCl}_3 + \text{CF}_3\text{COOD}$ ):  $\delta = 8.09$  (s, 1H), 7.45 (s, 1H), 7.18 (s, 2H), 4.66–3.95 (m, 8H), 1.81 (tt,  $J = 6.8, 3.6 \text{ Hz}$ , 8H) ppm;  $^{13}\text{C}$  NMR (100 MHz,  $\text{CDCl}_3 + \text{CF}_3\text{COOD}$ ):  $\delta = 162.0, 158.4, 158.1, 149.78, 144.3, 142.8, 118.4, 117.6, 115.9, 64.1, 63.7, 22.7$ .

*Poly(butylene-2,4-furandicarboxylate) (2,4-PBF)*. FTIR (neat):  $\nu = 3139, 2964, 1720, 1588, 1262, 1078, 979, 864, 761 \text{ cm}^{-1}$ ;  $^1\text{H}$  NMR (400 MHz,  $\text{CDCl}_3 + \text{CF}_3\text{COOD}$ ):  $\delta = 8.2$  (s, 1H), 7.5 (s, 1H), 4.4 (d, 4H), 1.9 (s, 4H) ppm;  $^{13}\text{C}$  NMR (100 MHz,  $\text{CDCl}_3 + \text{CF}_3\text{COOD}$ ):  $\delta = 163.8, 162.4, 150.1, 143.1, 118.7, 116.3, 64.4, 64.0, 23.0$  ppm.

*Polybutylenefurandicarboxylate [Henkel Mixture A] (PBF-2,5/2,4[H.M-A])*. FTIR (neat):  $\nu = 3118, 2964, 1721, 1581, 1272, 1225, 1142, 1079, 1031 \text{ cm}^{-1}$ ;  $^1\text{H}$  NMR (400 MHz,  $\text{CDCl}_3 + \text{CF}_3\text{COOD}$ ):  $\delta = 8.31$ – $8.18$  (m, 1H), 7.66–7.51 (m, 1H), 7.40–7.27 (m, 2H), 4.91–4.04 (m, 8H), 2.51–1.58 (m, 8H) ppm;  $^{13}\text{C}$  NMR (100 MHz,  $\text{CDCl}_3 + \text{CF}_3\text{COOD}$ ):  $\delta = 160.2, 151.9, 146.3, 119.7, 66.4, 24.6$ .

*Polybutylenefurandicarboxylate [Henkel Mixture B] (PBF-2,5/2,4[H.M-B])*. FTIR (neat):  $\nu = 3119, 2963, 1715, 1270, 1224, 1134, 1078, 1022 \text{ cm}^{-1}$ ;  $^1\text{H}$  NMR (400 MHz,  $\text{CDCl}_3 + \text{CF}_3\text{COOD}$ ):  $\delta = 8.11$  (s, 1H), 7.45 (s, 1H), 7.19 (s, 2H), 4.35 (d,  $J = 5.4 \text{ Hz}$ , 8H), 2.22–1.43 (m, 8H) ppm;  $^{13}\text{C}$  NMR (100 MHz,  $\text{CDCl}_3 + \text{CF}_3\text{COOD}$ ):  $\delta = 160.4, 159.9, 159.5, 159.5, 159.1, 146.4, 119.4, 115.7, 112.9, 65.9, 47.1, 24.9$ .

## ■ ASSOCIATED CONTENT

### Supporting Information

The Supporting Information is available free of charge on the ACS Publications website at DOI: 10.1021/acssuschemeng.9b04463.

The ( $^1\text{H}$  and  $^{13}\text{C}$ ) NMR spectra, activation energies for thermal degradation, TGA traces, WAXD diffractograms of all the copolyesters, more details on the modulated-temperature thermogravimetric analysis, and metrics assessment for the Henkel reaction (PDF)

## ■ AUTHOR INFORMATION

### Corresponding Authors

\*Email: shanmugam.thiyagarajan@wur.nl (S.T).

\*Email: antonella.esposito@univ-rouen.fr (A.E).

### ORCID

Shanmugam Thiyagarajan: 0000-0002-7905-4233

Antonella Esposito: 0000-0003-0507-1417

### Notes

The authors declare no competing financial interest.

## ■ ACKNOWLEDGMENTS

W. Teunissen and H. de Beukelaer, BSc. are acknowledged for GC–MS, STA, and DSC analysis (PerkinElmer). This work is part of the research program #737 EXPLOROMA of the Dutch Polymer Institute (DPI). The Région Normandie and the European FEDER are acknowledged for their financial support through the SCAMPI project (A.B.'s Ph.D. program). The authors also acknowledge the Erasmus+ program for supporting A.B.'s six-month internship in Wageningen.

## ■ REFERENCES

- (1) Bozell, J. J.; Petersen, G. R. Technology development for the production of biobased products from biorefinery carbohydrates—the US Department of Energy's "Top 10" revisited. *Green Chem.* **2010**, *12*, 539–554.
- (2) Gandini, A. Furan Monomers and their Polymers: Synthesis, Properties and Applications. In *Biopolymers – New Materials for Sustainable Films and Coatings*; John Wiley & Sons, Ltd: 2011; pp 179–209, DOI: 10.1002/9781119994312.ch9.
- (3) Gandini, A. The irruption of polymers from renewable resources on the scene of macromolecular science and technology. *Green Chem.* **2011**, *13*, 1061–1083.
- (4) Thiyagarajan, S.; Vogelzang, W.; J. I. Knoop, R.; Frissen, A. E.; van Haveren, J.; van Es, D. S. Biobased furandicarboxylic acids (FDCAs): effects of isomeric substitution on polyester synthesis and properties. *Green Chem.* **2014**, *16*, 1957–1966.
- (5) Knoop, R. J. I.; Vogelzang, W.; van Haveren, J.; van Es, D. S. High molecular weight poly(ethylene-2,5-furanoate); critical aspects in synthesis and mechanical property determination. *J. Polym. Sci., Part A: Polym. Chem.* **2013**, *51*, 4191–4199.
- (6) Jong, E. d.; Dam, M. A.; Sips, L.; Gruter, G. J. M. Furandicarboxylic Acid (FDCA), A Versatile Building Block for a Very Interesting Class of Polyesters. In *Biobased Monomers, Polymers, and Materials*; American Chemical Society: 2012; Vol. 1105, pp 1–13, DOI: 10.1021/bk-2012-1105.ch001.
- (7) Burgess, S. K.; Mikkilineni, D. S.; Yu, D. B.; Kim, D. J.; Mubarak, C. R.; Kriegel, R. M.; Koros, W. J. Water sorption in poly(ethylene furanoate) compared to poly(ethylene terephthalate). Part 1: Equilibrium sorption. *Polymer* **2014**, *55*, 6861–6869.
- (8) Burgess, S. K.; Kriegel, R. M.; Koros, W. J. Carbon Dioxide Sorption and Transport in Amorphous Poly(ethylene furanoate). *Macromolecules* **2015**, *48*, 2184–2193.
- (9) Burgess, S. K.; Wenz, G. B.; Kriegel, R. M.; Koros, W. J. Penetrant transport in semicrystalline poly(ethylene furanoate). *Polymer* **2016**, *98*, 305–310.
- (10) Wilsens, C. H. R. M.; Deshmukh, Y. S.; Noorder, B. A. J.; Rastogi, S. Influence of the 2,5-Furandicarboxamide Moiety on Hydrogen Bonding in Aliphatic–Aromatic Poly(ester amide)s. *Macromolecules* **2014**, *47*, 6196–6206.
- (11) Wilsens, C. H. R. M.; Noorder, B. A. J.; Rastogi, S. Aromatic thermotropic polyesters based on 2,5-furandicarboxylic acid and vanillic acid. *Polymer* **2014**, *55*, 2432–2439.
- (12) Wilsens, C. H. R. M.; Verhoeven, J. M. G. A.; Noorder, B. A. J.; Hansen, M. R.; Auhl, D.; Rastogi, S. Thermotropic Polyesters from 2,5-Furandicarboxylic Acid and Vanillic Acid: Synthesis, Thermal Properties, Melt Behavior, and Mechanical Performance. *Macromolecules* **2014**, *47*, 3306–3316.
- (13) Wilsens, C. H. R. M.; Wullems, N. J. M.; Gubbels, E.; Yao, Y.; Rastogi, S.; Noorder, B. A. J. Synthesis, kinetics, and characterization of bio-based thermosets obtained through polymerization of a 2,5-furandicarboxylic acid-based bis(2-oxazoline) with sebacic acid. *Polym. Chem.* **2015**, *6*, 2707–2716.
- (14) Thiyagarajan, S.; Pukin, A.; van Haveren, J.; Lutz, M.; van Es, D. S. Concurrent formation of furan-2,5- and furan-2,4-dicarboxylic acid: unexpected aspects of the Henkel reaction. *RSC Adv.* **2013**, *3*, 15678–15686.
- (15) Zaidi, S.; Thiyagarajan, S.; Bougarech, A.; Sebti, F.; Abid, S.; Majdi, A.; Silvestre, A. J. D.; Sousa, A. F. Highly transparent films of new copolyesters derived from terephthalic and 2,4-furandicarboxylic acids. *Polym. Chem.* **2019**, *10*, 5324–5332.
- (16) Bourdet, A.; Esposito, A.; Thiyagarajan, S.; Delbreilh, L.; Affouard, F.; Knoop, R. J. I.; Dargent, E. Molecular Mobility in Amorphous Biobased Poly(ethylene 2,5-furandicarboxylate) and Poly(ethylene 2,4-furandicarboxylate). *Macromolecules* **2018**, *51*, 1937–1945.
- (17) Sousa, A. F.; Matos, M.; Freire, C. S. R.; Silvestre, A. J. D.; Coelho, J. F. J. New copolyesters derived from terephthalic and 2,5-furandicarboxylic acids: A step forward in the development of biobased polyesters. *Polymer* **2013**, *54*, 513–519.

(18) Papageorgiou, G. Z.; Papageorgiou, D. G.; Terzopoulou, Z.; Bikiaris, D. N. Production of bio-based 2,5-furan dicarboxylate polyesters: Recent progress and critical aspects in their synthesis and thermal properties. *Eur. Polym. J.* **2016**, *83*, 202–229.

(19) Blaine, R. L.; Hahn, B. K. Obtaining Kinetic Parameters by Modulated Thermogravimetry. *J. Therm. Anal. Calorim.* **1998**, *54*, 695–704.

(20) Flynn, J. H. THE HISTORICAL DEVELOPMENT OF APPLIED NONISOTHERMAL KINETICS. In *Thermal Analysis*; Schwenker, R. F.; Garn, P. D., Eds. Academic Press: 1969; pp 1111–1126, DOI: 10.1016/b978-0-12-395734-4.50035-7.

(21) Blaine, R. A faster approach to obtaining kinetic parameters. *Am. Lab.* **1998**, *30*, 21–22.

(22) Terzopoulou, Z.; Tsanaktsis, V.; Nerantzaki, M.; Papageorgiou, G. Z.; Bikiaris, D. N. Decomposition mechanism of polyesters based on 2,5-furandicarboxylic acid and aliphatic diols with medium and long chain methylene groups. *Polym. Degrad. Stab.* **2016**, *132*, 127–136.

(23) Tsanaktsis, V.; Vouvoudi, E.; Papageorgiou, G. Z.; Papageorgiou, D. G.; Chrissafis, K.; Bikiaris, D. N. Thermal degradation kinetics and decomposition mechanism of polyesters based on 2,5-furandicarboxylic acid and low molecular weight aliphatic diols. *J. Anal. Appl. Pyrolysis* **2015**, *112*, 369–378.

(24) Giriya, B. G.; Sailaja, R. R. N.; Madras, G. Thermal degradation and mechanical properties of PET blends. *Polym. Degrad. Stab.* **2005**, *90*, 147–153.

(25) Wachsen, O.; Platkowski, K.; Reichert, K. H. Thermal degradation of poly-l-lactide—studies on kinetics, modelling and melt stabilisation. *Polym. Degrad. Stab.* **1997**, *57*, 87–94.

(26) Fox, T. G. Influence of Diluent and of Copolymer Composition on the Glass Temperature of a Poly-mer System. *Bull. Am. Phys. Soc.* **1956**, *1*, 123.

(27) Gordon, M.; Taylor, J. S. Ideal copolymers and the second-order transitions of synthetic rubbers. i. non-crystalline copolymers. *J. Appl. Chem.* **1952**, *2*, 493–500.

(28) Kwei, T. K. The effect of hydrogen bonding on the glass transition temperatures of polymer mixtures. *J. Polym. Sci., Polym. Lett. Ed.* **1984**, *22*, 307–313.

(29) Kuo, S. W.; Huang, C. F.; Chang, F. C. Study of hydrogen-bonding strength in poly( $\epsilon$ -caprolactone) blends by DSC and FTIR. *J. Polym. Sci., Part B: Polym. Phys.* **2001**, *39*, 1348–1359.

(30) Soccio, M.; Lotti, N.; Finelli, L.; Gazzano, M.; Munari, A. Aliphatic poly(propylene dicarboxylate)s: Effect of chain length on thermal properties and crystallization kinetics. *Polymer* **2007**, *48*, 3125–3136.

# DIELECTRIC RELAXATION IN AMORPHOUS POLY (ETHYLENE-2,5-FURANOATE): COMPARISON WITH OTHER POLYESTERS

Aurélie BOURDET \*, Antonella ESPOSITO \*, Shanmugam THIYAGARAJAN \*\*, Laurent DELBREILH \*, Rutger J.I. KNOOP \*\*, Eric DARGENT \*

\* Normandie Univ, UNIROUEN Normandie, INSA Rouen, CNRS, Groupe de Physique des Matériaux, 76000 Rouen, France  
 \*\* Wageningen Food & Bio-based Research, P.O. Box 17, 6700 AA Wageningen, The Netherlands

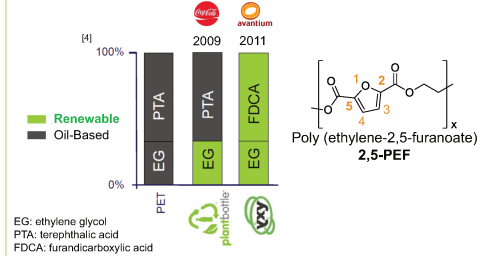
## Introduction

Over the last two decades, the depletion of fossil resources associated to climate change engendered international awareness. This is why biobased polymers present nowadays an interest for scientists and companies as a replacement of their petro-sourced homologues.

In the category of polyesters, poly (ethylene terephthalate) (PET) is the industrial reference for beverage packaging due to its appropriate physical properties (thermal, mechanical, optical and barrier properties)<sup>1</sup>. A closely related family of polyesters is obtained from 2,5-furandicarboxylic acid (2,5-FDCA). Poly (ethylene-2,5-furanoate) (2,5-PEF) has received much attention due to comparable thermal, yet improved barrier properties as compared to PET<sup>2,3</sup>.

In this work, amorphous 2,5-PEF was investigated by Differential Scanning Calorimetry (DSC) and Broadband Dielectric Spectroscopy (BDS) and compared with other polyesters, both bio- and petro-sourced. It was shown that PEF, in spite of similar thermal properties with respect to PET, has a different dielectric behavior. Through this study, the correlation between the two approaches (thermal vs. dielectric) to measure the glass transition temperature (T<sub>g</sub>) was established and the comparison between the considered polyesters was done via the relaxation map.

## Materials

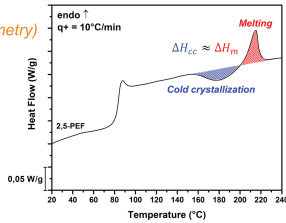


## Results and Discussion

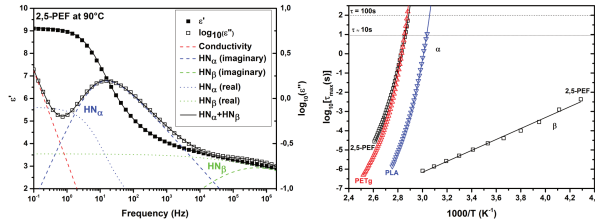
### DSC (Differential Scanning Calorimetry)

#### PROTOCOL

- ↑ 240 °C → hot plate
- ↔ 2 min
- ↓ Quenching → cold plate
- ⊙ measurement
- 0 °C to 190 °C → 10 °Cmin<sup>-1</sup>

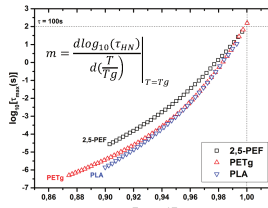


Samples	T <sub>g</sub> mid (°C)	ΔC <sub>p</sub> (Jg <sup>-1</sup> K <sup>-1</sup> )	T <sub>cc</sub> (°C)	T <sub>m</sub> (°C)
2,5-PEF	82 ± 1	0.42 ± 0.03	180 ± 1	215 ± 1
PET	73 <sup>3</sup> 76 <sup>1,5</sup>	0.34 <sup>6</sup>	130 <sup>6</sup>	243 <sup>3</sup> 247 <sup>5</sup>
PETg	76 <sup>6</sup>	0.28 <sup>7</sup>	/	/
PLA	62 <sup>8</sup>	0.51 <sup>8</sup>	127 <sup>8</sup>	157 <sup>8</sup>



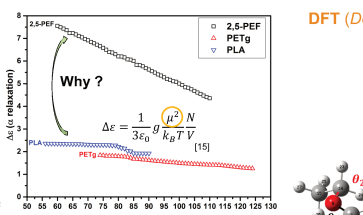
α and β relaxations can be fitted by Havriliak-Negami (HN) equation<sup>12,13</sup>:

$$\epsilon''(f) = \frac{\Delta\epsilon}{1 + (if/f_0)^{\alpha}\beta}$$



The Angell's classification<sup>14</sup> describes amorphous 2,5-PEF as "fragile" glass-formers.

α relaxation is associated to the rearrangement of the backbone (cooperative motions) → glass transition.  
 β relaxation depends on the chemical structure and the local molecular environment (localized motions).

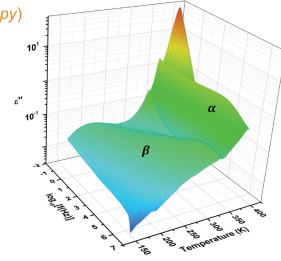


2,5-PEF presents an higher relaxation strength (Δε) compared to other polyesters.

### BDS (Broadband Dielectric Spectroscopy)

#### PROTOCOL

- ↑ 240 °C → hot plate
- ↔ 2 min
- ↓ Quenching → cold plate
- ⊙ measurement
- Temperature: -150 °C to 60 °C step: 10 °C
- 61 °C to 150 °C step: 1 °C
- Frequency: 2.10<sup>6</sup> Hz to 0.1 Hz



The 3D plot of the dielectric spectra for amorphous 2,5-PEF shows two processes:

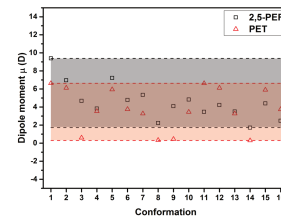
α relaxation follows a Vogel-Tamman-Fulcher (VFT) equation<sup>9-11</sup>:

$$\tau = \tau_0 \times \exp\left(\frac{DT_0}{T - T_0}\right)$$

β relaxation is in agreement with an Arrhenius law:

$$\tau = \tau_{0,\beta} \times \exp\left(\frac{E_{a,\beta}}{RT}\right)$$

Samples	T <sub>g=100s</sub> (°C)	T <sub>g=10s</sub> (°C)	D	T <sub>0</sub> (°C)	log <sub>10</sub> (τ <sub>0</sub> ) (s)	m	log <sub>10</sub> (τ <sub>0,β</sub> ) (s)	E <sub>a</sub> (kJmol <sup>-1</sup> )
2,5-PEF	73	77	5	28	-13	112	-15	56
PETg	75	77	3	44	-11	152		
PLA	54	54	5	17	-14	141		



Conformations were obtained by selecting 4 angles (θ<sub>1</sub>; θ<sub>2</sub>; θ<sub>3</sub> and θ<sub>4</sub>) on each monomer with two possible rotations (0 or 180°).

The dipole moment of 2,5-PEF can explain the higher value of Δε as compared to PET, PETg and PLA.

## Conclusions

- Amorphous 2,5-PEF presents two relaxations: α relaxation (glass transition) and β relaxation (local motion of ester group<sup>16</sup>).
- Amorphous 2,5-PEF is classified as a "fragile" glass-former<sup>14</sup>, but less fragile than PETg and PLA.
- The higher value of the relaxation strength for amorphous 2,5-PEF as compared to PETg and PLA can be explained by the symmetry of the molecule and the preferential orientation of the dipole moments present in the furan.

## Acknowledgments

The authors acknowledge financial support from the "Région Normandie". This work was performed in the frame of FEDER project SCAMPI.

## Contacts

aurelie.bourdet@etu.univ-rouen.fr  
 antonella.esposito@univ-rouen.fr



References  
 1. Stoclet et al., Polymer 72, (2015) 165-176  
 2. De Jong et al., ACS Symposium Series 1105, (2012) 1-13  
 3. Burgess et al., Macromolecules 47, (2014) 1383-1391  
 4. polymerinnovationblog.com  
 5. Thiyagarajan et al., Green Chem. 16 (2014) 1957-1966  
 6. Codou et al., Phys. Chim 18 (2016) 16647-16658  
 7. Couderc et al., J. Non-Cryst. Solids 353 (2007) 4334-4338  
 8. Cao et al., Thermochim. Acta (2003) 115-127  
 9. Vogel H, Phys Z. (1921) 645-6  
 10. Tammann et al., Z. Für Anorg. Allg. Chem. 156 (1926) 245-257  
 11. Fulcher, J. Am. Ceram. Soc. 8 (1925) 339-355  
 12. Havriliak et al., J. Polym. Sci. Part C Polym. Symp. 14 (1966) 99-117  
 13. Havriliak et al., Polymer. 8 (1967) 161-210  
 14. Angell, J. Non-Cryst. Solids. 73 (1985) 1-17  
 15. Schönals et al., Springer Berlin Heidelberg, (2003) 59-98  
 16. Nogales et al., J. Polym. Sci. Part B Polym. Phys. 37 (1999) 37-49

# PROPRIÉTÉS THERMIQUES ET MOBILITÉ MOLÉCULAIRE D'UNE NOUVELLE GÉNÉRATION DE COPOLYESTERS À BASE D'ACIDE FURANDICARBOXYLIQUE

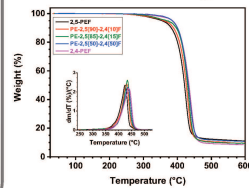
**Aurélien BOURDET\*, Antonella ESPOSITO\*, Shanmugam THIYAGARAJAN\*\*, Laurent DELBREILH\*, Marie-Rose GARDA\*, Rutger J.I. KNOOP\*\*, Eric DARGENT\***

\* Normandie Univ, UNIROUEN Normandie, INSA Rouen, CNRS, GPM, 76000 Rouen, France  
\*\* Food & Bio-based Research, WUR, P.O. Box 17, 6700 AA Wageningen, The Netherlands

**INTRODUCTION**  
 Parmi les polyesters, le poly (éthylène 2,5-furandicarboxylate) (2,5-PEF) est l'une des alternatives les plus prometteuses pour remplacer le poly (éthylène téréphtalate) (PET) en raison de ses propriétés comparables, voire supérieures à celles du PET [1,3].  
 Le 2,5-PEF présente une valeur du module de Young semblable à celle du PET mais un comportement fragile à la rupture [4]. C'est pourquoi une nouvelle génération de copolyesters obtenus à partir du mélange des deux isomères primaires [5], l'acide 2,5-furandicarboxylique (2,5-FDCA) et l'acide 2,4-furandicarboxylique (2,4-FDCA), pourrait constituer un moyen de réduire cette fragilité.

**DÉGRADATION THERMIQUE**

TGA (10 °C/min sous N<sub>2</sub>)

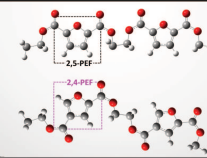


Echantillon	T <sub>5%</sub> (°C)	T <sub>max</sub> (°C)
2,5-PEF	362 ± 3	428 ± 1
PE-2,5[90]-2,4[10]F	372 ± 4	431 ± 3
PE-2,5[85]-2,4[15]F	372 ± 8	433 ± 3
PE-2,5[50]-2,4[50]F	384 ± 2	434 ± 4
2,4-PEF	388 ± 2	444 ± 1

Température d'utilisation des PEFs T ≤ 250 °C  
 L'augmentation du taux de 2,4-FDCA augmente légèrement la température de dégradation

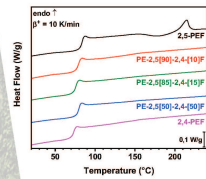
**MATÉRIAUX**

Echantillon	Ratio (H RMN)	M <sub>w</sub> (kg/mol)	M <sub>n</sub> (kg/mol)
2,5-PEF	100:00	18.2	15.3
PE-2,5[90]-2,4[10]F	90:10	14.7	09.1
PE-2,5[85]-2,4[15]F	85:15	15.2	09.2
PE-2,5[50]-2,4[50]F	50:50	23.3	13.2
2,4-PEF	00:100	11.4	08.5



**ANALYSE DSC CONVENTIONNELLE**

DSC (10 °C/min)

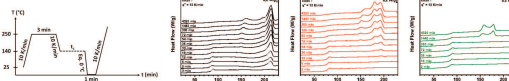


Echantillon	T <sub>g</sub> (°C)	Δc <sub>p</sub> (J/(g.K))	T <sub>m</sub> (°C)
2,5-PEF	82 ± 1	0.42 ± 0.03	215 ± 1
PE-2,5[90]-2,4[10]F	78 ± 1	0.42 ± 0.03	/
PE-2,5[85]-2,4[15]F	77 ± 2	0.45 ± 0.02	/
PE-2,5[50]-2,4[50]F	79 ± 1	0.43 ± 0.02	/
2,4-PEF	72 ± 1	0.42 ± 0.01	/

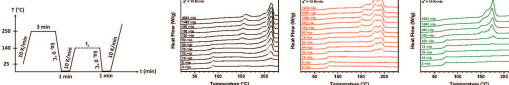
T<sub>g</sub> (copolymères) ≈ T<sub>g</sub>(2,5-PEF)  
 L'incorporation du 2,4-FDCA n'influence pas le Δc<sub>p</sub> mais impacte la cinétique de cristallisation (absence de pic de fusion)

**CINÉTIQUE DE CRISTALLISATION**

Depuis le fondu

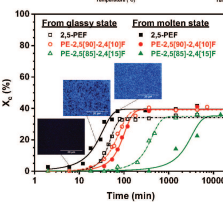


Depuis le vitreux



Carte de relaxation

Relaxation α :  
 Loi VFT [9-11]  
 $\tau = \tau_0 \exp\left(\frac{D_0}{T - T_0}\right)$   
 Relaxation β :  
 Loi d'Arrhenius  
 $\tau = \tau_0 \exp\left(\frac{E_a}{RT}\right)$

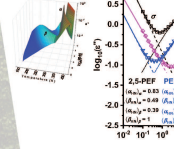


Degré de cristallinité

$X_c = \frac{\Delta H_m - \sum \Delta H_{cc}}{\Delta H_m}$   
 Cristaux de très petite taille (2,5-PEF ≈ 1 μm)  
 L'augmentation du taux de 2,4-FDCA augmente le temps de cristallisation  
 Polymorphisme [6-7]

**MOBILITÉ MOLÉCULAIRE**

DRS



Contributions de la permittivité imaginaire  
 Conductivité σ  
 2 fonctions d'Havriliak-Negami [8] pour extrapoler les relaxations α et β

$$\epsilon'' = \epsilon_{\infty} + \frac{\Delta\epsilon_{HN}}{[1 + (\omega\tau_{HN})^2]^2}$$

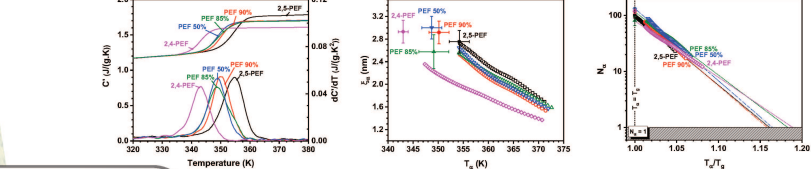
Relaxation α :  
 Les copolymères présentent un comportement plus proche de celui du 2,5-PEF  
 Relaxation β :  
 L'augmentation du taux de 2,4-FDCA augmente le temps de relaxation

Echantillon	T <sub>DRS</sub> (°C)	T <sub>DRS</sub> (°C)	m	E <sub>a</sub> (kJ/mol)
2,5-PEF	77	81 ± 2	117 ± 10	56
PE-2,5[90]-2,4[10]F	75	77 ± 2	112 ± 10	61
PE-2,5[85]-2,4[15]F	75	76 ± 3	112 ± 10	55
PE-2,5[50]-2,4[50]F	75	76 ± 2	118 ± 10	55
2,4-PEF	68	70 ± 1	125 ± 10	64

Indice de fragilité [12]

$m = \frac{d \log_{10}(\tau_{230})}{dT} \Big|_{T=T_g}$   
 L'incorporation du 2,4-FDCA n'impacte pas m et l'énergie d'activation  
 $T_{DRS} \approx T_{DRS-dsc}$

Donth étendu [13-16]



Longueur de coopérativité  
 $V_c = (\xi_c)^3 = \frac{(\tau_{glass} - \tau_{liquid})}{\rho(\delta T)^2} k_B T_g^2$

Nombre d'unités monomères  
 $N_c = \frac{\rho V_c N_A}{M_0}$

L'incorporation du 2,4-FDCA n'impacte pas la taille des CRR

**CONCLUSIONS**

- Les copolymères semblent suivre une loi de mélange (propriétés intermédiaires à celles des homopolymères).
- La présence d'une faible quantité de 2,4-FDCA est suffisante pour perturber de manière significative la cinétique de cristallisation des copolymères.
- Le rapport 2,5/2,4 n'a aucune influence sur les mouvements coopératifs, mais semble affecter les mouvements localisés.

**REMERCIEMENTS**

Les auteurs remercient la région Normandie et le fond européen FEDER pour leur soutien financier dans le cadre du projet SCAMPI.

**CONTACTS**

aurelie.bourdet@etu.univ-rouen.fr  
 antonella.esposito@univ-rouen.fr

**ABBREVIATIONS**

- TGA : ThermoGravimetric Analysis
- DSC : Differential Scanning Calorimetry
- DRS : Dielectric Relaxation Spectroscopy
- CRR: Cooperatively rearranging region

**RÉFÉRENCES**

[1] Wu, J et al., *Macromolecules*, 45 (2012) 5069-5080.  
 [2] Burgess, S.K. et al., *Polymer*, 55 (2014) 6861-6882.  
 [3] Burgess, S.K. et al., *Polymer*, 56 (2015) 305-310.  
 [4] Knoop, R.I.J. et al., *J. Polym. Sci. Part A: Polym. Chem.*, 51 (2013) 4191-4199.  
 [5] Thiyagarajan, S et al., *RSC Advances*, 3 (2013) 15678-15686.  
 [6] Tsanaktsis, V et al., *Crystal Growth & Design*, 15 (2015) 5505-5512.  
 [7] Mihm, L et al., *Polymer*, 10 (2018) 796.  
 [8] Havriliak, S et al., *J. Polym. Sci. Part C Polym. Symp.*, 14 (1966) 99-117.  
 [9] Vogel, H., *Phys Z*, 22 (1921) 645-646.  
 [10] Fulcher, G.S., *J. Am. Ceram. Soc.*, 8 (1925) 339-355.  
 [11] Tamman, C and Hesse, W. *Z. Für Anorg. Allg. Chem.*, 156 (1926) 245-257.  
 [12] Angell, C.A., *J. Non-Cryst. Solids*, 73 (1985) 1-17.  
 [13] Donth, E., *J. Non-Cryst. Solids*, 53 (1982) 325-330.  
 [14] Donth, E., *J. Polym. Sci. Part B Polym. Phys.*, 34 (1996) 2881-2892.  
 [15] Salter, A et al., *Phys. Rev. E*, 88 (2013) 042605.  
 [16] Salter, A et al., *Phys. Rev. E*, 81 (2010) 041805.

## Résumé

---

L'objectif de ce travail est d'explorer pour la première fois certaines propriétés physiques d'une nouvelle génération de copolyesters obtenus à partir d'un mélange physique de deux isomères : l'acide-2,5-furandicarboxylique (2,5-FDCA) et l'acide-2,4-furandicarboxylique (2,4-FDCA).

L'isomère 2,5-FDCA est aujourd'hui le plus étudié, car il est utilisé pour obtenir le Poly (Éthylène-2,5-Furanoate) (2,5-PEF), qui est le meilleur candidat biosourcé pour remplacer le géant de l'industrie plastique, le Poly (Éthylène-Téréphtalate) (PET). Son isomère, le 2,4-FDCA, a aussi été étudié puisqu'il permet d'obtenir le Poly (Éthylène-2,4-Furanoate) (2,4-PEF), qui possède une cinétique de cristallisation extrêmement lente. Il a été montré que la combinaison de ces deux isomères permet d'obtenir des copolymères ayant des propriétés ajustées et contrôlées.

Les dynamiques de relaxation moléculaire dans la phase amorphe, aussi bien localisées que coopératives, ont été étudiées dans une large gamme de fréquences et températures, selon les approches caractéristiques de l'étude des liquides formateurs de verre. Ensuite, l'étude a été orientée vers l'influence de la position du groupe carbonyle sur le furane sur l'aptitude à cristalliser et les cinétiques de cristallisation. Plusieurs techniques expérimentales ont été utilisées : calorimétrie différentielle à balayage (DSC), calorimétrie différentielle à balayage avec modulation de température (MT-DSC), spectroscopie de relaxation diélectrique (DRS) et mesure des courants de dépolarisation thermostimulés (TSDC).

**Mots-clés :** 2,5-PEF, 2,4-PEF, copolyesters, transition vitreuse, dynamiques moléculaires, cinétiques de cristallisation.

## Abstract

---

This work explored for the first time some physical properties of a new generation of copolyesters obtained from physical mixtures of two isomers: 2,5-furandicarboxylic acid (2,5-FDCA) and 2,4-furandicarboxylic acid (2,4-FDCA).

The 2,5-FDCA isomer is the most studied today because it is used to obtain Poly (Ethylene-2,5-Furanoate) (2,5-PEF), which is the best bio-based candidate to replace the giant of the plastic industry, Poly (Ethylene-Terephthalate) (PET). The 2,4-FDCA isomer has also been studied because it can be used to obtain Poly (Ethylene-2,4-Furanoate) (2,4-PEF), with an extremely slow kinetics of crystallization. It has been shown that the combination of these two isomers allows to obtain copolymers with adjusted and controlled properties.

The dynamics of molecular relaxation in the amorphous phase, both localized and cooperative, have been studied over a wide range of frequencies and temperatures, according to approaches typically used to study glass-forming liquids. Then, the investigation was directed towards the influence of the position of the carbonyl group on the furan ring on the ability to crystallize and the kinetics of crystallization. Several experimental techniques have been used: differential scanning calorimetry (DSC), modulate-temperature differential scanning calorimetry (MT-DSC), dielectric relaxation spectroscopy (DRS) and measurement of thermos-stimulated depolarization currents (TSDC).

**Keywords:** 2,5-PEF, 2,4-PEF, copolyesters, glass transition, molecular dynamics, crystallization kinetics.